DOE/MC/29101 – 5801
(DE98002010)

High-Resolution Subsurface Imaging and Neural Network Recognition: Non-Intrusive Buried Substance Location

Final Report
January 26, 1997

By:
Ben K. Sternberg
Mary M. Poulton

Work Performed Under Contract No.: DE-AC21-92MC29101

For

U.S. Department of Energy
Office of Environmental Management
Office of Technology Development
1000 Independence Avenue
Washington, DC 20585

U.S. Department of Energy
Office of Fossil Energy
Federal Energy Technology Center
Morgantown Site
P.O. Box 880
Morgantown, West Virginia 26507-0880

By
Laboratory for Advanced Subsurface Imaging
Department of Mining & Geological Engineering
University of Arizona
Tucson, Arizona 85721

Disclaimer

ABSTRACT

A high-frequency, high-resolution electromagnetic (EM) imaging system has been developed for environmental geophysics surveys. Some key features of this system include: (1) rapid surveying to allow dense spatial sampling over a large area, (2) high-accuracy measurements which are used to produce a high-resolution image of the subsurface, (3) measurements which have excellent signal-to-noise ratio over a wide bandwidth (31 kHz to 32 MHz), (4) elimination of electric-field interference at high frequencies, (5) large-scale physical modeling to produce accurate theoretical responses over targets of interest in environmental geophysics surveys, (6) rapid neural network interpretation at the field site, and (7) visualization of complex structures during the survey.

Four major experiments were conducted with the system: (1) Data were collected for several targets in our physical modeling facility. (2) We tested the system over targets buried in soil. (3) We conducted an extensive survey at the Idaho National Engineering Laboratory (INEL) Cold Test Pit (CTP). The location of the buried waste, category of waste, and thickness of the clay cap were successfully mapped. (4) We ran surveys over the acid pit at INEL. This was an operational survey over a hot site. The interpreted low-resistivity region correlated closely with the known extent of the acid pit.

ACKNOWLEDGMENTS

The high-resolution EM imaging system was successfully completed and operated due to the efforts of a large number of students and staff at the University of Arizona, including:

Charles Abernethy
Darin Ashley
John Baldridge
Ralf Birken
Dennis Bowers
Brad Carroll
Kin Chan
Robert Chiu
Pat Debroux
Ray DeChamps
Angela Dixon
Philip Erdie
Robert Esterline
Clark Fitzsimmons
Bret Hammers
Mary Hegmann
Maren Henley
Graham Irvine
James Laird
Tsylya Levitskaya
Terry Leach
Marc Levitt
Gary Lewis
Andrew Lim
Danny Long
James Madison
Robert Mallan
Jeff McDermott
Robert McGill
Trent McKinley
David Milligan
Thomas O'Haire
Vince Pawlowski
Michael Pegnam
Philip Sevier
Dave Stephens
Melissa Stubben
Emily Sullivan
Liang Tao
Scott Thomas
Jeff Toxey
Cary White
Derek White
Xianjin Yang
Zhaowen Yang
Catherine York
Pixuan Zhou

The "High-Resolution Subsurface Imaging and Neural Network Recognition: Non-Intrusive Buried Substance Location" Project was sponsored by the U.S. Department of Energy's Morgantown Energy Technology Center, under Contract No. DE-AC21-92MC29101 A001. We sincerely appreciate the support of this group.

The high-resolution EM imaging system has evolved over many years. Support for this development has included: Electric Power Research Institute, The Copper Research Center, U.S. Geological Survey, U.S. Bureau of Mines, Dept. of Energy, U.S. Army, and University of Arizona.

TABLE OF CONTENTS

TABLE OF CONTENTS--Continued

LIST OF ACRONYMS

1D	One Dimensional
2D	Two Dimensional
3D	Three Dimensional
AFCAL	Adjacent Frequency Calibration
ANSI	American National Standards Institute
ATV	All Terrain Vehicle
AVGTS	Avra Valley Geophysical Test Site
CRB	Colorful Rainbow
CTP	Cold Test Pit
DLL	Dynamic Link Libraries
DOE	Department of Energy
EDIS	Ellipticity Data Interpretation System
EM	Electromagnetic
EMID	Electromagnetic Integrated Demonstration
EMSIS	Electromagnetic Subsurface Imaging System
FCC	Federal Communications Commission
GPIB	General Purpose Interface Bus
GPR	Ground Penetrating Radar
HASCAL	High Accuracy Simultaneous Calibration
HF	High Frequency
IDL	Interactive Data Language
INEL	Idaho National Engineering Laboratory
LASI	Laboratory for Advanced Subsurface Imaging
LBL	Lawrence Berkeley Laboratory
LF	Low Frequency
MF	Medium Frequency
PC	Personal Computer
PE	Processing Element
PVC	Polyvinyl Chloride
RF	Radio Frequency
RMS	Root Mean Square
RWMC	Radioactive Waste Management Complex
RX	Receiver
TDEM	Time Domain Electromagnetics
TTL	Transistor Transistor Logic
TX	Transmitter
UA	University of Arizona
VETEM	Very Early Time Electromagnetics

EXECUTIVE SUMMARY

BACKGROUND

Ground Penetrating Radar (GPR) has been shown to be a powerful tool for environmental investigations. Unfortunately, in many areas the attenuation of radar energy is much too great for radar to be effective. In the southwestern United States, for example, the depth of penetration of radar energy in basin-fill sediments is typically only one meter. In order to reliably obtain a usable depth of penetration for environmental investigations, it is necessary to use lower frequencies than are normally used in GPR investigations.

A high-frequency EM imaging system that overcomes the depth restrictions of ground penetrating radars has been developed for the frequency range 31 kHz to 32 MHz. The system is an extension of an existing imaging system which has a frequency range of 30 Hz to 30 kHz (Sternberg et al., 1991). The 31 kHz-to-32 MHz frequency range is necessary to provide high resolution over the range of depths that are of interest in environmental geophysics surveys.

SUMMARY OF THE SYSTEM DEVELOPMENT AND CAPABILITIES

The ellipticity system developed under this contract was an extension of the basic design of an existing low-frequency system (30 Hz to 30 kHz) developed at the Laboratory for Advanced Subsurface Imaging (LASI) in the late 1980s, as well as other, more recent, developments. Many new technological advances had to be made in order to extend the frequency range to the 31 kHz to 32 MHz range. The line-source transmitter was replaced with a loop source. Nested coils were used in the transmitter and receiver antennas. Coil-cutting relays were built to reduce interference between coil segments. Very narrow-band filters were designed to reduce noise. Unique programmable gain amplifiers were designed. A new simultaneous calibration procedure was implemented to provide high accuracy data. Coefficients were derived to provide rotation-invariance for the receiver antenna. A fiber-optic link was built to link the transmitter and receiver. A telemetry system was installed to transmit data to the interpretation computer. All field equipment was mounted in ruggedized boxes for easy field implementation. All hardware was put under computer control using a graphical user interface. Extreme care had to be taken at all stages of design and construction to not introduce any electronic noise or interference into the system. All of the above tasks are non-trivial items. Developing a working system at high frequencies was a major technological breakthrough in electromagnetic geophysics. There are no systems in existence that offer comparable capability to the one described here.

We currently transmit 11 frequencies sequentially in binary steps over the range 31 kHz to 32 MHz. The transmitter uses a sinusoidal signal supplied from the receiver via a fiber-optic cable. The signal is amplified by a power amplifier and sent to a narrow-band tuned transmitter coil. The tuning is automatically controlled with digital signals supplied via a second fiber-optic cable from the receiver. Fiber-optic cables are required to avoid interference from the transmitter directly into the receiver as would occur if a metallic wire were used between the transmitter and receiver.

The signals are received at transmitter/receiver separations of generally 2 to 8 meters using a tuned three-axis receiving coil. The signals from each axis are amplified by a preamplifier on the coil frame, conveyed to programmable filters and programmable amplifiers, and then digitized by a 100 MS/S digitizing oscilloscope. The programmable filters, amplifiers and tuning are all controlled automatically via RS232 interface from an environmentally sealed and ruggedized computer. A waveform generator provides a calibration signal to the calibration coil located on the receiver coil. A second channel on the waveform generator provides the signal for the transmitter through the fiber-optic link. The digitizer and waveform generator are controlled via GPIB interface. The waveform generator and digitizer are precisely synchronized through a timing-clock connection. The data from the receiver coil are signal-averaged, filtered, and relayed to an interpretation computer via an RF telemetry link. The interpretation computer is located in a remote recording truck and uses neural networks and data display for interpretation in the field.

The transmitter and receiver modules are mounted on all-terrain vehicles (ATVs). These ATVs are 6-wheel drive, amphibious vehicles, and can handle extremely rough terrain. The transmitter coil is located on a boom in front of one ATV. Ahead of, or off to the side of, the transmitter ATV is the receiver ATV with the receiver coil located on a boom extending out the back.

We have chosen to calculate ellipticity of the magnetic field from the observed magnetic field quantities. We define H_x as the component of the magnetic field in the direction along the survey line. H_y is in the direction perpendicular to the survey line, and H_z is the vertical component. If the transmitter is emitting a sinusoidally varying signal, the total magnetic field at the receiver will trace an ellipse in the XZ plane as a function of time. The ellipticity is defined as the ratio of the major to minor axes of the ellipse.

DATA INTERPRETATION

The two fundamental components of the automated interpretation scheme are the neural networks and the data visualization shell. The data visualization shell provides the user interface to the neural networks, graphs of sounding curves, 1D forward modeling program, images of the data, and interpreted sections. The only interaction the user has with the trained neural networks is the selection of the networks to use for the interpretation through the visualization shell.

The data interpretation system makes possible a first-pass, real-time interpretation with neural networks directly in the field. The acquired ellipticity data are transferred either after each sounding is recorded or at any interval along the survey line via a wireless telemetry system from the acquisition computer on the survey line to the interpretation computer in the truck. All the parameters, which the system is capable of recording, are transferred as one binary sounding file for each station. An extraction program is then run to extract ellipticities from the sounding file for input to the interpretation and visualization software.

The software operates in a manual mode to give the user maximum flexibility in interpretation and display. The user selects all the networks through which the data should be routed. Each network interpretation is passed to a 1D forward modeling program so the ellipticity curves can be compared to the measured data. The fit of each interpreted sounding to the field data is calculated as the mean-squared error for the 11 frequencies in each sounding. The user decides which network gives the best fit and re-selects that network for the interpretation. The network is re-run for the sounding and the interpretation is plotted in a 2D section.

We have created 94 separate neural networks to do the 1D interpretation. On a 486 50MHz PC the neural network interpretation for one transmitter-receiver separation using 16 networks takes less than one second. To run four networks and compute the forward models for each network to find the best fit to the field data takes less than one minute, if no dielectric constant information is needed. If dielectric constant information is required, the forward modeling time for a two-layer case takes approximately one minute. Currently the interpretation and visualization system can only accommodate 1D interpretations. Interpretation of 3D targets is accomplished with separate networks not incorporated into the system due to the need to tailor each 3D interpretation to the requirements of the specific site.

EXAMPLES OF APPLICATIONS

The Laboratory for Advanced Subsurface Imaging (LASI) high-resolution subsurface imaging system transmits electromagnetic fields in order to probe the earth. The depth of penetration is determined by the frequency of the electromagnetic fields and the spacing between the transmitter and receiver. From the received electromagnetic fields, the electrical resistivity (and dielectric constant at high frequencies) are determined at various depths along a profile line. A cross section displaying resistivity (or dielectric constant) may be interpreted in terms of buried objects, fluid content, or varying lithology.

The technology used in the LASI high-resolution subsurface imaging system has developed over a period of approximately 10 years. These developments have been concentrated primarily in three frequency ranges: Low Frequency or LF - 30 Hz to 30

kHz; Medium Frequency or MF - 1 kHz to 1MHz; and High Frequency or HF - 30 kHz to 30 MHz. In the following five pages, we show some examples of applications of this technology. The examples include use of the LF, MF, and HF technology. Although each technology was developed through specific funding sources for specific problems, the complete set of technologies and frequency ranges are applicable to a wide set of problems encountered by government and private industries.

Mapping Buried Waste

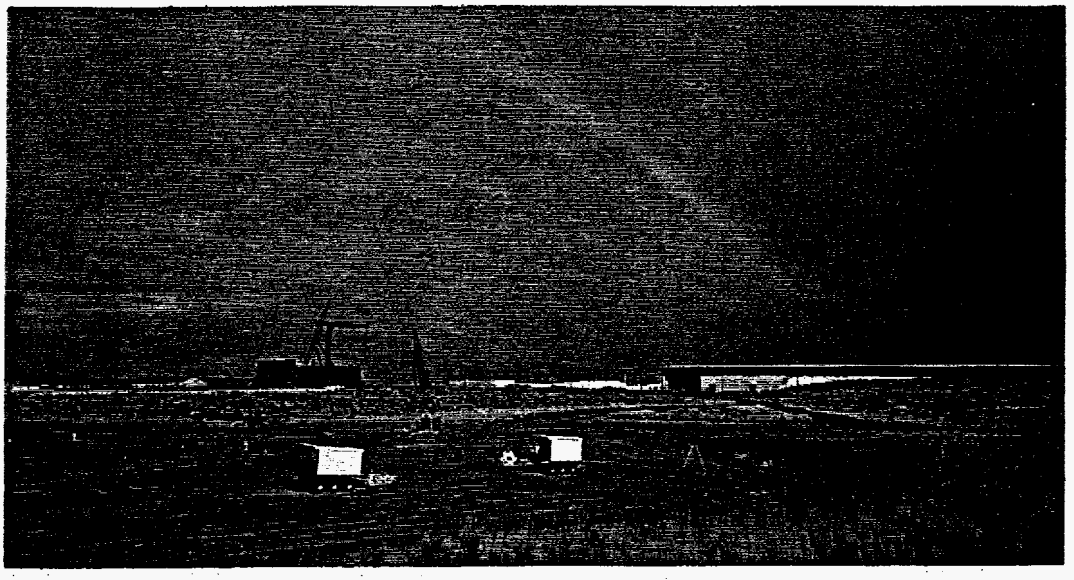

This photograph shows a survey being conducted at the Idaho National Engineering Laboratory (INEL), Cold Test Pit (CTP). The two All-Terrain Vehicles (ATVs) in the foreground contain the electromagnetic transmitter and receiver. The radioactive Waste Management Complex (RWMC) and colorful rainbow (CRB) are in the background. The CTP was designed to test subsurface imaging technology over a known set of targets. This technology will eventually be applied to mapping the unknown waste distribution in the RWMC.

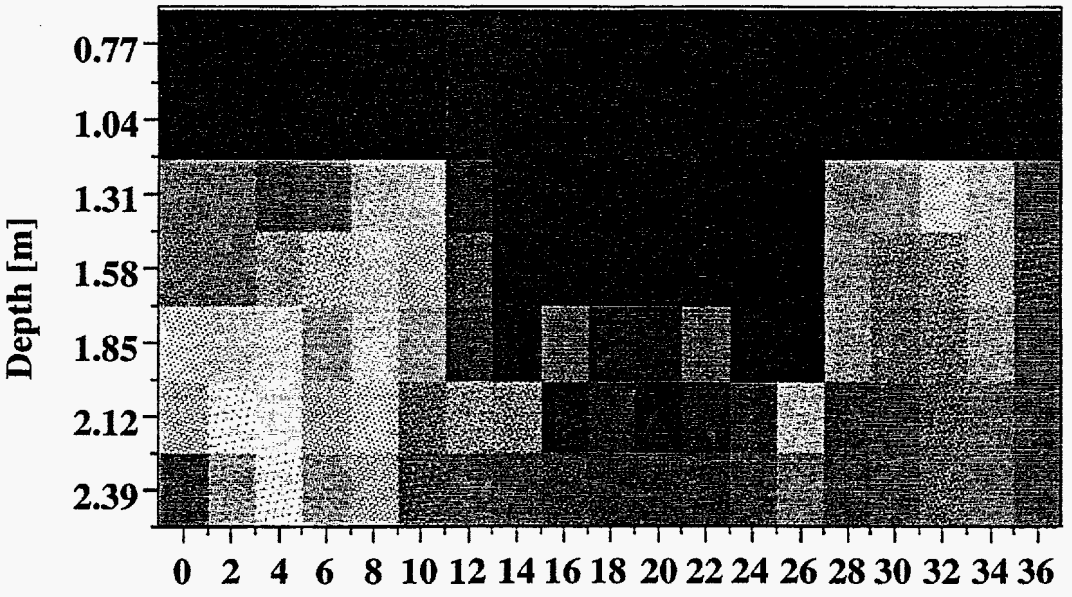

This cross section shows the resistivity distribution over the buried waste at the CTP. These data were collected with the HF system and a coil separation of 8 m. The color scale is related to the electrical resistivity of the ground. The horizontal scale is profile distance in meters. The changes in electrical resistivity outline the edges of the buried waste very accurately. This subsurface image also shows the thickness of the overlying clay cap. Furthermore, variations of the electrical resistivity correlate with different types of waste within the pit.

Mapping a Plume of Underground Fluid

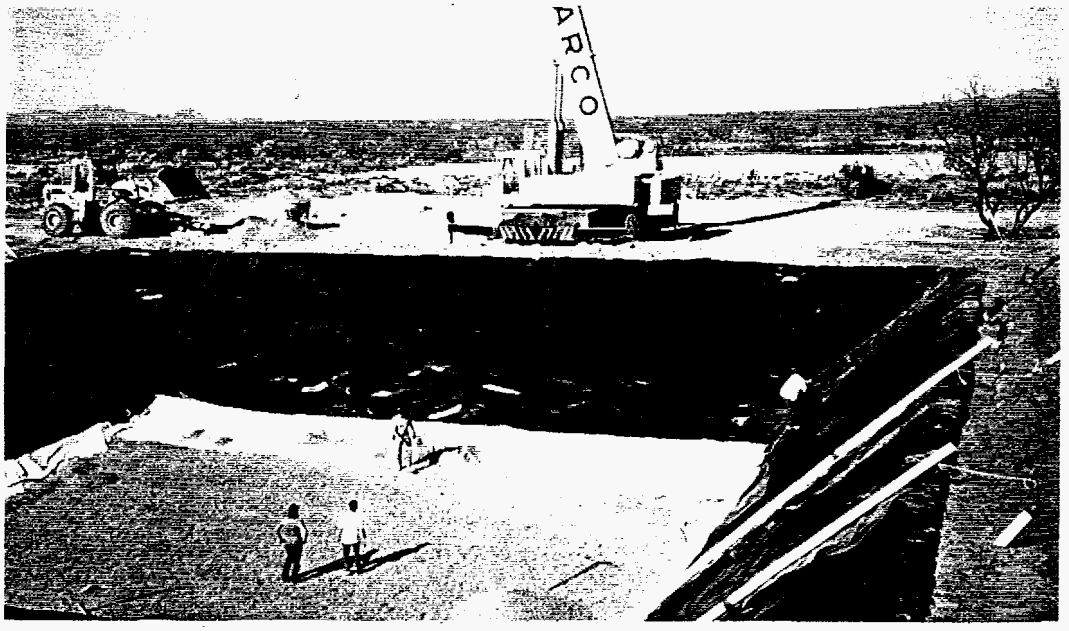

This photograph shows a lined basin constructed at the University of Arizona, Avra Valley Geophysical Test Site. The basin is 30 m by 30 m by 5 m deep. The entire basin was lined with high-density polyethylene (HDPE); drain pipes and gravel were placed in the bottom and the basin was refilled with native soil. This test site provides a closed system for injection and retrieval of fluids. During the summer of 1992, 24,170 liters of water were injected along a 1 m by 25 m strip at the center of the basin.

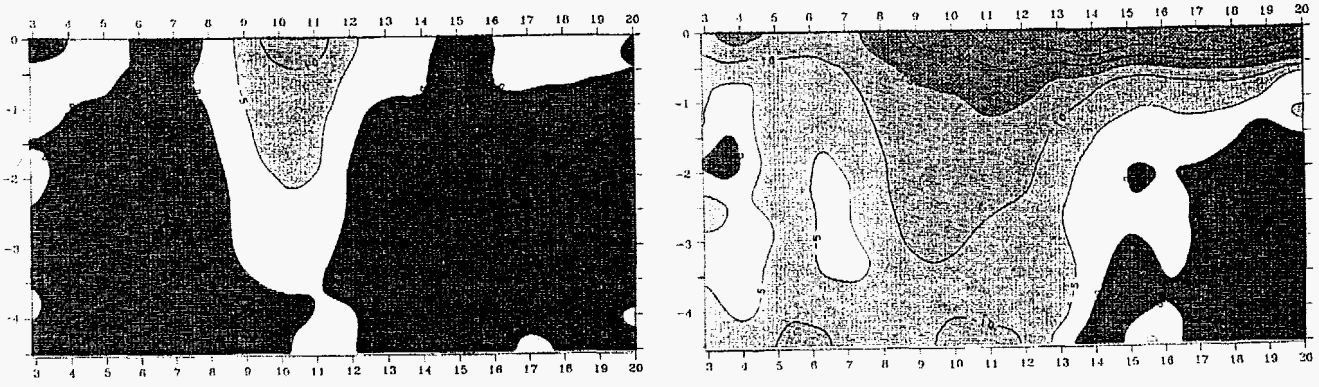

The figure on the left shows the difference in electrical resistivity of the ground between the beginning of the injection and one day after the start. The horizontal scale is profile distance in meters. The vertical scale is depth in meters. The small blue region (more negative than -10 ohm-m) shows the location of the plume of injected water. These data were collected with the LF system. A long-line source was oriented parallel and offset 10 m from the injection region. The receiver line was perpendicular to the line source and the injection region. The figure on the right shows the difference in electrical resistivity of the ground between the beginning of the injection and 17 days after the start of the injection. The blue area (more negative than -10 ohm-m) has increased in depth and spread out. There was a very close correspondence between these images of the fluid location determined from the surface measurements and images based on 25 electric well-log and neutron probe measurements located in the center of the basin. The high-accuracy calibration method used in the ellipticity system makes it possible to accurately map the flow of fluids over a long period of time.

Mapping Disturbed Ground

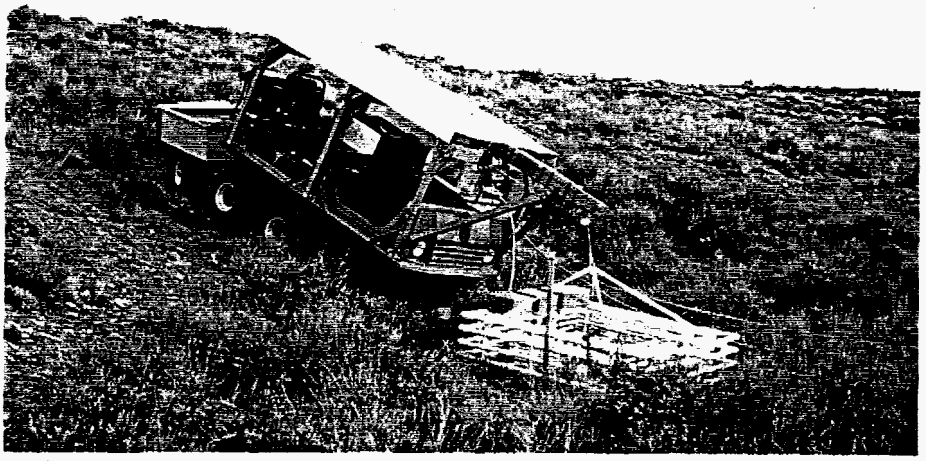

This photograph shows the 6-wheel drive all-terrain vehicle (ATV) carrying the transmitter coil at a site near Rock Springs, Wyoming. The site contained some rugged topography which the ATVs were able to handle quite easily. The profile lines were run over the site of an abandoned underground coal mine which was on fire. The objective was to map the location of the current fire front.

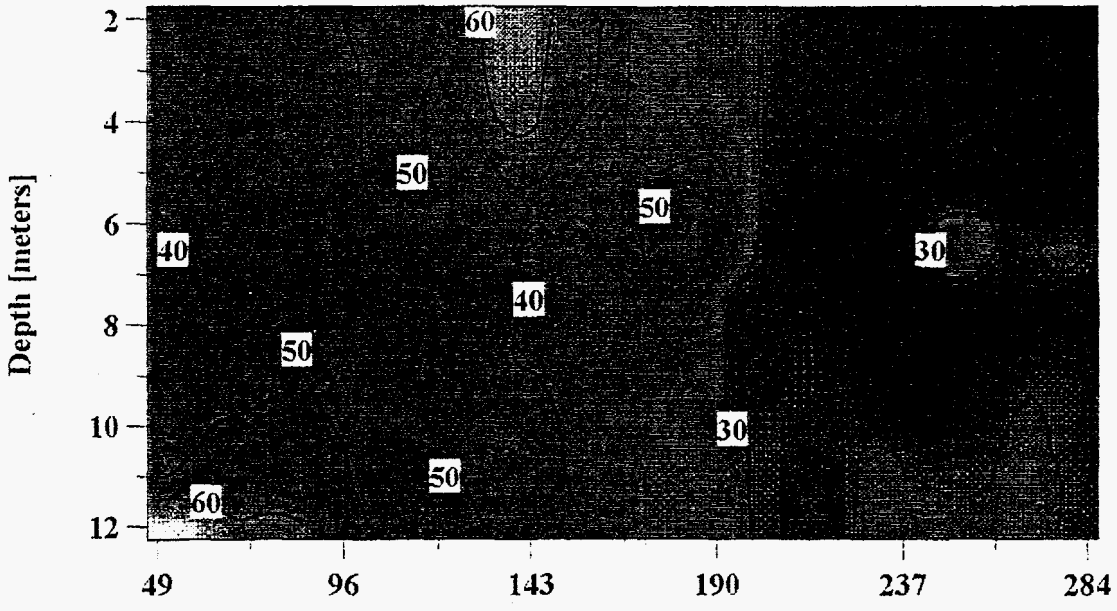

This figure shows one of the cross sections of electrical resistivity versus depth. The horizontal scale is profile distance in meters. These data were collected with the MF system and a coil spacing of 32 m. The low resistivities on the right of this figure are interpreted to be due to disturbed ground caused by the underground fire. The interpreted disturbed zone on this subsurface image as well as adjacent profile lines were used to produce a map of the fire front which was in excellent agreement in those areas where the fire front was known from independent information.

Mapping Tunnels

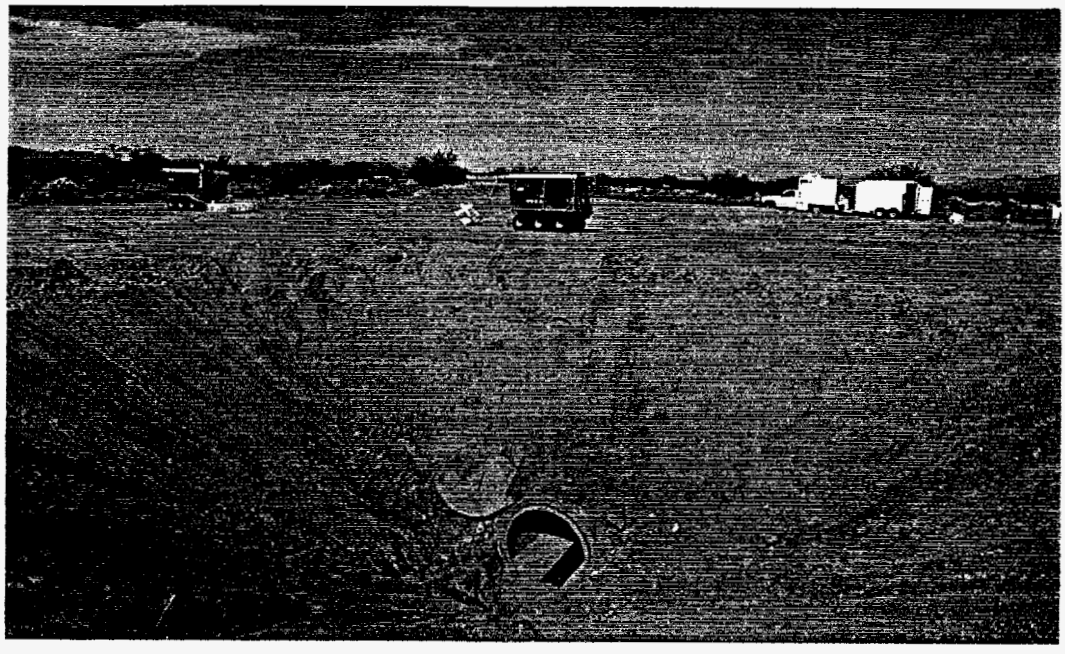

This photograph shows a tunnel located at the University of Arizona, Avra Valley Geophysical Test Site. The tunnel is a 1 m diameter, reinforced concrete pipe, buried 3 m below the surface. The transmitter and receiver ATVs are visible above the tunnel entrance surveying a profile line. Also visible in the background is an instrument truck which houses the data interpretation computer. Data are telemetered from the ATVs to the instrument truck for near-real-time interpretation. This in-field interpretation allows adjustment and refinement of the survey parameters before the equipment is moved from the site as well as immediate decisions concerning other follow-up work such as drilling or remediation.

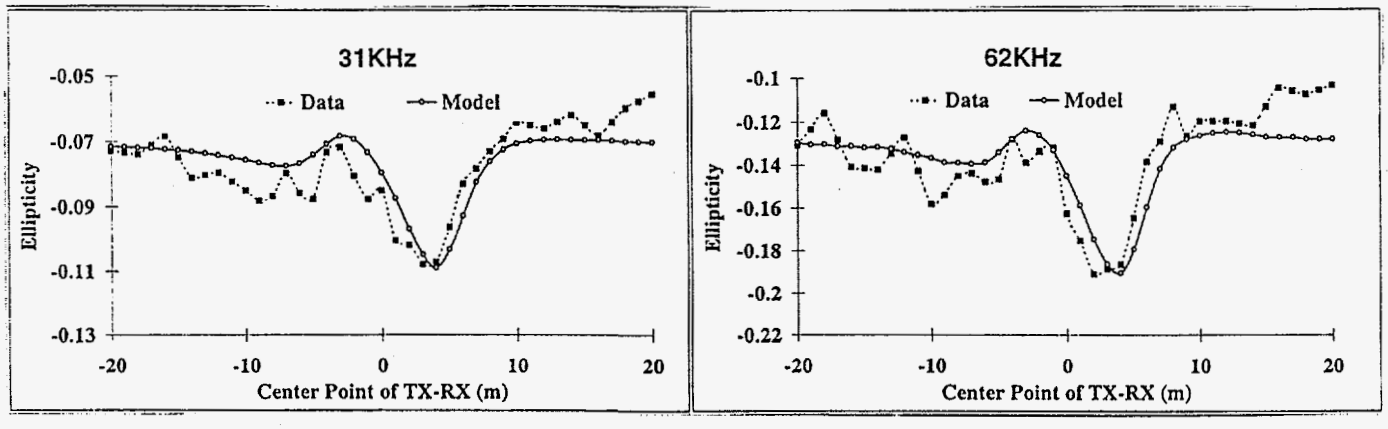

These two plots show the measured magnetic fields over the tunnel (recorded as the ellipticity of the magnetic field). Also shown is a calculation of a theoretical magnetic field ellipticity curve for the known tunnel location and size. There is a good match between the theoretical and measured curves. The theoretical curve is sensitive to the location and depth of the tunnel and these parameters are therefore well determined by these data. This system was also used over a tunnel at the Nevada Test Site (NTS). This tunnel was at a depth of 30 meters. Again the LASI high-resolution subsurface imaging system detected the tunnel and determined its location and depth. Both the MF and the HF systems were used at the Avra survey with a coil separation of 9 m. The MF system was used at NTS with a coil separation of 90 m.

Mapping Contaminated Soils

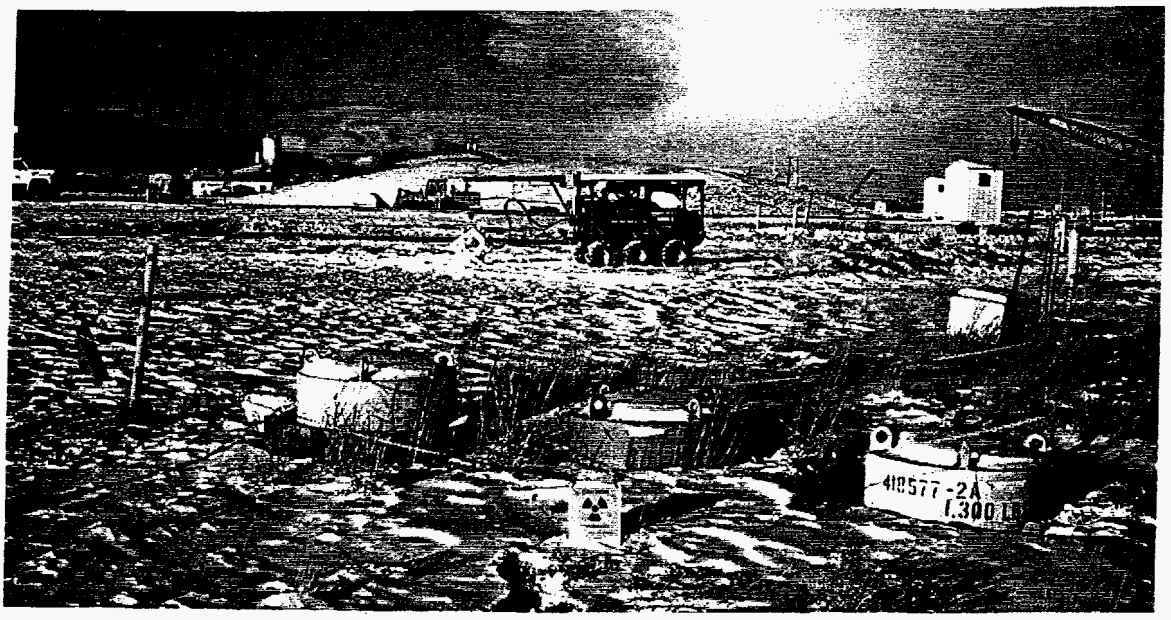

This photograph shows a survey being conducted at the INEL, RWMC, acid pit. This site had been used in the past for dumping acid containing radioactive materials and other contaminants into the soil. The precise location of the contaminants was not well known. This was an operational survey to provide information for remediation of the site. The site also contains some surface radioactivity as shown by the sign in the foreground.

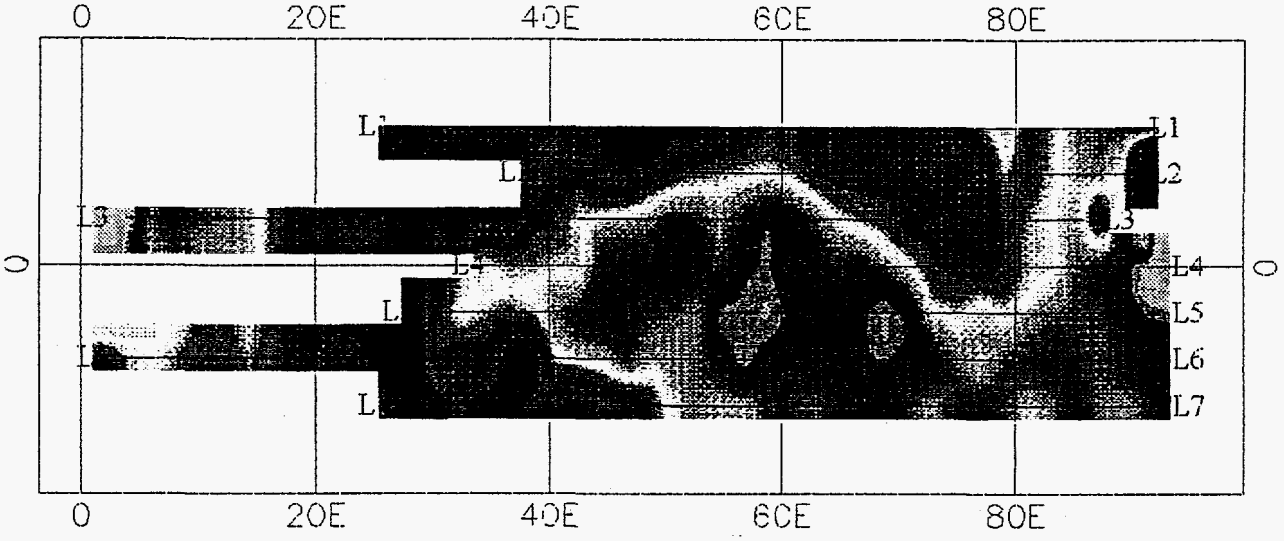

This plan map shows the distribution of subsurface resistivities based on ellipticity measurements at a frequency of 62 kHz. This frequency corresponds to a depth range of approximately 2-to-2.5 meters. These data were collected with the HF system at a coil spacing of 8 m. The red color (which corresponds to low electrical resistivities, of the order of 25 ohm-m) in the center of the map shows the location of the most heavily contaminated soil. The blue color (of the order of 40 ohm-m) shows background soil response. The red color on the far left of the map shows the location of solid waste in an adjacent disposal cell. The red color on the far right shows the location of buried utilities beneath a road. Other frequencies were used to map the concentration of contaminants at various depths. This survey provided much more detailed information on contaminant location than previous electromagnetic (EM) conductivity surveys at this site. The soils at this site are too conductive for ground penetrating radar (GPR) to be effective. The LASI EM systems can provide high-resolution subsurface maps in a wide variety of circumstances where other conventional methods are too limited.

ASSESSMENT OF CURRENT STATUS AND FUTURE PLANS

The objective of this project was to develop a high-frequency electromagnetic sounding system which was optimized for the relatively shallow depths of investigation found in environmental investigations. We believe we have been very successful in developing an efficient system which can rapidly profile the shallow subsurface and produce cross sections which can locate important objects for environmental purposes. In the process of developing this subsurface imaging system, a number of new and unique techniques have evolved, including new technology for sensing and acquiring the magnetic fields that are used for the measurements. We have designed a procedure for eliminating electric-field interference so that accurate measurements can be made at high frequencies. We have also developed new and innovative methods using neural networks for displaying and interpreting the data.

This system provides the potential for much greater depth of investigation (1-30 m) than GPR in conductive soils. It also provides wider bandwidth along with rapid surveying than conventional EM systems. In particular, it provides high-frequency data from which the dielectric constant of the subsurface can be interpreted.

Our demonstration surveys, at the INEL and other locations, have shown that this system is a significant advance in the state-of-the-art for high-resolution subsurface imaging. We have successfully mapped features with greater spatial and depth resolution than conventional EM techniques.

The system developed here currently exists in prototype form. Although the prototype is a fairly large system, it is very flexible and is particularly suitable for optimization at specific field sites. This technology can be adapted to lightweight field recording systems which would be more suitable for routine application by field crews with minimal training. The cost for a small, portable system which incorporates the new developments from this project would probably be of the order of $100,000, i.e. about the same as current multi-frequency general-purpose geophysical instrument systems. We have discussed the adaptation of this technology with several companies which are interested in pursuing commercialization of this technology. We have also discussed the adaptation of this technology to airborne measurements with one company.

Although this technology could be commercialized now, we feel the next step is to develop a more diverse collection of case histories at DOE facilities to fully demonstrate the system's capabilities and limitations. Once this is accomplished, it should be easier to focus commercialization efforts on the key strengths of the system.

PURPOSE

Ground Penetrating Radar (GPR) has been shown to be a powerful tool for environmental investigations. Unfortunately, in many areas the attenuation of radar energy is much too great for radar to be effective. In the southwestern United States, for example, the depth of penetration of radar energy in basin-fill sediments is typically only one meter. In order to reliably obtain a usable depth of penetration for environmental investigations, it is necessary to use lower frequencies than are normally used in GPR investigations.

A high-frequency EM imaging system that overcomes the depth restrictions of ground penetrating radars has been developed for the frequency range 31 kHz to 32 MHz. The system is an extension of an existing imaging system which has a frequency range of 30 Hz to 30 kHz (Sternberg et al., 1991). The 31 kHz-to-32 MHz frequency range is necessary to provide high resolution over the range of depths that are of interest in environmental geophysics surveys.

INTRODUCTION

This report is divided into two parts: (1) a description of the EM imaging system hardware and neural network interpretation software. The description includes system developments on this contract, earlier developments, and other developments which occurred in parallel with this contract; (2) The results of a survey at the Idaho National Engineering Lab (INEL) Cold Test Pit (CTP) and Acid Pit. Further results are presented from measurements at the University of Arizona Avra Valley Geophysical Test Site and from measurements at the University of Arizona physical modeling tank.

BACKGROUND

The ellipticity system developed under this contract was an extension of the basic design of an existing low frequency system (30 Hz to 30 kHz) developed at LASI in the late 1980s, as well as other, more recent, developments. Neural network interpretation had been successfully used on a limited data set collected with that system.

Many new technological advances had to be made in order to extend the frequency range to the 31 kHz to 32 MHz range. The line-source transmitter was replaced with a loop source. Nested coils were used in the transmitter and receiver antennas. Coil-cutting relays were built to reduce interference between coil segments. Very narrow-band filters were designed to reduce noise. Unique programmable gain amplifiers were designed. A new simultaneous calibration procedure was implemented to provide high accuracy data. Coefficients were derived to provide rotation-invariance for the receiver antenna. A fiber-optic link was built to link the transmitter and receiver. A telemetry system was installed to transmit data to the interpretation computer. All field equipment was mounted in ruggedized boxes on ATVs for easy field implementation. All hardware was put under computer control using a graphical user interface. A data interpretation and visualization system was created that consolidated neural network interpretation, data visualization, forward modeling and 1D inversion. Extreme care had to be taken at all stages of design and construction to not introduce any electronic noise or interference into the system.

All of the above tasks are non-trivial items. Developing a working system at high frequencies was a major technological breakthrough in electromagnetic geophysics. There are no systems in existence that offer comparable capability to the one described here.

METHODOLOGY

HIGH-RESOLUTION SUBSURFACE ELECTROMAGNETIC IMAGING SYSTEM

Figure 1 shows a block diagram of the high-frequency EM imaging system. We currently transmit 11 frequencies sequentially in binary steps over the range 31 kHz to 32 MHz. The transmitter uses a sinusoidal signal supplied from the receiver via a fiber-optic cable. The signal is amplified by a power amplifier and sent to a narrow-band tuned transmitter coil. The tuning is automatically controlled with digital signals supplied via a second fiber-optic cable from the receiver. Fiber-optic cables are required to avoid interference from the transmitter directly into the receiver as would occur if a metallic wire were used between the transmitter and receiver.

The signals are received at transmitter/receiver separations of generally 2 to 8 meters using a tuned three-axis receiving coil. The signals from each axis are amplified by a preamplifier on the coil frame, conveyed to programmable filters and programmable

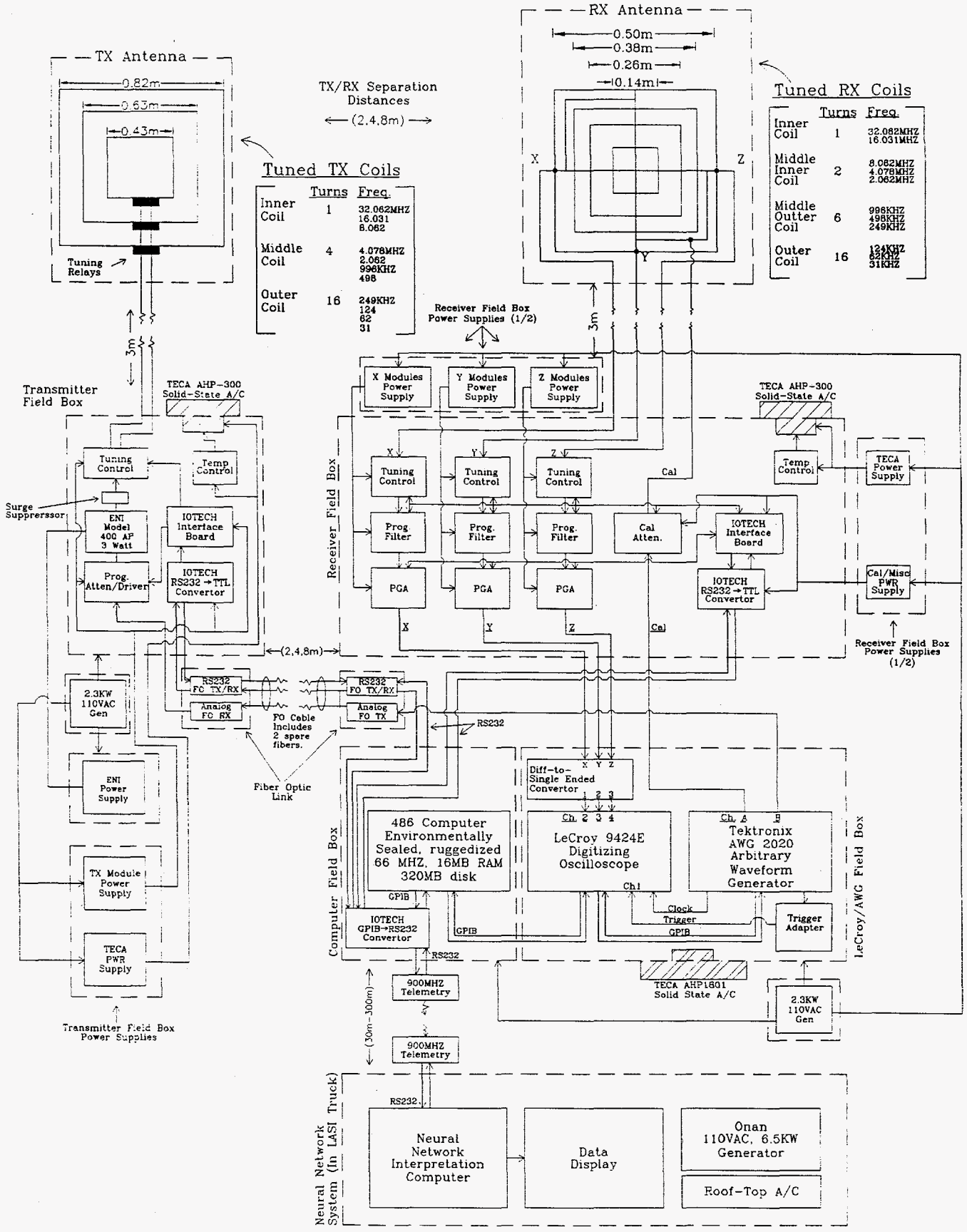

Figure 1. Block diagram of the high-frequency high-resolution ellipticity system.

amplifiers, and then digitized by a 100 MS/S digitizing oscilloscope. The programmable filters, amplifiers and tuning are all controlled automatically via RS232 interface from an environmentally sealed and ruggedized computer. A waveform generator provides a calibration signal to the calibration coil located on the receiver coil. A second channel on the waveform generator provides the signal for the transmitter through the fiber-optic link. The digitizer and waveform generator are controlled via GPIB interface. The waveform generator and digitizer are precisely synchronized through a timing-clock connection. The data from the receiver coil are signal-averaged, filtered, and relayed to an interpretation computer via an RF telemetry link. The interpretation workstation is located in a remote recording truck. The computer uses neural networks (described in a later section) and displays the data for interpretation in the field.

The transmitter and receiver modules are mounted on all-terrain vehicles (ATVs). These ATVs are 6-wheel drive, amphibious vehicles, and can handle extremely rough terrain. The transmitter coil is located on a boom in front of one ATV. Ahead of or off to the side of the transmitter ATV is the receiver ATV with the receiver coil located on a boom extending out the back.

We have chosen to calculate ellipticity of the magnetic field from the observed magnetic field quantities. Hoversten (1981), in a comparison of time- and frequency-domain EM sounding techniques, showed that the frequency-domain ellipticity measurement is superior to any other frequency-domain or time-domain measurement for EM soundings. He also showed that "the ellipticity measurement provides smaller parameter standard errors than the time-domain data". "In addition, the model parameters arrived at through the least squares inverse are much less correlated with each other when ellipticity is used."

We define H_X as the component of the magnetic field in the direction along the survey line. H_Y is in the direction perpendicular to the survey line, and H_Z is the vertical component. If the transmitter is emitting a sinusoidally varying signal, the total magnetic field at the receiver will trace an ellipse in the XZ plane as a function of time. The ellipticity is defined as the ratio of the major to minor axes of the ellipse.

$$e = \left| \frac{H_2}{H_1} \right| \tag{1}$$

The ellipticity (e) can be determined directly from measurements of the relative magnitude and phase of the H_X and H_Z fields.

$$e = \left| \frac{H_z \cos\alpha - H_x \sin\alpha}{H_z \sin\alpha + H_x \cos\alpha} \right| \tag{2}$$

where:

$$\tan(2\alpha) = \frac{2|H_z / H_x| \cos[\phi_z - \phi_x]}{1 - |H_z / H_x|^2} \qquad (3)$$

and ϕ_Z and ϕ_X are phases of vertical and horizontal components of the total field. The ellipticity measurement is discussed in Spies and Frischknecht (1991).

A number of novel features are included in the system design:

(1) The calibration coil supplies a calibration signal to the receiver coil at the same time that the data are being collected. The calibration coil is coupled equally to all three axes of the receiver coil. It is parallel to the x-axis coil over one quadrant, then follows the y-axis coil for another quadrant, then the z-axis coil for a quadrant, and continues on around completing a closed loop. This allows equal calibration signals on all three receiver axes simultaneously with the data measurement. The cal-coil driver has a high output impedance so that the calibration coil does not interfere with the received signal. Four calibration frequencies are transmitted, which are offset slightly in frequency from the data frequency and surround the data frequency. The system response at the data frequency is then interpolated from these four nearby frequency responses. A key feature is that the calibration is performed simultaneously with the data acquisition, thereby preventing any errors due to drift in the system response, as well as greatly increasing the speed of data acquisition. This procedure is known as AFCAL (Adjacent Frequency CALibration). It is an adaptation of the HASCAL method (High-Accuracy Simultaneous CALibration) described by Sternberg and Nopper (1990).

The motivation for making as high an accuracy measurement as possible is based on previous publications which show that if we were able to obtain unlimited precision in our measurements, we would be able to uniquely determine the variation of conductivity with depth. For example, Fullager (1984) investigated horizontal-loop frequency soundings and demonstrated that these methods "are, in principle, imbued with unlimited resolving power". Unfortunately, only a small amount of error in the measured electromagnetic fields can lead to a large amount of error in the interpreted subsurface resistivity structure. Our goal is to obtain as high-accuracy measurements as possible.

A further requirement for obtaining high resolution is the need to obtain data over a large and densely sampled spatial area and at many frequencies. The entire data acquisition process in this system is totally automated. A complete sounding may be made in less than one minute. Therefore, dense spatial sampling can be obtained, as well as rapid surveys of large areas. The wide bandwidth of this system fulfills the need for many frequencies. Although we certainly will not obtain unlimited resolution, we believe that the approach used in this system will provide greatly increased resolution over the current state-of-the-art.

(2) Both the transmitter and receiver coils have been optimized to obtain highly accurate data over a wide bandwidth. The coils consist of nested segments with

increasing area and increasing number of turns in the outer coils for the lower frequencies. Therefore, adequate sensitivity is obtained over the entire bandwidth. A great deal of effort has gone into the design of these coils; in particular, each coil segment is decoupled from the surrounding nested coils and each coil segment has been optimized for a particular frequency range.

(3) The standard procedure for calculating ellipticity uses just H_z and H_x. However, for high-accuracy measurements we also record the H_y component perpendicular to the transmitter-receiver line and determine the ellipticity from all three vectors. This method uses a mathematical rotation of the observed magnetic fields to the major and minor axes of the ellipse and is described in Bak et al. (1993). Basically, this procedure first determines the azimuth of the electromagnetic field polarization and then determines the ellipticity in this azimuth. The mathematical rotation greatly speeds up the measurement of ellipticity in comparison with mechanically orienting the receiver coils, which is a very time-consuming process. The coil can simply be placed on the ground in any orientation and the rotation algorithm automatically rotates the field components to the major and minor axis values of the magnetic-field ellipse.

(4) This system records in a frequency range which includes effects from both conduction currents and displacement currents. It is difficult to obtain reliable numerical modeling calculations of theoretical responses to complex targets in this frequency range. We have adopted a different procedure which involves the use of full-size physical models. A large modeling tank has been constructed at our test site in Avra Valley, Arizona, west of the University of Arizona campus. The tank is 20 m long by 3 m deep by 6 m wide. The transmitter and receiver coils are kept stationary to avoid variations in response due to background effects. Various targets are then moved in the tank along a profile line under the coils. Repeated measurements are made with the targets at different depths, orientations, and with different types of targets. This allows us to generate a large number of theoretical model responses for data interpretation, including neural network training.

(5) A method has been developed for canceling electric-field interference at the high frequencies used in this EM system. This involves averaging the coil-output voltage at two locations of the coil.

PICTORIAL OVERVIEW OF THE EM SYSTEM

Considerable effort during this project has been directed toward the construction of a prototype high-resolution subsurface imaging system. The block diagram in Figure 1 summarized the overall design. The following photographs show the various modules that comprise the complete prototype field system.

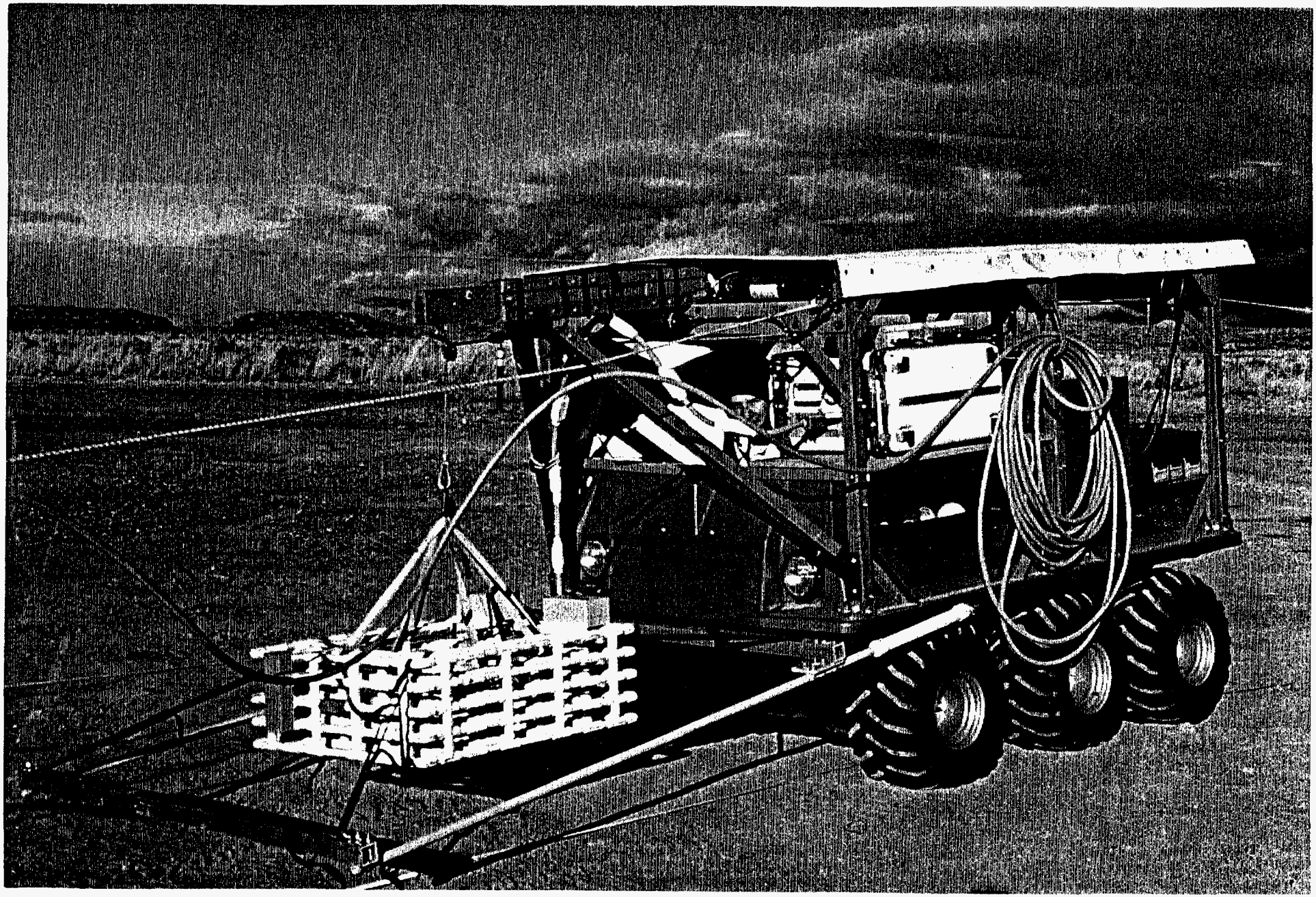

Figure 2. Photograph of the transmitter all-terrain vehicle (ATV) with the transmitting antenna suspended from the boom in front of the ATV. The transmitter ATV and the receiver ATV are linked by the gray fiber-optic cable.

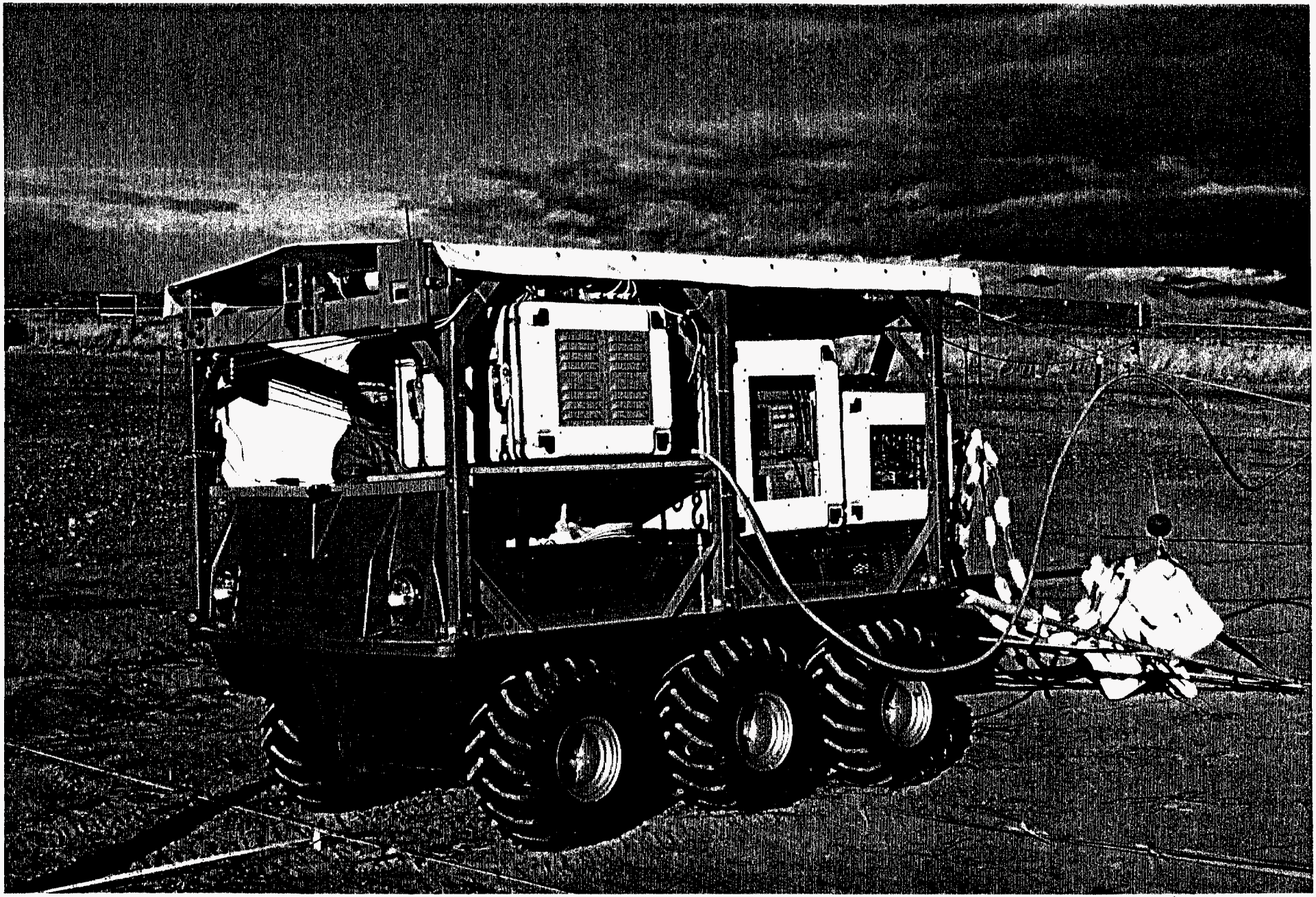

Figure 3. Photograph of the left side of the receiver all-terrain vehicle. In normal field operation this receiver ATV leads and the transmitter ATV follows along the profile line. The white instrument enclosures along the side of the ATV contain the field computer, digitizing oscilloscope, waveform generator, amplifiers, and filters.

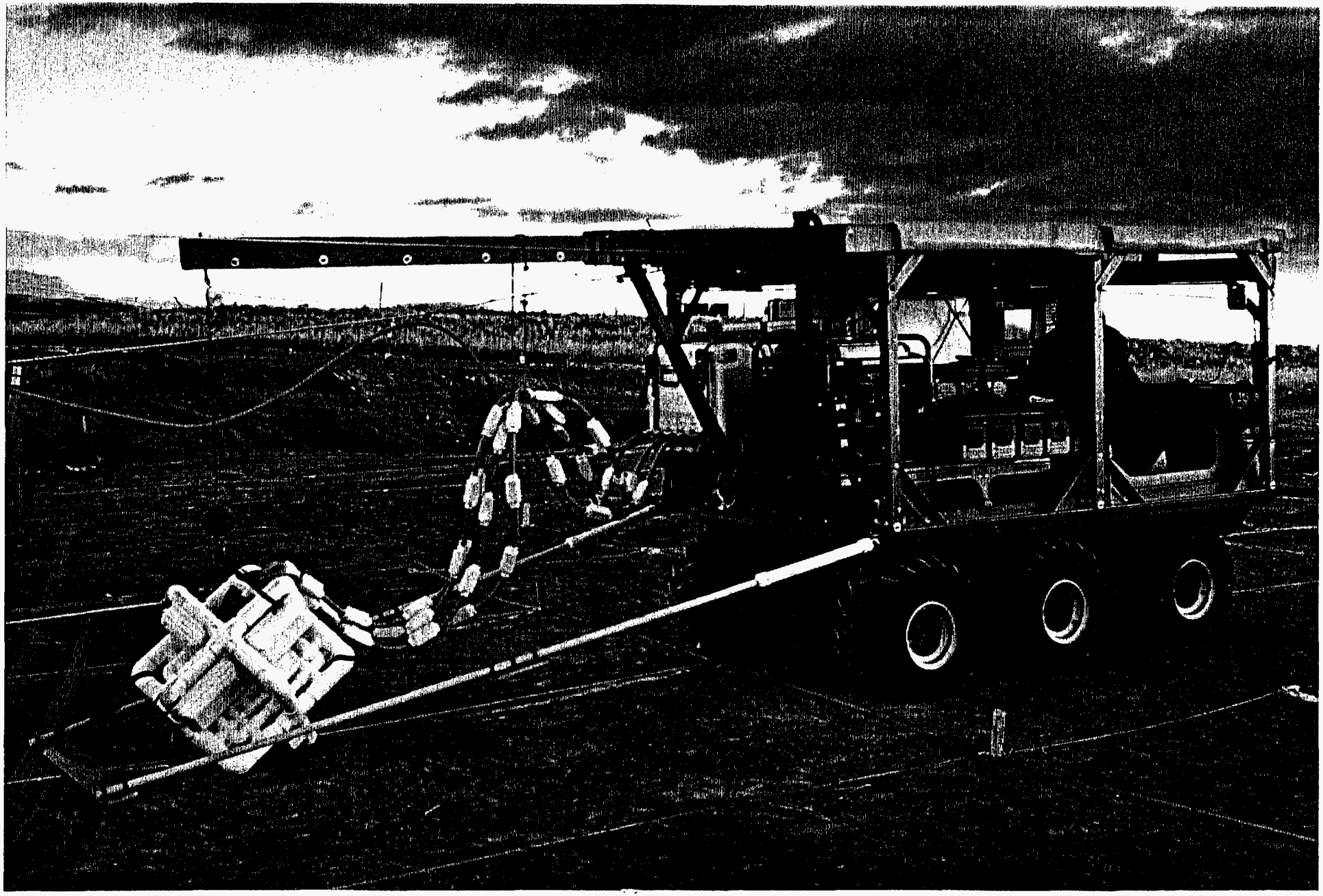

Figure 4. Photograph of the right side of the receiver all-terrain vehicle with the receiver antenna suspended from the boom projecting behind the ATV.

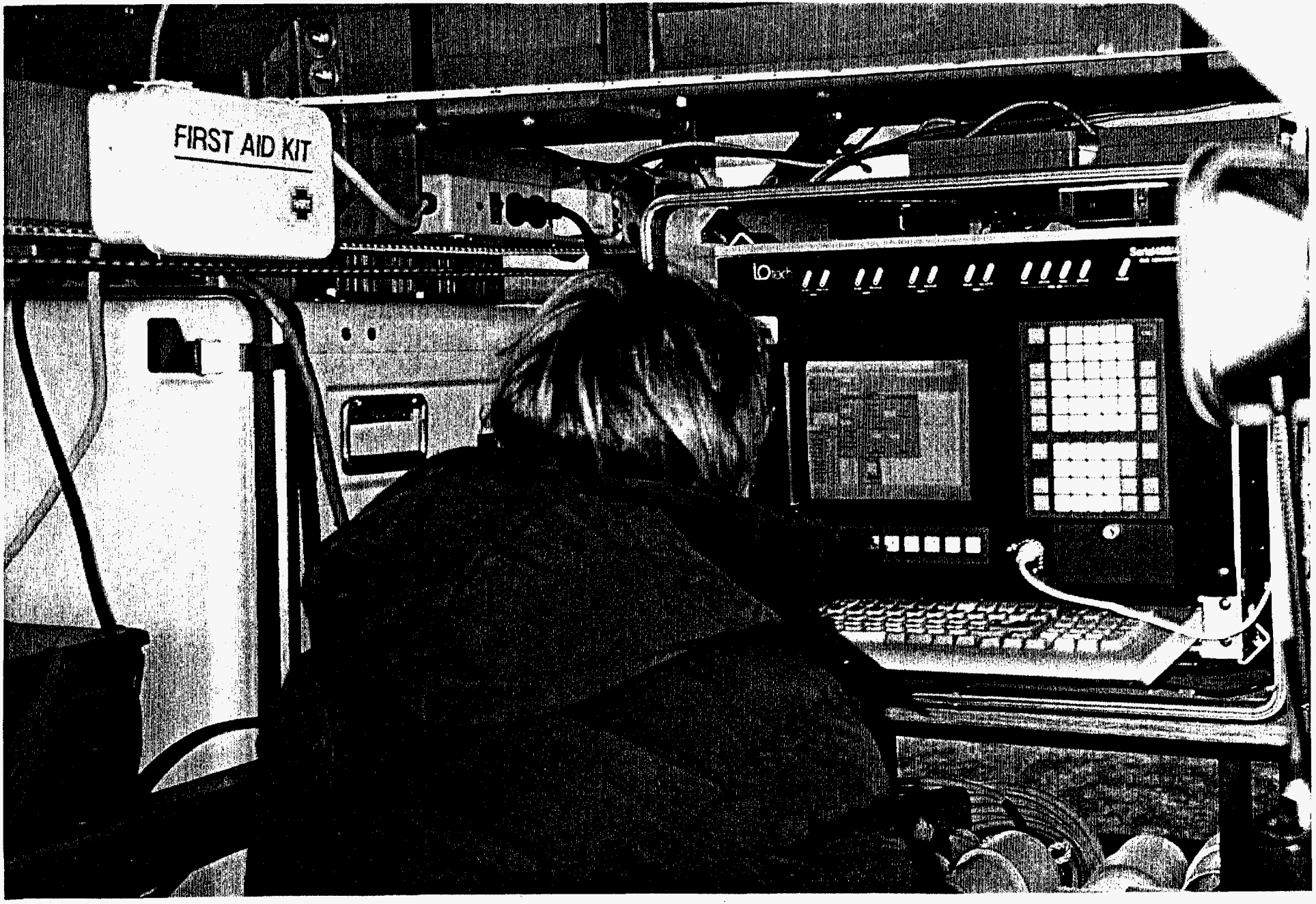

Figure 5. Photograph of the environmentally-sealed and ruggedized field computer. This computer controls all data acquisition and processing functions.

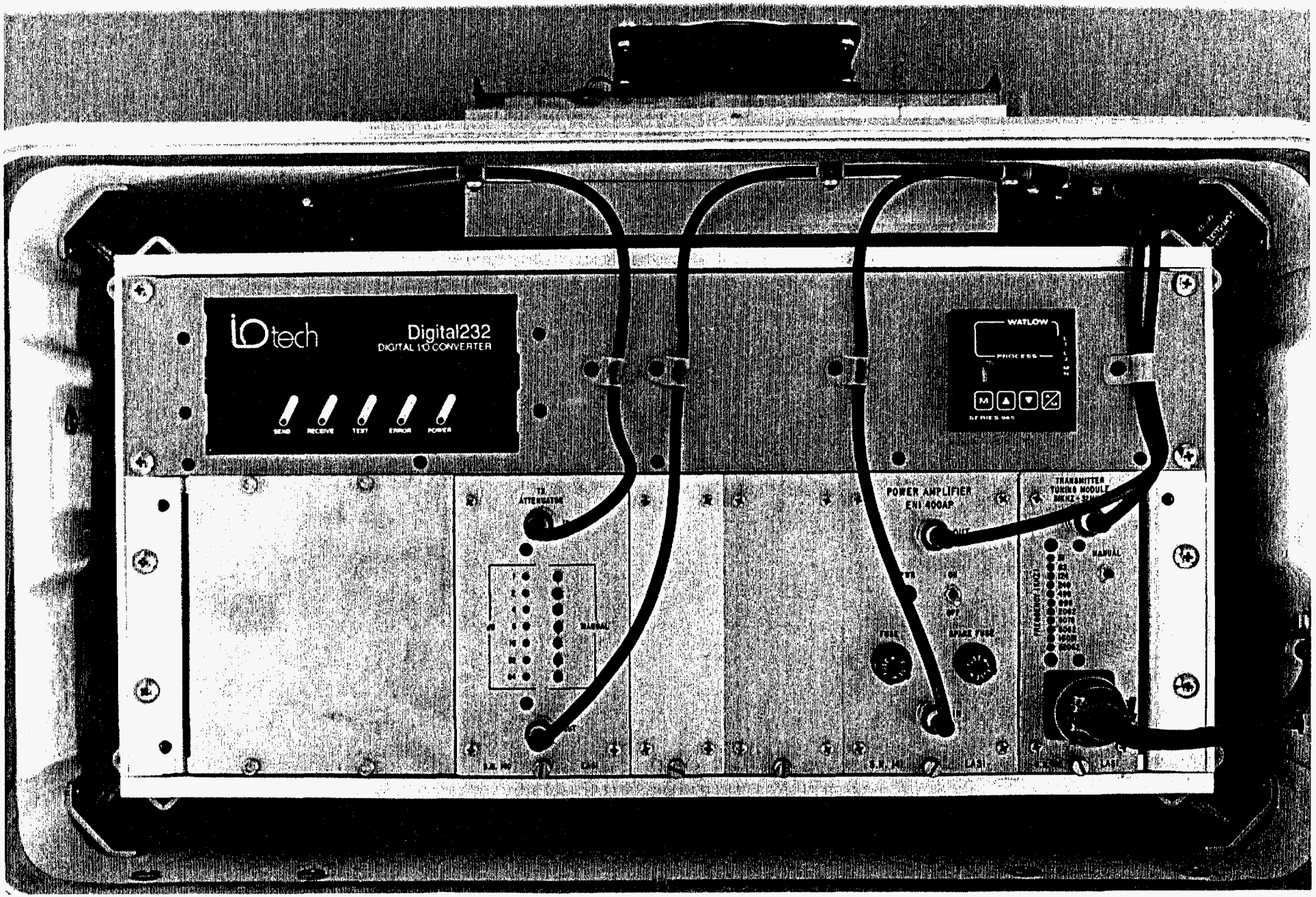

Figure 6. Photograph of the transmitter modules. Near the left on the lower panel is the transmitter attenuator. To the right is the 31KHz-32MHz power amplifier. On the bottom right is the transmitter tuning module. On the top left is the RS232 -to-TTL converter, and on the upper right is the temperature controller for the TECA solid-state air conditioner mounted on the top of the enclosure.

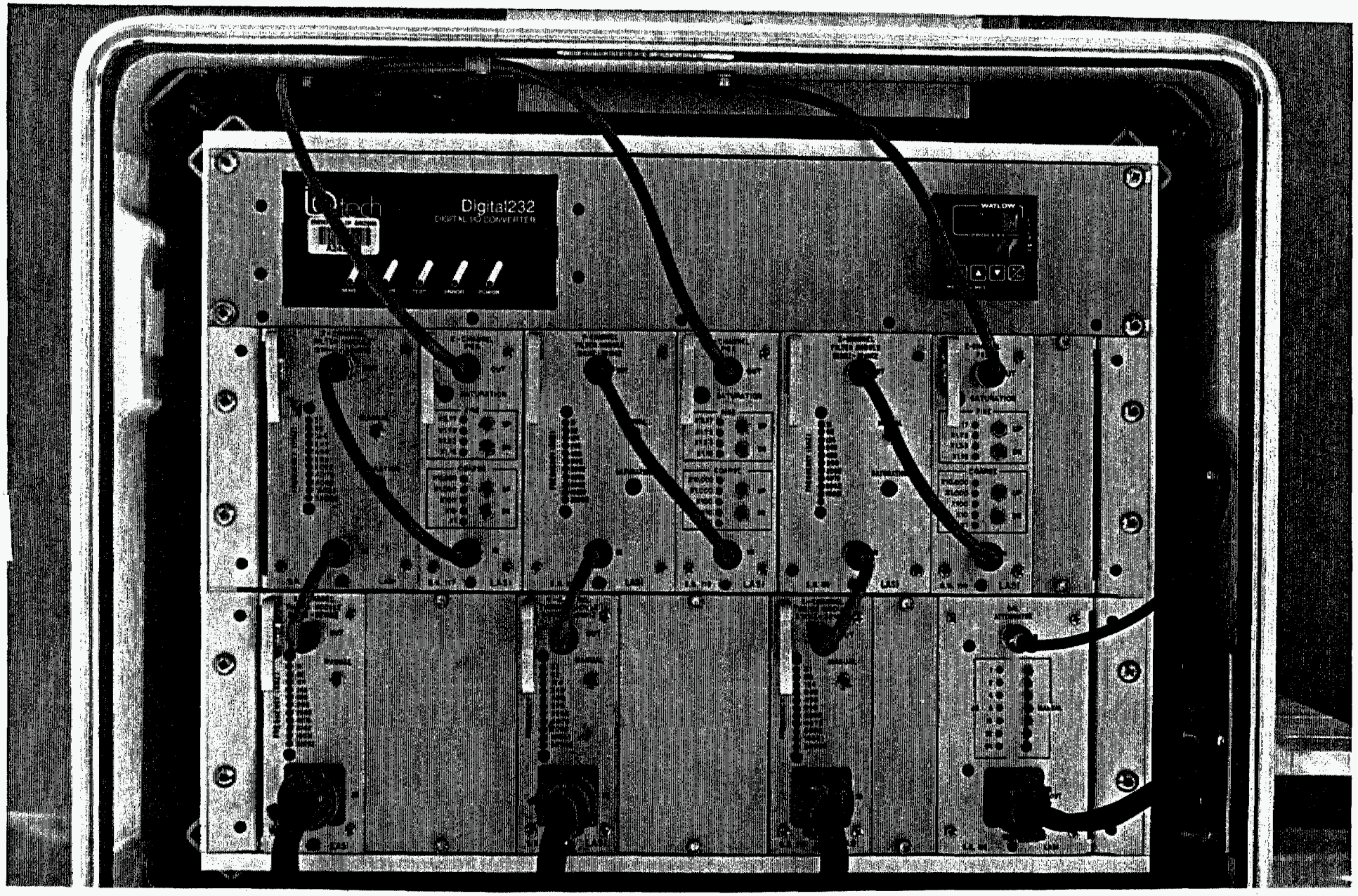

Figure 7. Photograph of the receiver modules. There are three modules for each of three channels (coil axes). In the lower left corner is the x-channel tuning module; above that is the x-channel filtering module; and to the right of that is the x-channel programmable gain amplifier. The next set of three modules is for the y-channel, and the next set of three modules is for the z-channel. In the lower right-hand corner is the calibrator attenuator. In the upper left is the RS232-to-TTL converter, and in the upper right is the temperature controller for the TECA solid-state air conditioner, which is mounted on the top of the enclosure.

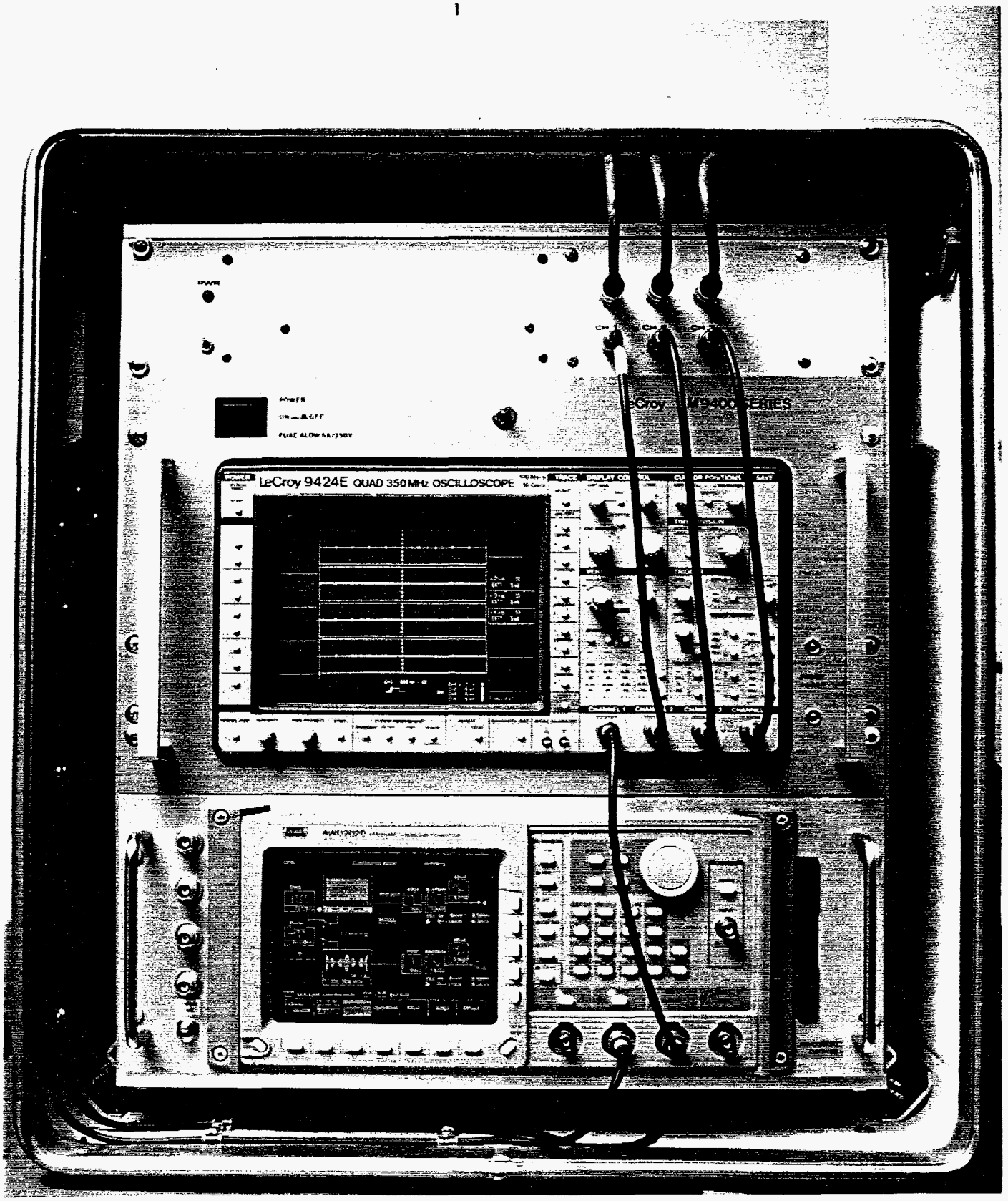

Figure 8. Photograph of the digitizing oscilloscope and arbitrary waveform generator.

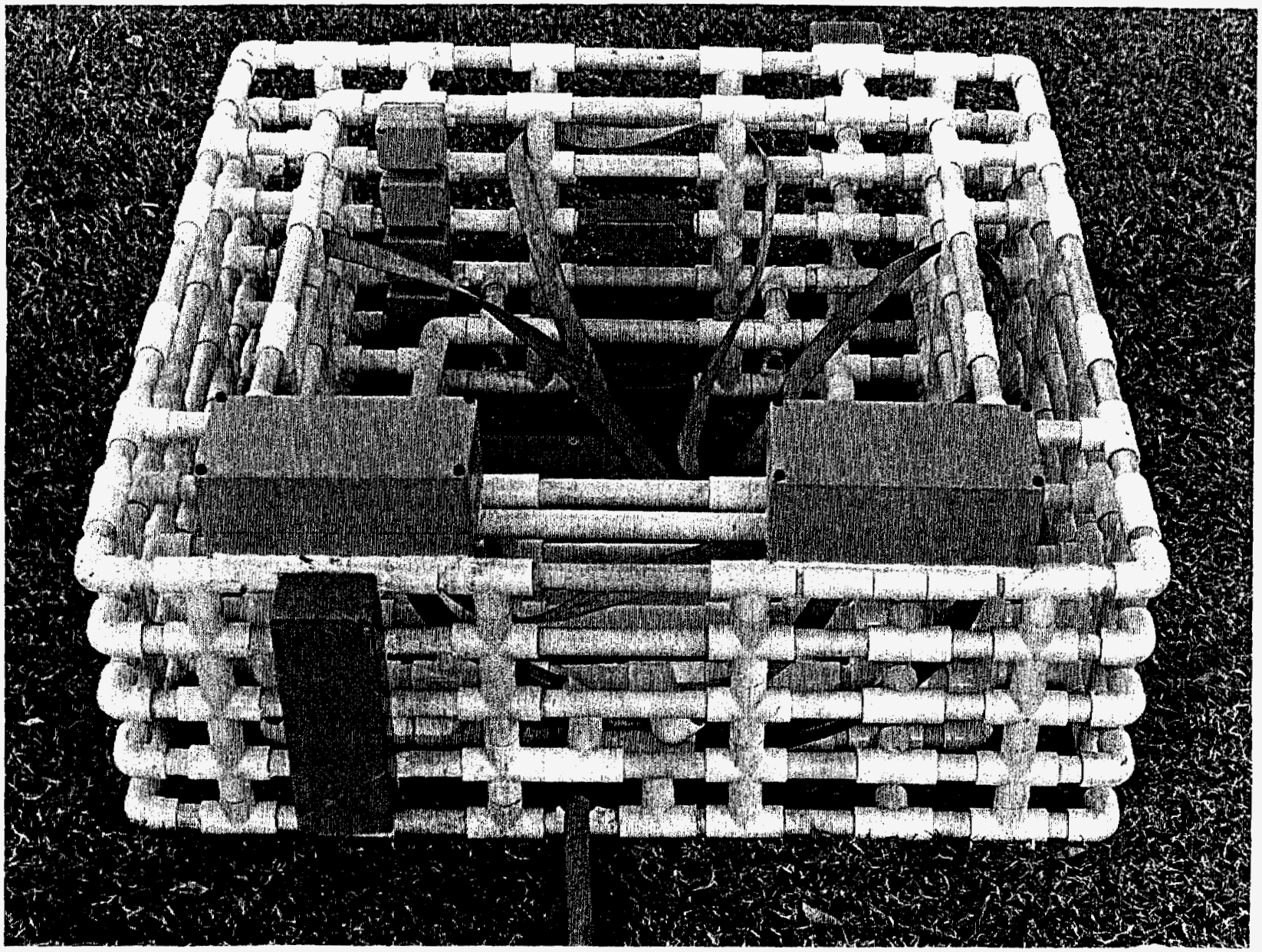

Figure 9. Photograph of the 31kHz-32MHz transmitting antenna. The antenna consists of three nested sections. There are 16 turns in the outer section (4 turns in each of the top four PVC pipes). This coil is used for the lowest frequencies. The middle section has 4 turns (1 turn in each of the top four PVC pipes). This coil is used for the middle frequencies. The inner section is a 1-turn coil and is used for the highest frequencies. The tuning modules are mounted in the boxes located on top of the nested coils, and the relay cutting coils are mounted in the boxes along the sides of the coil.

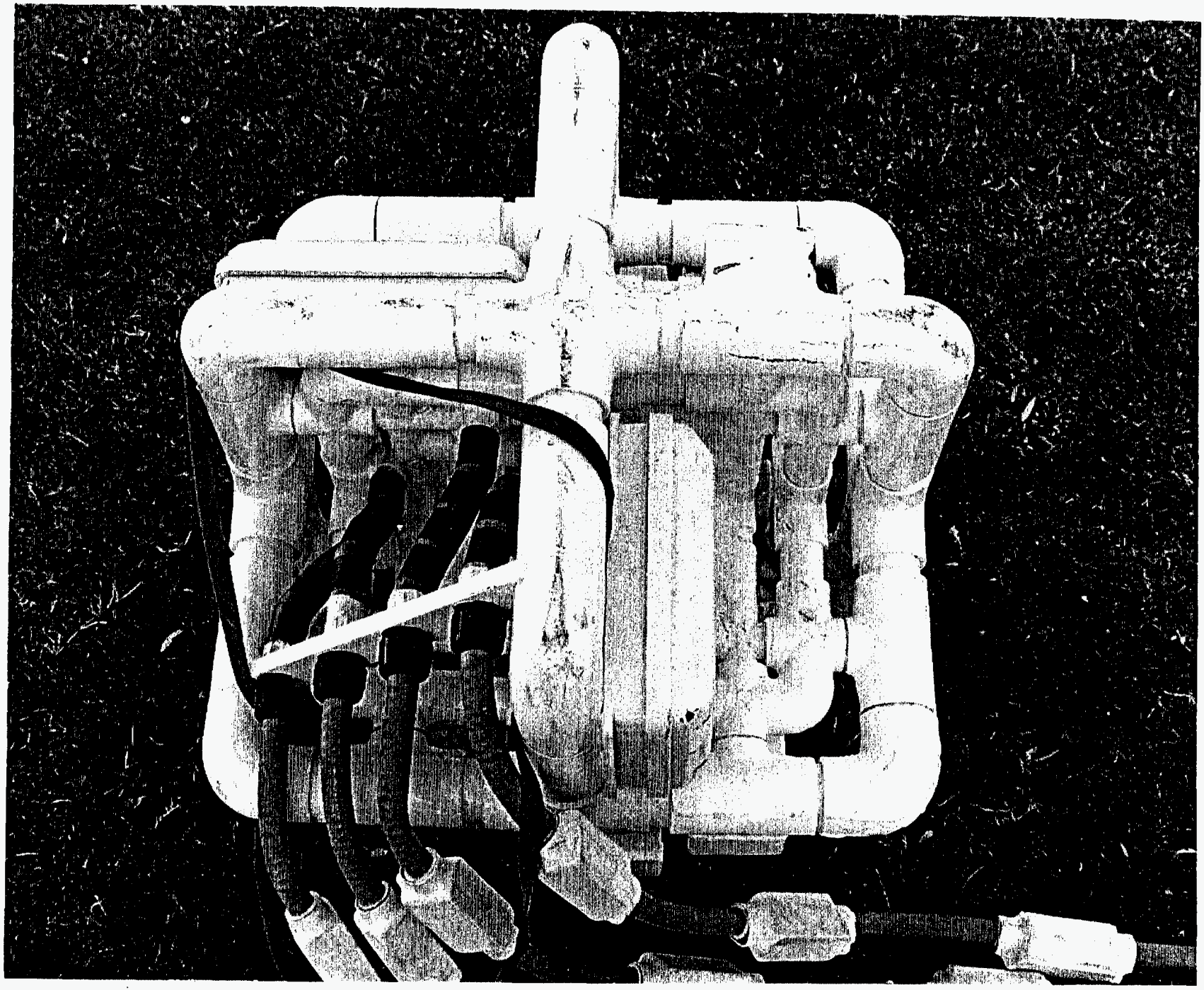

Figure 10. Photograph of the receiving coil. The conduit cables on the bottom of the photograph contain the feed lines for the x-y-z channels and the calibrator driver. The boxes mounted on the coil contain the preamplifiers for the x, y and z receiver channels and the cal-driver. The coil consists of four nested segments with 1, 2, 6 and 16 turns, respectively.

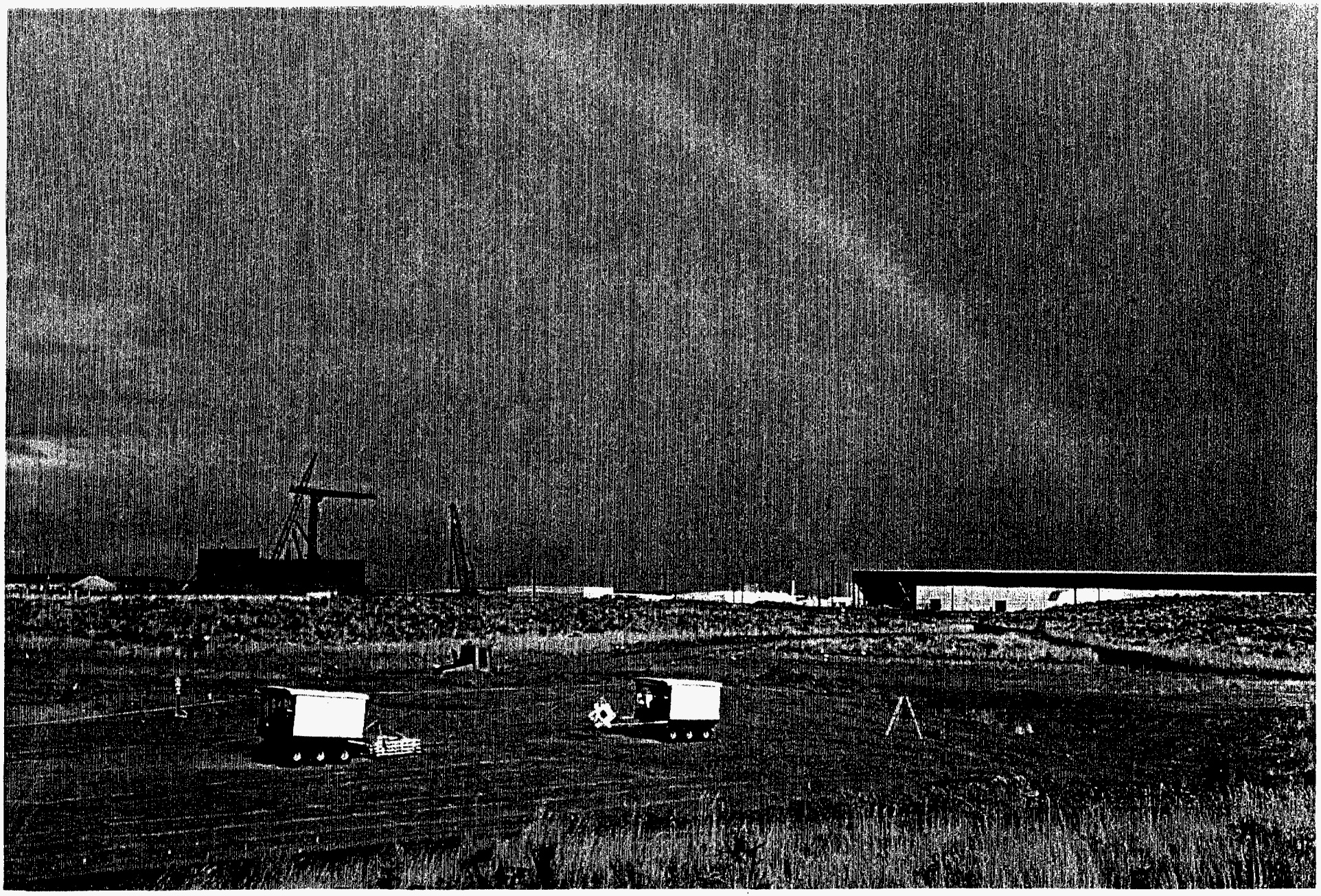

Figure 11. Photograph of the transmitter and receiver ATVs during the survey at the Idaho National Engineering Laboratory (INEL) Cold Test Pit (CTP) survey. The Radioactive Waste Management Complex (RWMC) and colorful rainbow (CRB) are in the background.

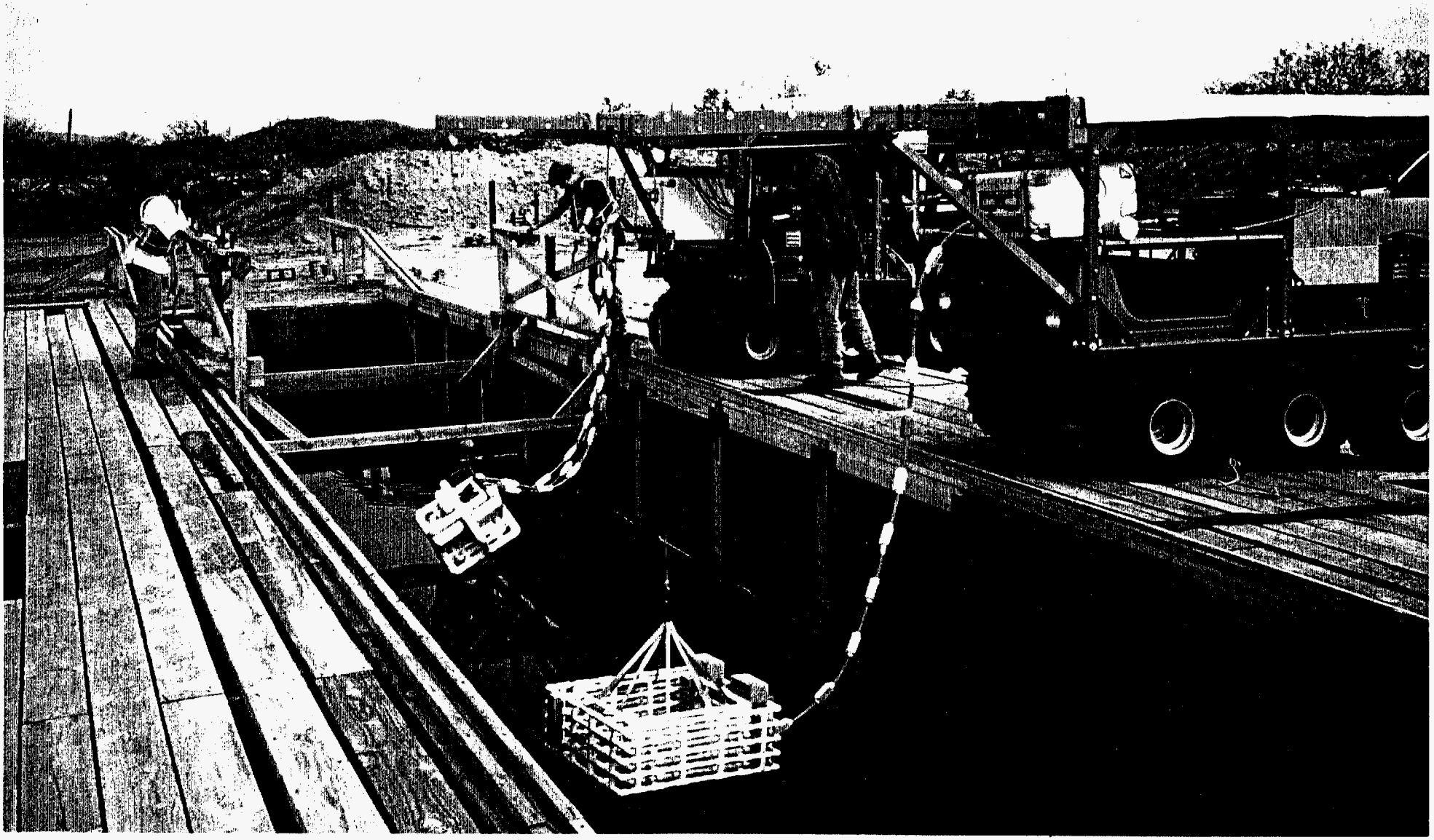

Figure 12. Photograph of the physical modeling facility during experiments to determine the ellipticity response to various objects (e.g. barrels, pipes, and sheets). The walls of this tank were covered with shotcrete containing fiberglass for added strength. There is no metal reinforcing rod used in this physical modeling tank. A trolley (shown in front of the transmitter ATV), with targets suspended at various depths, is moved down the length of the tank during the measurements.

EMSIS DESCRIPTION

EMSIS (Electromagnetic Subsurface Imaging System) is the computer software program that controls all of the hardware functions, automates the complete sounding, and performs the initial data processing. A functional description of the EMSIS software is given in a separate report (see List of Related Reports at the end of this report).

FCC AND ANSI REGULATION COMPLIANCE

Due to the RF energy produced by the LASI HF ellipticity system, pertinent standards that control maximum emission for personnel safety were found. Maximum allowable RF power-density for personnel safety at very short range is 100 mW/cm^2 for 300 kHz to 3 MHz, $900/f^2$ (f in MHz) mW/cm^2 for 3 MHz to 30 MHz, and 1.0 mW/cm^2 for 30 MHz to 300 Mhz. Maximum allowable radiated field-intensity for FCC compliance at longer range is 15 mV/m.

Measurements were made with the HF ellipticity system operating at full power. Long range (i.e., 300 m) measurements were recorded at the University of Arizona's Avra Valley Test Site, and short range (i.e. within about 1 m) measurements were made in the Rock Lab of the Mines Building, University of Arizona.

Data indicate full Federal Code compliance of the radiated fields except for the 3 frequencies: 2 MHz, 4 MHz, and 8 MHz, which were slightly above the maximum radiated field-intensities for FCC compliance of 15 mV/m at 300 m from the transmit coil. Additional measurements were made for these channels to determine the amount of attenuation needed on the transmitter coil for FCC compliance, and these attenuations will be used during operation of the HF ellipticity system in sensitive areas.

RF levels may be dangerous to personnel in very close proximity to the transmit antenna. It is recommended that personnel stay away from the antenna (>0.5 m) during field-operation of the ellipticity system.

CANCELLATION OF ELECTRIC-FIELD INTERFERENCE

The LASI high-resolution subsurface imaging system measures the ellipticity of the received magnetic field. A three-dimensional mathematical rotation algorithm (Bak et al., 1993; Thomas, 1996) is used to calculate the ellipticity from all three axes of the receiver coil. With this algorithm, the ellipticity should not change when the receiving coil is rotated about its center point. Because of slight nonorthogonality of the three axes of the coil, misalignment of the calibration coil, and cross talk between the three axes, there are small variations at all frequencies as the coil is rotated. These errors can be greatly reduced by calculating coil angles, calibration-coil coupling coefficients, and cross-talk coefficients which minimize the variation in ellipticity as the coil is rotated. Bak et al. (1993) and Thomas (1996) describe the details of this procedure. Rotating the coil is a useful test to verify that the measured data are accurate.

Figure 13 shows the result of rotating a data set from the University of Arizona, Avra Valley Geophysical Test Site. At the low and middle frequencies, there is good agreement between all the ellipticity curves corresponding to the many different orientations of the receiver coil. At the higher frequencies (and particularly 32 MHz), the curves are spread out over an increasingly large range of ellipticities. The coil-angle corrections, calibration-coil coefficients, and cross-talk coefficients are able to produce rotational invariance at all frequencies except the highest frequencies. There is clearly a source of interference which prevents us from obtaining rotational invariance at these high frequencies.

Figure 14a shows the behavior of the individual axes of the receiving coil for 32 MHz. The top set of curves are for the real components of the X, Y, and Z axes. The bottom set of curves are for the imaginary components of the X, Y, and Z axes. The coil was rotated in its plane for these tests. There is a large sinusoidal variation apparent in these fields as the coil is rotated from a 0° position around to a 360° position in 45° increments. The magnetic field flux through a coil does not change as the coil is rotated about the axis of the coil. This variation in signal output from the coil is due to electric field pickup by the coil. At the highest frequencies used in this system, the coil dimensions are greater than 0.01 wavelength in free space. At these dimensions, a coil will act as an electric-field dipole in addition to a magnetic-field loop antenna. Note that electrostatic shielding is effective in eliminating low-frequency electric-field pickup but does not reduce high-frequency electric-field pickup when the dimensions of the coil are greater than 0.01 wavelength. The coil we used is electrostatically shielded so there is no electric field interference at low frequencies. The large variation in signal output at high frequencies as the coil is rotated is expected since the effective electric field dipole length is determined by the cable feed point location. As the coil is rotated in its plane, the effective electric-field dipole is sometimes in minimum coupling to the electric field and sometimes maximum coupled, depending upon the location of the feedpoint.

Figure 14b shows the results of averaging pairs of points which are separated by 180°. If any pair of points separated by 180° is used, the resulting averaged voltage is the same; in other words we do have rotationally invariance even at the highest frequencies. This averaging procedure has effectively reduced the electric-field interference. Note that the coil must be rotated in its plane to accomplish this averaging.

Whiteside and King (1964) describe a doubly-loaded coil to reduce electric field interference. Effectively this accomplishes the same function as averaging pairs of measurements separated by 180°.

As will be shown in the next section on testing the system, this averaging method is very effective for reducing electric-field interference. Mechanically rotating the coil is a cumbersome and time consuming process, but it has been useful for verifying the complete system operation. In the future, we plan to construct receiving coils which simultaneously measure the 0° and 180° coil voltages and sum these two voltages to automatically cancel the electric field interference.

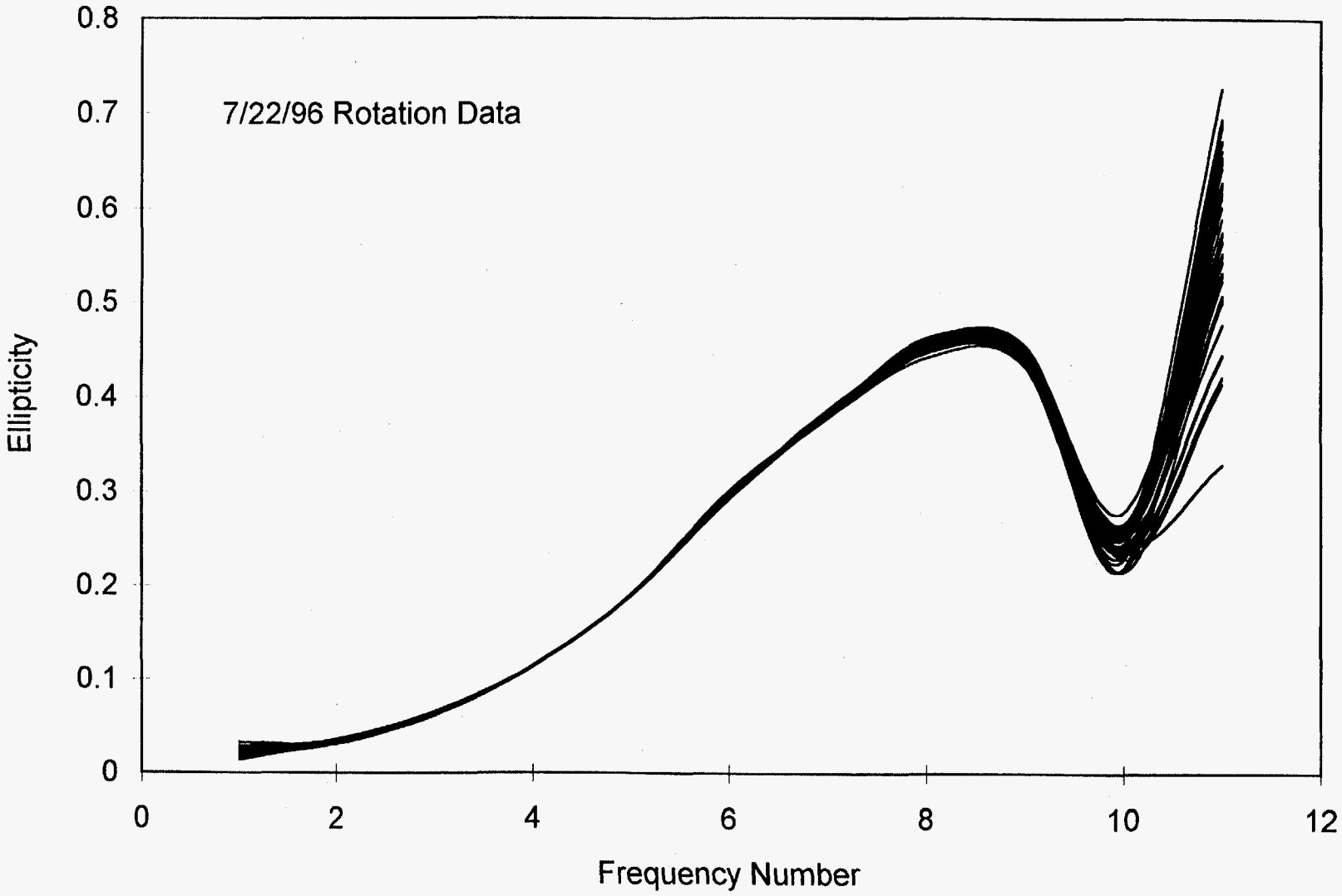

Figure 13. Example of ellipticity curves as the receiving coil is rotated about its center point.

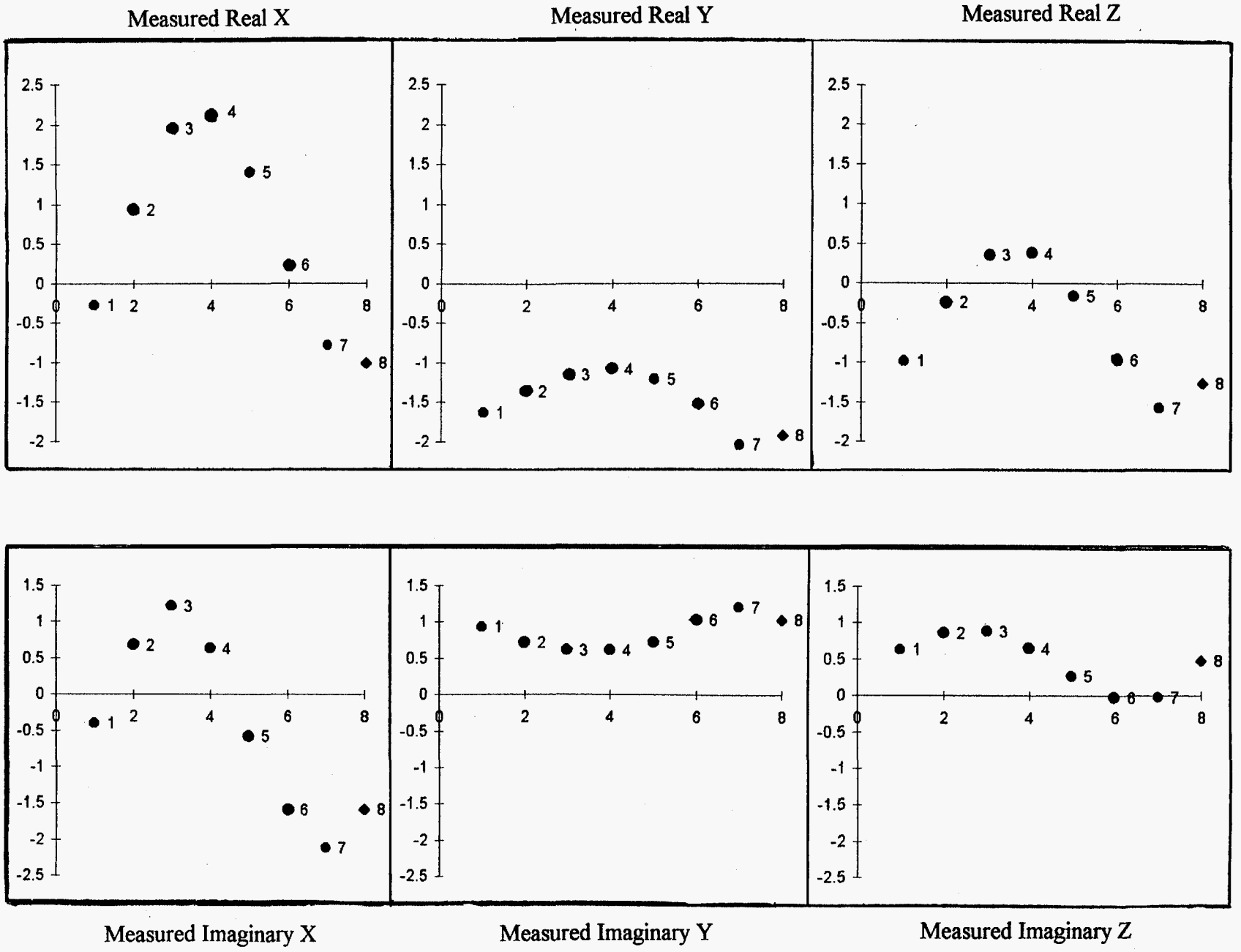

Figure 14a. Measured real and imaginary components for each receiving coil axis as the coil is rotated in the plane of each coil axis.

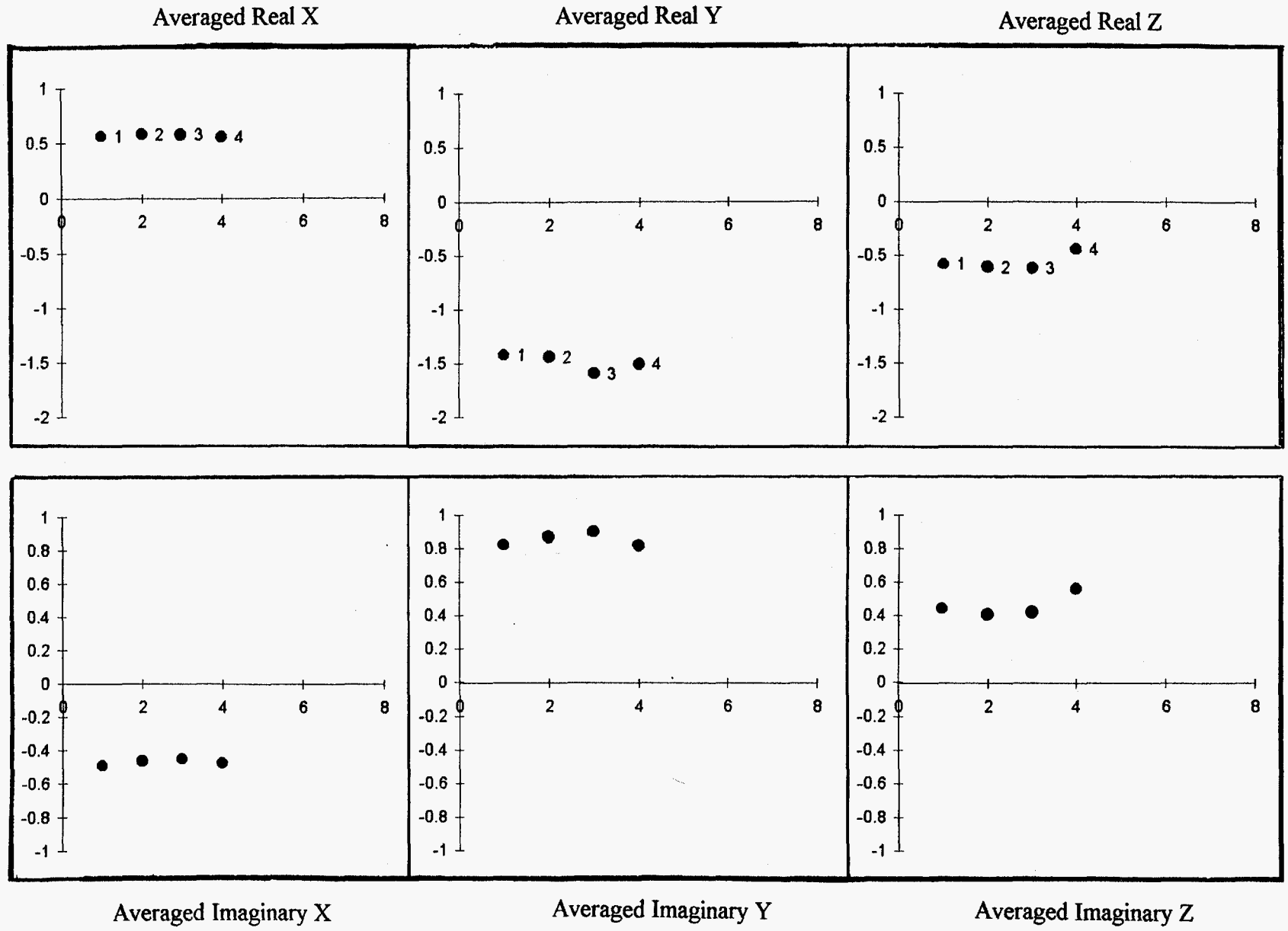

Figure 14b. Result of averaging measurements which are separated by 180 degrees.

TESTING THE LASI HIGH-RESOLUTION SUBSURFACE IMAGING SYSTEM

In order to obtain a complete system test, we required a sounding over a very well known earth. We attempted to characterize several test sites using shallow induction well logs and laboratory measurements on collected samples. We found that all of the sites we studied had electrical properties that varied significantly both laterally and vertically. In order to fully characterize the site, so that we would know exactly what the resistivity and dielectric-constant model was, we found we would have to drill so many holes that we might perturb the site from the drilling.

We therefore decided to build our own "earth" with precisely known and uniform electrical properties. We riveted together thirty-five 1.2 m by 3.0 m aluminum sheets into an 8 m by 15 m sheet. Anti-oxidant was applied to the joints to make a good electrical contact. The sheet thickness was 0.001 m, which was larger than the skin depth at all our frequencies. The small electrical resistivity of aluminum (approximately 10^{-8} ohm-m) made this earth appear to be a perfect conductor. We ran a short survey over the joints to see if there was any inhomogeneity at the joints. There was no measurable change in the magnetic field ellipticity at these joints. Figure 15 shows a photograph of the LASI high-resolution imaging system set up over the aluminum sheet. The transmitter and receiver coils visible near the center of this photo were raised on stands because the modeling code we will compare measured data with can not handle the coils very close to a highly conducting sheet.

Figures 16a, 16b, and 16c show the measured ellipticity curves over the aluminum sheet for transmitter - receiver separations of 2, 4, and 8 meters. The values are constant at low and middle frequencies as we rotate the coil, but diverge at the higher frequencies, and in particular at 32 MHz. The values at 2 and 4 MHz have been omitted since there is a small nonlinearity in the calibration coil response at 2 and 4MHz which effects some data sets. In all these cases there is a large electric-field interference effect at 32 MHz. The ellipticity at this frequency depends entirely on how we set the coil down on the ground.

Figures 17a, 17b, and 17c show the ellipticity curves over the aluminum sheet after applying the electric-field averaging procedure for transmitter-receiver separations of 2, 4, and 8 meters. Measurements were made with the feedline from the coil first at 0° and then at 180°. These two voltage readings (real and imaginary components) were then averaged to eliminate the electric-field interference. Also shown on these plots are the theoretical calculations of ellipticity for a model with a 0.001 m thick sheet with a resistivity of 10^{-8} ohm-m. The University of California, Berkeley computer code EM1DSH was used for these calculations. This code calculates fields over a finite size sheet or over a layered earth. There is a good match between the theoretically calculated curves and the ellipticity calculated from the averaged fields at all frequencies, including 32 MHz. We believe this test provides a comprehensive check of the entire system.

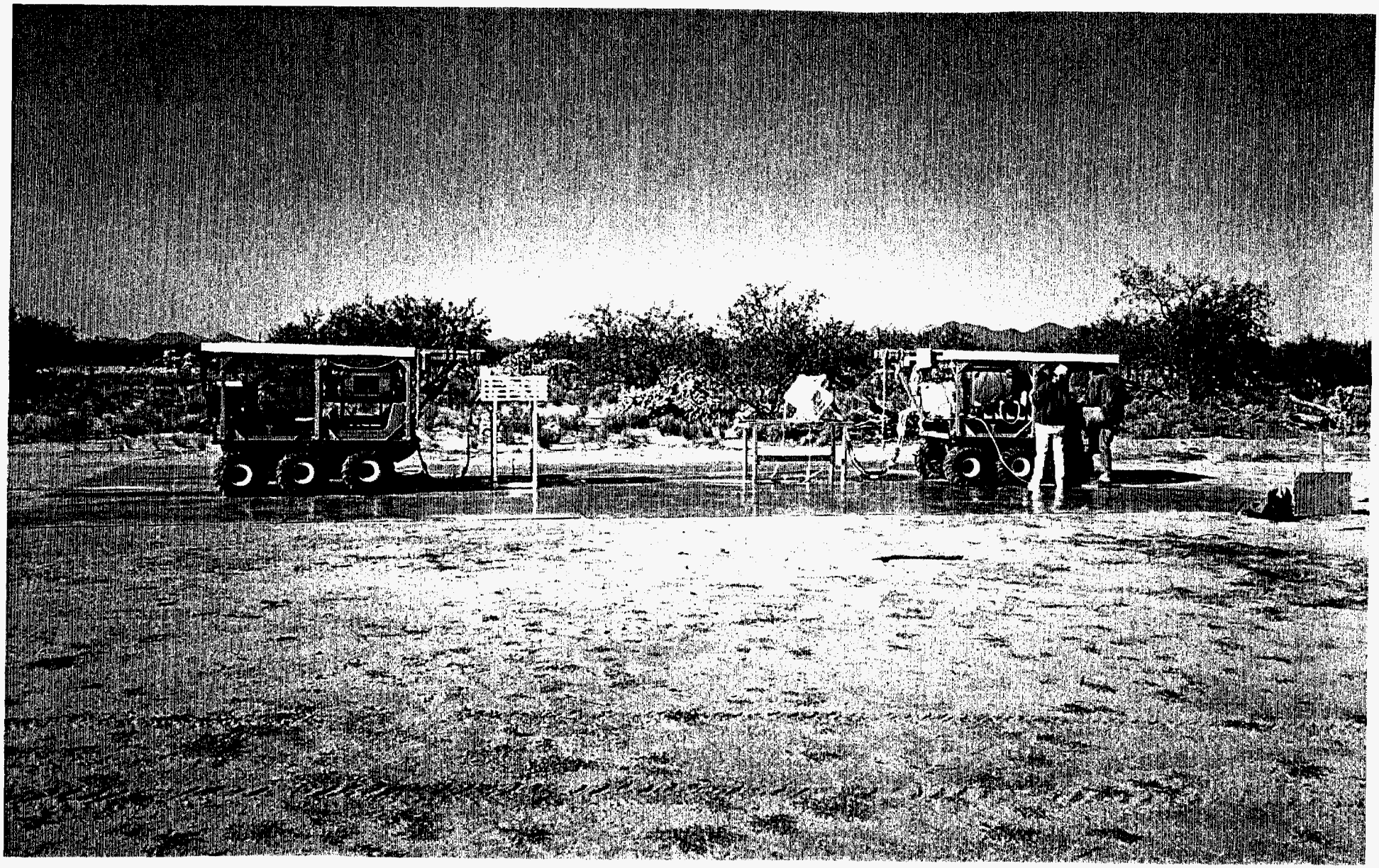

Figure 15. Photograph of ellipticity measurements over the large aluminum sheet. Transmitter on the left and receiver on the right.

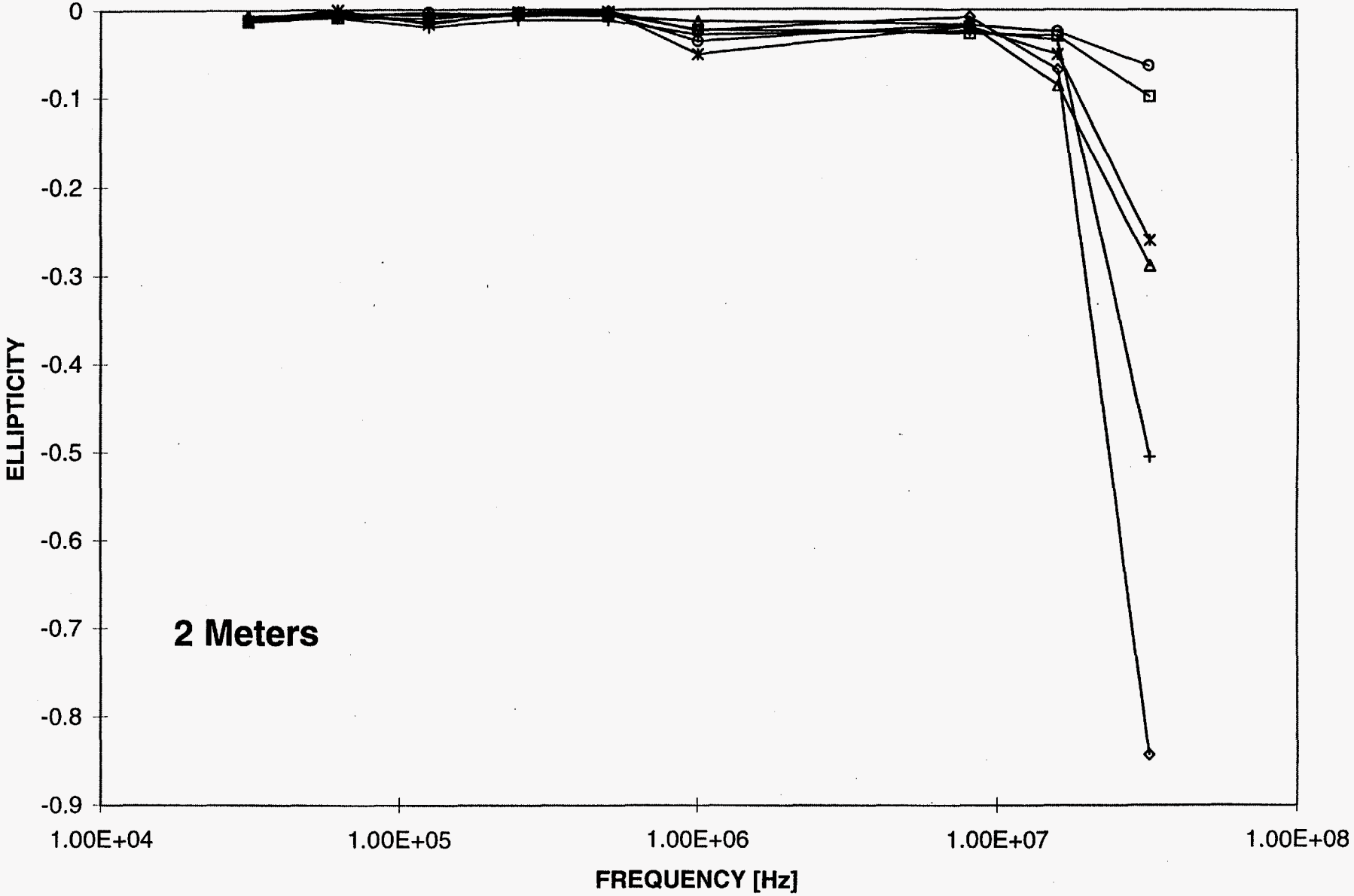

Figure 16a. Ellipticity measurements over an aluminum sheet at 2 m separation without averaging the fields as the coil is rotated.

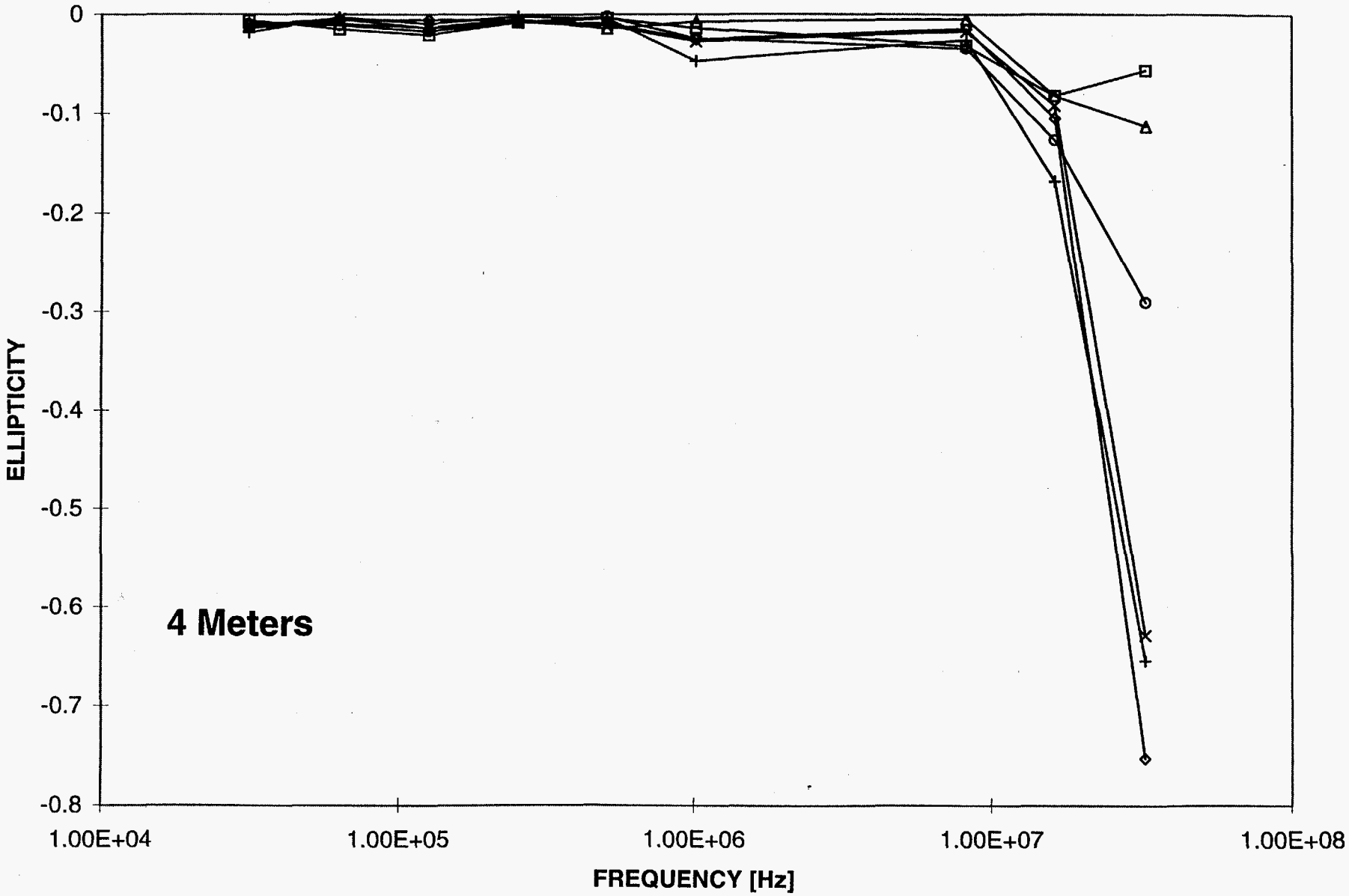

Figure 16b. Ellipticity measurements over an aluminum sheet at 4 m separation without averaging the fields as the coil is rotated.

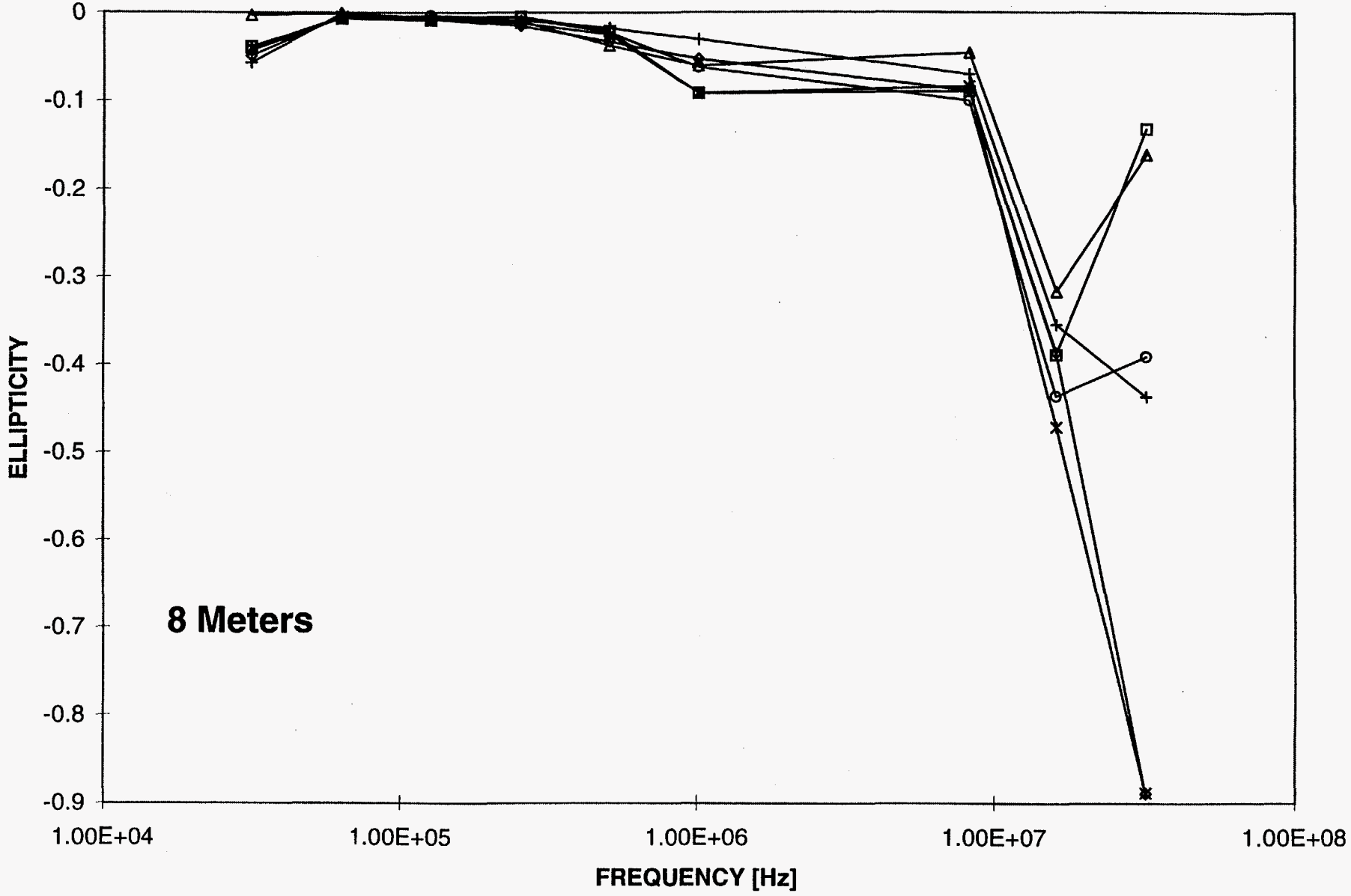

Figure 16c. Ellipticity measurements over an aluminum sheet at 8 m separation without averaging the fields as the coil is rotated.

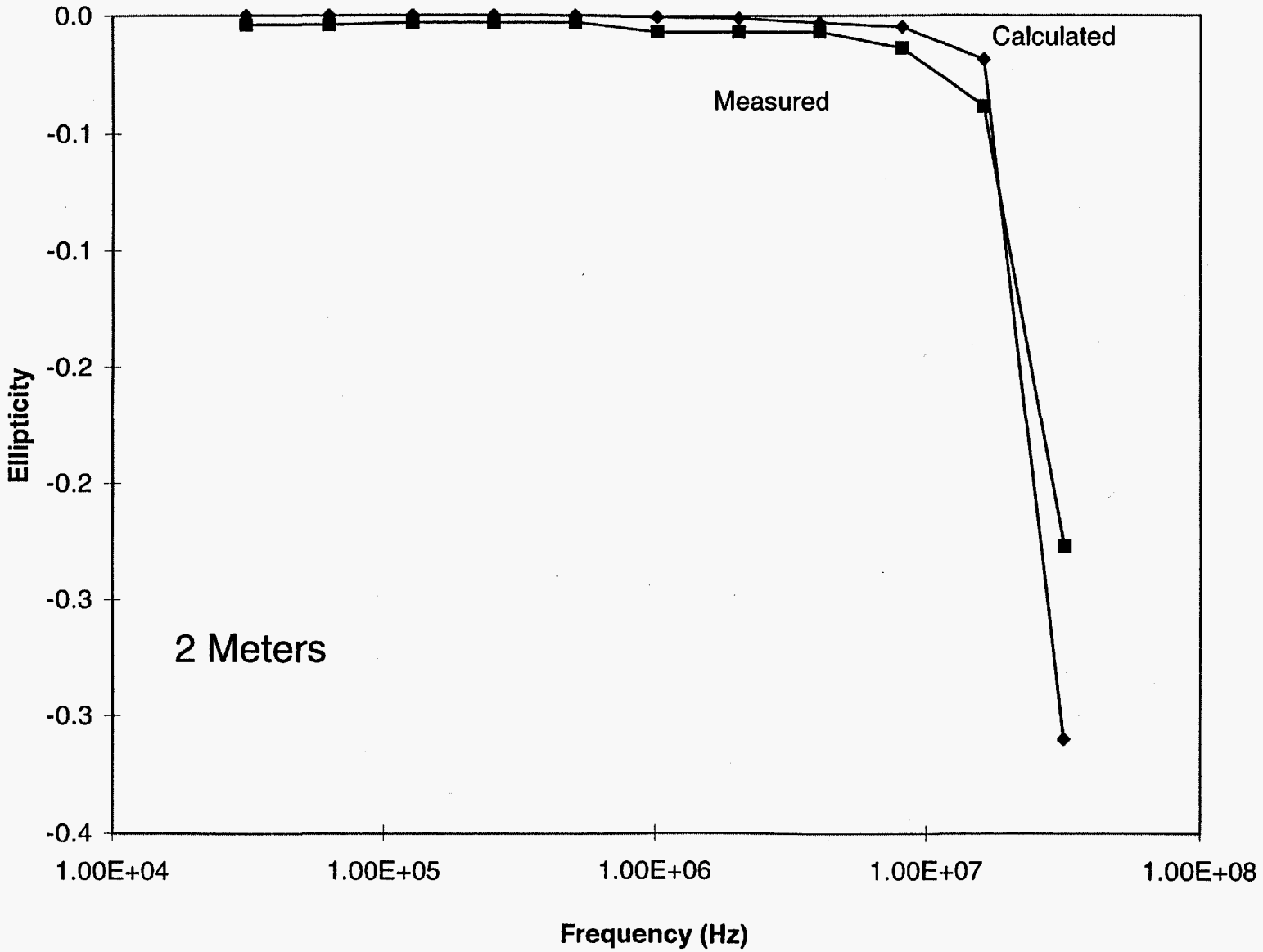

Figure 17a. Ellipticity measurements over an aluminum sheet at 2 m separation with averaging of measured field pairs separated by 180 degrees as the coil is rotated. Calculated ellipticities over a 10^{-8} ohm-m conductor are also shown.

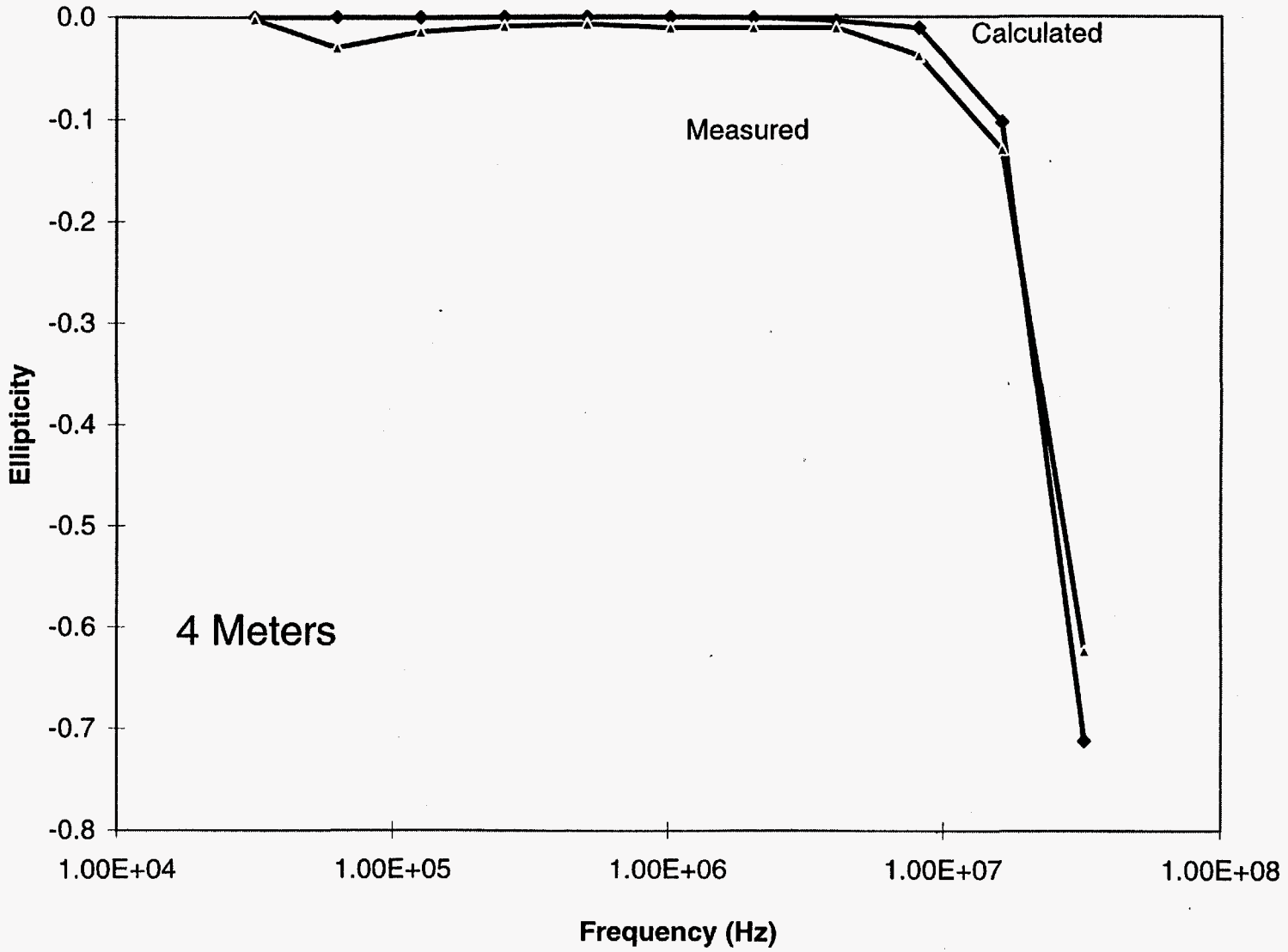

Figure 17b. Ellipticity measurements over an aluminum sheet at 4 m separation with averaging of measured field pairs separated by 180 degrees as the coil is rotated. Calculated ellipticities over a 10^{-8} ohm-m conductor are also shown.

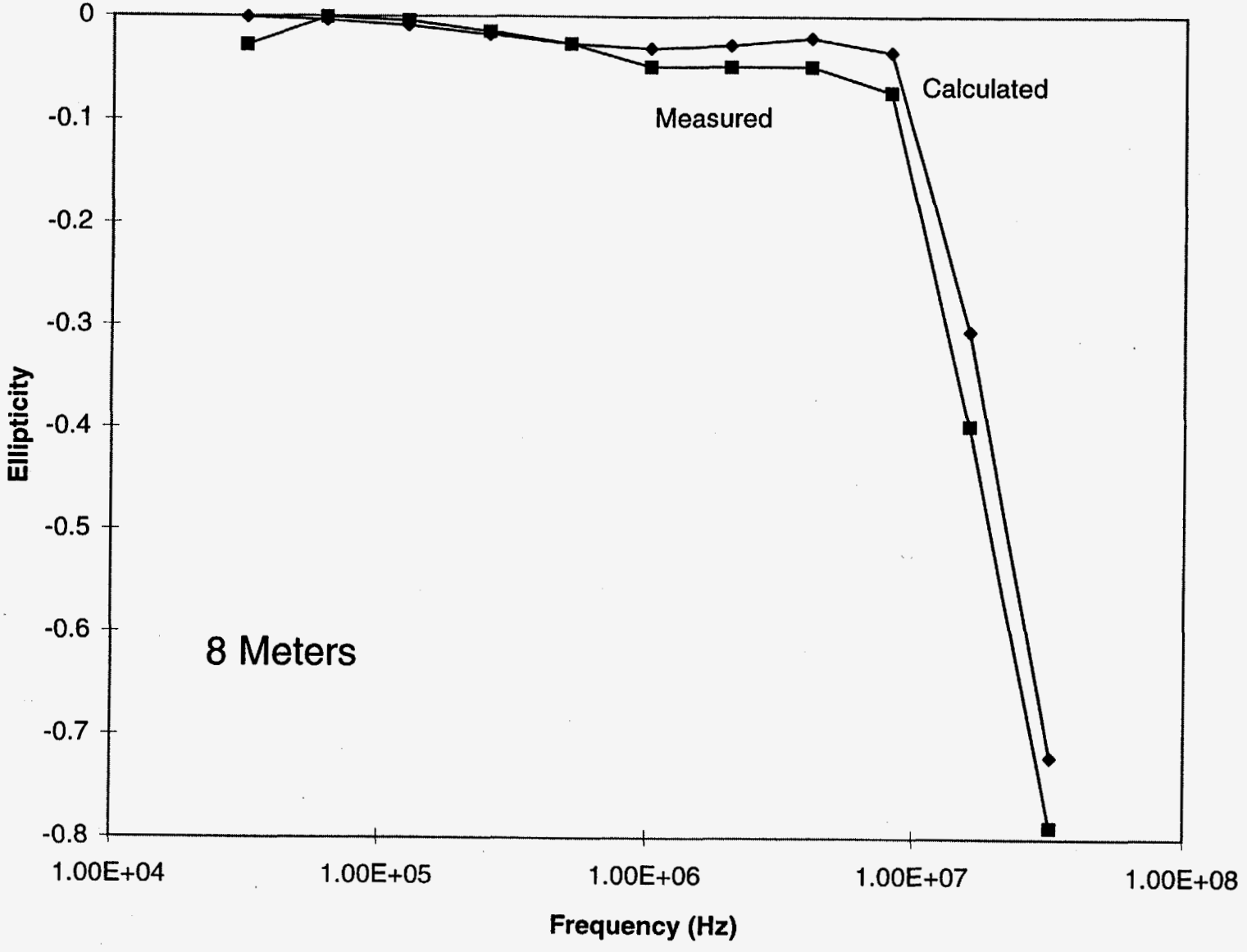

Figure 17c. Ellipticity measurements over an aluminum sheet at 8 m separation with averaging of measured field pairs separated by 180 degrees as the coil is rotated. Calculated ellipticities over a 10^{-8} ohm-m conductor are also shown.

NEURAL NETWORK INTERPRETATION AND DATA VISUALIZATION SYSTEM

Overview

The two fundamental components of the automated interpretation scheme are the neural networks and the data visualization shell. The data visualization shell provides the user interface to the neural networks, graphs of sounding curves, 1D forward modeling program, images of the data, and interpreted sections and is described in detail in the report "Data Visualization and Interpretation System" by Birken and Poulton. The only interaction the user has with the trained neural networks is the selection of the networks to use for the interpretation through the visualization shell. The neural networks are described in detail in the report "Neural network interpretation of high-frequency ellipticity data: 31 kHz to 32 MHz" by Poulton and Birken.

The data interpretation system makes possible a first-pass, real-time interpretation with neural networks directly in the field. The acquired ellipticity data will be transferred either after each sounding is recorded or at any interval along the survey line via a wireless telemetry system from the acquisition computer on the survey line to the interpretation computer in the truck. All the parameters the system is capable of recording are transferred as one binary sounding file for each station. An extraction program called "XFER" must be run to extract ellipticities from the sounding file for input to the interpretation and visualization software.

The ellipticity data interpretation system (EDIS) operates in a manual mode to give the user maximum flexibility in interpretation and display. The user selects all the networks through which the data should be routed. Each network interpretation is passed to a 1D forward modeling program so the ellipticity curves can be compared to the measured data. The fit of each interpreted sounding to the field data is calculated as the mean-squared error for the 11 frequencies in each sounding. The user decides which network gives the best fit and re-selects that network for the interpretation. The network is re-run for the sounding and the interpretation is plotted in a 2D section.

We have created 94 separate neural networks to do the 1D interpretation for the 31 kHz to 32 MHz frequency range. On a 486 50MHz PC the neural network interpretation for one transmitter-receiver separation using 16 networks takes less than one second. To run four networks and compute the forward models for each to find the best fit to the field data takes less than one minute if no dielectric information is required; if dielectric information is required the forward modeling time for a two-layer case takes approximately 1 minute. Currently the interpretation and visualization system can only accommodate 1D interpretations. Interpretation of 3D targets is accomplished with separate networks not incorporated into the system due to the need to tailor each 3D interpretation to the requirements of the specific site.

We will first describe the neural network interpretation system for cases where no dielectric information is required and then discuss how dielectric constants are estimated with neural networks.

Neural Network Interpretation Without Dielectric Constants

Ellipticity data are transferred from the field data acquisition computer via the RF telemetry link to the data interpretation computer housed in the field truck. The data interpretation consists of neural networks operating in mapping mode (1D). Our approach to the neural network processing is to divide the interpretation into many parts and use several small networks. The interpretation system uses three different transmitter-receiver separations of 8 m, 4 m, and 2 m. The functions of the networks are divided into halfspace interpretations and layered-earth interpretations. Four networks are used at each separation for layered-earth interpretations and 10 are used for halfspace interpretations. Layered earth interpretations are not performed at the 2 m separation. More than 12,000 models per separation were used for training. Two network paradigms were used for training, a radial basis function algorithm and a modular neural network algorithm. The networks perform parameter estimation. Each network is capable of producing an interpretation in a few milliseconds on a 486 PC. The networks were tested on field data from several experiments and the results are discussed in each section.

Apparent resistivity is the resistivity of a homogeneous halfspace that gives the same response as that observed in the field data. At a relatively homogeneous site the apparent resistivity may resemble the true resistivity. In a layered earth environment (1D), or a 2D or 3D environment the apparent resistivities will not accurately reflect the true electrical properties of the earth but will still reflect changes in electrical properties throughout the site.

We refer to piecewise apparent resistivity when we use data from a subset of frequencies to calculate the apparent resistivity. The apparent resistivity values from the frequency subsets are then concatenated to produce a resistivity pseudosection at a particular station. The piecewise apparent resistivity networks are a powerful interpretation tool because they can fit ellipticity curves that do not conform to a halfspace response, or a layered earth response.

A separate set of networks is used for each transmitter-receiver separation. The apparent resistivity networks use as input ellipticity values from two adjacent frequencies and a third parameter that indicates the sign of the slope from one frequency to the next. The output is the apparent resistivity.

Radial basis function networks were used for training the piecewise apparent resistivity networks. Nine separate networks are used for each transmitter-receiver separation. Data from the 32 MHz channel is not used in the interpretation due to inconsistent data

quality. The first network uses as input log10 values of the absolute value of the ellipticity recorded at 31 kHz and 64 kHz and a value of -1 if the ellipticity at 64 kHz is less than the value at 31 kHz (i.e. the log10 value of frequency n is greater than the value at frequency n+1). The output is the log10 value of apparent resistivity. The second network uses data from 64 kHz and 128 kHz. The same format applies for each network. For frequencies above 2 MHz the effect of dielectric constant becomes important.

The estimates of apparent resitivity from these networks is on average within 5% or better of the true apparent resistivity based on testing with synthetic data. We are confident that for apparent resistivities less than 500 ohm-m that the neural network estimates will be within a few percent of the true result.

We have implemented three networks that use as input 10 ellipticities from a sounding and output the best-fit half-space model. The same training sets were used for the one-layer apparent resistivity networks as the piecewise networks. Radial basis function networks of the same design were also used but with 10 inputs rather than 3. Log10 values of the absolute values of ellipticity were used as input and the log10 values of apparent resistivity was used as output. These networks are of limited use as their fit to the data is only good when surveys are conducted over true halfspaces; gradational changes in resistivity structure along with 2D or 3D effects will result in less accurate interpretations.

We refer to the networks that interpret 1D models as two-layer or three-layer networks. This nomenclature does not refer to the number of layers in the neural network but rather the number of earth-layers in the model. We will be using a short-hand notation for all of these networks that describes the geometry of the layers and the transmitter-receiver separation. For example, a two-layer network in which all of the models have a first layer resistivity greater than that of the second layer and for measurements at an 8 m separation is labeled an RC8 network, meaning the first layer is resistive, the second layer is more conductive.

We used modular neural networks to train all of the two-layer cases. Networks were not trained for the 2 m separation since the depth of penetration was too small to resolve much layering. The same modular neural network design was used for all networks: 13 input processing elements (PEs), five expert networks each with 5 hidden PEs, a hidden layer with 7 PEs, and 3 output PEs. The hyperbolic tangent function was used in the expert networks and the hidden layer; a linear function was used for the output layer. A time-varying learning schedule was used to adjust the step size and momentum parameters during the course of training.

The inputs to the networks include ellipticities from 32 kHz to 2 MHz. We did not use ellipticities above 2 MHz in these networks because the dielectric constant begins to have a significant effect on ellipticity above this. In addition to the seven ellipticities, we also coded the maximum ellipticity and its frequency location, the difference between

the peak ellipticity and the ellipticities at adjacent frequencies, and the area under the ellipticity sounding curve. All input values, except for the frequency number of the peak value, are converted to log10 values prior to calculation. The output parameters are the log10 values of the resistivities and the base 10 value of thickness.

The accuracy of the two-layer networks depends on the contrast between the resistivities of each layer, the layer geometry (i.e. conductive over resistive or vice versa), the magnitudes of the resistivities, and the separation distance. On average, we find that for a conductive over resistive case, for 4 m and 8 m separations, and all contrasts, the first layer has an absolute error of 20 ohm-m, the second layer an absolute error of 73 ohm-m, and the thickness of the first layer has an absolute error of 0.48 m. For a resistive over conductive case, the first layer has an average absolute error of 100 ohm-m, the second layer an average absolute error of 6 ohm-m and the thickness error is 0.31 m.

A variety of data representations for the input patterns were tried including using the Fourier transform, using maximum entropy calculations, using slopes of the sounding curves, and using base 10 values only. None of these approaches led to as accurate thickness estimates as the approach described above.

As in the two-layer case described above, the three-layer networks were trained only for 4 m and 8 m separations. Two types of networks were trained for each separation: RCR and CRC or R1 > R2 and R3>R2 and vice versa. Future modifications to the networks should eliminate the constraint on the lower layer and allow it to have any resistivity value. We used 6,860 training models for the 8 m networks and 3,500 models for the 4 m networks. Total layer thickness was limted to one half the coil separation and maximum thickness for a single layer was limited to one half the total thickness so for the 8 m separation the maximum thickness of any single layer was 2 m. Future networks should remove this constraint and focus only on the total thickness constraint so that we could have, for example, a top layer with a thickness of 3.75 m and a second layer with a thickness of 0.25 m. Modular neural networks were used to train the three-layer networks.

We refer to cases where the first and third layer resistivities are less than the second layer as a conductive over resistive over conductive case or CRC. We find in general for these networks that the first conductive layer is always very well resolved and the underlying resistive layer is usually rather poorly resolved. The underlying conductive halfspace is less well resolved than the first layer but always better than the resistive middle layer. We also find that resistivities above 1,000 ohm-m are not distinguishable by the neural nets.

We refer to cases where the first and third layer resistivities are greater than the second layer as a resistive over conductive over resistive case or RCR. We find in general for these networks that the resistivity and thickness estimates are better than the CRC case. The resistive layers are often better resolved than the conductive layer. The

thickness of the conductive layer is often poorly resolved. The resistive layer estimate performs a classification so we can determine if the resistivity is low, medium, or high. The thickness of the conductive layer is more accurately estimated than that of the resistive layer.

As with the two-layer networks, the accuracy of the three-layer networks depends on contrast, geometry, resistivity magnitude and separation distance. For the CRC case we find average absolute errors of 36, 84, and 8 ohm-m for the three layers respectively and 0.32 and 0.31 m for the thickness of the layers respectively. For the RCR case we observe average absolute errors of 195, 24, and 130 ohm-m for each layer respectively and 0.49 and 0.70 m for each thickness. These numbers indicate that we have more confidence in the estimates for resistivity and thickness of conductive layers than resistive ones.

Neural Network Estimation Of Dielectric Constants

For the halfspace networks we used 10 frequencies to estimate one value each of resistivity and dielectric constant. We have excluded 32 MHz from all interpretations because it does not match model calculations without first correcting it with the electric field cancellation algorithm. The current method for implementing the electric field cancellation algorithm is not practical to implement for a field operation that requires dense spatial sampling. The exclusion of 32 MHz information does degrade our estimates of dielectric constant. For future field studies when an automatic electric field cancellation algorithm is implemented, the 32 MHz data can be easily included in the neural network interpretation.

For the piecewise apparent resistivity networks we use three frequencies at a time to estimate one value of resistivity and dielectric constant. We use nine separate networks. The network containing frequencies 8, 16, and 32 MHz is not used because of difficulties with 32 MHz data. Data from 8, and 16 MHz are included in the network that uses data from 4, 8, and 16 MHz. Ellipticity values are input to the neural networks as base 10 logarithmic numbers. The resistivities and dielectric constants are also estimated as log10 values.

Both the halfspace and piecewise apparent resistivity networks have a resistivity range of 1 to 10,000 ohm-m and a dielectric constant range of 1 to 100. We trained the networks with 10 resistivities per decade and 20 dielectric constants per decade.

The addition of dielectric constant as an output parameter necessitates a different approach for training than that previously described for the layered-earth networks. If we tried to estimate two resistivities, one thickness, and two dielectric constants simultaneously for a two-layer earth case we would require a training set with 168,960 models for each separation. It is theoretically possible to train a neural network with a data set this large but the computational expense would be huge. An alternate

approach is to subdivide the problem by using fixed thicknesses. Each network would be trained to recognize patterns from layers with one particular thickness. We used a thickness interval of 20 cm with a minimum layer thickness of 20 cm and a maximum layer thickness of 2.4 m for a 4 m separation and 4.8 m for an 8 m separation. Each network estimates two values of resistivity and dielectric constant. We trained 12 networks to solve the two-layer case for a 4 m separation and 24 networks for an 8 m separation.

The two-layer earth networks use 10 frequencies from 31 kHz to 16 MHz. The ellipticities from 32 MHz are actually included in the input pattern but learning is disabled for that frequency. Such an approach allows us to easily re-train the networks to include 32 MHz when accurate field data are collected at that frequency. Raw ellipticity values are used rather than log10 values. The output parameters, however, are still logarithmic values. The two-layered earth networks have a resistivity range from 10 to 1,000 ohm-m with four resistivities per decade; the dielectric constant ranges from 1 to 100 also with four values per decade. We used nearly 280,000 models for training. Only antenna separations of 4 m and 8 m were considered.

Dielectric constants for models with less than 50 ohm-m resistivity cannot be easily resolved in our frequency range. Generally speaking, the more resistive the model the better the estimate of dielectric and the worse the estimate of resistivity (Birken and Poulton, 1997a). Six models for a 4 m antenna separation are plotted in figures 18-21 to show the variation in ellipticity as a function of frequency as the top layer resistivity, top layer dielectric, lower layer resistivity and lower layer dielectric are varied; the thickness of the top layer is held constant at 1 m. We note that once the top layer resistivity reaches 500 ohm-m, we have little change in ellipticity until frequencies near 100 MHz are reached. If the top layer resistivity is held constant at 100 ohm-m and the dielectric constant is varied, we see little change in ellipticity until after 1 MHz but continued improvement in resolution as frequency increases. The second layer resistivity is difficult to resolve once the resistivity exceeds 100 ohm-m. And finally, the second layer dielectric constant is nearly impossible to resolve except at frequencies above 30 MHz and even then only for dielectric constants greater than 10. Analysis of other models indicates better resolution of dielectric constant as the resistivity increases.

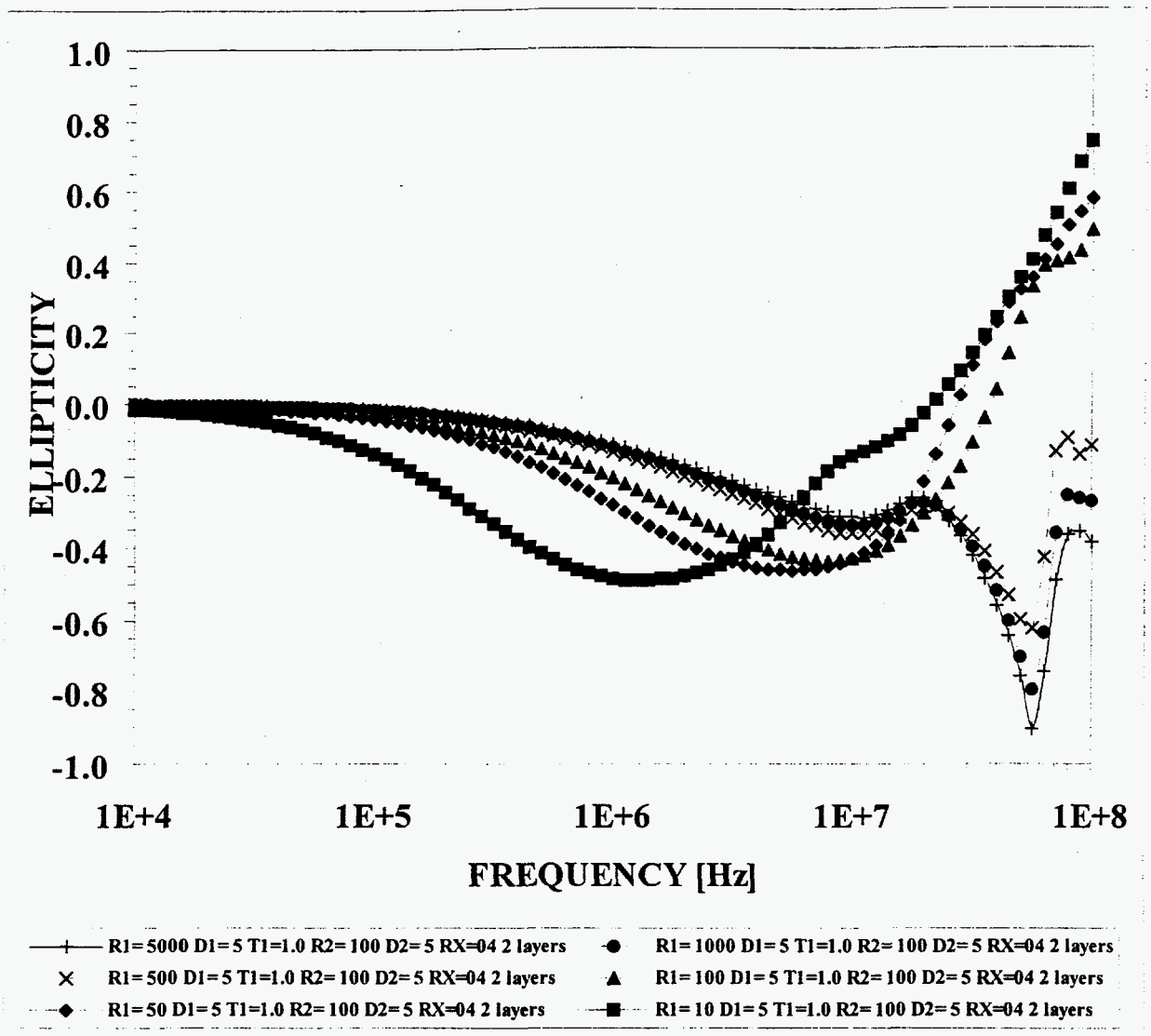

Figure 18. Sensitivity of ellipticity to changes in top layer resistivity for a two-layer model, 4 m antenna separation. The top layer dielectric constant is 5, the lower halfspace resistivity is 100 ohm-m, the lower halfspace dielectric constant is 5 and the top layer thickness is 1 m.

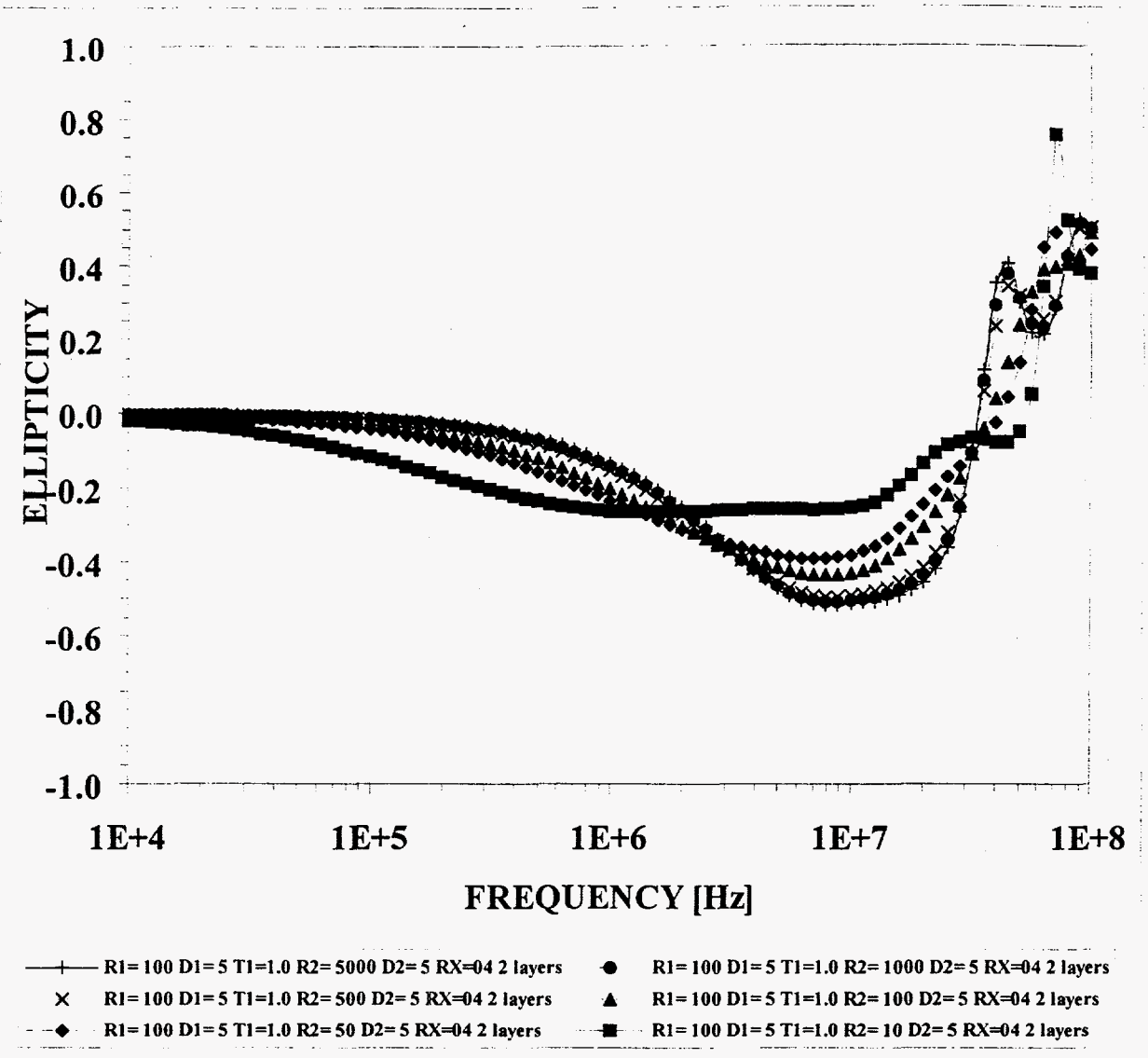

Figure 19. Sensitivity of ellipticity to changes in lower layer resistivity for a two-layer model, 4 m antenna separation. The top layer dielectric constant is 5, the top layer resistivity is 100 ohm-m, the lower halfspace dielectric constant is 5 and the top layer thickness is 1 m.

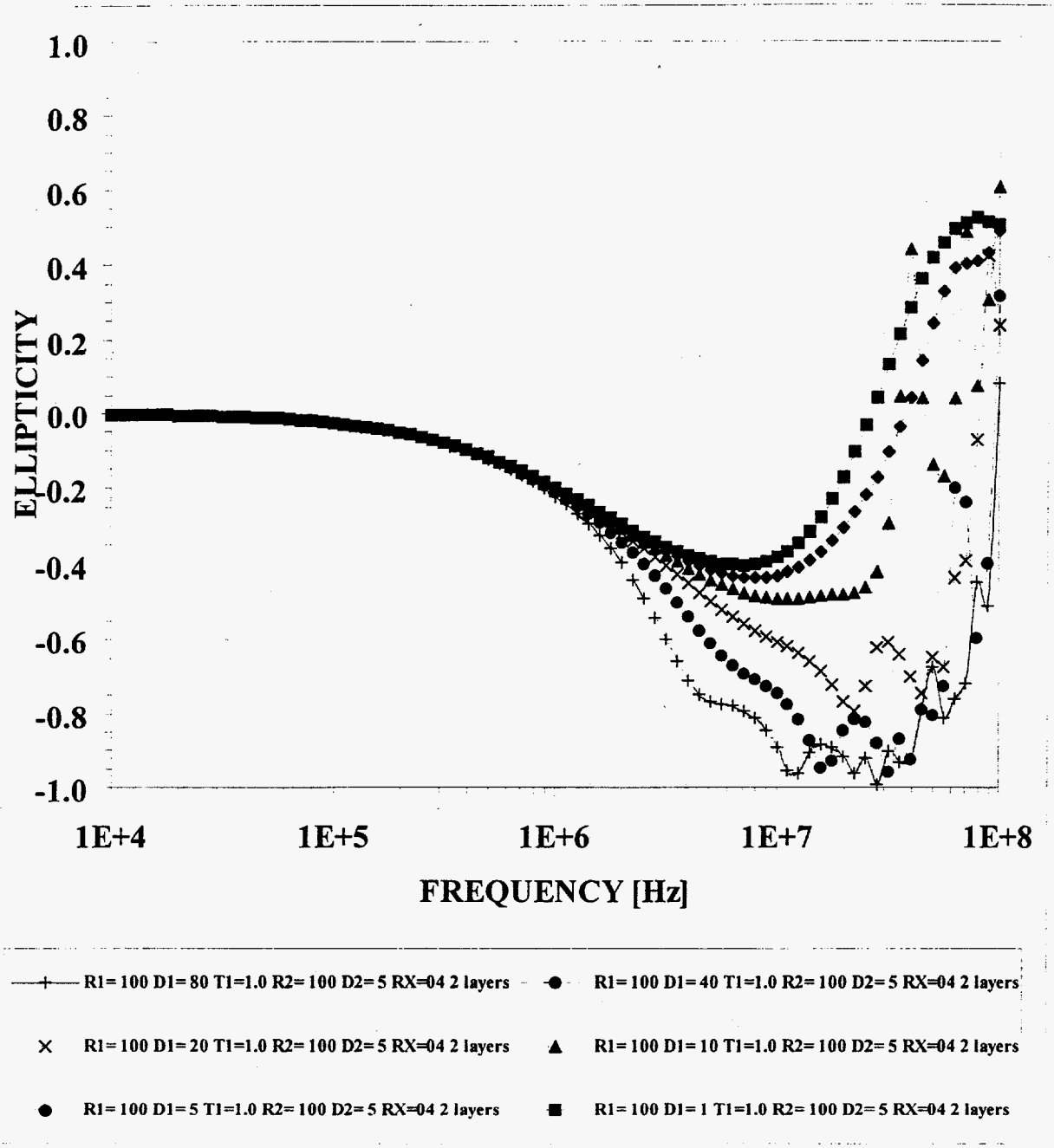

Figure 20. Sensitivity of ellipticity to changes in top layer dielectric constant for a two-layer model, 4 m antenna separation. The top layer resistivity is 100 ohm-m, the lower halfspace resistivity is 100 ohm-m, the lower layer dielectric constant is 5 and the top layer thickness is 1 m.

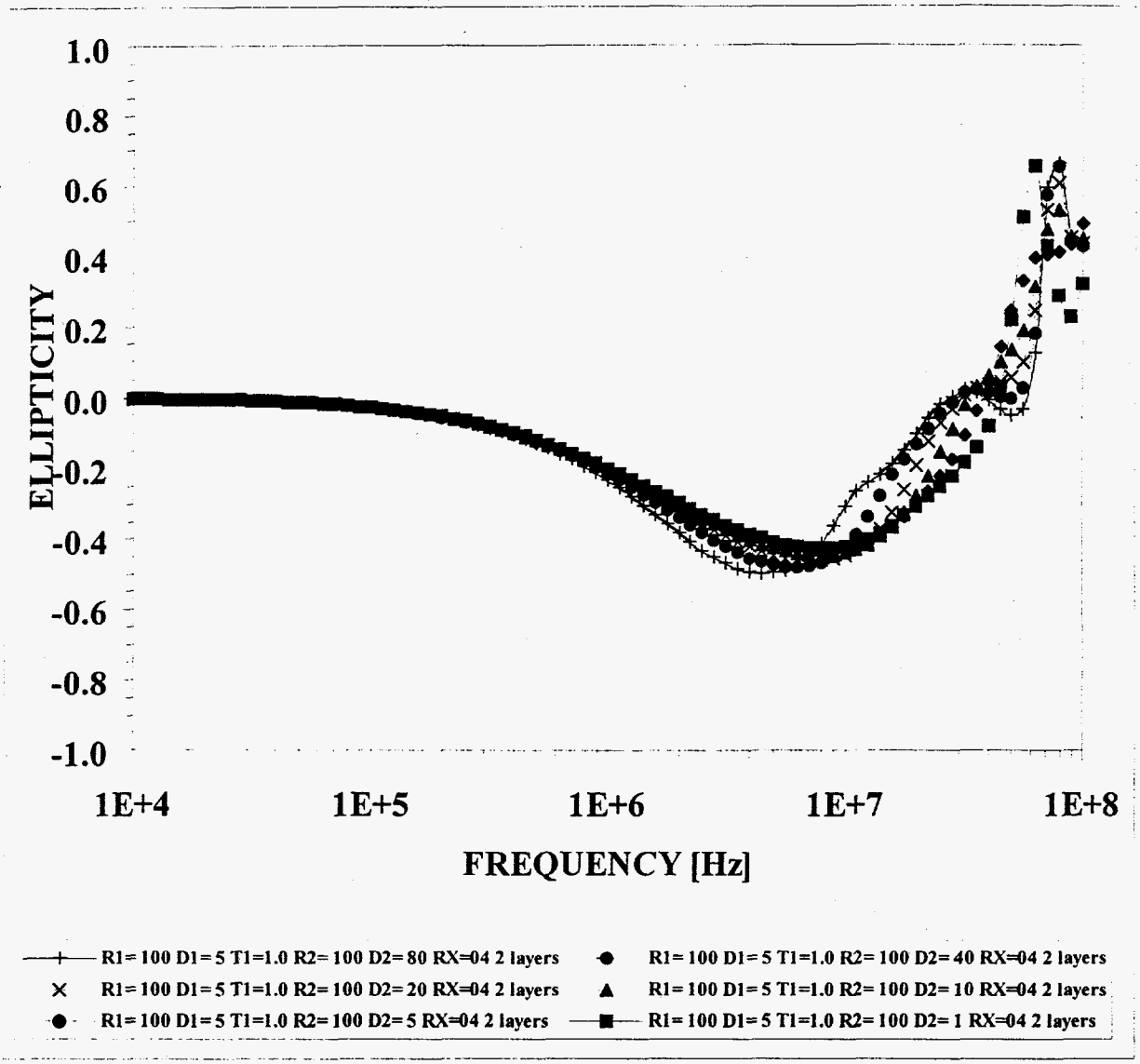

Figure 21. Sensitivity of ellipticity to changes in lower layer dielectric constant for a two-layer model, 4 m antenna separation. The top layer resistivity is 100 ohm-m, the lower halfspace resistivity is 100 ohm-m, the top layer dielectric constant is 5 and the top layer thickness is 1 m.

The neural networks cannot accurately map ellipticities to an earth model if the sensitivity is very low, hence the trends seen in figures 18-21 are also observed in the network training results. Average percent errors on training data are presented in Table 1. Notice that errors are smaller for conductive layers than for resistive ones. Also notice that the errors for dielectric constant are smaller for the resistive layers. As the top layer increases in thickness and becomes more resolvable, the sensitivity to the dielectric constant for the underlying halfspace rapidly worsens. The errors for resistivity are calculated based on the log10 values of the estimates while the errors for dielectric constant are calculated using the base 10 values. The estimates for the first

layer resistivity are very sensitive to the thickness of the layer while the estimate errors for the underlying halfspace appear to be fairly constant.

In figures 22a,b we show the improvement in fits to synthentic two-layer cases by including the dielectric constant in the estimate. Notice that the fits with or without dielectric constant are the same up to 1 MHz.

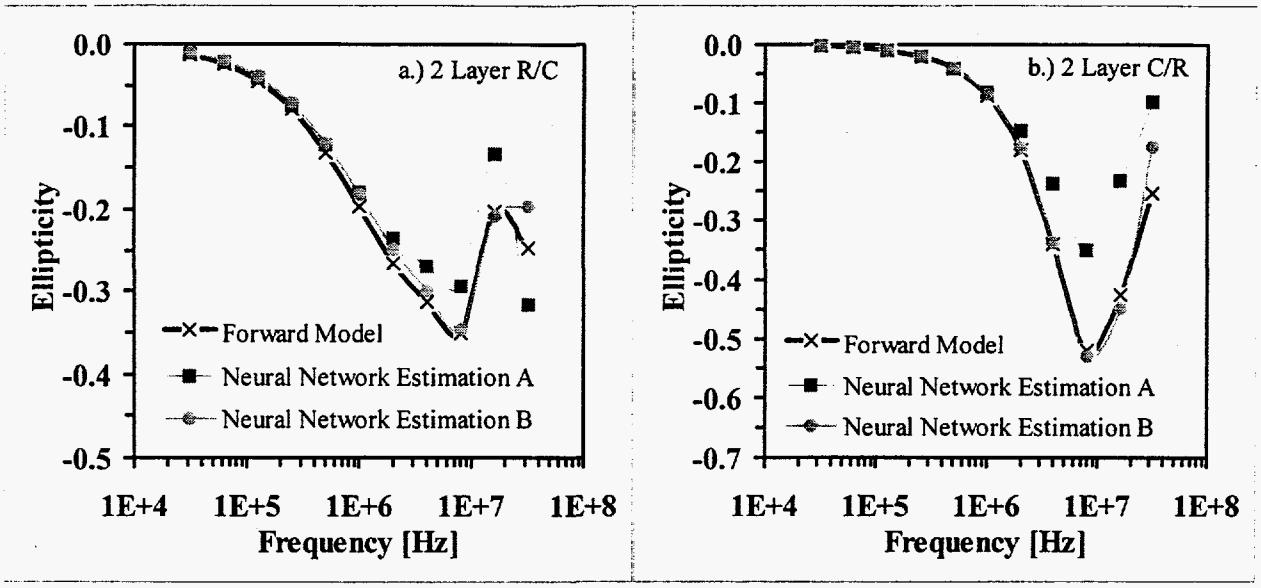

Figure 22: Two-layer neural network estimations for two synthetic two-layer cases. a.) Resistive over conductive case. Forward model (squares): 200 Ωm (ε=1) 1 m thick over 50 Ωm (ε=10); Fit A from two-layer resistive over conductive neural network (squares): 324 Ωm 1.0 m thick over 49 Ωm; Fit B from 1 m fixed two-layer network (circles): 259 Ωm (ε=1.7) over 56 Ωm (ε=8.0). b.) Conductive over resistive case. Forward model (crosses): 200 Ωm (ε=1) 1 m thick over 800 Ωm (ε=10), Fit A from two-layer conductive over resistive neural network (squares): 290 Ωm 0.1 m thick over 330 Ωm, Fit B from 1 m fixed two-layer network (circles): 221 Ωm (ε=2.2) over 639 Ωm (ε=10.3).

THICK-NESS	R1		R2		D1		D2	
	c/r	r/c	c/r	r/c	c/r	r/c	c/r	r/c
20 cm	11.5	11.7	4.4	2.7	97.2	63.8	51.6	57.7
40	7.4	8.8	4.9	3.9	81.0	47.9	80.5	79.5
60	4.8	6.2	4.8	3.2	59.6	38.5	73.4	82.5
80	3.8	4.9	4.9	3.9	49.6	38.8	87.4	101.0
1 m	3.1	4.2	5.0	4.2	46.2	32.3	87.7	130.8
1.2	2.5	4.0	5.4	4.8	40.3	30.3	105.5	132.8
1.4	2.6	3.6	5.9	4.7	38.4	26.8	131.8	138.9
1.6	1.8	2.9	4.9	4.7	30.9	23.6	155.9	154.3
1.8	1.5	2.6	5.6	4.8	24.6	23.5	165.7	161.5
2.0	1.2	2.1	4.6	4.2	19.2	15.2	171.3	162.4
2.2	1.5	2.6	5.3	5.2	23.9	14.3	178.0	172.2
2.4	0.9	1.7	5.9	3.9	23.0	16.6	171.4	168.2

Table 1. Average percent errors on training data for two-layer earth models using a 4 m antenna separation. The first number in each column is the average error for models where the first layer is more conductive than the underlying halfspace; the second number is the average error when the first layer is more resistive than the underlying halfspace.

DATA VISUALIZATION SOFTWARE

The Ellipticity Data Interpretation System (EDIS) is designed to make possible a first-pass real-time interpretation with neural networks directly in the field. EDIS is developed based on the Interactive Data Language (IDL) graphics software for WINDOWS on a personal computer. EDIS goes beyond the built-in routines of IDL, it uses the IDL capabilities of interacting with DOS based programs, WINDOWS based programs and dynamic link libraries (DLL).

Display capabilities in EDIS are for sounding curves, interpreted sections, and raw ellipticity data. The user may select up to twelve sounding curves to display at one time. The difference between the last two selected curves is automatically displayed on a graph below the sounding curves. Raw ellipticity data can also be displayed versus frequency number in 2D sections. Interpreted data are displayed in 2D sections that show the color-coded resistivities or dielectric constants. The y-axis of the sections indicates the thicknesses of the interpreted layers. Several sections can be displayed at one time for other offsets or lines. EDIS also has the capability to rapidly display survey profile plots for each frequency.

The field data can be displayed and compared to previous stations. Quality control is performed by comparing combined neural network and forward modeling results with the field data. The forward modeling capability includes dielectric constants. Displayed RMS errors inform about the performance of the neural networks to fit the field data. After deciding on a particular neural network for the interpretation of a specific station the neural network results will be written to disk and can be used to build up a resistivity or ellipticity section interactively. Currently EDIS manages 146 neural networks, including the conversion of the field data to the input required by each specific neural network, running the neural network C-programs, and decoding their output to resistivity model information. Several printing options and utilities are also available within EDIS. EDIS can also process data in batch mode so that entire survey lines can be processed simultaneously.

RESULTS AND DISCUSSION

FIELD EXPERIMENTS

Our verification experiments had three levels of complexity: simple targets in a homogeneous medium; simple targets in soil; and complex targets at a DOE laboratory. The first level of experimentation was conducted in the physical modeling facility at the Avra Valley Geophysical Test Site. This facility is used to examine responses of simple targets in a homogeneous host environment as a function of target size, position, depth, and conductivity. The nature of the response can be used to separate target response from geologic noise for data collected over targets buried in soil. We also gain information on the resolution of the system from these data. Neural networks were trained on the physical modeling data to estimate target position and to distinguish between target response and background response.

The second level of experimentation we describe extends the concept of the physical modeling experiments to simple targets buried in soil or suspended in a water-filled pipe. These experiments allow us to test the system and interpretation in material that has heterogeneities that can be similar in size and magnitude to that of the target. We can gain more information on which frequencies respond to small, shallow targets, the resolution of the system, and the character of the ellipticity sounding curves. We tested the piecewise apparent resistivity networks using these data.

The third level of experimentation was conducted at the Idaho National Engineering Laboratory Cold Test Pit, near Idaho Falls, Idaho in late 1995 and at the Acid Pit at INEL in late 1996. These experiments allowed us to test the system under more realistic conditions in terms of type and quantity of targets, soil conditions, and survey area size. We tested the layered-earth neural networks, and the piecewise apparent resistivity networks with the data from the Cold Test Pit. The networks were tested on-site and in near-real time and also remotely and off-line. Neural networks were also trained on these data to locate areas of waste and background and to categorize the type of waste.

PHYSICAL MODELING FACILITY

The modeling tank is 3 m deep, 23 m long, and 6 m wide (see Figure 23). The tank is lined with shotcrete containing Fibermesh to control leakage and for structural stability. A wood framework surrounds the tank and supports two decks which run the length of the tank (see Figure 12). The decks straddle the center of the tank with 3 m separating them. A wooden trolley runs down the center of the tank on wood tracks. Targets are suspended from the trolley and moved into any position in the tank. Care was taken during design and construction of the trolley to ensure that it contained no metal components below the water line. The volume of the tank is 360 m^3 or 95,055 gallons. Even with the Fibermesh additive in the shotcrete, it was expected that the tank would

leak. Leakage of water into the surrounding soil should raise the conductivity of the soil to a level closer to the conductivity of the water in the tank, thus decreasing effects from the walls of the tank. A 10,000 gallon tank is connected via PVC pipe to the tank and can be used to top off the tank.

Physical Modeling Experiments

The tank was filled to a depth of approximately 2 m during our experiments. Rapid leakage from cracks prevented filling to a greater depth. The receiver and transmitter antennas were fixed in position over the center of the tank. The antennas were not moved horizontally during the experiment but did have to be raised and lowered to allow passage of the trolley due to the lower than anticipated water level. Targets were suspended from the trolley and moved in 2 m and 0.5 m increments along the length of the tank. The antennas were placed on top of the water surface but not touching the water. Target depths were measured from the top of the water surface at the start of each trial. The resistivity of Tucson tap water, of which this water is representative, is approximately 30 ohm-m. The receiver antenna was fixed at station 2 m and the transmitter was at station -2 m. A four meter antenna separation was used for all trials. Data from 31 and 62 kHz were not used because the induction numbers at these frequencies was too far outside the designed range to give usable data. We will be referring to ellipticity magnitudes in an absolute value sense rather than in terms of the negative values plotted in the figures. The negative sign is a notation convention; an ellipticity of -0.2 is larger than a value of -0.1.

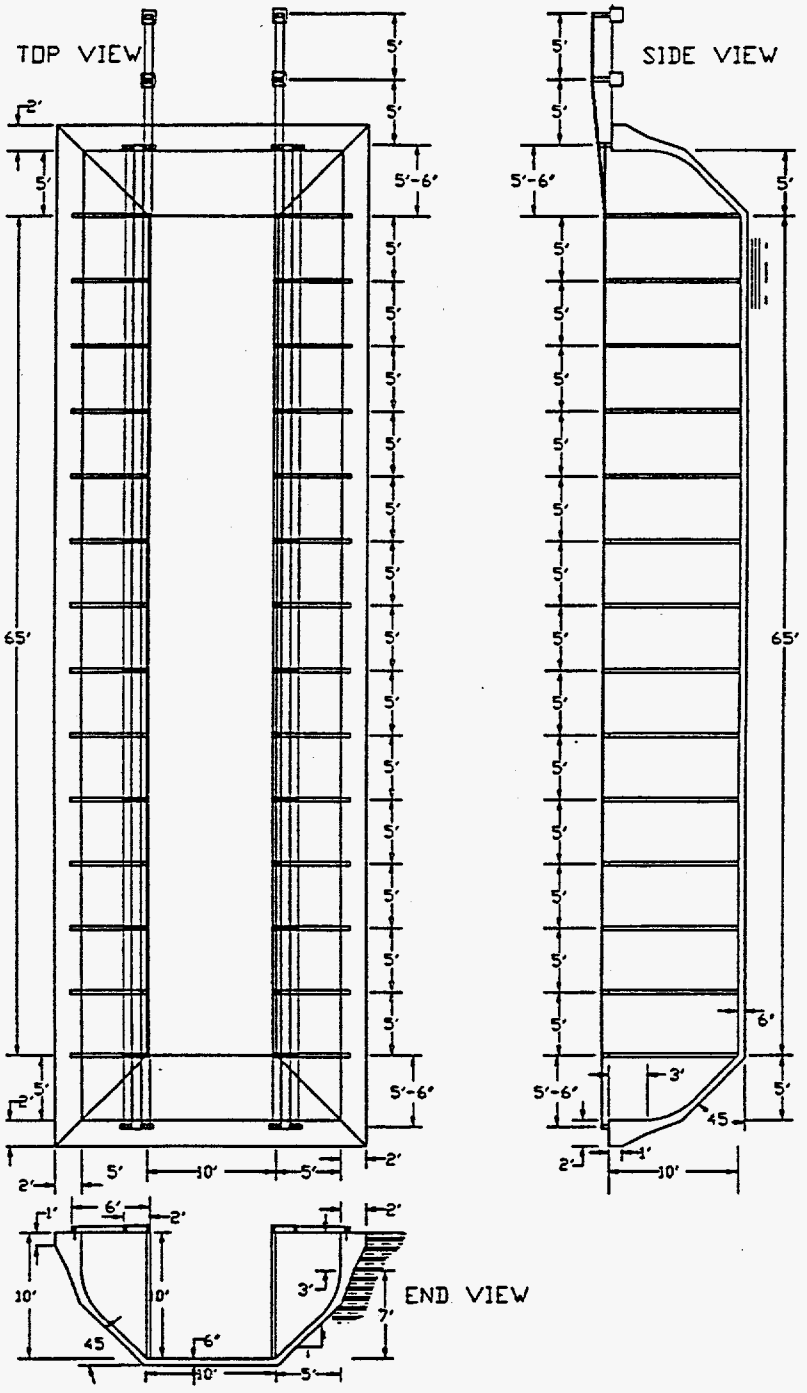

Figure 23. **Engineering drawings of the physical modeling tank. Units on the drawings are in feet and inches.**

The following is a description of each trial.

55-GALLON BARREL

The first target used was a horizontal 55-gallon barrel (oriented with its long axis perpendicular to the profile line). The barrel was 0.85 m tall and had a diameter of 0.58 m. The barrel was lowered to a depth of 0.63 m.(i.e. 0.63 m from water surface to top of the barrel). This depth coincides with the depth of one of the drums buried in soil at the test site. Figures 24-26 show ellipticity profiles along the length of the tank. A 2 m station spacing was used for this trial. We observe from the profile plots that the anomaly response is quite complicated across frequencies. The anomaly magnitudes are of a detectable size, especially at the higher frequencies.

ALUMINUM SHEET

An aluminum sheet, 1.83 m long and 0.31 m wide with its long dimension oriented perpendicular to the profile line, was lowered to a depth of 0.30 m and moved the length of the tank in 2 m and 0.5 m intervals. The 0.5 m intervals were used between stations 2m and -2m to allow better resolution of the target. The ellipticity profiles are shown in figures 27-29. The minimum and maximum ellipticity response occurs approximately when the target is under the receiver (maximum at station 2 m) and when it is under the transmitter (minimum at station -2 m). The high-frequency response tends to show a maximum centered closer to the target. The character of the anomaly is similar in shape for the barrel and the sheet. The sheet is narrower than the barrel. The anomaly amplitudes for the sheet are slightly less than for those of the barrel. The denser station spacing shows more detail over the target which may have been aliased in the barrel data.

The sheet was lowered to a depth of 1.03 m and the trial repeated twice. The original and repeated data are shown in Figures 30-32. A station spacing of 2 m was used for these trials. The repeats are generally good. Much of the deviation is attributed to changing the vertical position of the antennas to allow the trolley to pass. When we tested the repeatability at individual stations without moving the antennas, the repeated values were in excellent agreement. The character of the ellipticity curves is different at the higher frequencies compared to the 0.30 m depth data. The amplitude of the ellipticity is also larger at the 1.03 m depth than at the 0.30 m depth but the anomaly amplitudes are smaller for the deeper depth.

We wanted to make sure the response we were observing was dominated by the target and not by the trolley so a trial was conducted with the trolley moved along the length of the tank but with no targets suspended. The results of the trolley trial are plotted on top of the sheet at 1.03 m depth in Figures 33-35 to show the level of response due to the trolley. The trolley response is flat at all frequencies and of lower magnitude than the response with a target. Therefore we are confident that dominant response in the data is due to the target.

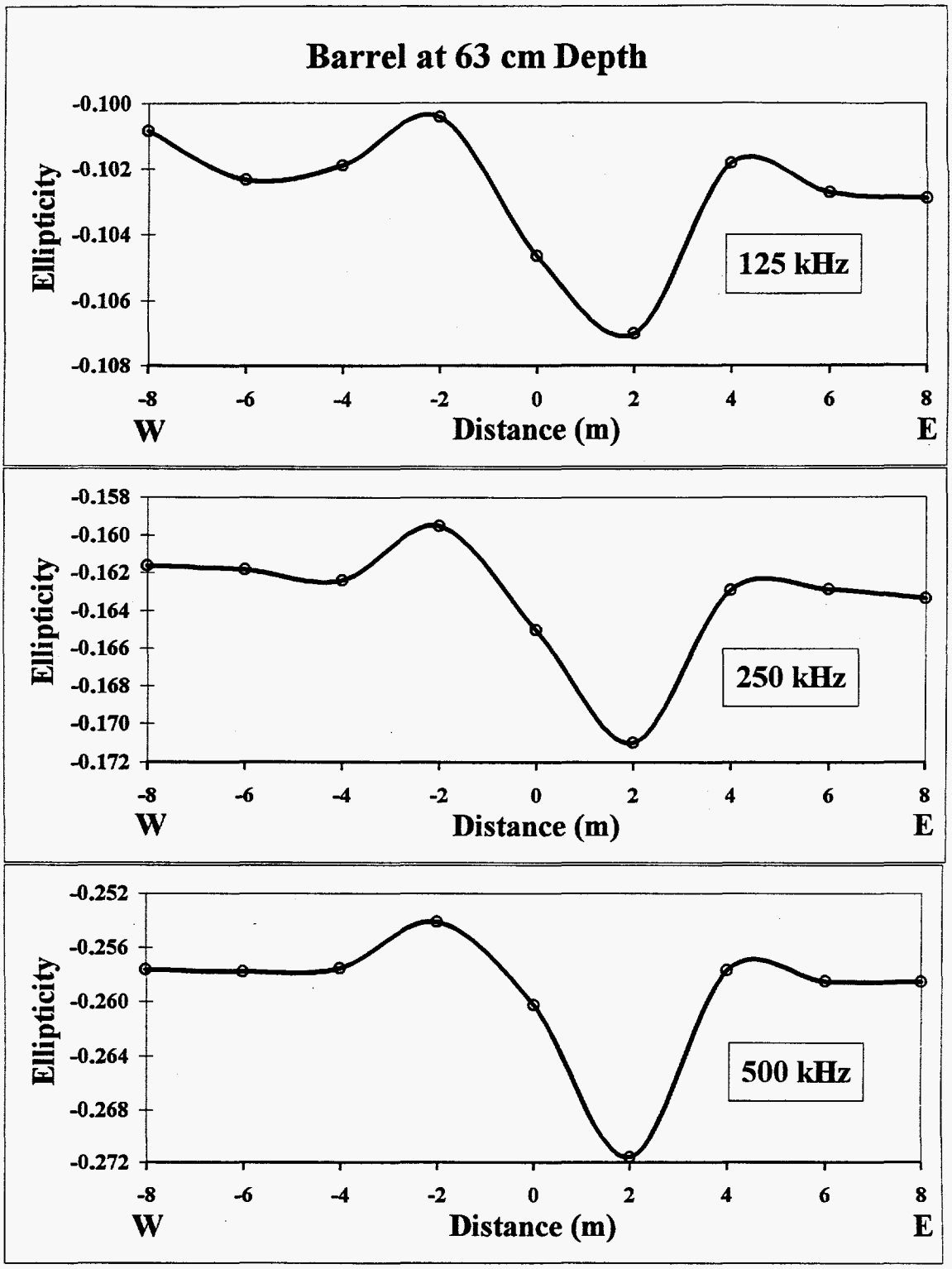

Figure 24. Ellipticity profile plots for a 55-gallon drum at a depth of 0.63 m in the physical modeling tank for frequencies of 125, 250, and 500 kHz.

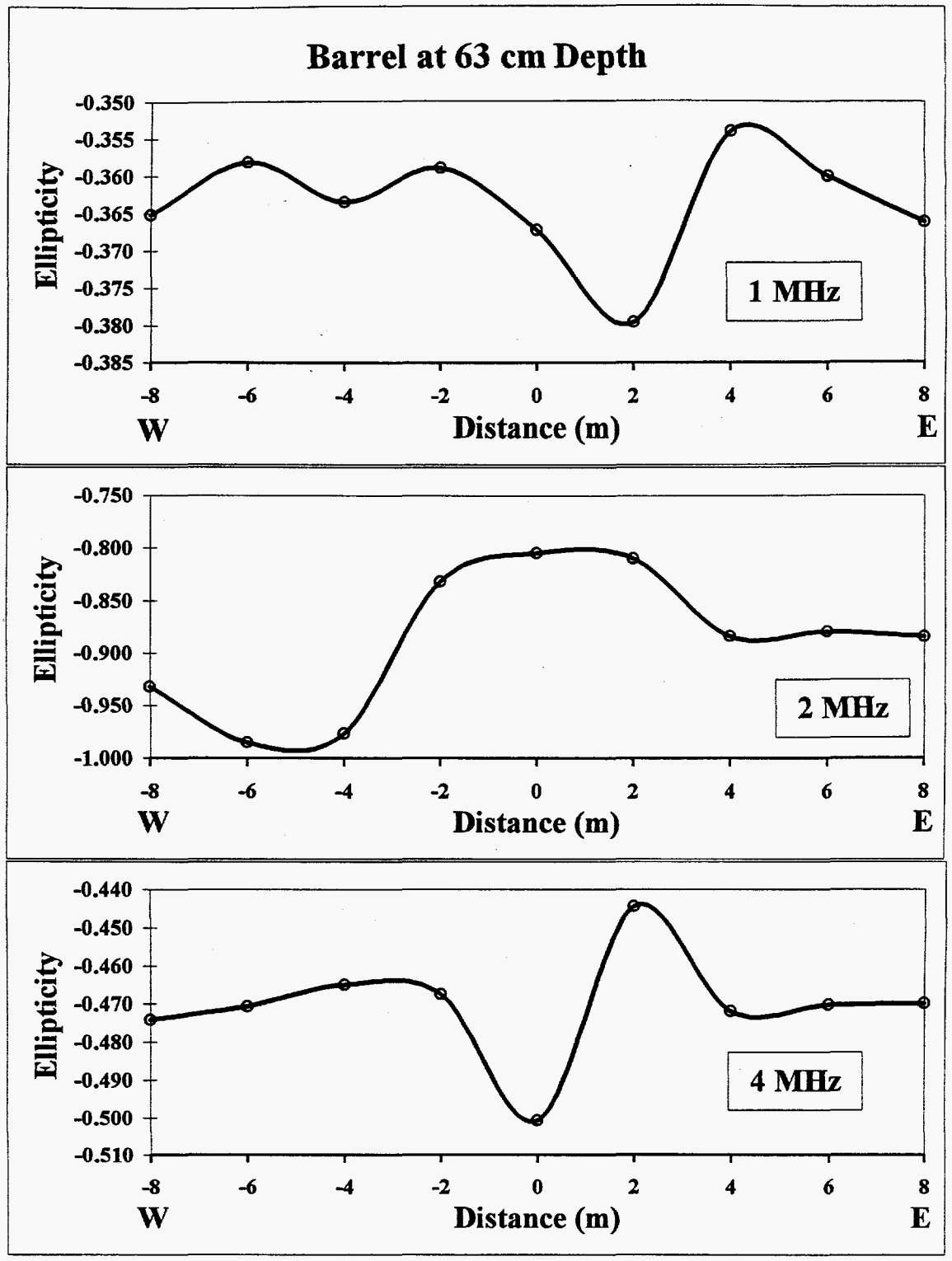

Figure 25. Ellipticity profile plots for a 55-gallon drum at a depth of 0.63 m in the physical modeling tank for frequencies of 1, 2, and 4 MHz.

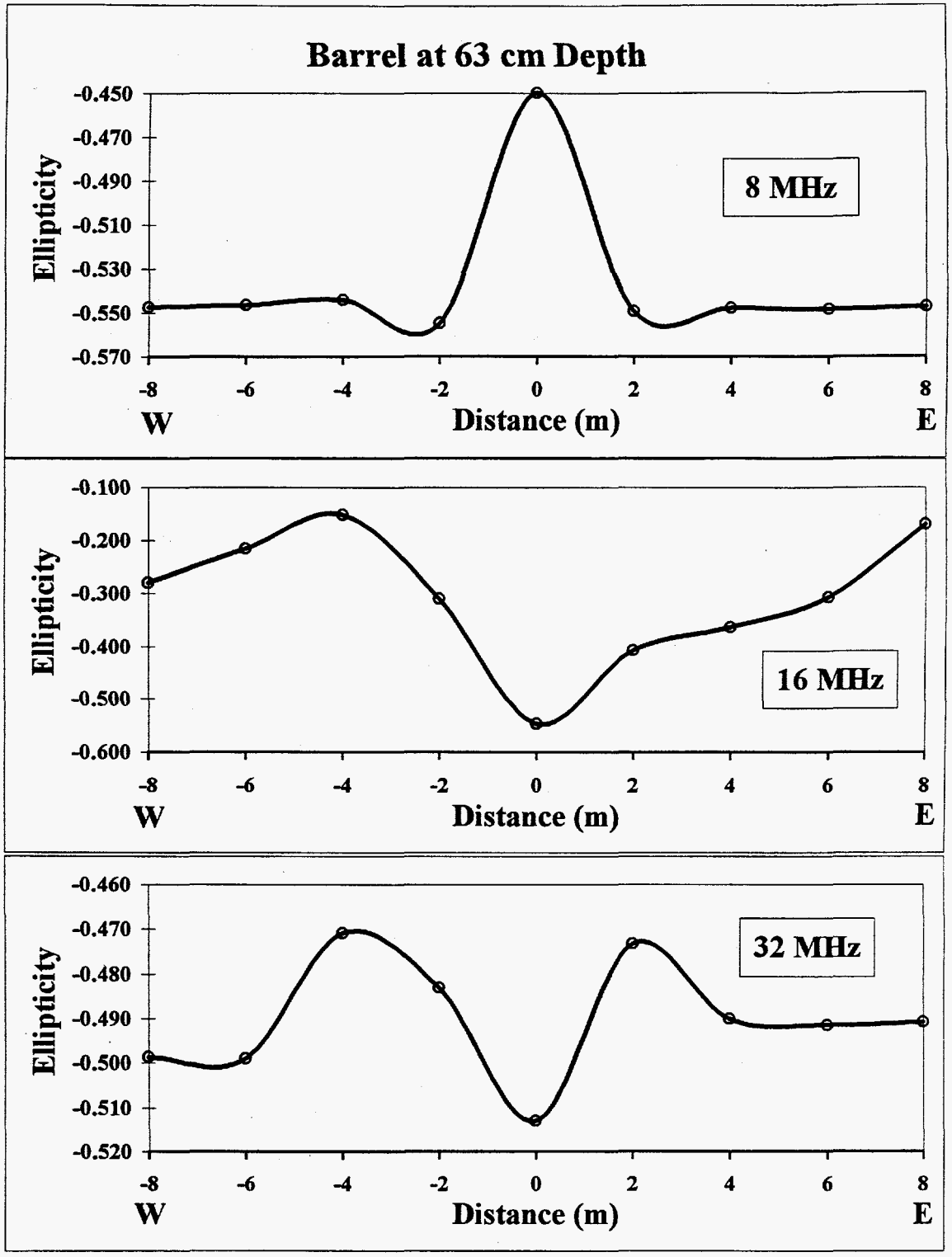

Figure 26. Ellipticity profile plots for a 55-gallon drum at a depth of 0.63 m in the physical modeling tank for frequencies of 8, 16, and 32 MHz.

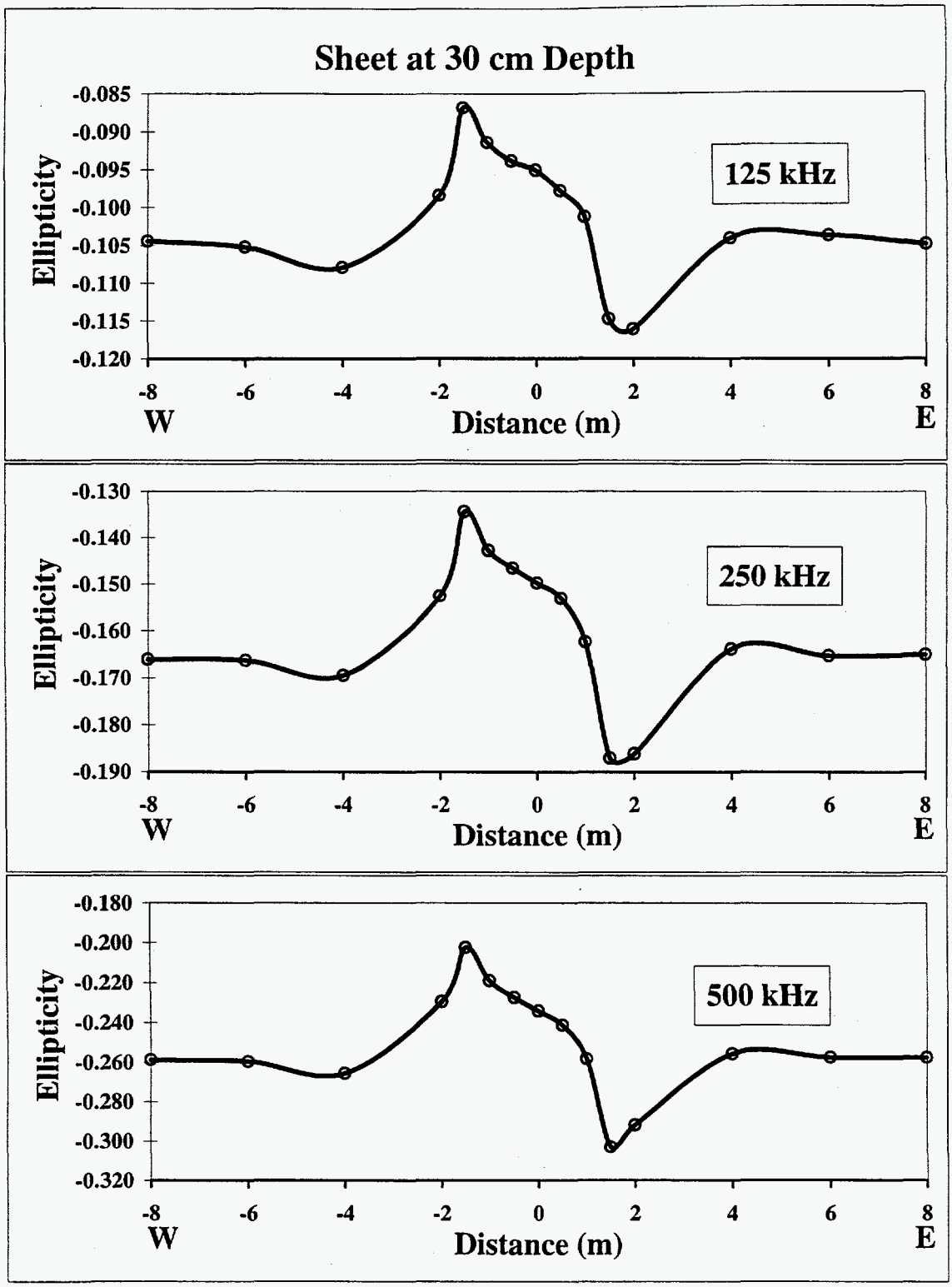

Figure 27. Ellipticity profile plots for an aluminum sheet at a depth of 0.3 m in the physical modeling tank for frequencies of 125, 250, and 500 kHz.

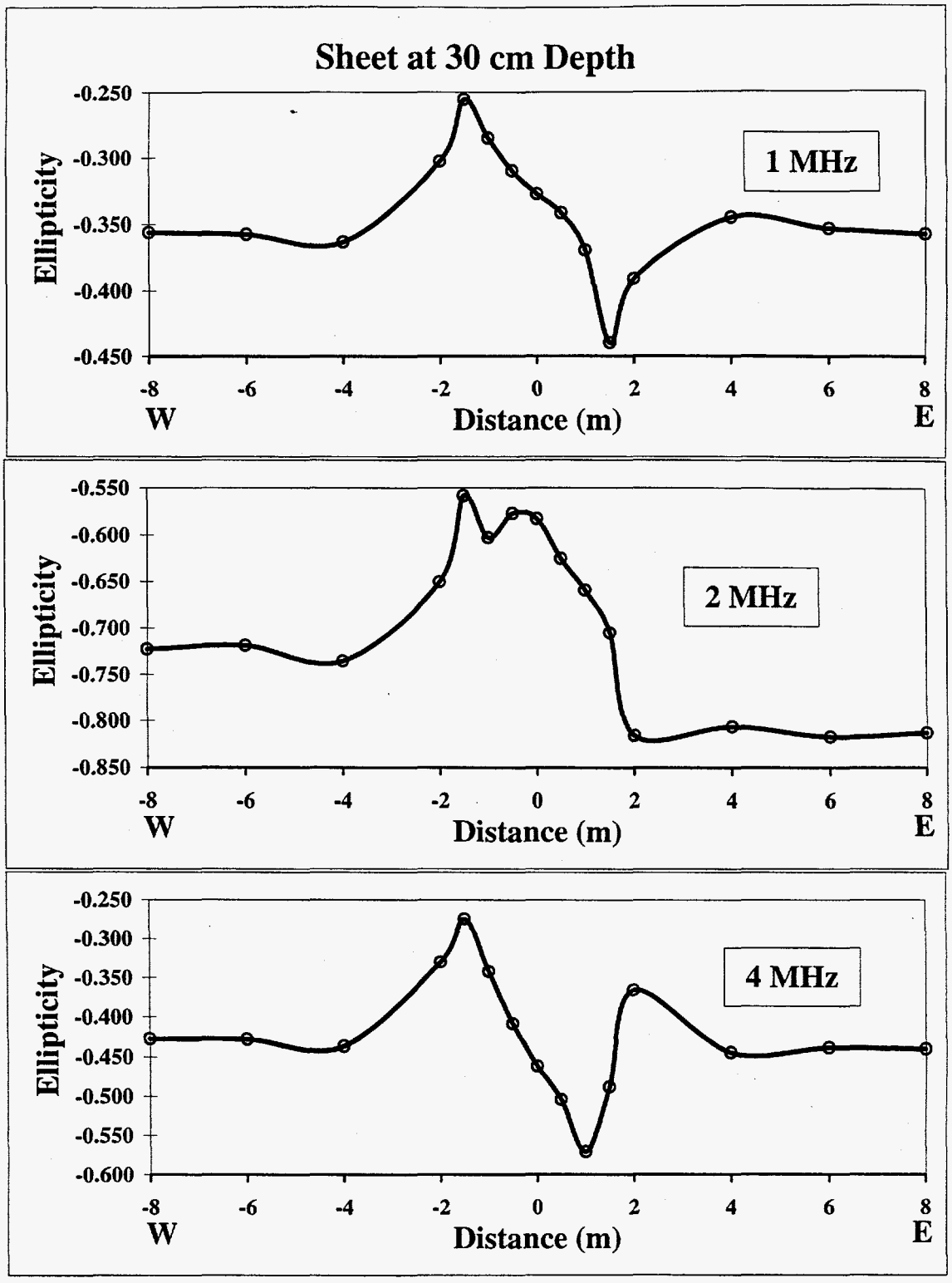

Figure 28. Ellipticity profile plots for an aluminum sheet at a depth of 0.3 m in the physical modeling tank for frequencies of 1, 2, and 4 MHz.

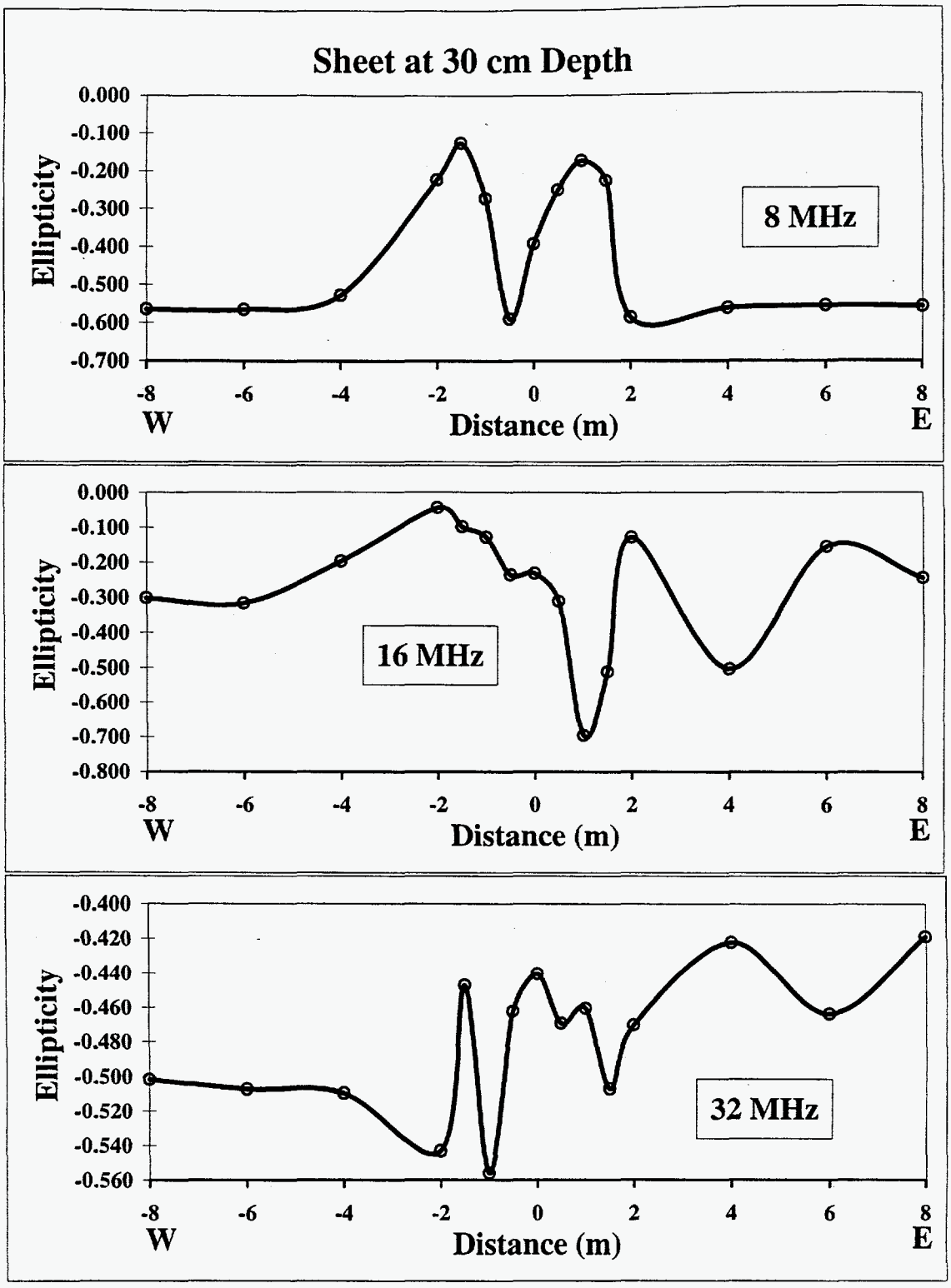

Figure 29. Ellipticity profile plots for an aluminum sheet at a depth of 0.3 m in the physical modeling tank for frequencies of 8, 16, and 32 MHz.

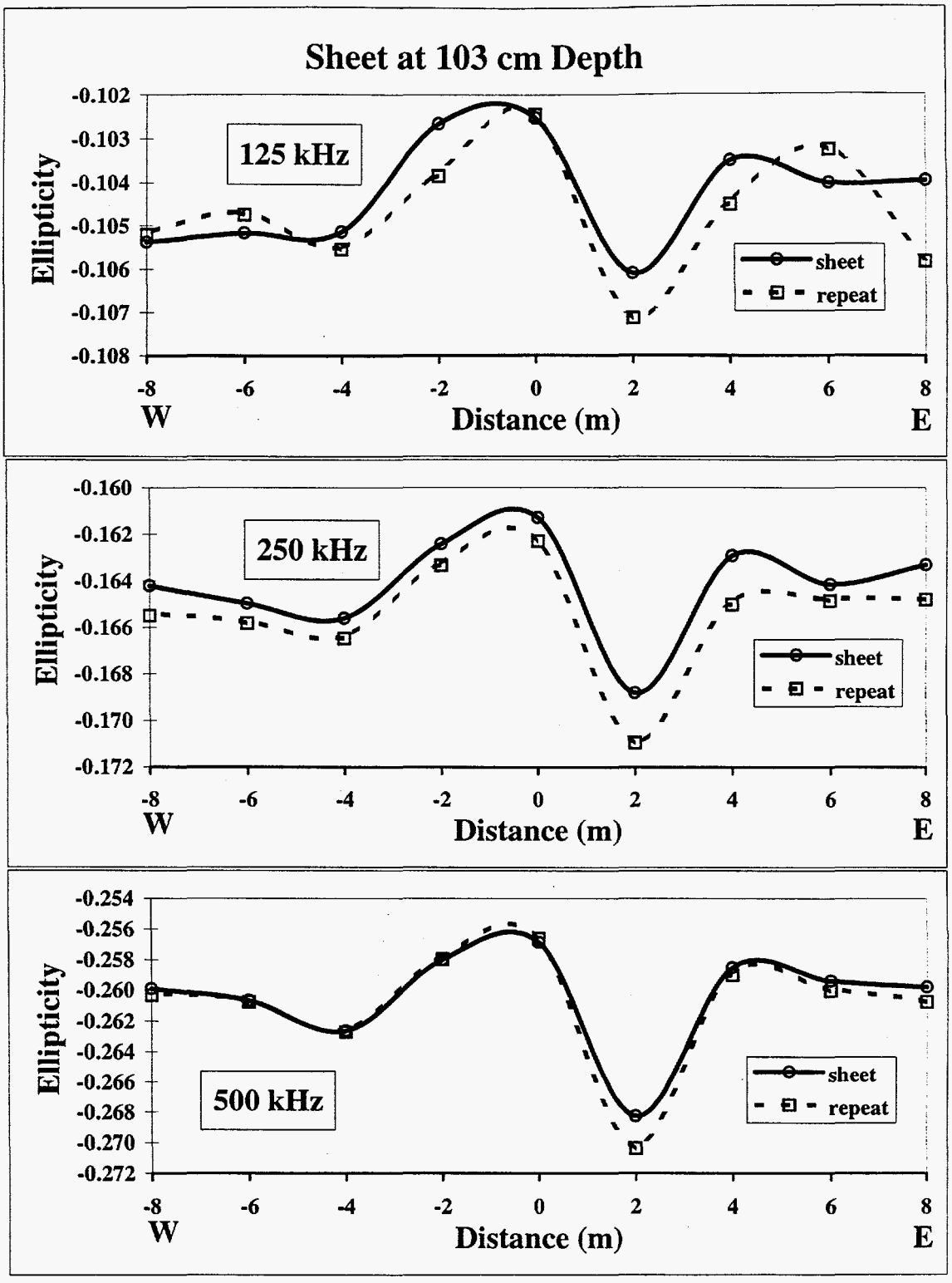

Figure 30. Ellipticity profile plots for an aluminum sheet at a depth of 1.03 m in the physical modeling tank for frequencies of 125, 250, and 500 kHz. The repeated profile is also shown.

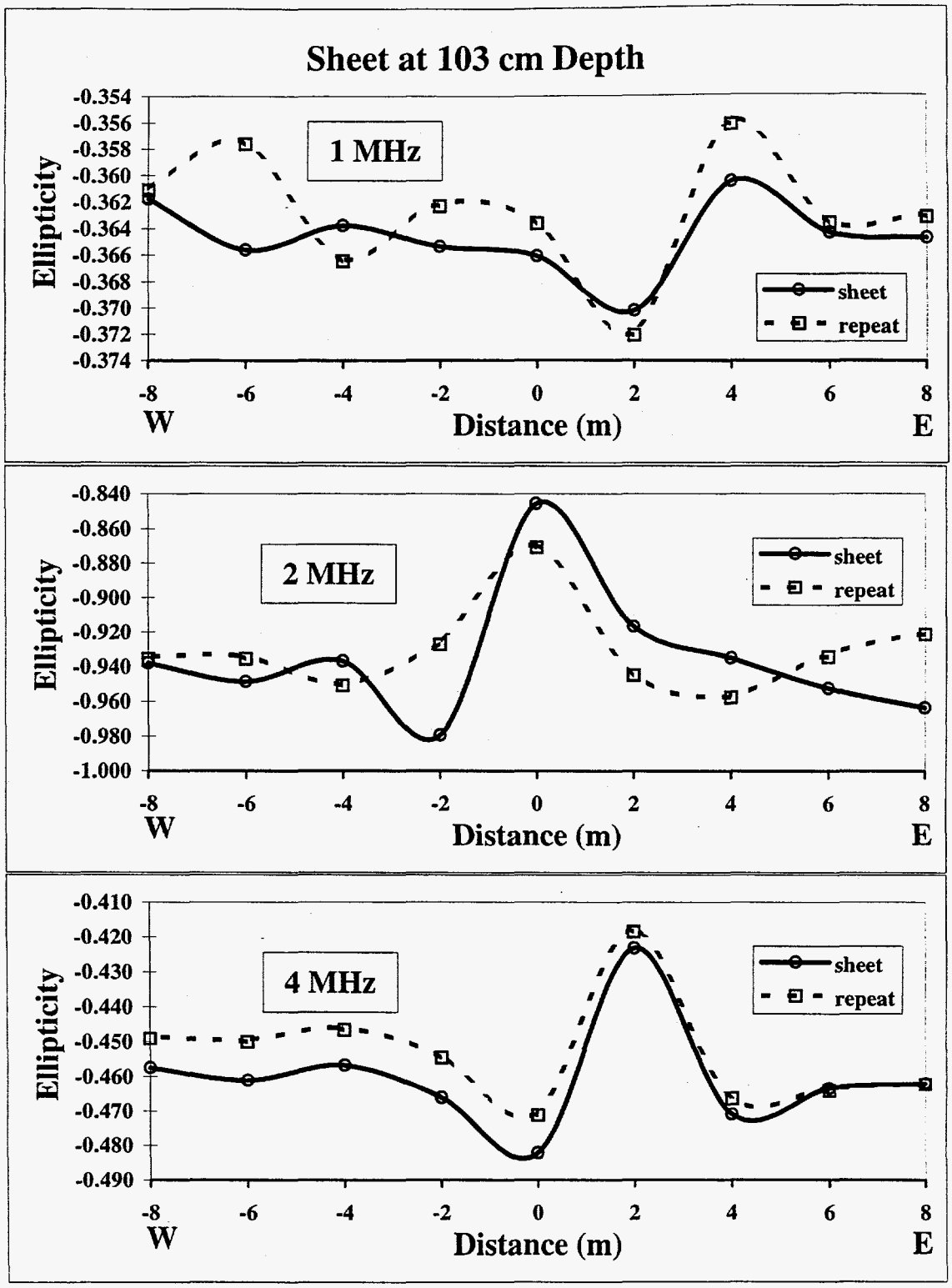

Figure 31. Ellipticity profile plots for an aluminum sheet at a depth of 1.03 m in the physical modeling tank for frequencies of 1, 2, and 4 MHz. The repeated data are also shown.

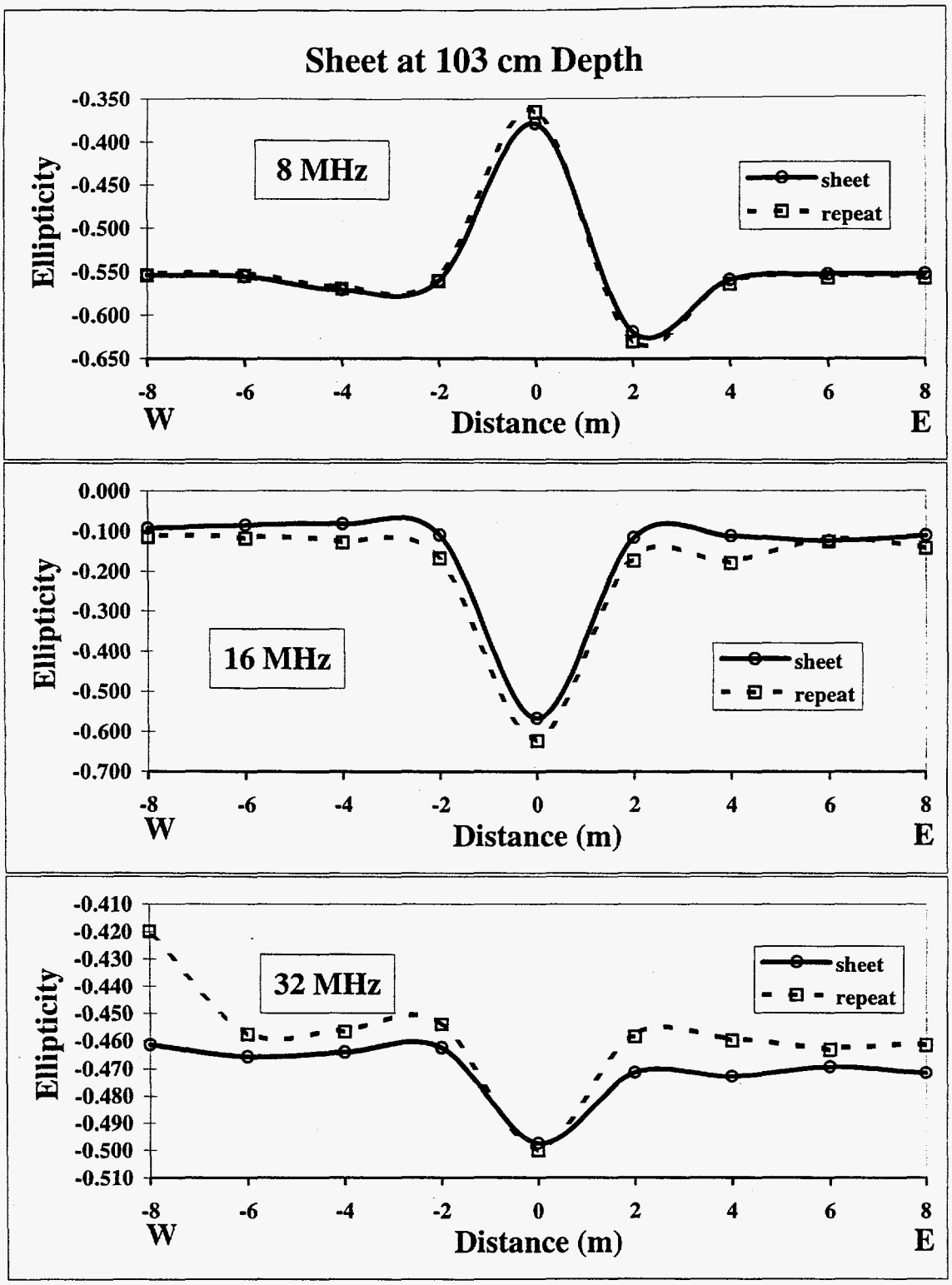

Figure 32. Ellipticity profile plots for an aluminum sheet at a depth of 1.03 m in the physical modeling tank for frequencies of 8, 16, and 32 MHz. The repeated data are also shown.

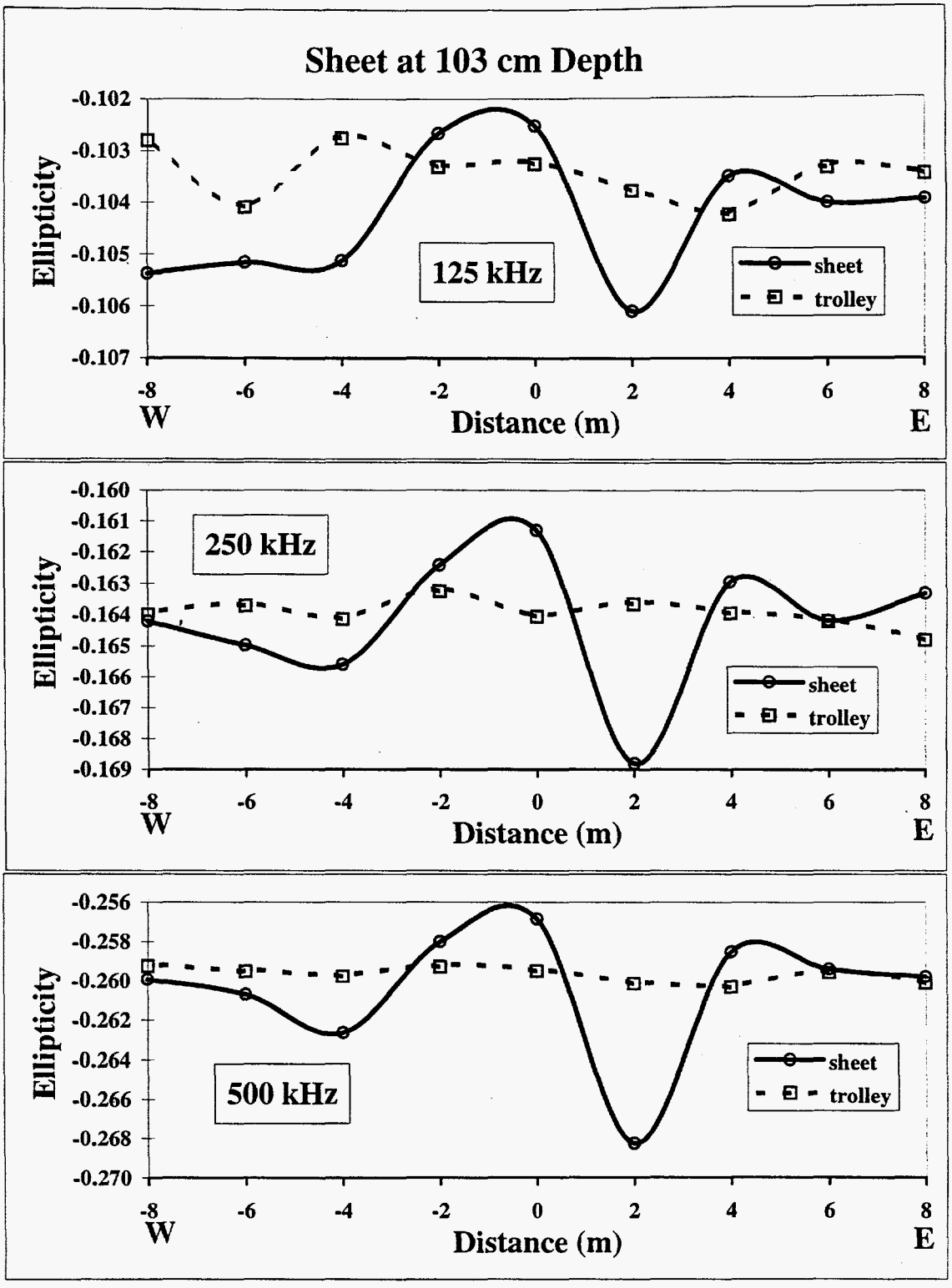

Figure 33. Ellipticity profile plots for an aluminum sheet at a depth of 1.03 m in the physical modeling tank for frequencies of 125, 250, and 500 kHz. The response from the trolley with no target is superimposed.

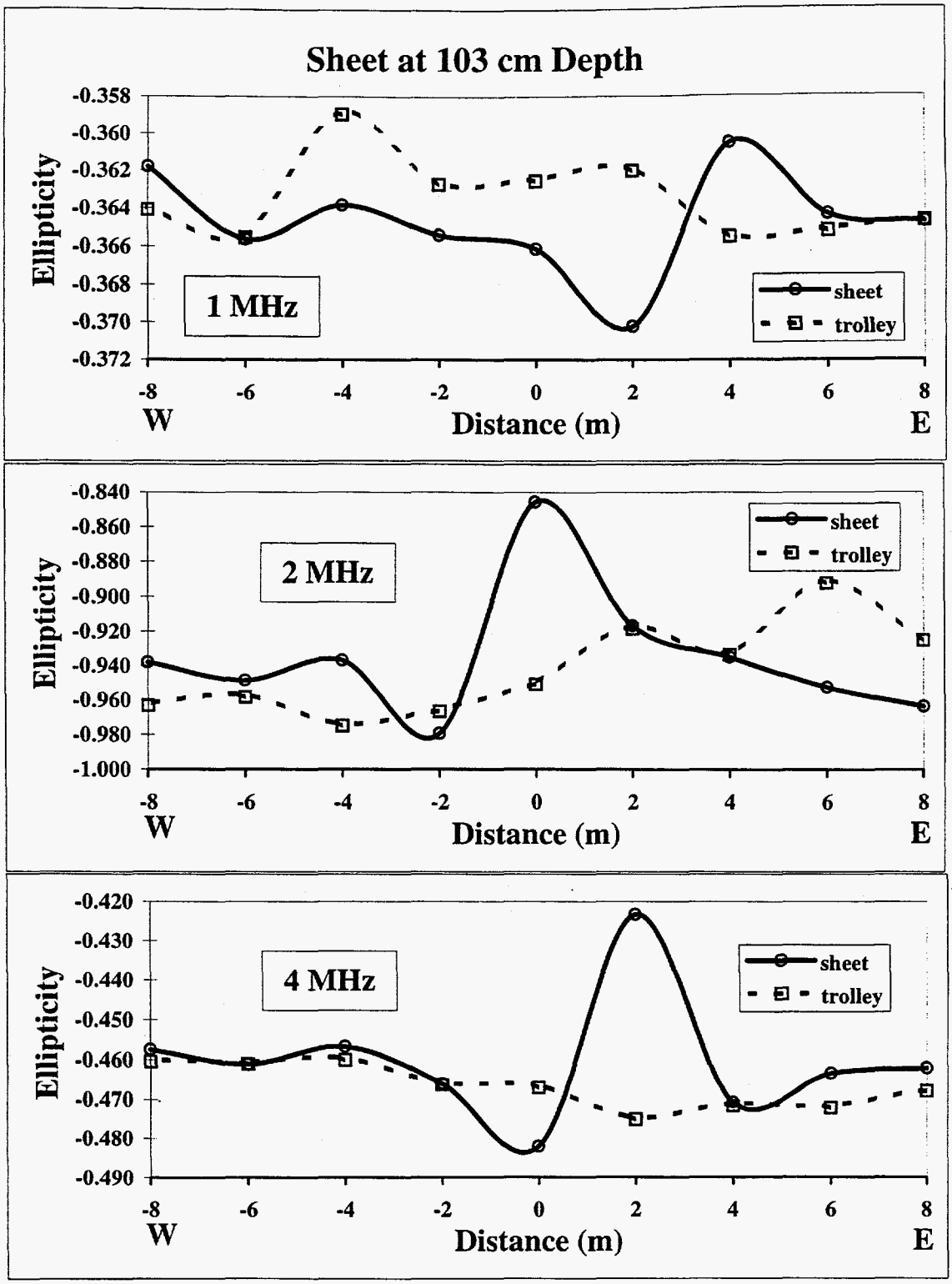

Figure 34. Ellipticity profile plots for an aluminum sheet at a depth of 1.03 m in the physical modeling tank for frequencies of 1, 2, and 4 MHz. . The response from the trolley with no target is superimposed.

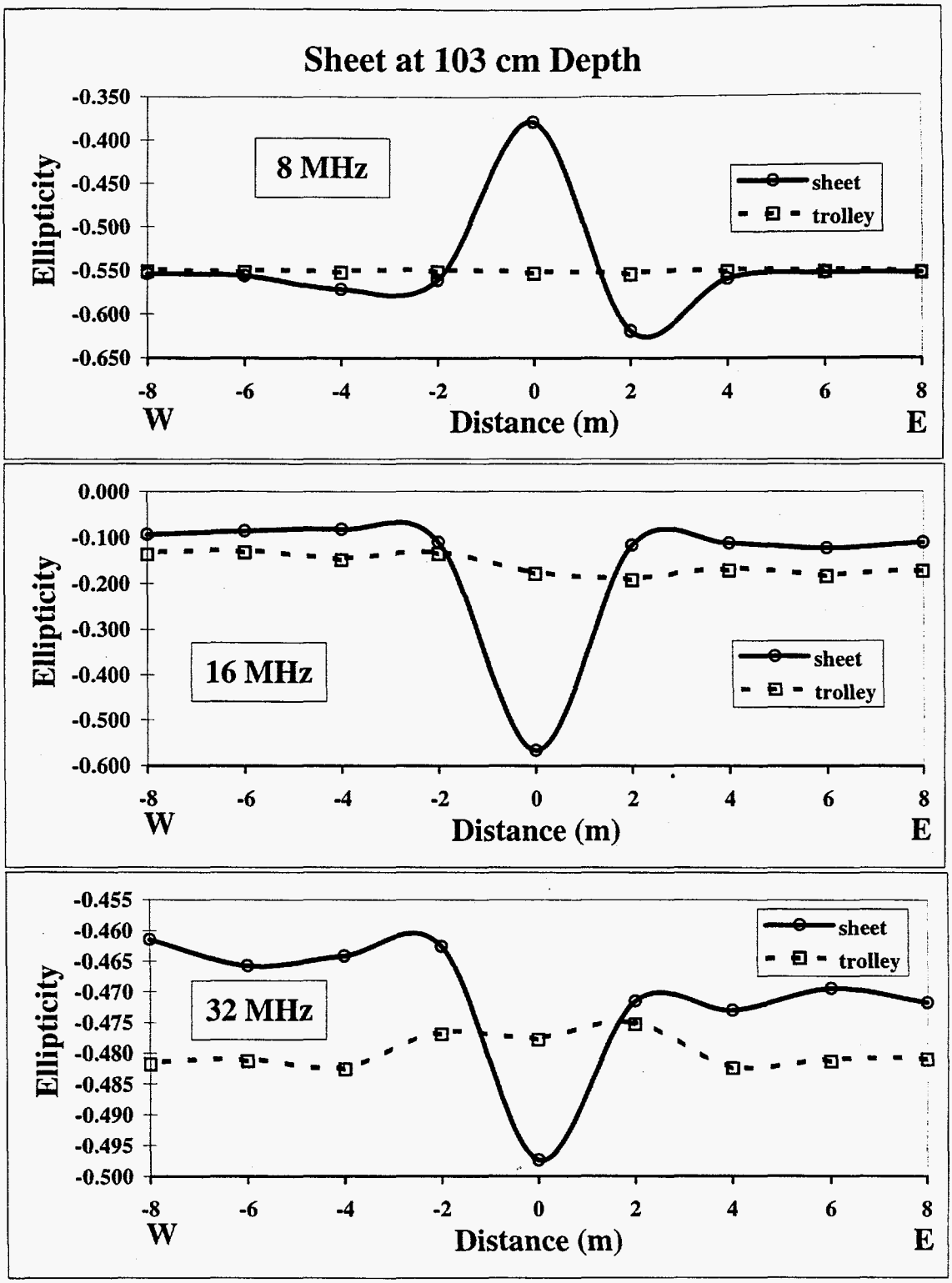

Figure 35. Ellipticity profile plots for an aluminum sheet at a depth 1.03 m in the physical modeling tank for frequencies of 8, 16, and 32 MHz. The response from the trolley with no target is superimposed.

We were able to match the shape of the sheet response with a sheet-modeling program (Hoversten and Becker, 1995). This program does not incorporate a dielectric constant so we were not able to match the amplitude of the response given the great difference between the dielectric constant for water relative to soil.

STEEL PIPE

A steel pipe, 2.07 m long with an outer diameter of 0.07 m and a wall thickness of 0.00635 m was oriented with its long axis perpendicular to the profile line. The pipe was suspended at three different depths: 0.25 m, 0.75 m, and 1.25 m. All three trials used a station spacing of 2 m beyond the antennas and 0.5 m between the antennas. The pipe at 0.25 m depth (Figures 36-38) shows a very similar response to that of the sheet at 0.30 m. The ellipticity magnitudes are slightly lower for the pipe than for the sheet at the lower frequencies, and much lower at the higher frequencies. The pipe at 0.75 m has smaller ellipticity values than the shallower pipe (see Figures 39-41). The character of the profiles is similar.

The pipe at 1.25 m depth has larger ellipticity values than the shallower pipe because the background values are shifted to higher values (Figures 42-44). The magnitude of the anomaly is smaller for the deeper target. The character of the profile curves is identical to those from the 0.75 m depth except at 16 and 32 MHz.

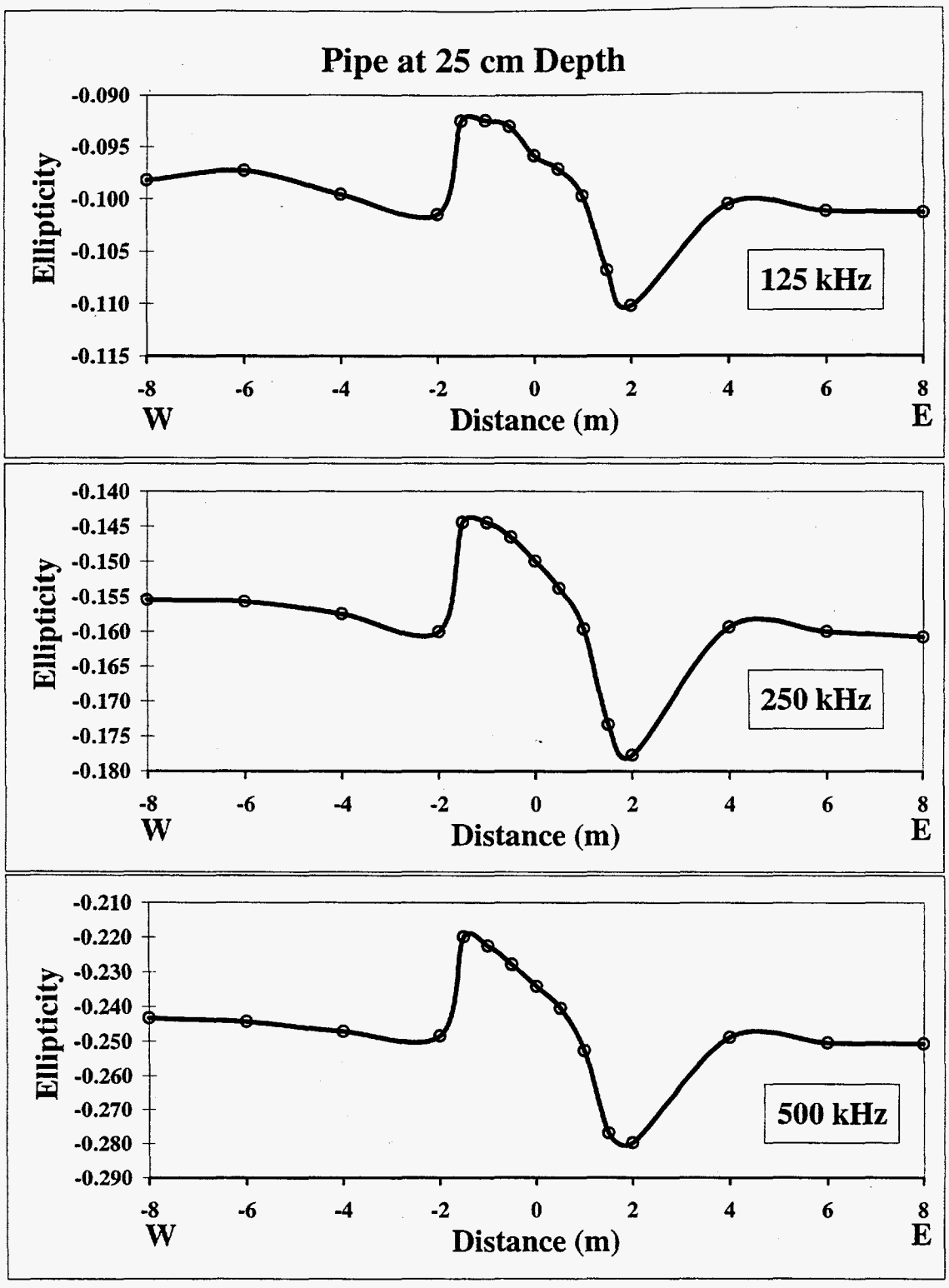

Figure 36. Ellipticity profile plots for a steel pipe at a depth of 0.25 m in the physical modeling tank for frequencies of 125, 250, and 500 kHz.

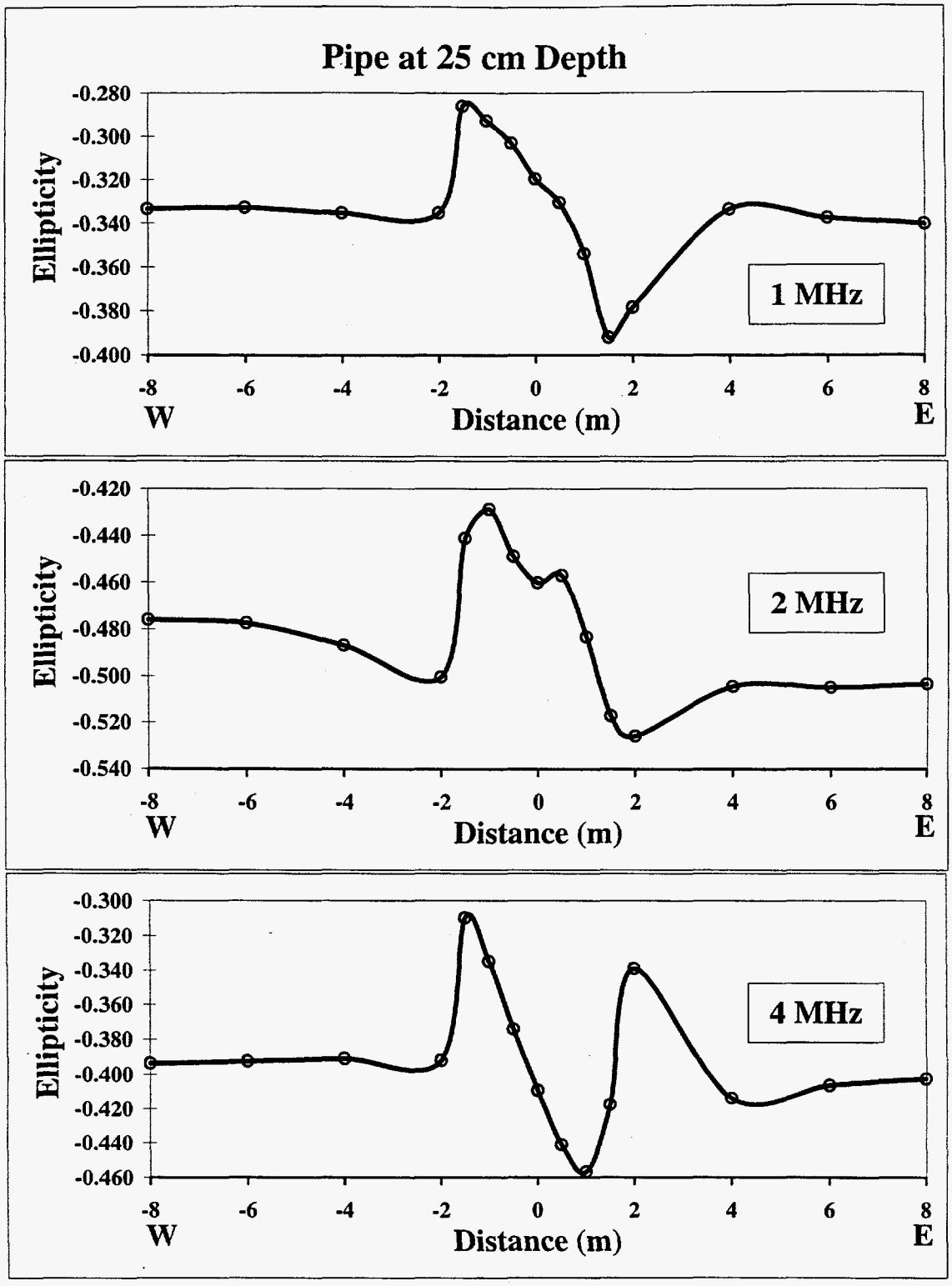

Figure 37. Ellipticity profile plots for a steel pipe at a depth of 0.25 m in the physical modeling tank for frequencies of 1, 2, and 4 Mhz.

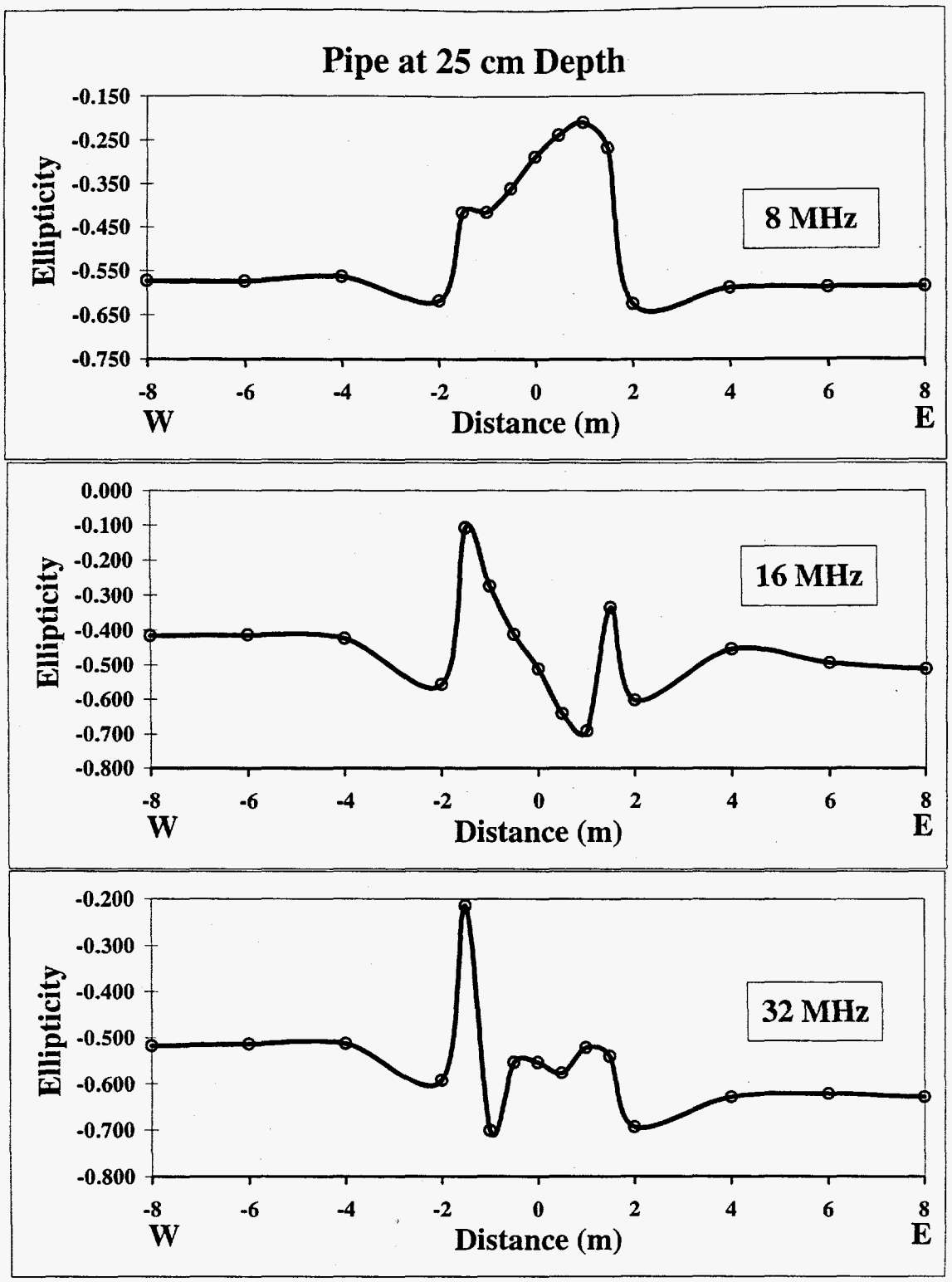

Figure 38. Ellipticity profile plots for a steel pipe at a depth of 0.25 m in the physical modeling tank for frequencies of 8, 16, and 32 MHz.

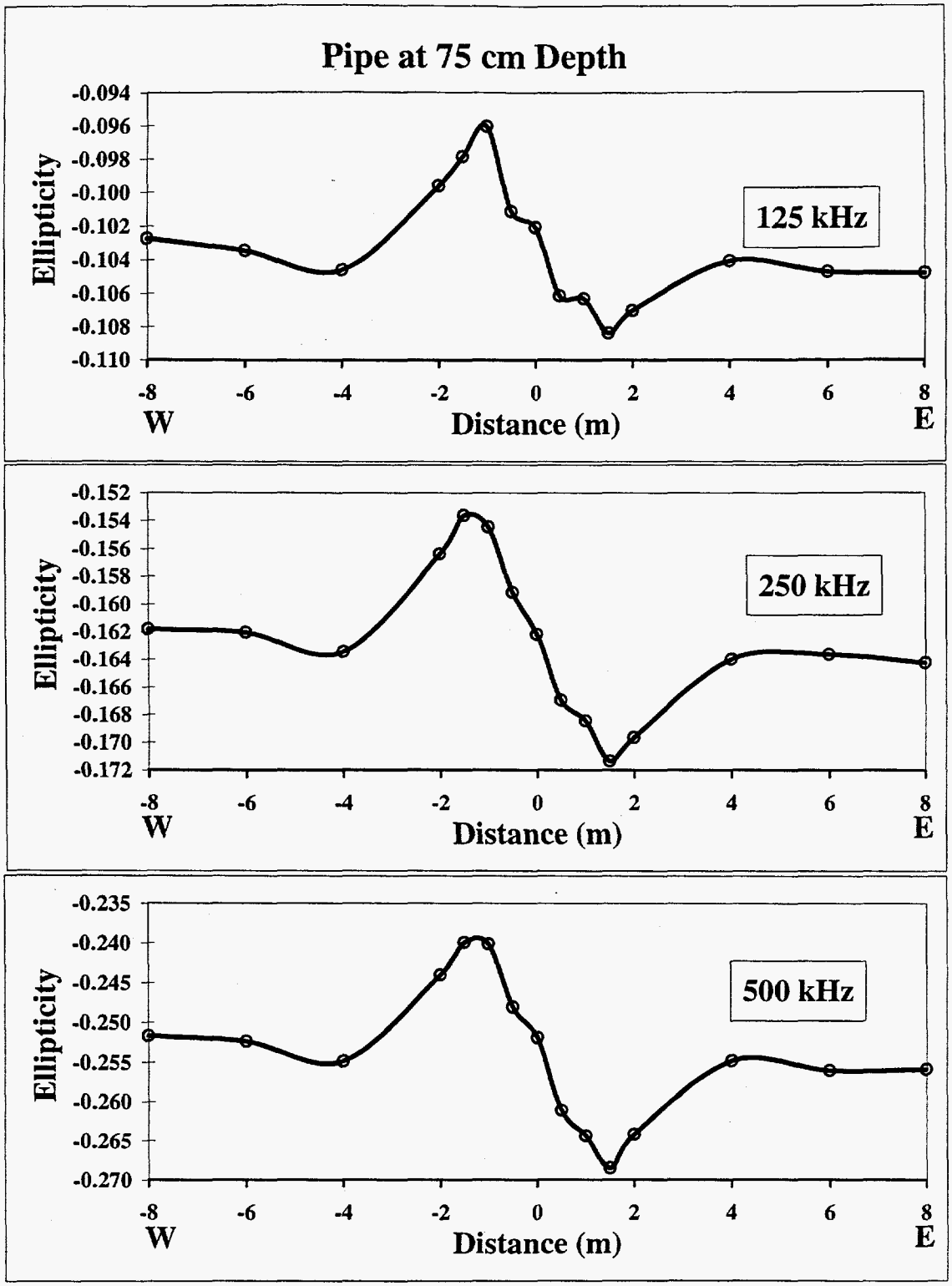

Figure 39. Ellipticity profile plots for a steel pipe at a depth of 0.75 m in the physical modeling tank for frequencies of 125, 250, and 500 kHz.

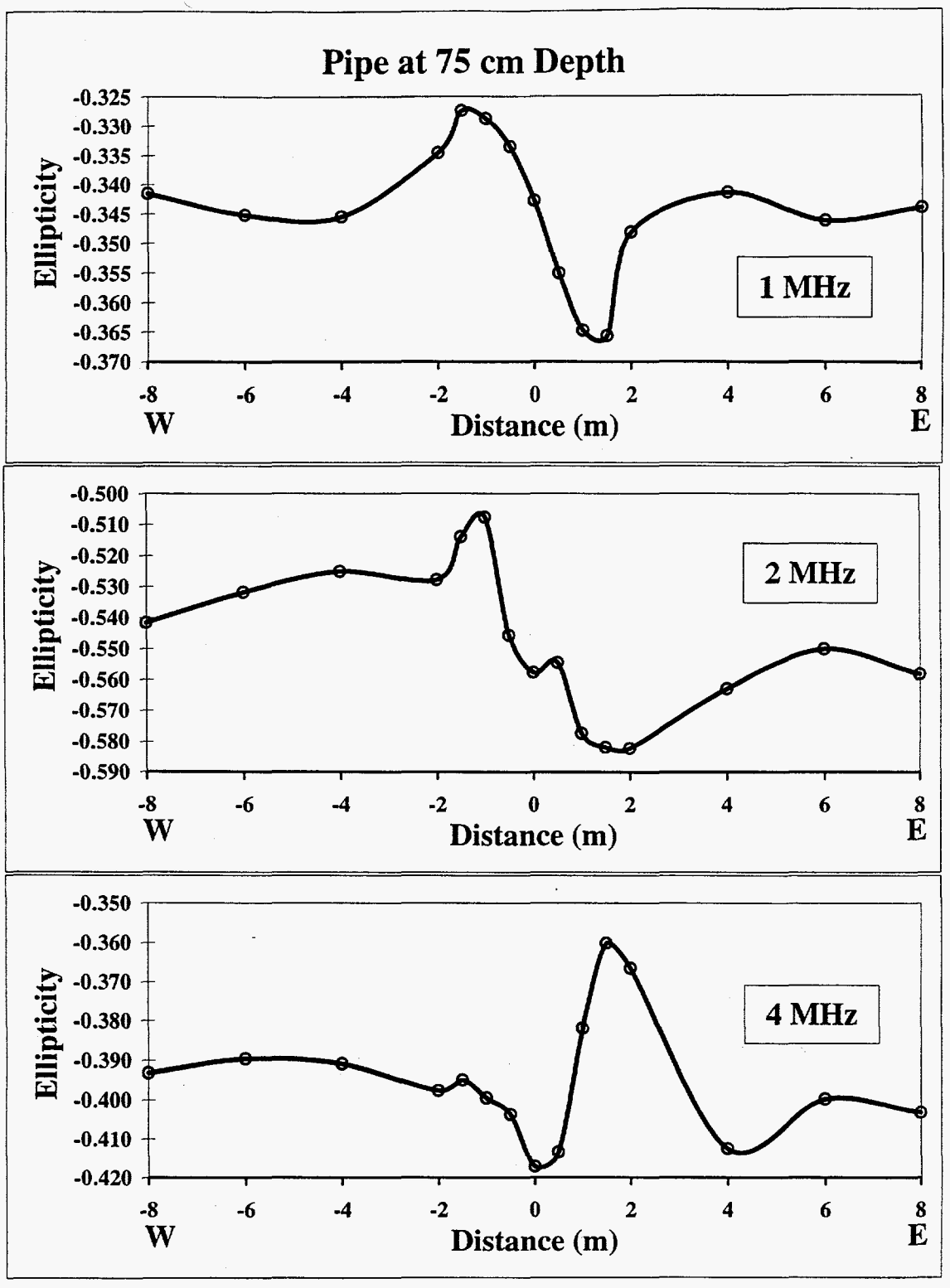

Figure 40. Ellipticity profile plots for a steel pipe at a depth of 0.75 m in the physical modeling tank for frequencies of 1, 2, and 4 Mhz.

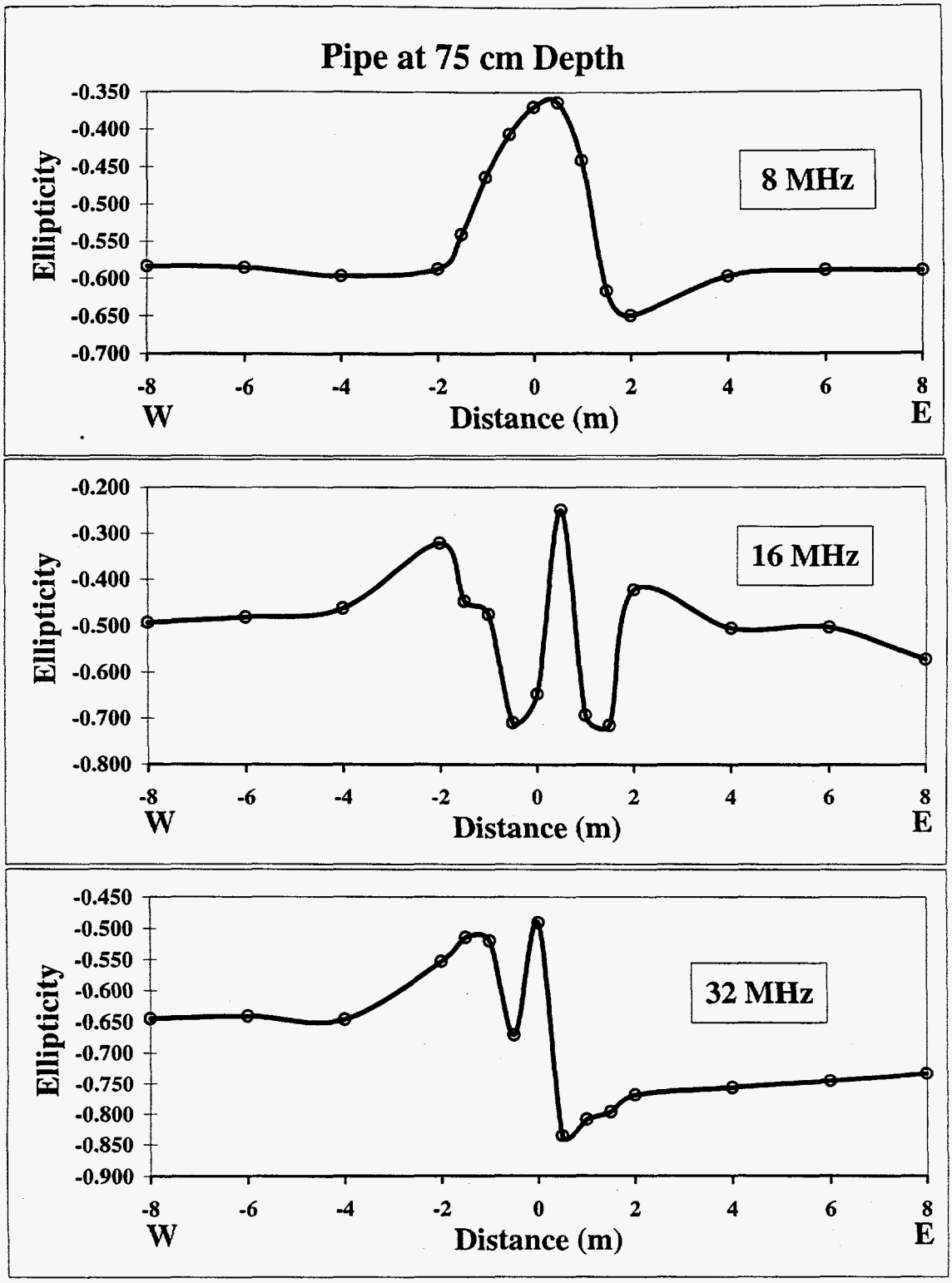

Figure 41. Ellipticity profile plots for a steel pipe at a depth of 0.75 m in the physical modeling tank for frequencies of 8, 16, and 32 MHz.

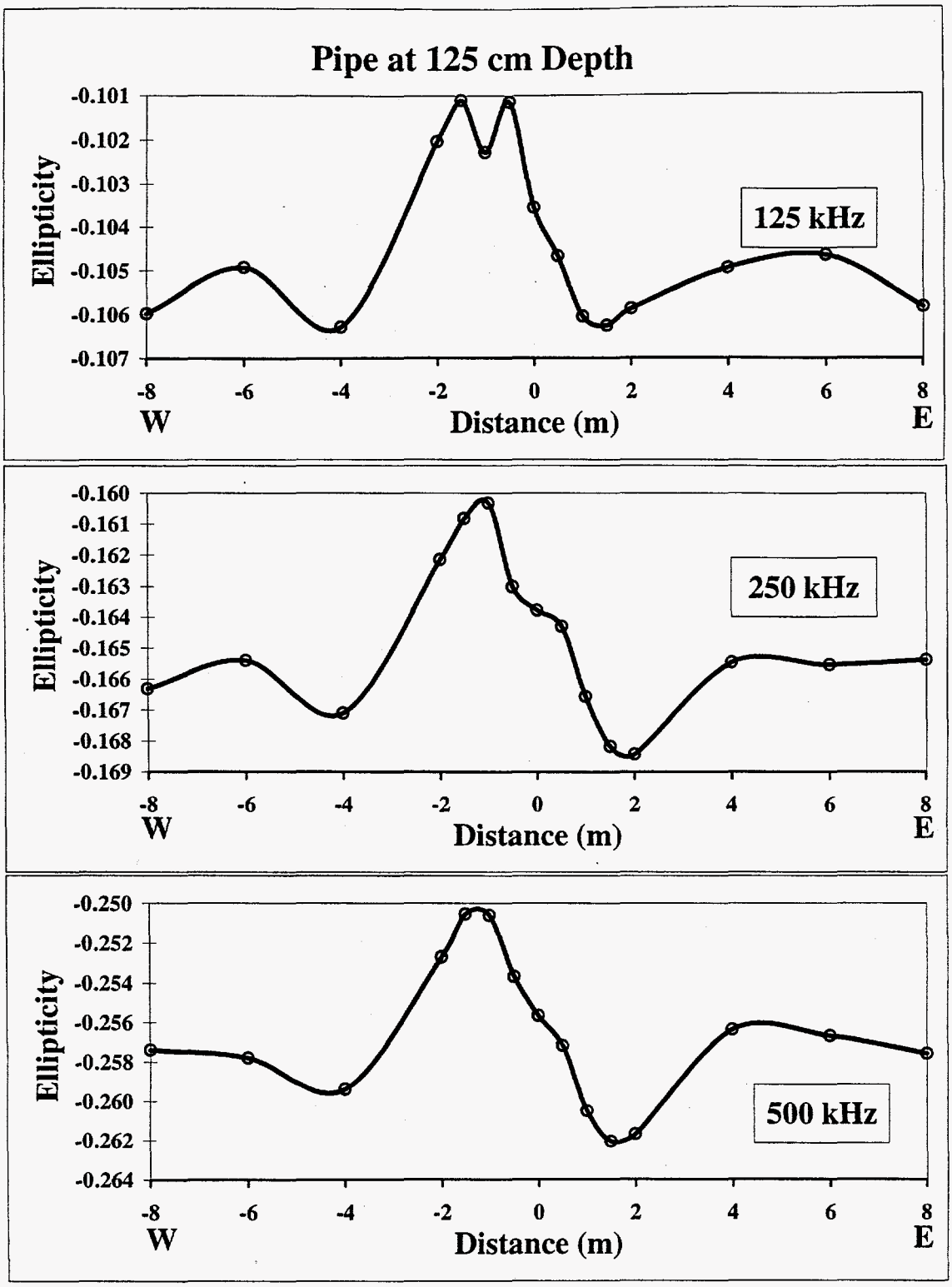

Figure 42. Ellipticity profile plots for a steel pipe at a depth of 1.25 m in the physical modeling tank for frequencies of 125, 250, and 500 kHz.

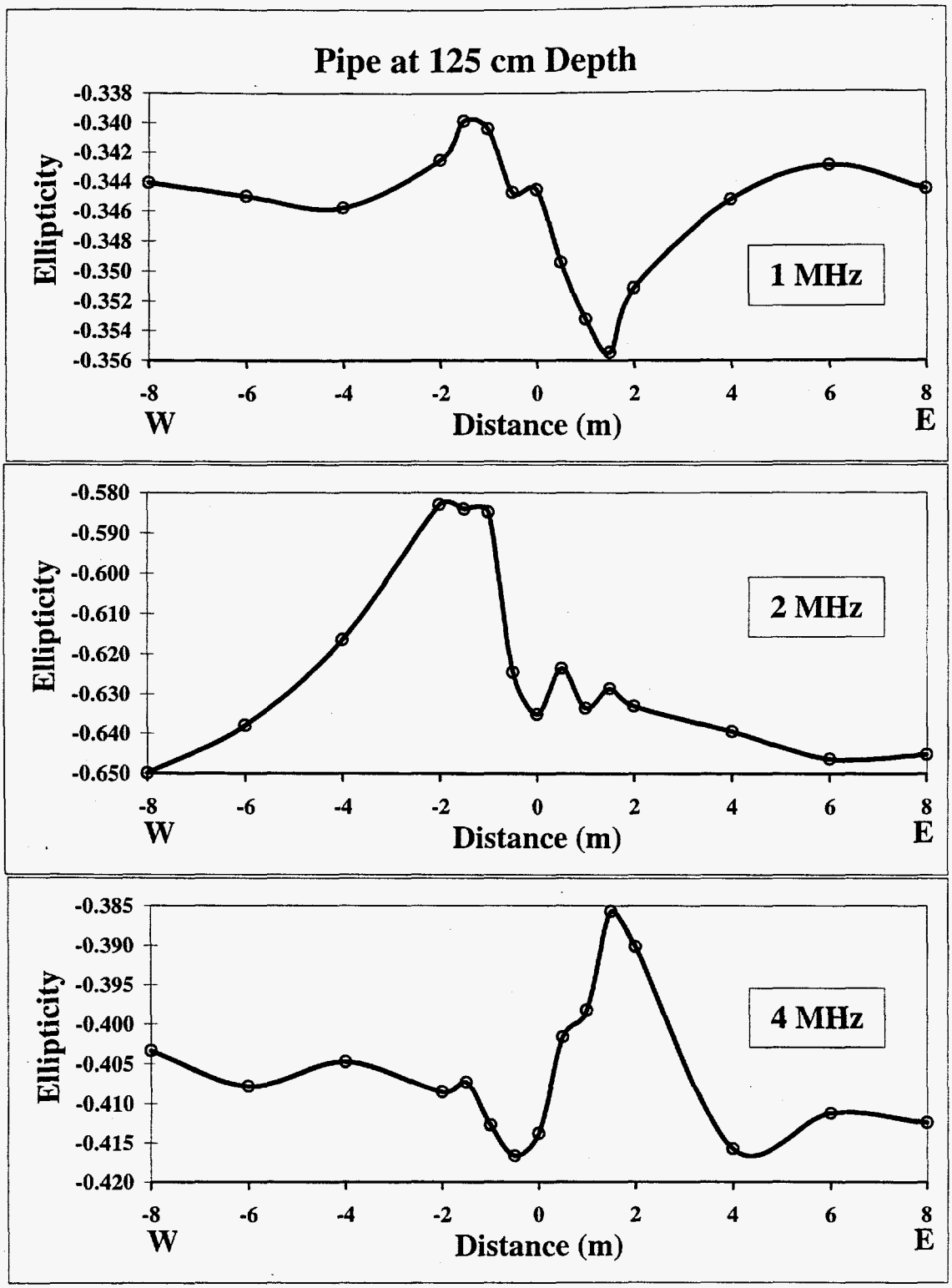

Figure 43. Ellipticity profile plots for a steel pipe at a depth of 1.25 m in the physical modeling tank for frequencies of 1, 2, and 4 MHz.

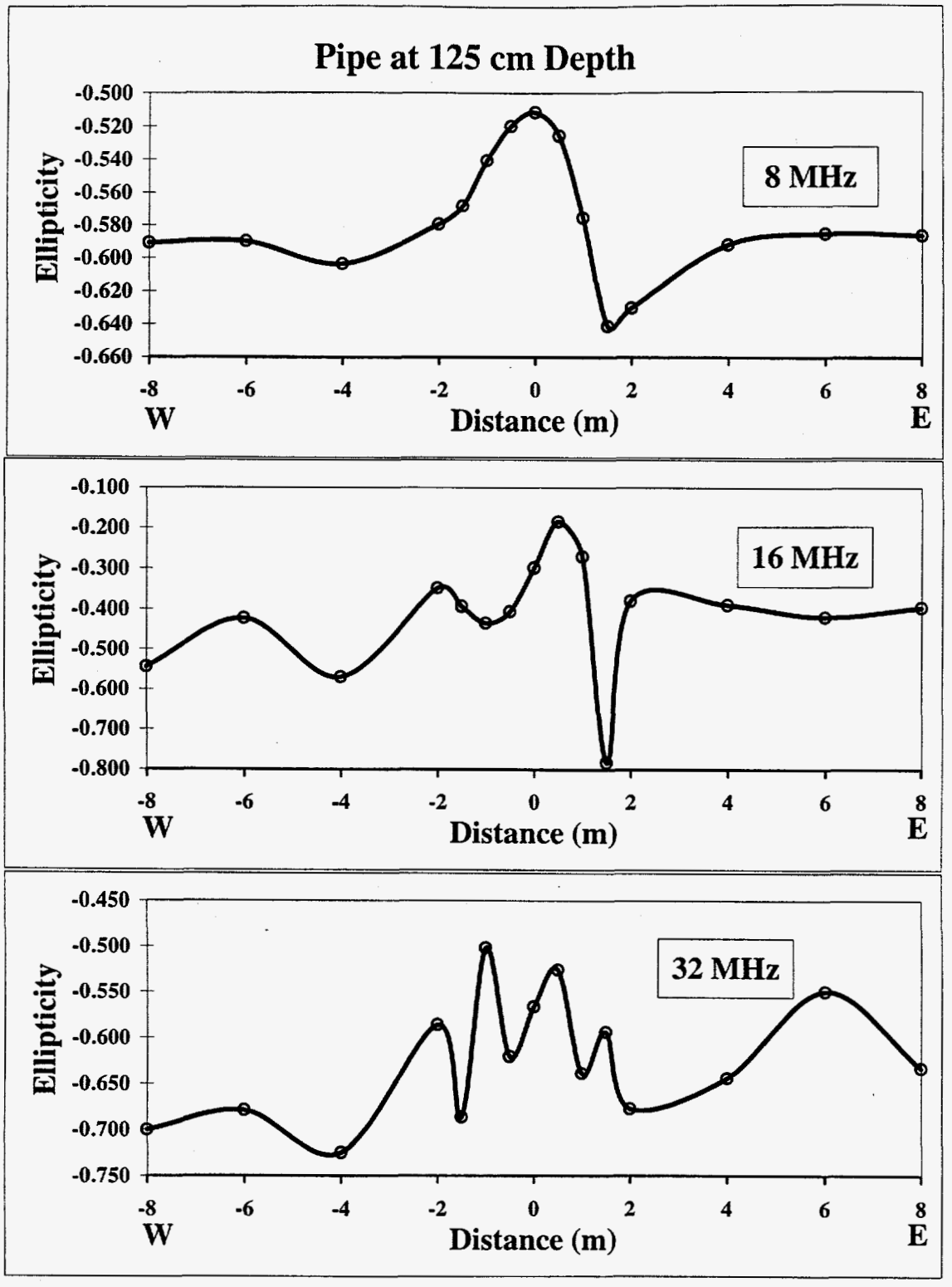

Figure 44. Ellipticity profile plots for a steel pipe at a depth of 1.25 m in the physical modeling tank for frequencies of 8, 16, and 32 MHz.

Physical Modeling Neural Network Results

We notice a characteristic signature for the targets in this experiment: when a conductive target is underneath the receiver we measure large (absolute value) ellipticities; when the target is under the transmitter we measure small (absolute value) ellipticities. These values will translate to conductive (large ellipticity) and resistive (small ellipticity) apparent resistivities when processed by a neural network.

We trained two neural networks with the physical modeling data: one network that distinguishes between target and background and a second network that estimated the horizontal position and depth of the target. We had data from nine experiments available for training and testing: a drum at 0.63 m depth, a drum at 1.03 m depth, the trolley with no target, a pipe at depths of 0.30 m, 0.75 m, and 1.25 m, and a sheet at depths of 0.30 m and 1.03 m. The pipe data and the 0.30 m deep sheet data had station spacings of 2 m from -8 m to -2 m and 2 m to 8 m. The spacing was 0.5 m between -2 m and 2 m. The rest of the data used only a 2 m spacing for training and testing. Data were labeled as target if the target was under or between one of the two antennas (-2 m to 2 m). The horizontal position was the distance from the target to the midpoint between the antennas. We discarded data from 31 kHz and 62 kHz because the induction numbers were too far out of range to give high quality data. We also discarded 32 MHz data, although some 32 MHz results were quite clean.

For the target versus background classification we used a radial basis function network with 8 inputs, 50 functions in the classification layer, 3 hidden nodes, and 1 output node. The output was coded as -1 for background and +1 for target. The repeat data set for the sheet at 1.03 m depth was withheld for testing. The network was trained for 20,000 iterations. The RMS error for the training data was 0.077. The classification rate was perfect, no stations were misclassified. For the test data, one station was misclassified as background when it was really target. This station was directly beneath one of the antennas.

The target position estimation used a modular neural network to estimate the horizontal position of the target relative to the midpoint between the antennas and also the depth beneath the water surface of the target. Since the water level was continuously fluctuating during the course of the experiments we expect more error in the depth estimates. The network used the same 8 inputs as described in the classification network above. Two local experts, each with three hidden nodes were used in addition to a global hidden layer with three nodes. Two output nodes were used, one for horizontal position and one for depth. A hyperbolic tangent function was used for the hidden layer activations; a linear output function was used for the output layer. The network was trained for 30,000 iterations. Forty-two samples were used for training and six samples were randomly withheld for testing. Three of the samples were repeat data for the 1.03 m deep sheet. The RMS error for the training data was 0.141. The correlation coefficient for the horizontal position was 0.985; the correlation coefficient for the depth was 0.984. The correlation coefficients for the test data were 0.887 and

0.781 respectively. The average absolute position errors on the test data were 0.30 m for the horizontal location and 0.15 m for the depth. Most of the error for the horizontal position came from the pipe data at 0.75 m depth and -0.5 m position. These results could be improved with consistent station spacing for all targets and a constant water level.

FIELD TESTS AT AVRA VALLEY

We collected field data at the Avra Valley Geophysical Test Site from late April, 1994 until the present. Many of the field tests were performed to verify system performance at various stages of development, to collect data for the rotation-invariance inversion, and the electric field cancellation algorithm. The field tests used to test our interpretations over select targets are described below.

We interpreted soundings in the vicinity of a PVC-cased drill hole. The soundings near the drill hole were used to verify the apparent resistivity interpretations from the neural networks and compare them to information from induction well logs performed in the drill hole. The piecewise apparent resistivity neural networks were able to accurately fit the data for each separation. For the 4 m separation, the network that processes ellipticities from 500 kHz and 1 MHz tends to underestimate the resistivity. This error is consistent enough that we believe it is a problem with the network training. Figure 45 shows how the neural network-estimated models fit the field data.

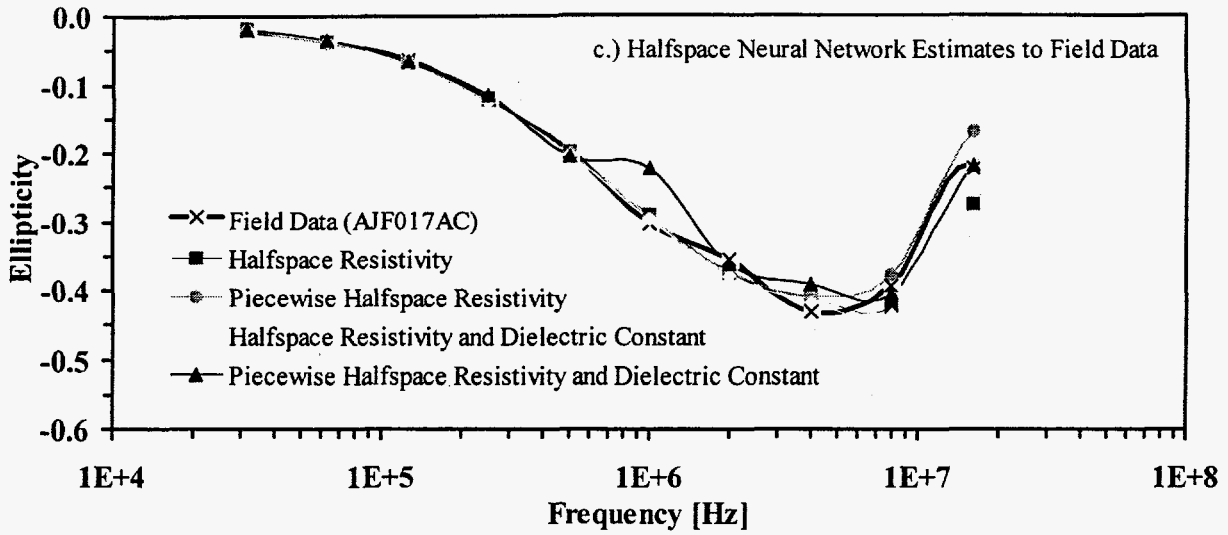

Figure 45: Halfspace neural network estimations for sounding AJF017AC. Halfspace resistivity estimated model (squares): 50.5 Ωm; Piecewise halfspace resistivity estimated model (circles): 47 Ωm, 52 Ωm, 49 Ωm, 50 Ωm, 49 Ωm, 51 Ωm, 54 Ωm, 26 Ωm, and 24 Ωm; Halfspace resistivity and dielectric constant estimated model (diamonds): 48.8 Ωm (ε=2.9); Piecewise halfspace resistivity and dielectric constant estimated model (triangles): 52 Ωm (ε=10), 51 Ωm (ε=11), 53 Ωm (ε=10), 49 Ωm (ε=13), 84 Ωm (ε=2), 61 Ωm (ε=4), 84 Ωm (ε=2), 29 Ωm (ε=4).

We buried a 20 m long 45.7 cm diameter PVC pipe in soil. The PVC pipe is filled with water and allows us to move 3D-targets such as small sheets or steel pipes through the PVC pipe while keeping the antennas in a fixed position, comparable to the physical modeling tank. The PVC pipe has screws through the walls of the pipe which are spaced around and along the pipe to allow currents to flow between the target in the water and the surrounding soil. Prior to burial of the pipe we buried an aluminum sheet in the same spot and collected data over it with stationary antennas while the sheet was pulled through the soil.

We collected data with an antenna separation of 4 m over the PVC pipe. An aluminum sheet 5.55 m long by 0.3 m wide at a depth of 1 m was pulled through the pipe. Figure 46 compares the response to the aluminum sheets in the physical modeling tank, PVC pipe and soil (Birken et al., 1996) at 250 kHz and 4 MHz. We note the similarities in the shapes of the anomalies, independent of the background ellipticity and the same characteristic ellipticity high under the receiver and low under the transmitter as we observed for metallic targets in the physical modeling experiments. The peaks appear slightly shifted, which could be attributed to the relatively coarse sample interval for some of the profiles over soil. A very interesting aspect is that the size of the anomalies for the three sheets in soil are very similar for 4 MHz (figure 46b), which is a frequency

that is highly affected by dielectric effects. But for 250 kHz (figure 46a) the size of the anomaly in the profile over the 17 m long sheet is about four times as strong as the other three. The other two profiles over soil are very similar in both figures, which indicates that a water filled PVC pipe can give comparable results to the same target buried in soil, but provide more flexibility for the physical modeling. The background matches so well because the PVC pipe was buried at the same location after the sheet-in-soil experiment took place. The results from the water-filled tank have a uniform background response (figure 46a) which makes it easier to extract the target signature and to compare computer models. The modeling tank seems to give comparable results for frequencies below 1 MHz, since the background ellipticity shift can be explained by different background resistivities (30 ohm-m for the water in the tank and about 60 ohm-m for the soil). We also observed significant effects on anomaly amplitudes as a function of sheet length for frequencies below 1 MHz. For frequencies above 1 MHz displacement currents become an important factor. The shape of the anomaly for the sheet in water is similar to those of sheets in soil but of lower overall amplitude. Sheet length does not appear to alter the amplitudes at high frequencies.

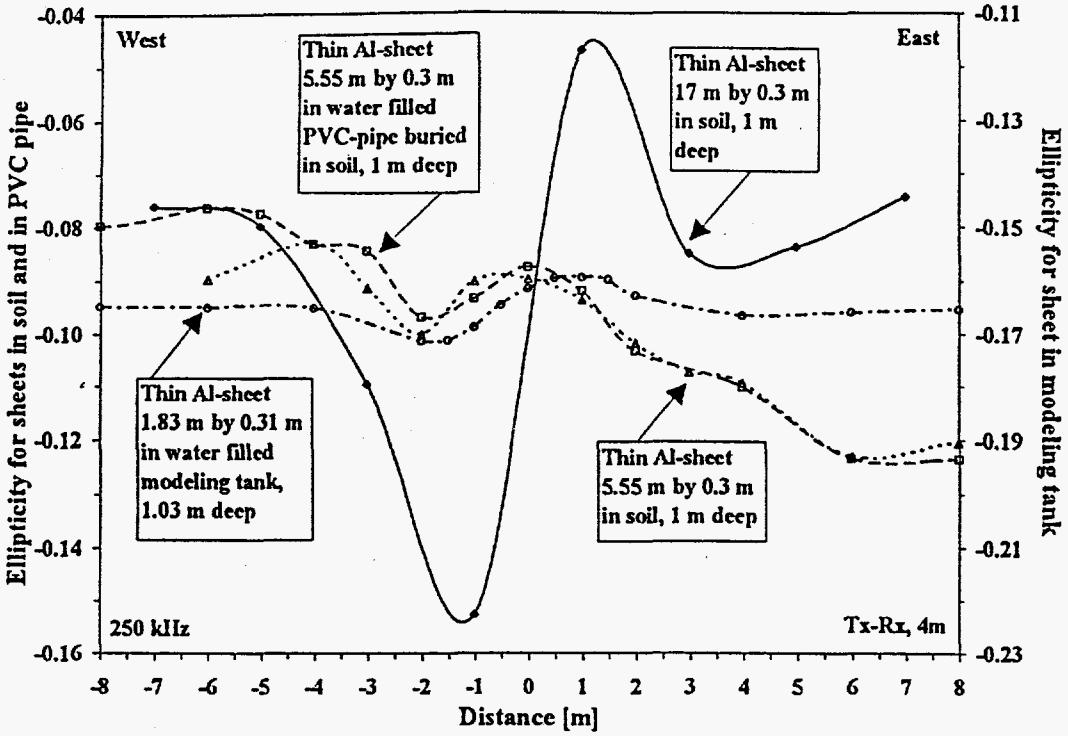

Figure 46a. Ellipticity profiles over four thin aluminum sheets with different dimensions as described in text. Sheets are centered at 0 m. Data are collected at 250 kHz with an antenna separation of 4 m and the transmitter west of the receiver. Profiles are run from west to east.

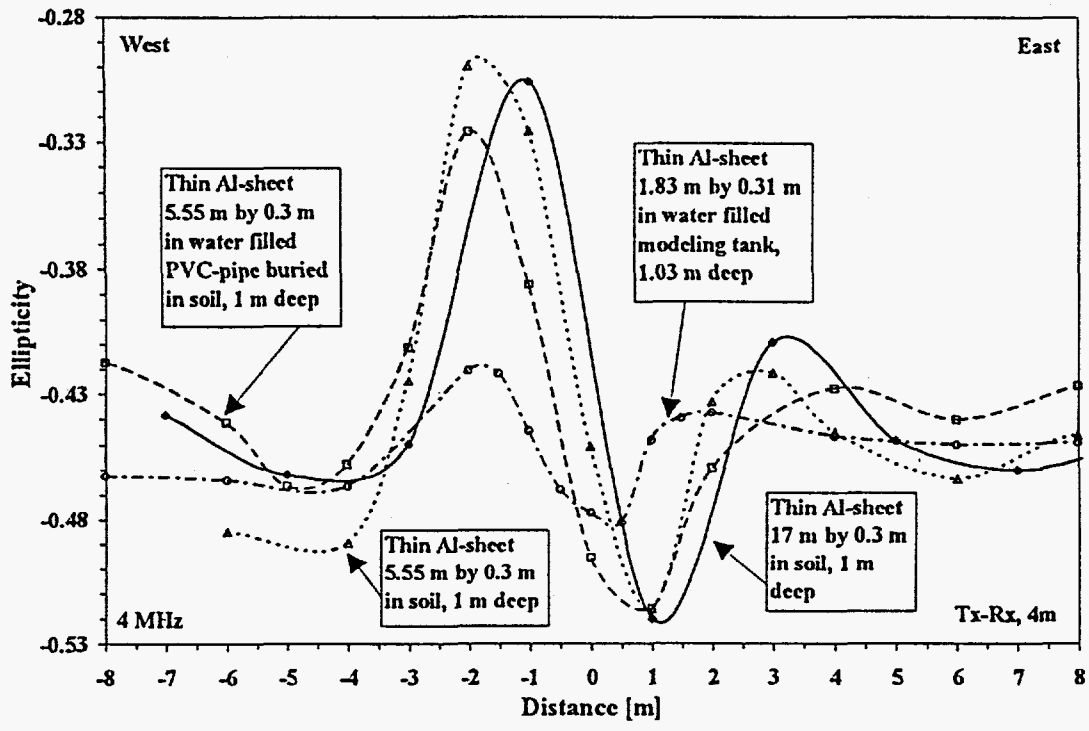

Figure 46b. Ellipticity profiles over four thin aluminum sheets with different dimensions as described in text. Sheets are centered at 0 m. Data are collected at 4 MHz with an antenna separation of 4 m and the transmitter west of the receiver. Profiles are run from west to east.

To test system response and to learn more about target signatures in a heterogeneous background, several isolated targets were buried at depths of 1 m or less. The targets are summarized in Table 2.

TARGET TYPE	COMMENT	DEPTH	SIZE	LOCATION
55-gallon barrel	horizontal, painted	0.63 m	0.85 m tall, 0.58 m diameter	D3
55-gallon barrel	horizontal, unpainted	0.5 m	0.85 m x 0.58 m	D4
55-gallon barrel	horizontal, painted	1 m	0.85 m x 0.58 m	D2
55-gallon barrel	vertical, painted	0.5 m	0.85 m x 0.58 m	D1
10, 55-gallon barrels	horizontal, painted, touching	1.0 m	8.5 m x 0.58 m	D2
Aluminum sheet	horizontal	1.0 m	17 m long, 0.3 m wide	D2
Aluminum sheet	horizontal	1.0 m	5.55 m long, 0.3 m wide	D2
Corrugated aluminum sheet	horizontal	1.0 m	3 m x 5 m	D1
Corrugated aluminum sheet	horizontal	1.0 m	5 m x 9 m	D1
2, Steel office desks	buried top down	1.0 m	0.75 m x 1 m	D1

Table 2. Description of targets buried at the test site over which surveys were conducted. Location information refers to the experimental cell at the Avra Valley Test Site.

The configuration of the targets in cell D1 at the test site are shown in Figure 47.

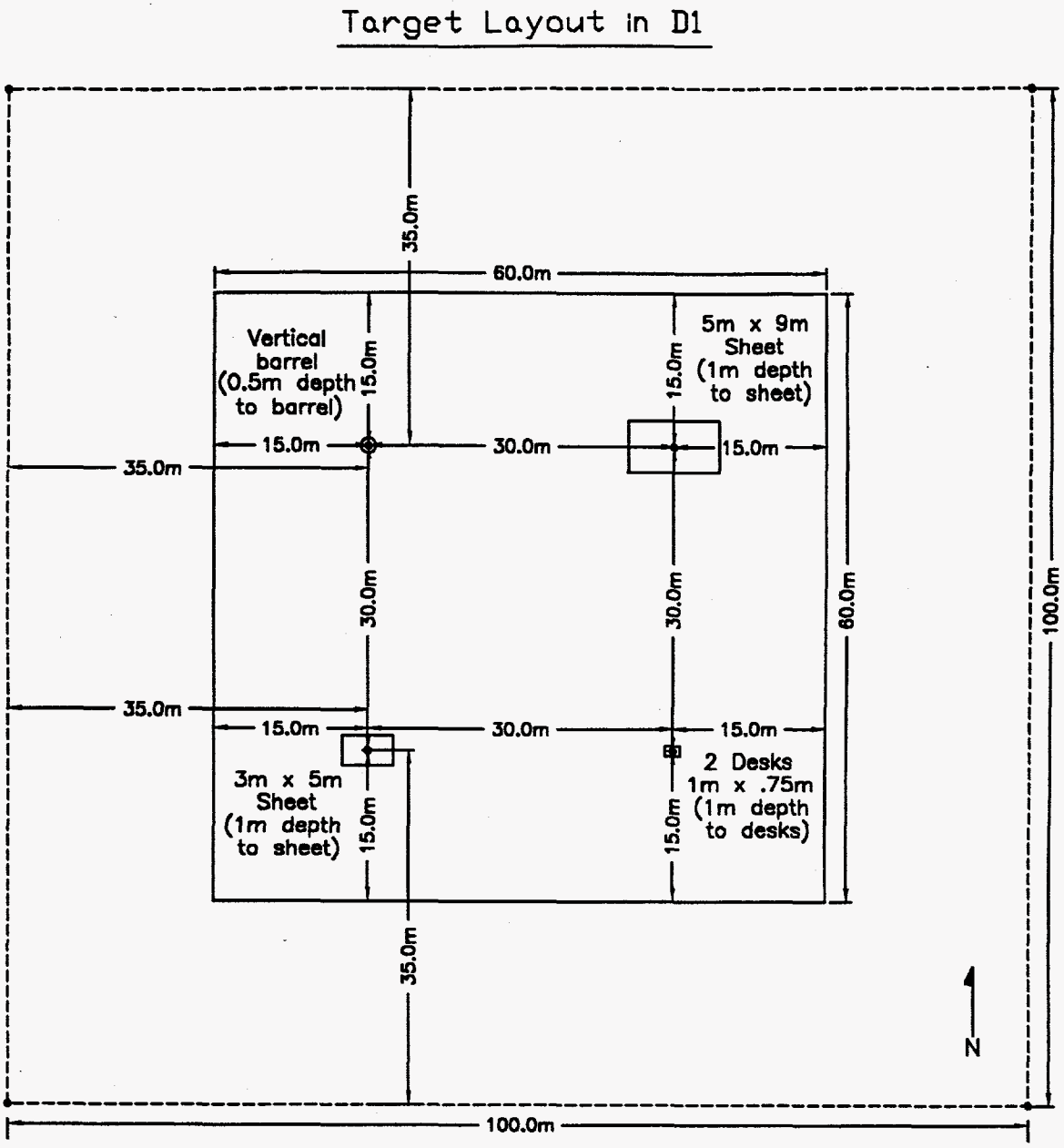

Figure 47. Location of targets in experiment cell D1 at the Avra Valley Geophysical Test Site.

An unpainted barrel in cell D4 was buried as part of an experiment to determine what effects surface impedance variations due to such things as paint could have on our data. After collecting data over the barrel, we dug it up, wrapped it in plastic, and re-buried it to test the effect of surface coating. We saw a response to the barrel indicated by an increase in absolute values of ellipticity at station 0 m. The background response was constant across station 0 m. When the barrel was wrapped in plastic we saw a detectable difference from background but of lower amplitude than that of the bare-metal barrel. All data were collected with an antenna separation of 4 m.

We will consider a buried object to be detected if we can identify a response from it that differs significantly from background. We consider the object to be located if we can estimate its position and geoelectric properties. Using data from several experiments we can explore the ability of our 1D mapping networks to interpret data from objects with the goal of detecting buried objects and providing good starting models for 3D inversions (Birken and Poulton, 1997b).

Figures 48-51 show the response to a barrel buried 0.63 m deep in cell D3. This was a barrel that had been buried for quite some time before the ellipticity survey. There was a larger response when the barrel was removed due presumably to the changed soil resistivity from the excavation. Note also the large, broad anomaly due to background variations. Figures 52-55 show the response over two desks buried 1 m deep in cell D1.

An apparent problem with the gain settings during these surveys led to much larger noise levels on some of these data sets than is normal for this system. There is also some disagreement between the measured ellipticities for: (1) the background line and (2) the line with the target present at large distances from the target. This was because the two line locations were not exactly coincident.

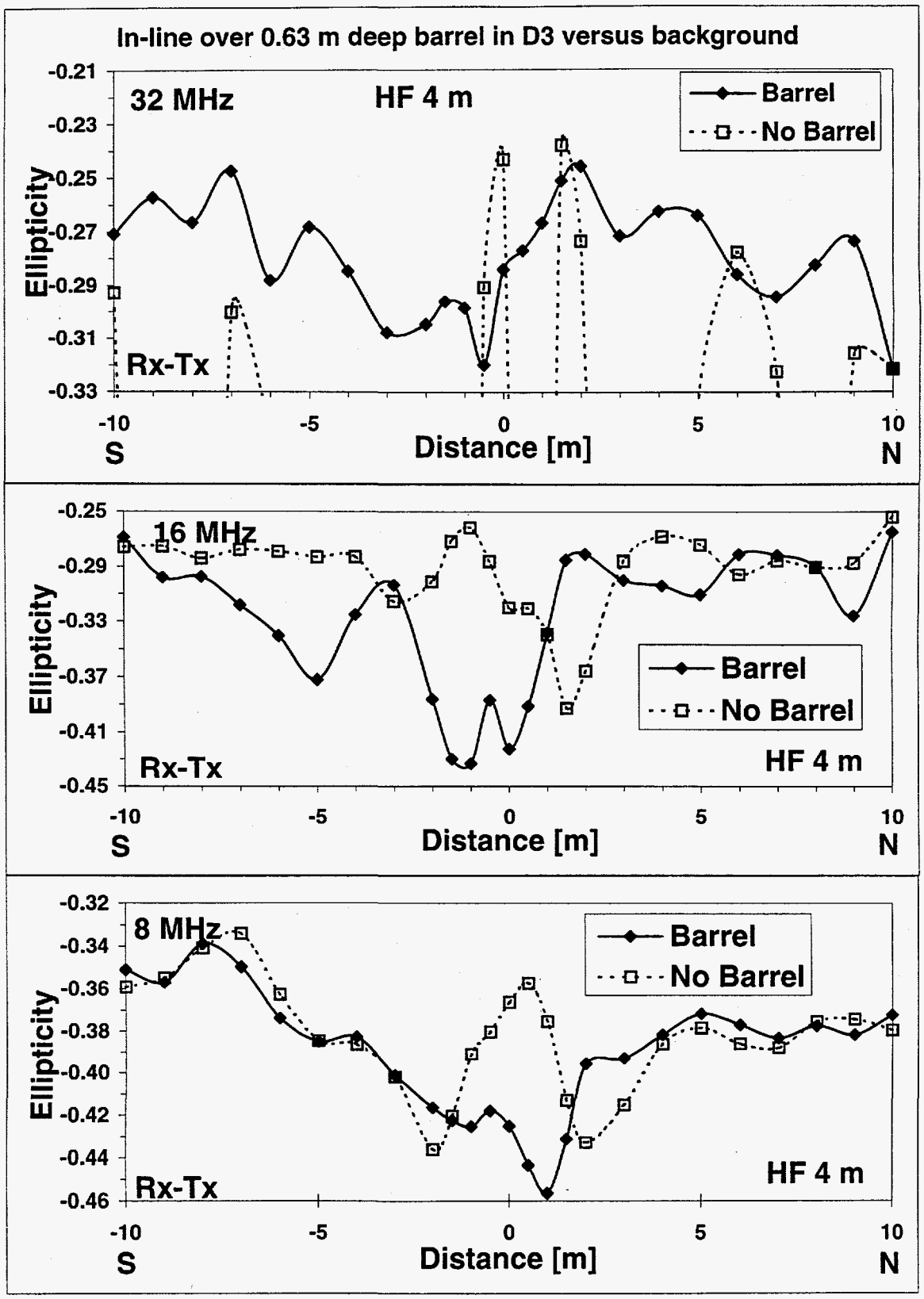

Figure 48. Ellipticity profiles for 32 - 8 MHz, 4 m antenna separation over a 55-gallon barrel buried 0.63 m deep.

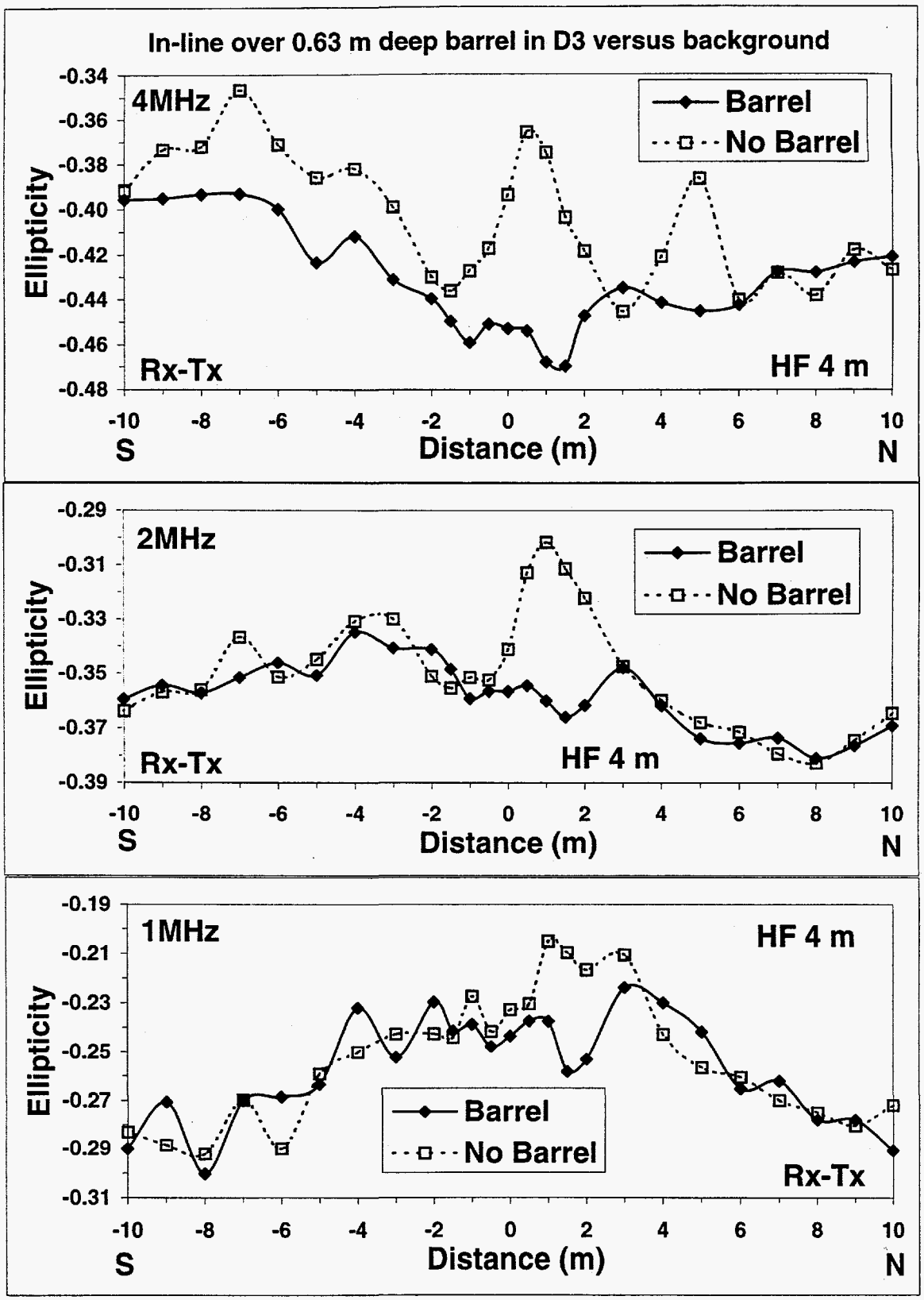

Figure 49. Ellipticity profiles for 4 - 1 MHz, 4 m antenna separation over a 55-gallon barrel buried 0.63 m deep.

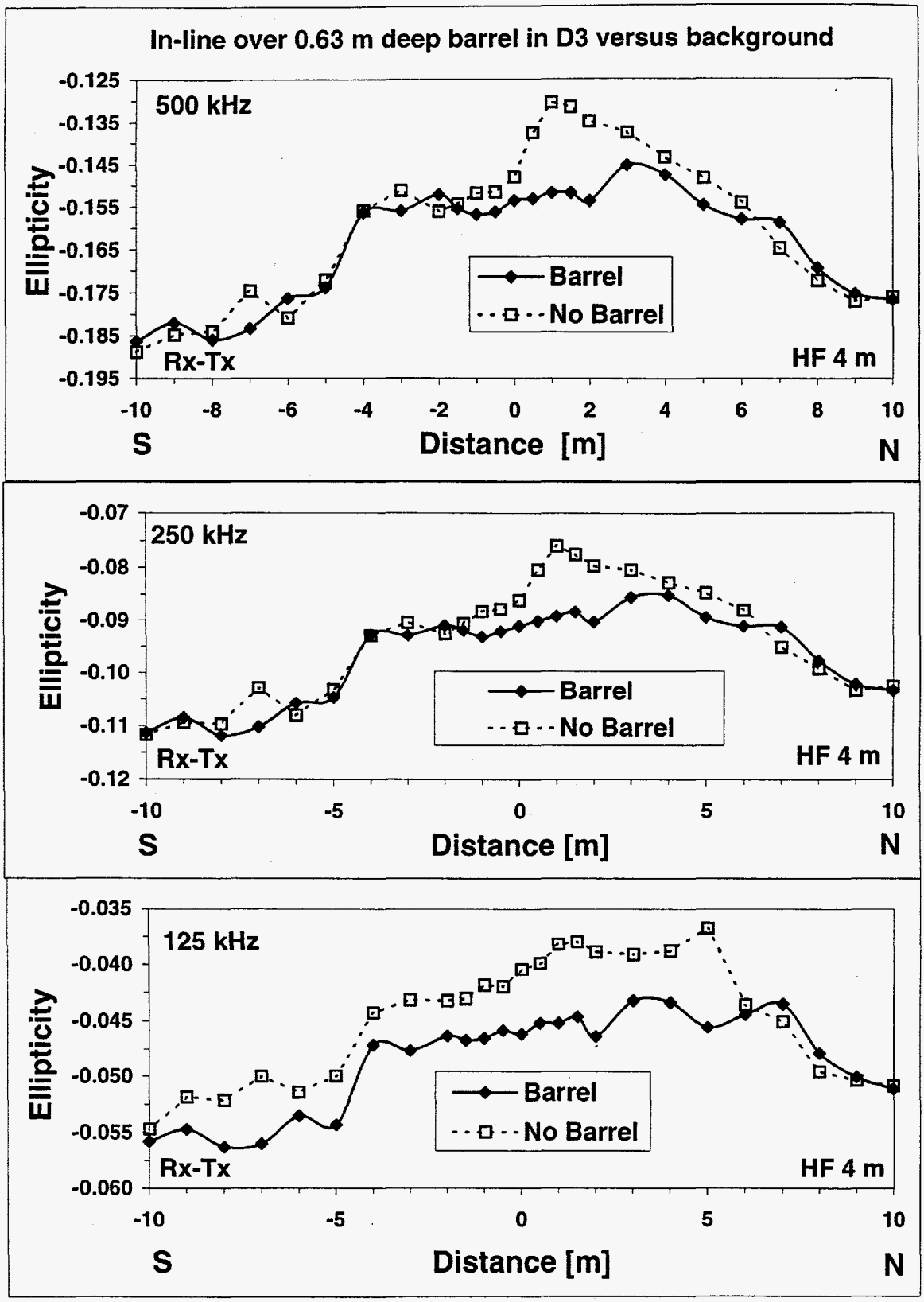

Figure 50. Ellipticity profiles for 500 - 125 kHz, 4 m antenna separation over a 55-gallon barrel buried 0.63 m deep.

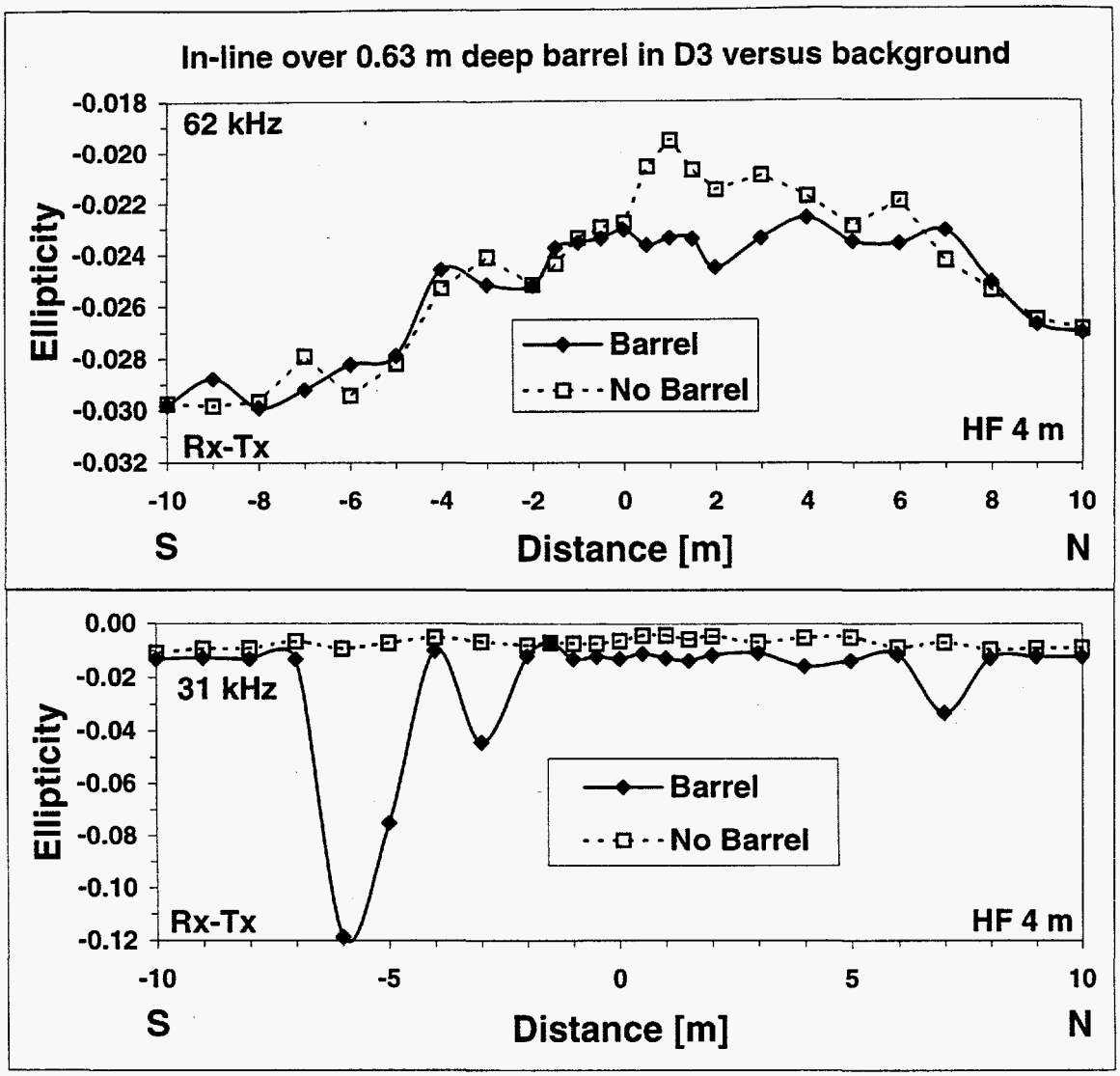

Figure 51. Ellipticity profiles for 62 and 31 kHz, 4 m antenna separation over a 55-gallon barrel buried 0.63 m deep.

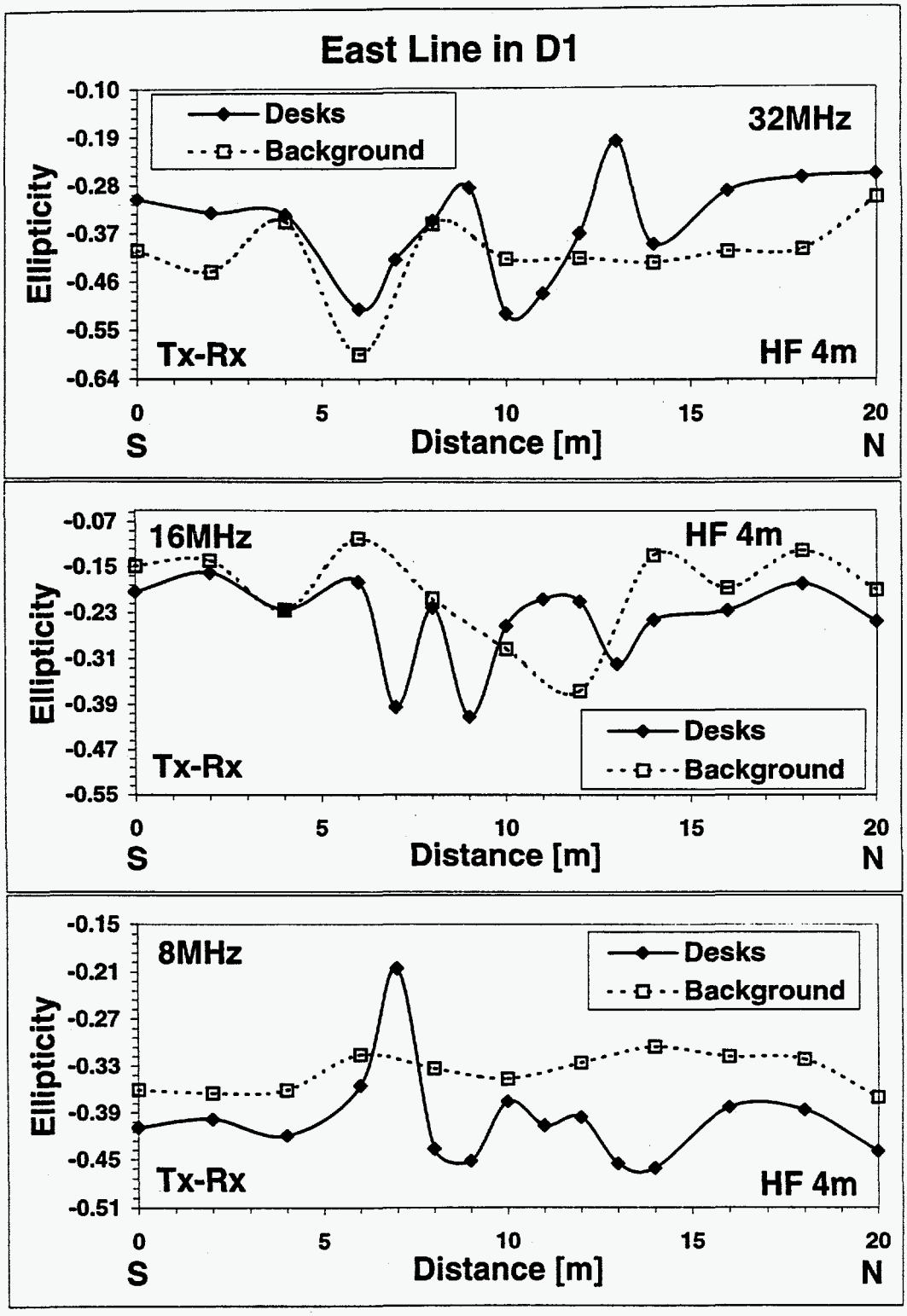

Figure 52. Ellipticity profiles for 32 - 8 MHz, 4 m antenna separation over two metal office desks buried 1.0 m deep. The east line runs in a north-south direction on the east side of cell D1 (see figure 47).

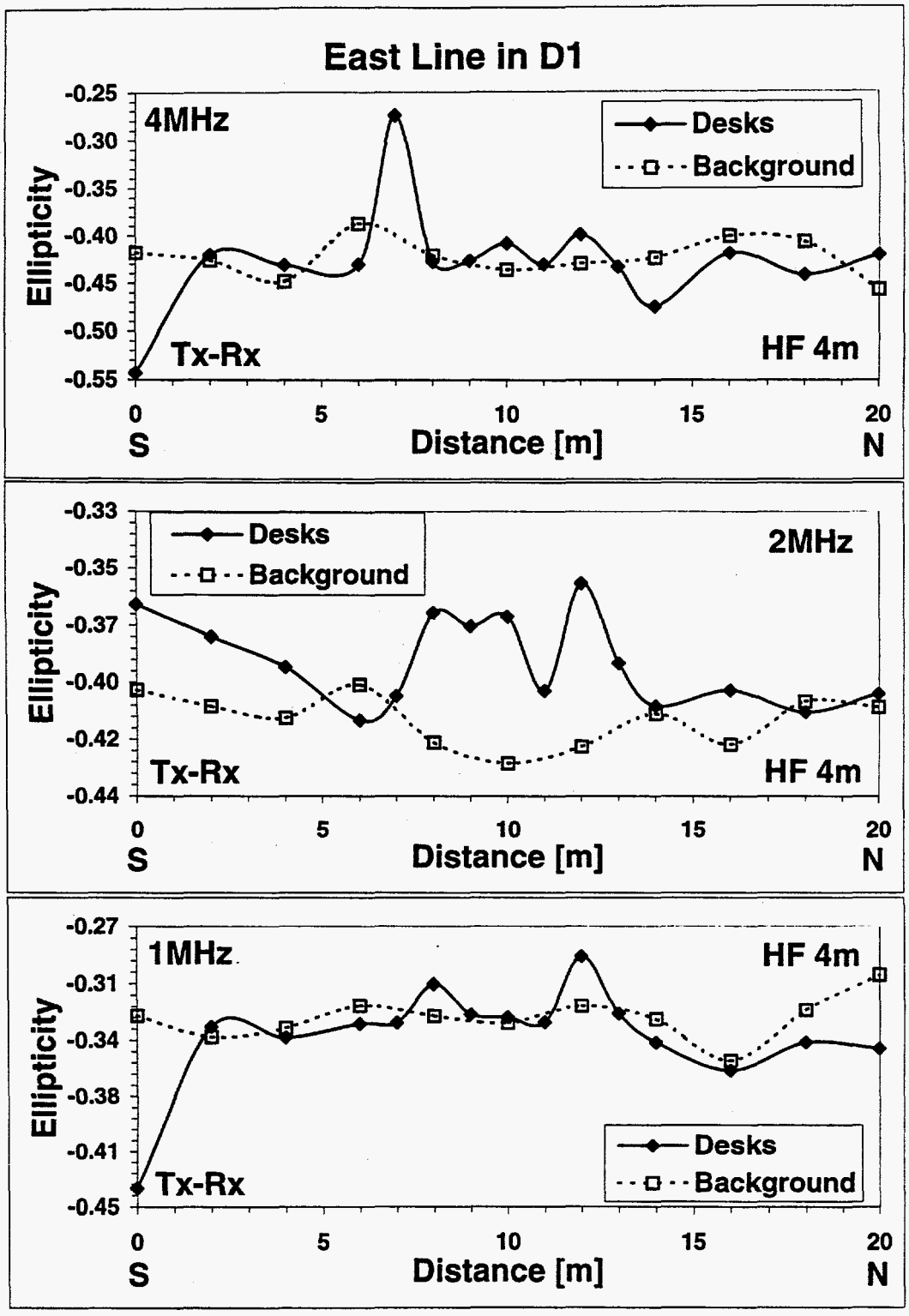

Figure 53. Ellipticity profiles for 4 - 1 MHz, 4 m antenna separation over two metal office desks buried 1.0 m deep. The east line runs in a north-south direction on the east side of cell D1 (see figure 47).

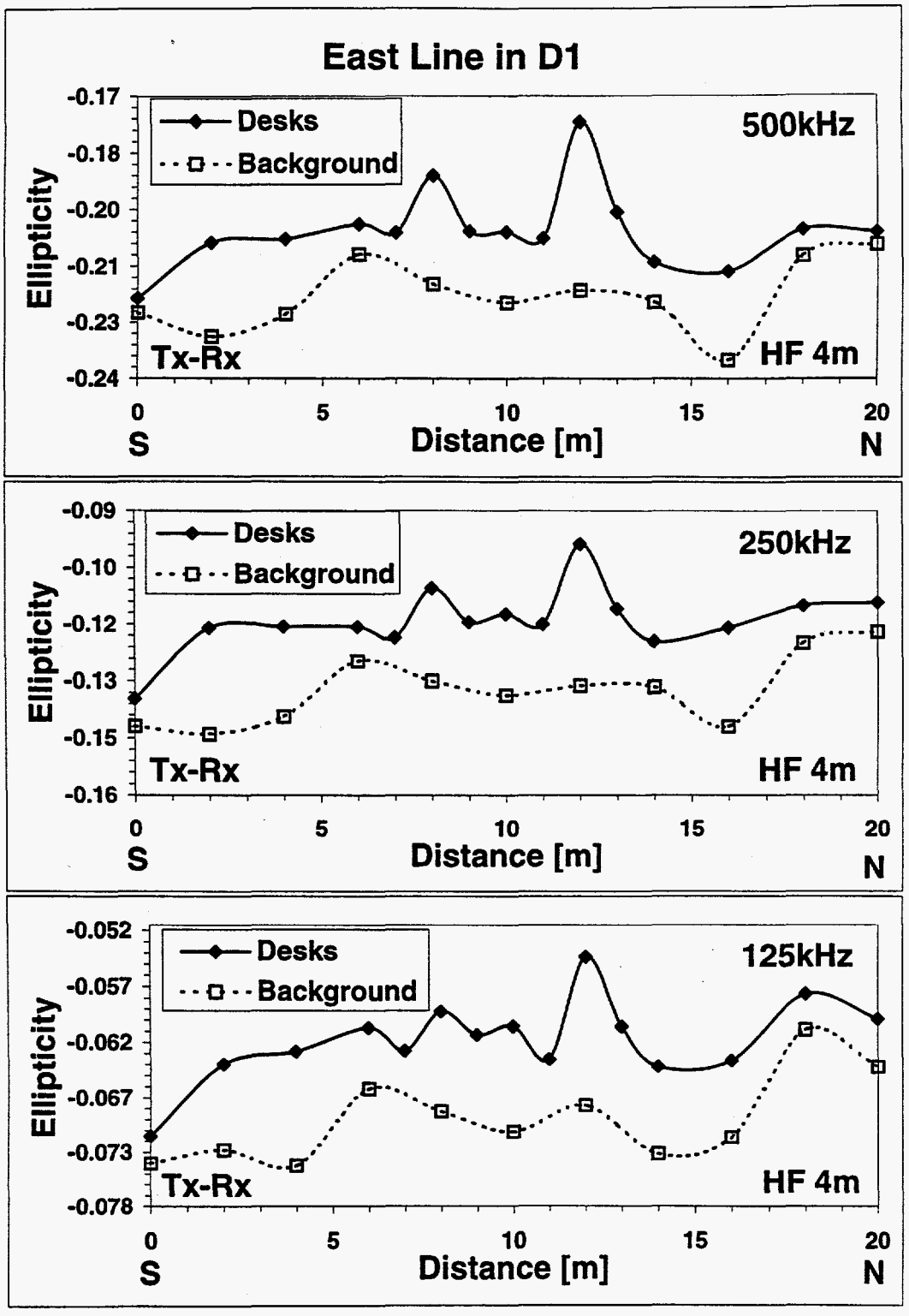

Figure 54. Ellipticity profiles for 500 - 125 kHz, 4 m antenna separation over two metal office desks buried 1.0 m deep. The east line runs in a north-south direction on the east side of cell D1 (see figure 47).

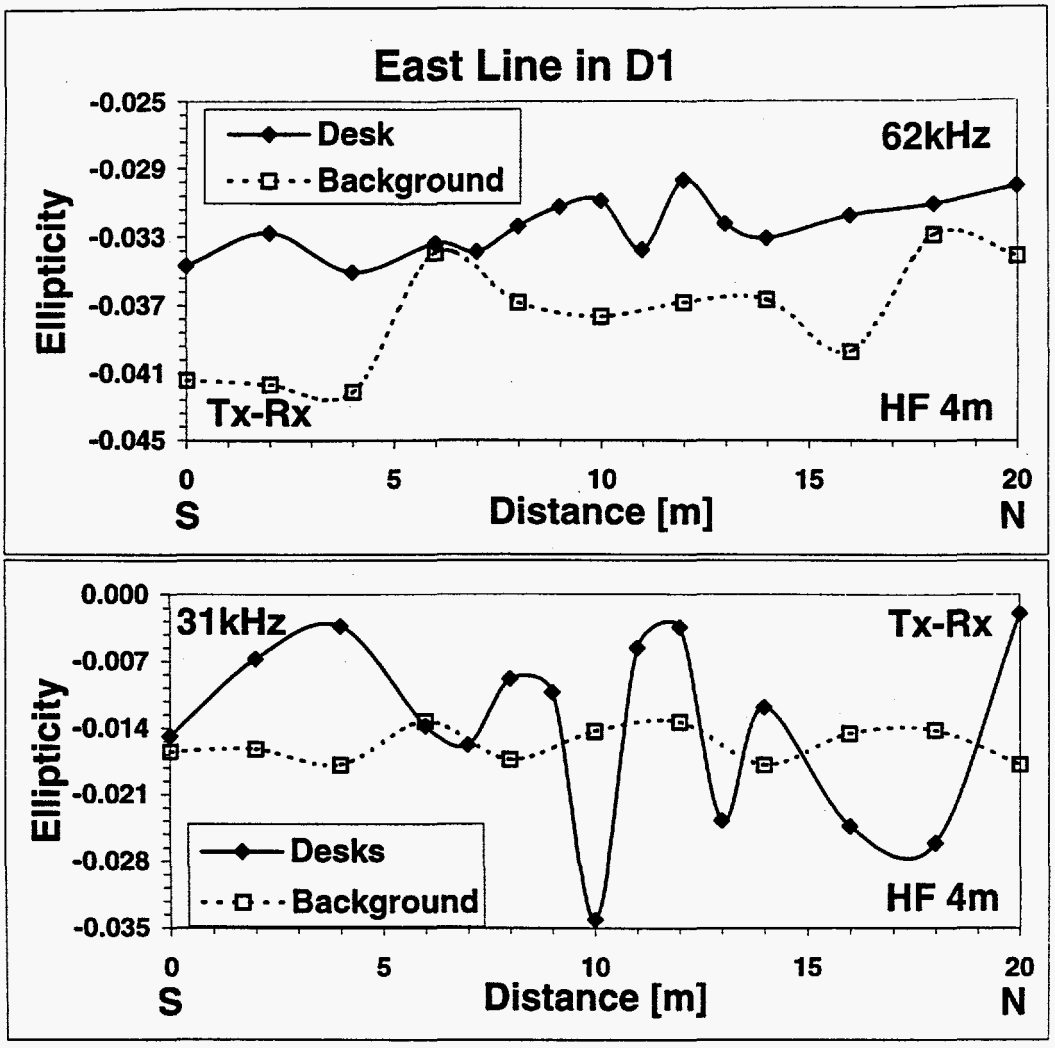

Figure 55. Ellipticity profiles for 62 and 31 kHz, 4 m antenna separation over two metal office desks buried 1.0 m deep. The east line runs in a north-south direction on the east side of cell D1 (see figure 47).

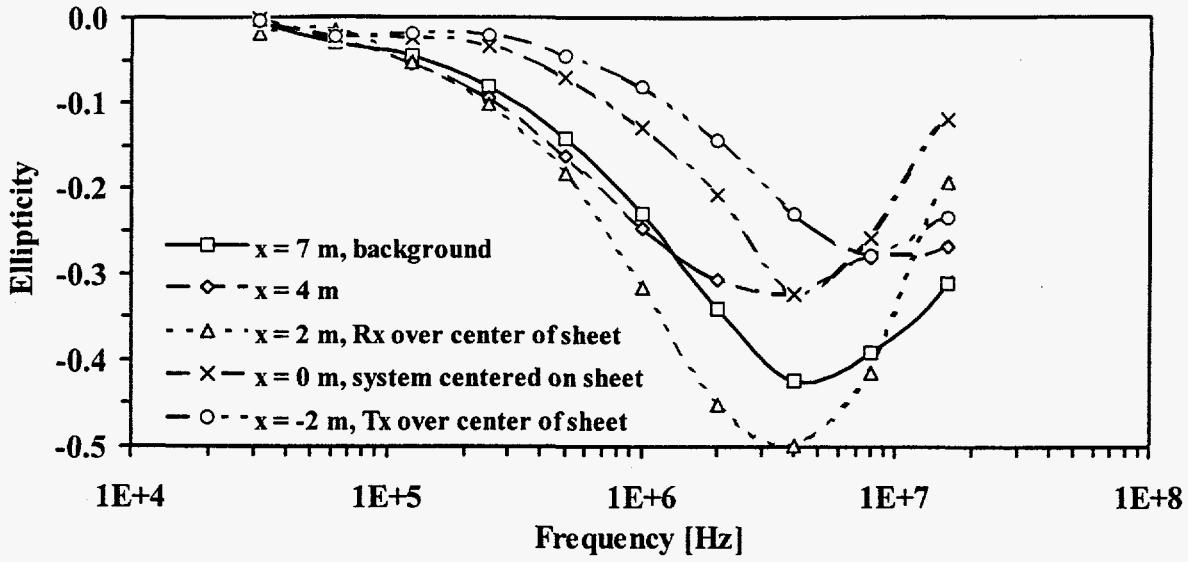

Figure 56: Ellipticity sounding curves for five stations selected from the profile shown in figure 57.

Piecewise neural networks will not provide accurate resistivity or dielectric constant values in 3D cases, but do accurately indicate the spatial locations of anomalies that can be used to identify 3D situations and in some cases even detect the target. We have tested the 1D networks with field data collected over objects buried at the Avra Valley Geophysical Test Site, near Tucson, Arizona in order to learn the pattern of the 1D response to buried objects. Figure 57 shows several ellipticity profiles from -7 m to 7 m over the center of the long side of a 5 m by 3 m aluminum sheet, buried at a depth of 1 m. Comparing the sounding curves at five stations along this profile indicates large variations (figure 56), mainly because the target is a relatively large, shallow conductor.

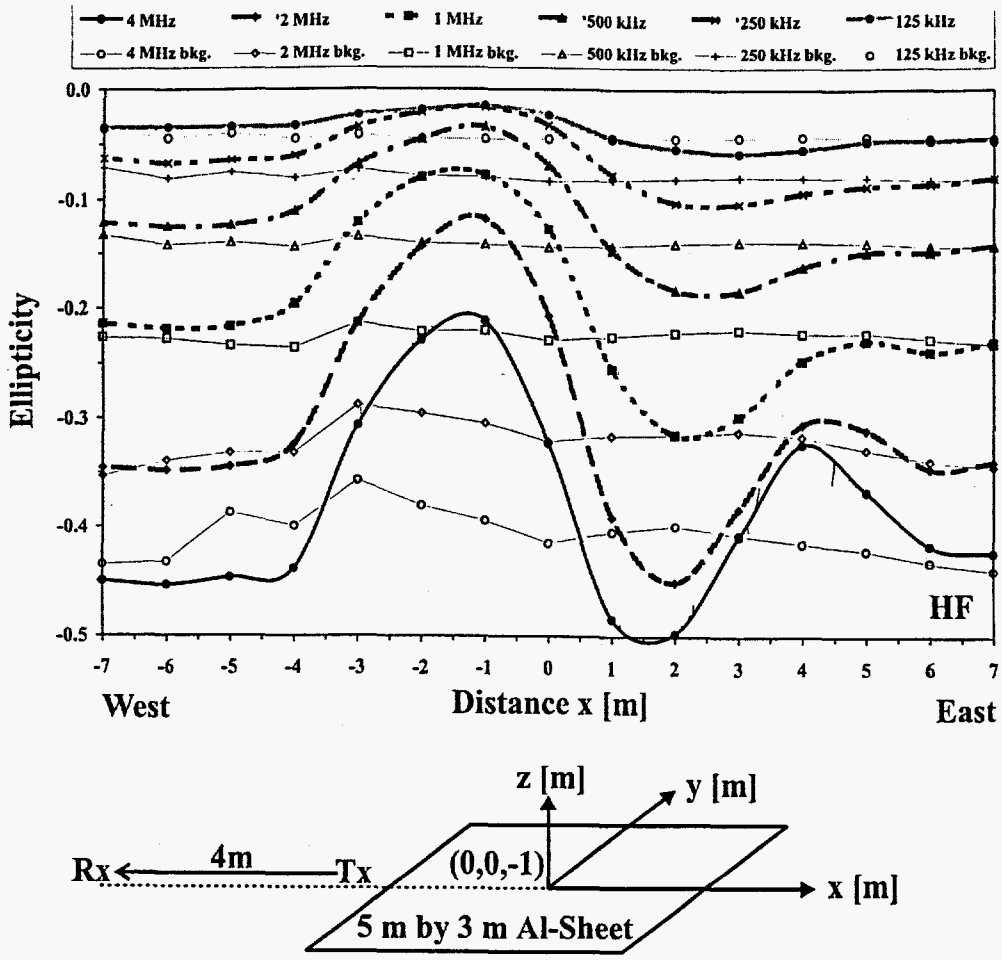

Figure 57: Ellipticity profiles for 125 kHz, 250 kHz, 500 kHz, 1 MHz, 2 MHz, and 4 MHz over the long side of a 5 m by 3m Aluminum sheet buried 1 m deep. These profiles are compared to ellipticity profiles at the same frequencies, parallel, 7 m away from the center of the sheet. The soundings were collected with a coil separation of 4 m and the survey was ran from East to West as shown in the diagram underneath the profile plots.

Assuming a 1D piecewise interpretation of the profiles in figure 57, we expect that going from East to West the resistivity with respect to the background will decrease to a minimum at x = 2 m with the decreasing ellipticity. Then after crossing the center point of the anomaly increases to a maximum at x = -1 m before leveling off to the background values again. Selected 1D halfspace and layered earth neural network interpretations were found to provide a reasonable fit to the field data and confirm the discussed changes along the profile. We start with a sounding at the x = 7 m background station, which fits an 80 Ωm halfspace very well (figure 58a). At the station x = 2 m the ellipticity curves reach their minimum (figure 57) and as predicted, a two layer conductive over resistive model fits the field data (figure 58b). As soon as the ellipticity increases (figure 57) a two layer resistive over conductive model fits the field data better (figure 58c for x =

0 m, and figure 58d for x = -2 m). Observing these kinds of varying model estimates, combined with the anomaly observed in the ellipticity profiles (figure 57), is a clear indication that the 1D halfspace and layered earth models are not a valid interpretation in a range over the target +/- approximately half of the separation on either side. However, the piecewise neural network interpretations reflect these high low patterns, as shown in the following examples (figures 59, 60, and 61), and provide a qualitative interpretation that could not be achieved by creating a resistivity depth section patching layered earth models together.

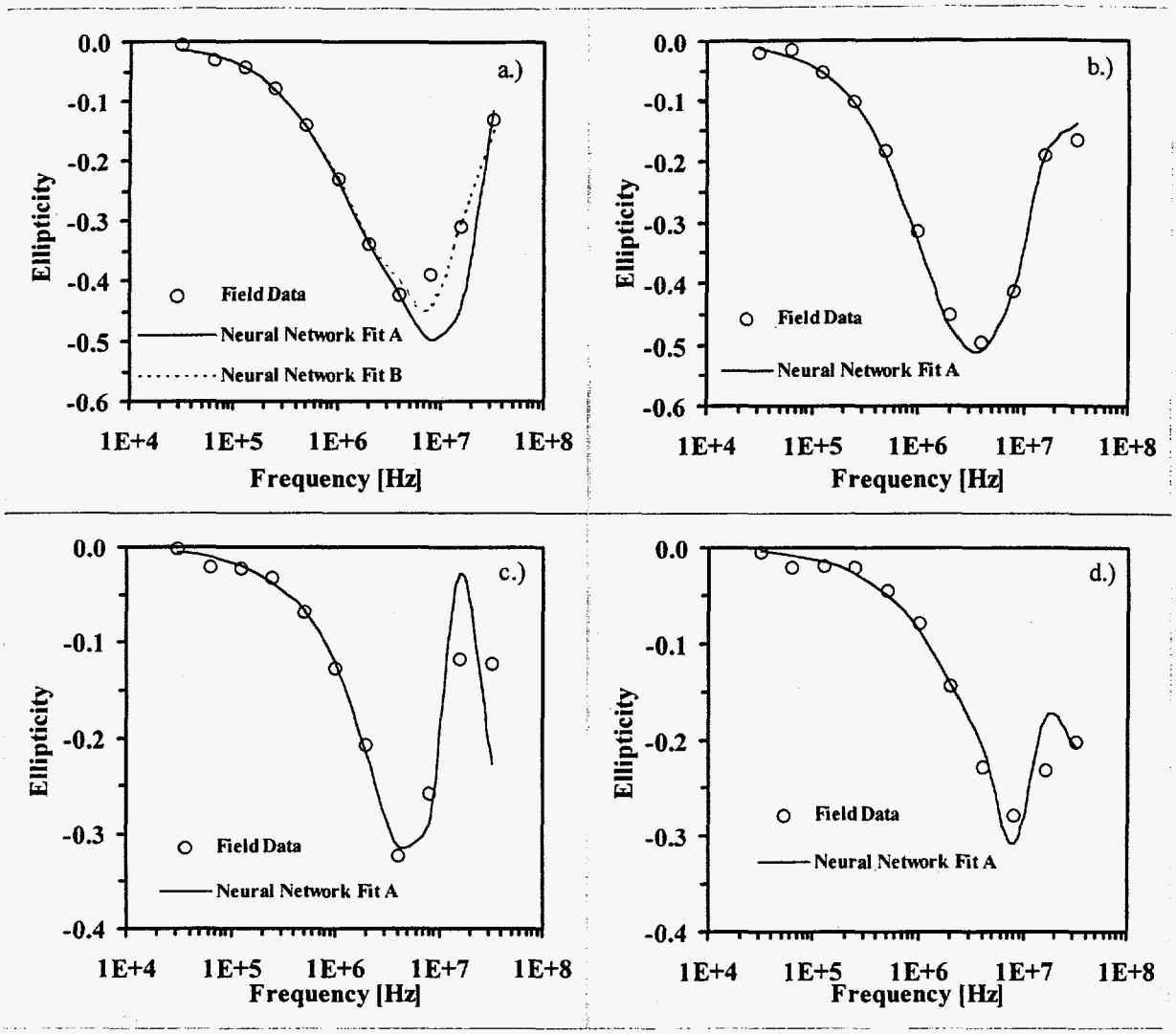

Figure 58: Four graphics showing 1D neural network estimations for four stations along the profile shown in figure 57. a.) Station x = 7 m, field data versus neural network estimated halfspace models: A 80 Ωm (ε=8) and B 80 Ωm (ε=1) 1 m thick over 80 Ωm (ε=10). b.) Station x = 2 m, field data versus neural network estimated two-layer model: 40 Ωm (ε=1) 1 m thick over 150 Ωm (ε=80). c.) Station x = 0 m, field data versus neural network estimated two-layer model: 1000 Ωm (ε=2) 1.5 m thick over 80 Ωm (ε=80). d.) Station x = -2 m, field data versus neural network estimated two-layer model: 1100 Ωm (ε=1.6) 1.4 m thick over 120 Ωm (ε=10).

Figures 59a and 59b show the resulting resistivity depth sections as estimated by the piecewise halfspace neural network from the sounding curves that build the ellipticity profiles shown in figure 57. Figure 59a shows the background results and figure 59b the results of the profile over the center of the sheet. For comparison we show two additional resistivity sections (figures 59c and 59d) which are created in exactly the same way using ellipticity sounding curves from a 3D thin sheet forward model representing the exact field set-up, as shown in the diagram of figure 57. Section 59c shows a profile for the background response as expected 7 m away from the center (profile in x-direction at y = 7 m) based on numerical forward modeling. A comparison of both background sections (figures 59a and 59c) show a good agreement. A similar agreement can be observed comparing the field data section (figure 59b) with the section from the numerical forward modeling (figure 59d) over the sheet. The general pattern shows a resistive high on the west side of the target and a conductive anomaly east of it, as discussed earlier. The depth scale is derived from a depth of investigation algorithm developed by Thomas (1996) and is only approximate. A plan view of ellipticities at 125 kHz over the 3 m by 5 m sheet is shown in figure 62. The top plot is field data and the bottom plot is model data. We note an excellent correspondence for the anomaly over the sheet in both plots.

Since this represents now a true 3D situation the resistivities don't represent the true earth properties anymore and have to be taken as anomaly detectors. The upper and lower resistivity estimates appear to be noisier than the center portion of the section 59a and 59b which is due to an increased noise level in the corresponding frequencies. The anomalies also appear wider than the sheet itself which is due to the 4 m transmitter-receiver separation and the fact that we plot the sounding at the midpoint of the array. Therefore we must estimate the horizontal extension of the anomaly to be approximately half a separation smaller on either side.

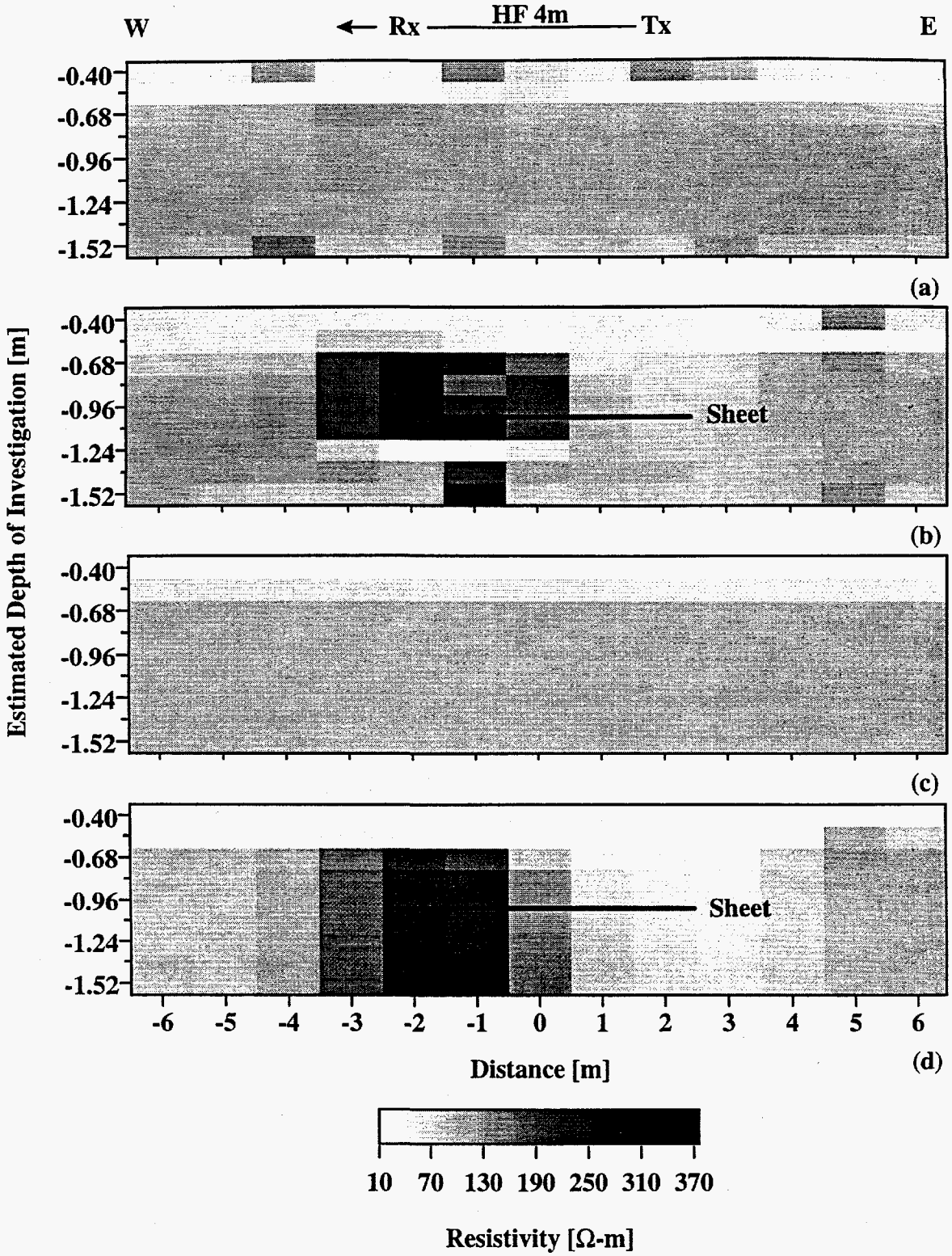

Figure 59. Apparent resistivity pseudosections from the piecewise neural networks for a 3 m by 5 m aluminum sheet buried at a depth of 1.0 m. a) Apparent resistivity for the background prior to burial of the sheet. b) Apparent resistivity derived from field data. c) Apparent resistivity derived from a model calculation using the values from a) for the model. d) Apparent resistivity from a model calculation using the exact field setup as that used in a) and b).

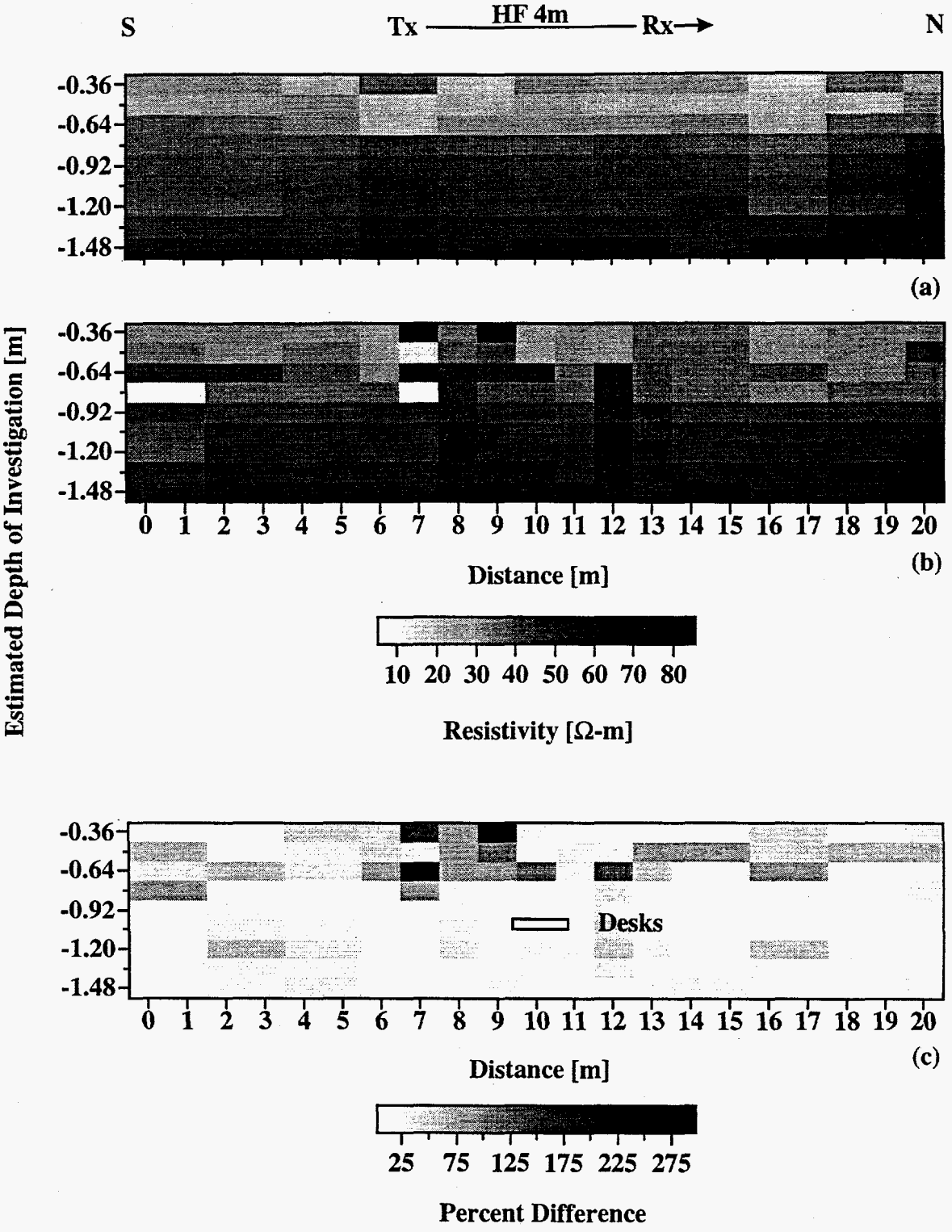

Figure 60. Apparent resistivity pseudosections for a) background and b) metal office desks. Values are from the piecewise apparent resistivity networks. c) percent difference between background and target resistivities.

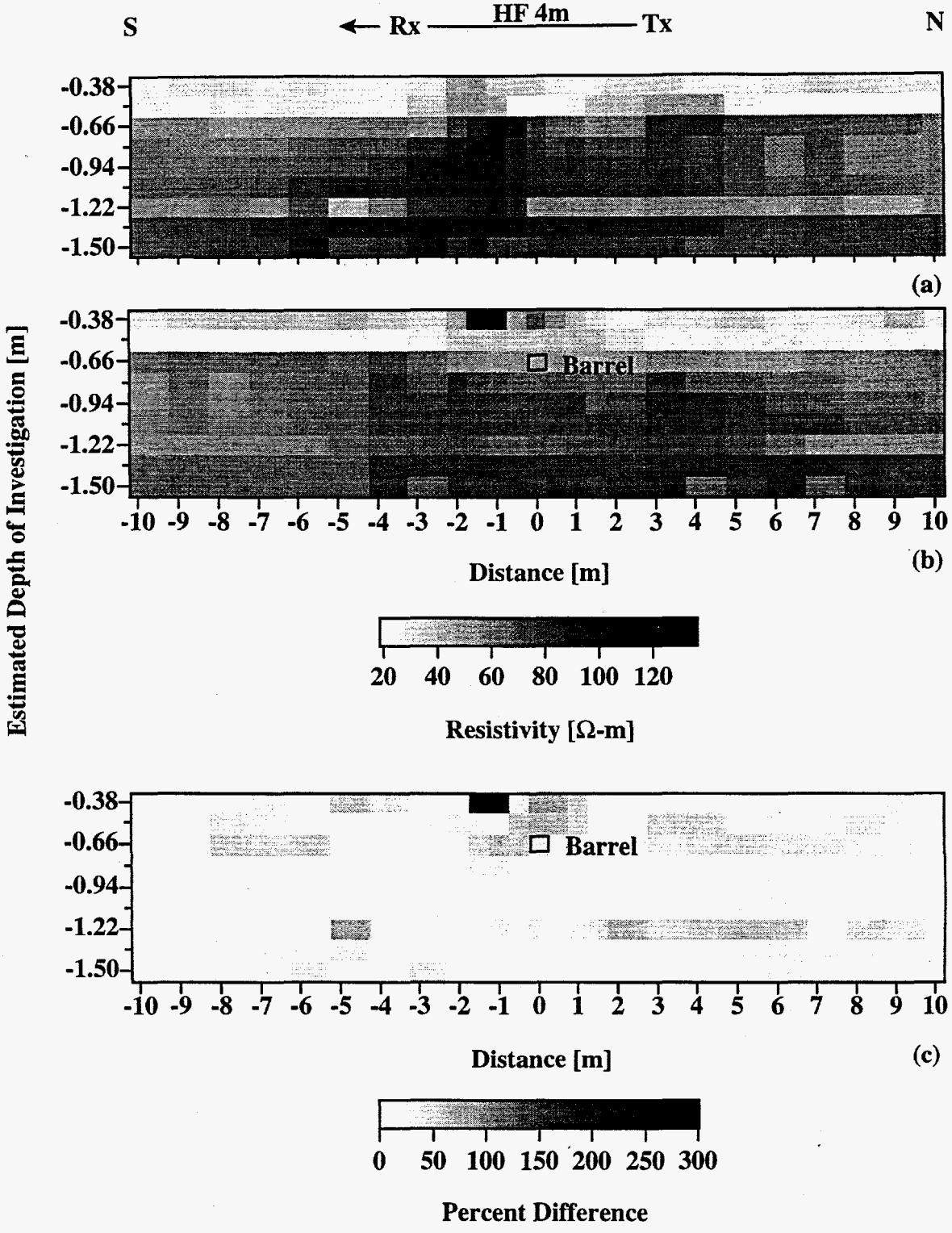

Figure 61. Apparent resistivity pseudosections for a) background and b)55-gallon barrel. Values are from the piecewise apparent resistivity networks. c) percent difference between background and target resistivities.

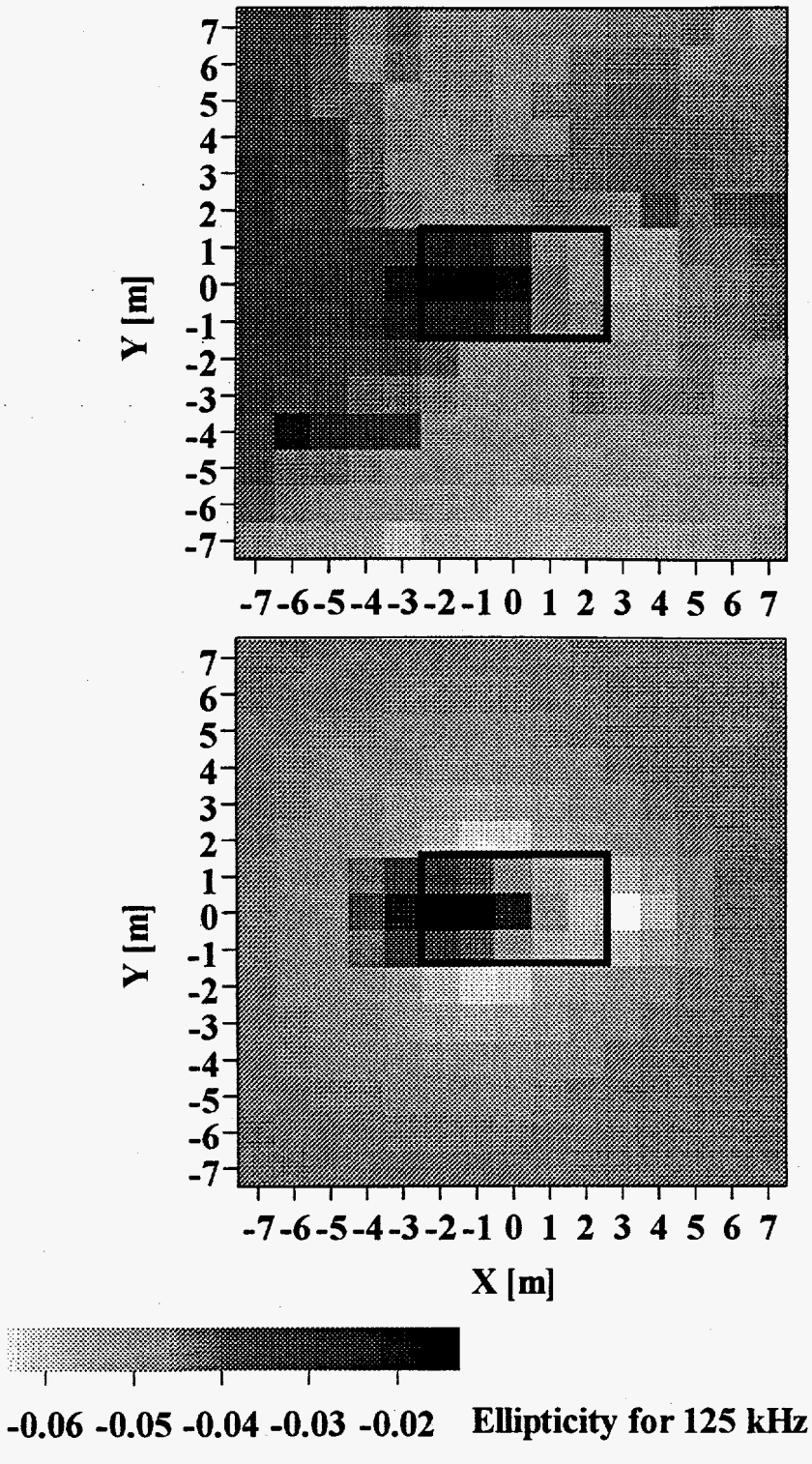

Figure 62. Plan maps of ellipticity for 125 kHz, 4 m antenna separation over the 3 m by 5 m aluminum sheet. The top figure is field data and the bottom figure is model data using the same field setup as the top figure and that in figure 59.

Another way of presenting the anomaly in a section if a background profile is available, is to calculate the percent difference between the two resulting sections. This was done for the sections presented in figures 60 and 61. The resistivity depth section in figure 60a represents the background, after the 55-gallon barrel (depth of burial = 0.63 m) was removed from the site. The section with the barrel in the ground is shown in figure 60b. Again we detect a very subtle anomaly on either side of the barrel. It is very hard to see the anomaly, because the target is a very small conductor. In this case the percent difference section 60c provides a different look at the anomaly that enhances it a little bit. Nevertheless, not knowing what pattern to look for, the anomaly can be easily overlooked. Figure 61 shows the anomaly of a slightly larger conductive target. Two metal office desks are buried 1 m deep in the ground as indicated in the sections 61b and 61c. The background profile (figure 61b) was acquired before the desks were buried. The anomaly in the profile over the desk is subtle but detectable at stations 8 m and 12 m in figures 61b and 61c.

We conclude from these experiments that the piecewise apparent resistivity networks can be used to detect conductive 3D objects based on characteristic resistivity lows when the receiver crosses the object and resistivity highs when the transmitter crosses the object. Because our data plotting convention uses the midpoint of the Tx-Rx separation as the station location, anomalies appear to extend one-half the antenna separation further on each side of an object than its actual width.

The depths calculated by Thomas (1996) for the apparent resistivity sections tend to underestimate depths for the objects. The depth estimation algorithm is relatively insensitive to the apparent resistivity values and more sensitive to frequency range and antenna separation. Hence, while we can detect objects in apparent resistivity sections, those objects are not always accurately locatable.

IDAHO NATIONAL ENGINEERING LABORATORY COLD TEST PIT SURVEY

Survey Overview

We conducted a survey at the Idaho National Engineering Laboratory (INEL) near Idaho Falls, Idaho from November 28 through December 1, 1995. The Very-Early Time Electromagnetics (VETEM) project, sponsored by Department of Energy (DOE), has been conducting a comparison study of several electromagnetic geophysical methods at the Cold Test Pit (CTP) of the Radioactive Waste Management Complex (RWMC) since October 1995. We conducted our survey as part of our contractual agreement with the DOE Morgantown Energy Technology Center in accordance with the survey plan designed by the VETEM group. We have also given copies of our data to the VETEM group for further interpretation.

The CTP is a simulated waste pit providing known targets and waste forms for accurate evaluation and calibration of procedures, technologies, and equipment. We were not

given specific information on the thickness of the capping material, depth to the waste, type of targets, depth to bedrock, or resistivities of the earth materials and targets. We do have approximate information on thickness of the cap, resistivities, general types of targets, and areas where bedrock is shallow.

We measured ellipticity along nine separate survey lines (Figure 63) with multiple transmitter-receiver offsets and different frequency ranges for a total of 16 survey lines. Soundings were collected at 307 stations across the CTP. A frequency range from 31 kHz to 31 MHz (HF-system) was used for data collection on 12 of 16 lines and a range of 1 kHz to 1 MHz (MF-system) was used for the remaining four lines. The survey is summarized in Table 3. We found after two initial surveys at 4 m separation that we could not penetrate deep enough with this transmitter-receiver separation so the remaining lines were profiled with an 8 m or 16 m separation.

Unpacking and setting up the system took approximately two hours. We collected data at over 300 stations in 30 hours of surveying. Average data collection time was about one minute to acquire data and two minutes to set up on the next station. We did not experience a single hardware or software malfunction during the course of the survey.

Five types of processing were done with the data: plotting the ellipticity along profile lines for each frequency; 1D neural network interpretation with no depth given for piecewise apparent resistivity; estimation of depth for piecewise apparent resistivities using an algorithm developed at LASI; 1D inversions; neural network classification of the data as waste or background and type of waste. Each of these methods will be described in turn.

Ellipticity Profiles

Plotting profiles of the received data provides a first look at the data and can be used as a form of quality assurance. Anomalies can be spotted in the profiles but we have no information on the resistivity values or depth. Ellipticity profiles for selected frequencies are shown in Figures 56-70.

In general, we observe an anomaly in almost all the frequencies in the center of the profiles shown in Figure 64 to 70. These lines are over an area of the CTP, where the survey area map (Figure 63) indicates that the pit is continuously filled with objects. A different anomaly can be observed in the ellipticity profiles (Figure 71 and 72) which ran over the individual targets (Figure 63). A very distinctive anomaly can be seen in the ellipticity profiles for 250 kHz, 500 kHz, and 1 MHz of line 55S (Figure 72), indicating the large object formed by the crushed drums and the steel tank (Figure 63). Line 70S is supposed to be a background line over undisturbed soil or refilled material, but no targets. The ellipticity profiles (Figure 73 and 74) show just a slight decrease in ellipticity to the east for almost all the displayed frequencies. The MF 16 m survey over line 70S, however, shows an anomaly at the east end of the line, especially for the

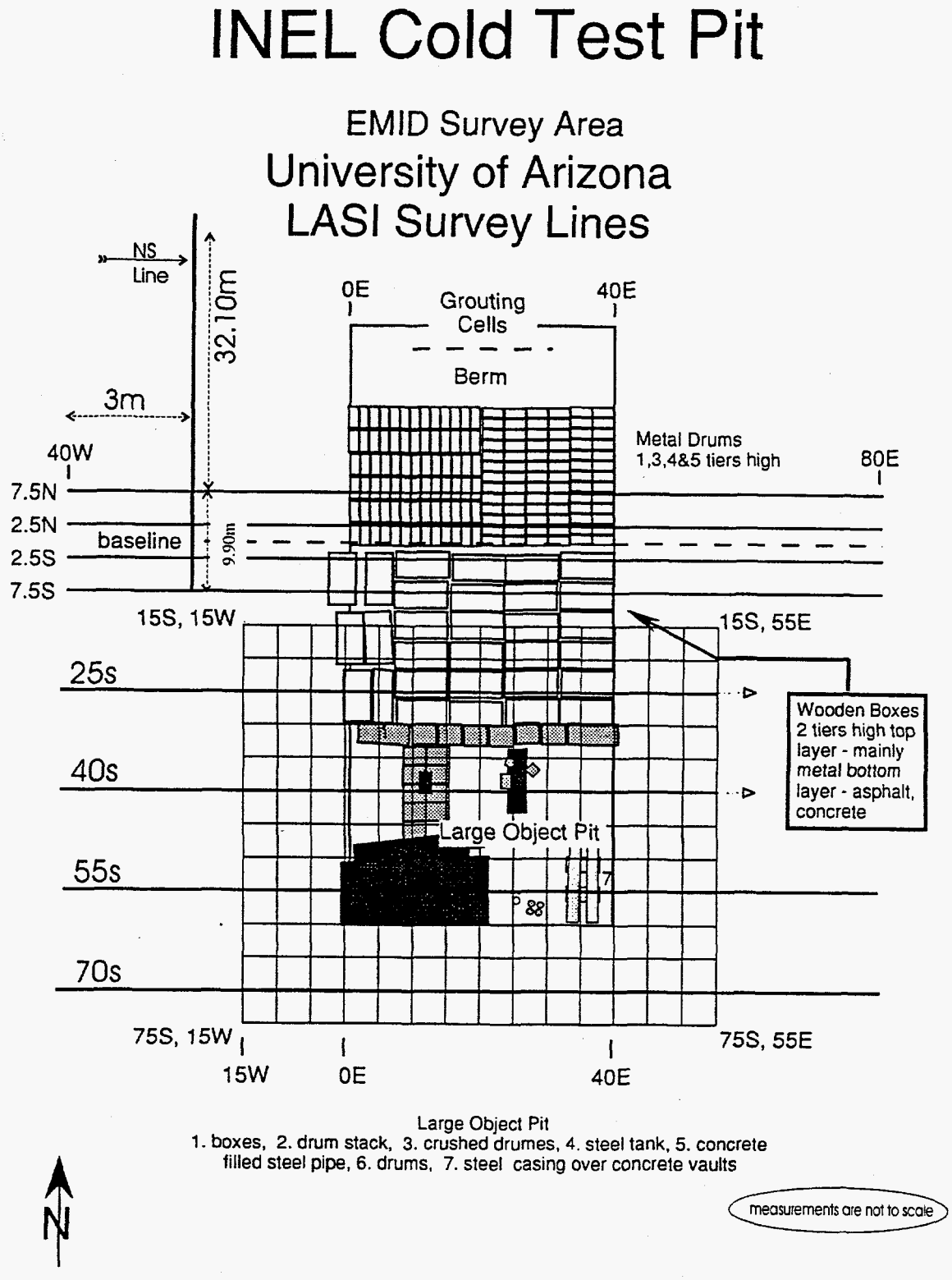

Figure 63. **Map showing the INEL CTP and the nine lines surveyed by the LASI ellipticity survey.**

frequencies 4 kHz, 8 kHz, 16 kHz, and 32 kHz (Figure 78). This trend can also be observed in the ellipticity profiles shown in Figure 77.

Date	Line	Survey ID	Line ID	Direction	Start [m]	End [m]	Station-Spacing [m]	Coil-Spacing [m]	Number of Stations	Stacks	System
11/28/95	7.5S	AHP	AD	W-E	0	36	1	4	37	100	HF
11/29/95	7.5N	AHP	AE	W-E	0	36	1	4	37	25	HF
11/29/95	7.5N	AHP	AF	W-E	0	36	2	8	19	100	HF
11/29/95	7.5S	AHP	AG	W-E	0	36	2	8	19	100	HF
11/29/95	2.5S	AHP	AH	W-E	0	36	2	8	19	100/50	HF
11/30/95	2.5N	AHP	AJ	W-E	0	36	2	8	19	50	HF
11/30/95	70S	AHP	AK	W-E	0	36	2	8	19	50	HF
11/30/95	55S	AHP	AL	W-E	0	36	2	8	19	50	HF
11/30/95	40S	AHP	AM	W-E	0	36	2	8	19	50	HF
11/30/95	40S	AHP	AN	W-E	0	36	4	8	10	50	HF
12/1/95	25S	AHP	AO	W-E	0	36	2	8	19	50	HF
12/1/95	NS	AHP	AP	N-S	0	42	2	8	22	50	HF
12/1/95	70S	AHR	AB	W-E	0	36	4	8	10	25	MF
12/1/95	40S	AHR	AC	W-E	0	36	2	8	19	25	MF
12/1/95	40S	AHR	AD	W-E	0	36	4	16	10	50	MF
12/1/95	70S	AHR	AE	W-E	0	36	4	16	10	50	MF

Table 3. Summary of the LASI ellipticity survey lines. HF = High-Frequency System (32kHz - 32MHz), MF = Medium-Frequency System (1kHz - 1mhz). Station 0 m is equivalent to station 40W on the local CTP grid. The west boundary of the waste starts at approximately 12.2 m in our coordinate system, the east boundary is at approximately 24.4 m.

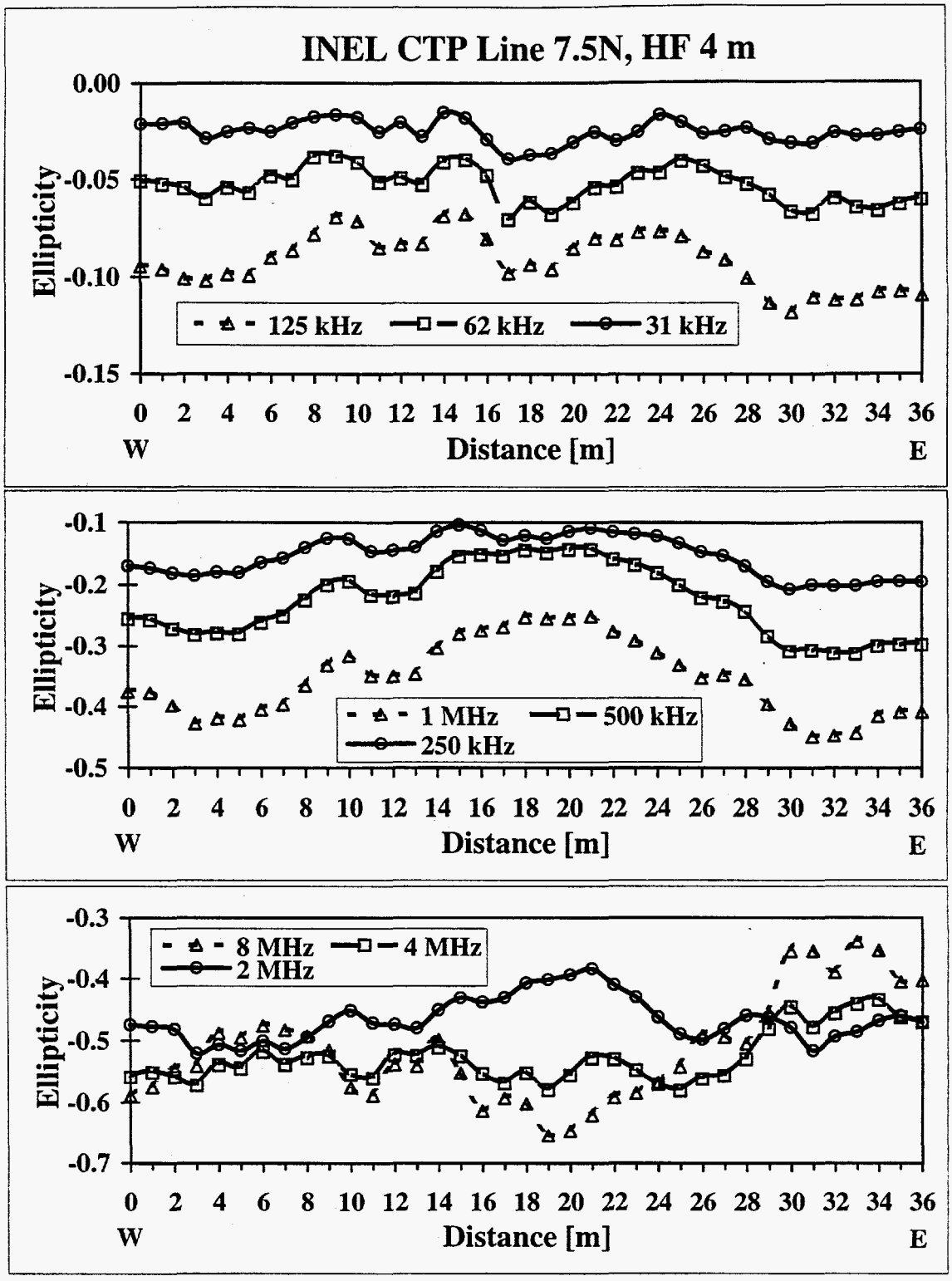

Figure 64. Ellipticity raw data profiles for 9 frequencies from 31 kHz to 8 MHz along INEL CTP line 7.5N for a 4 m HF survey.

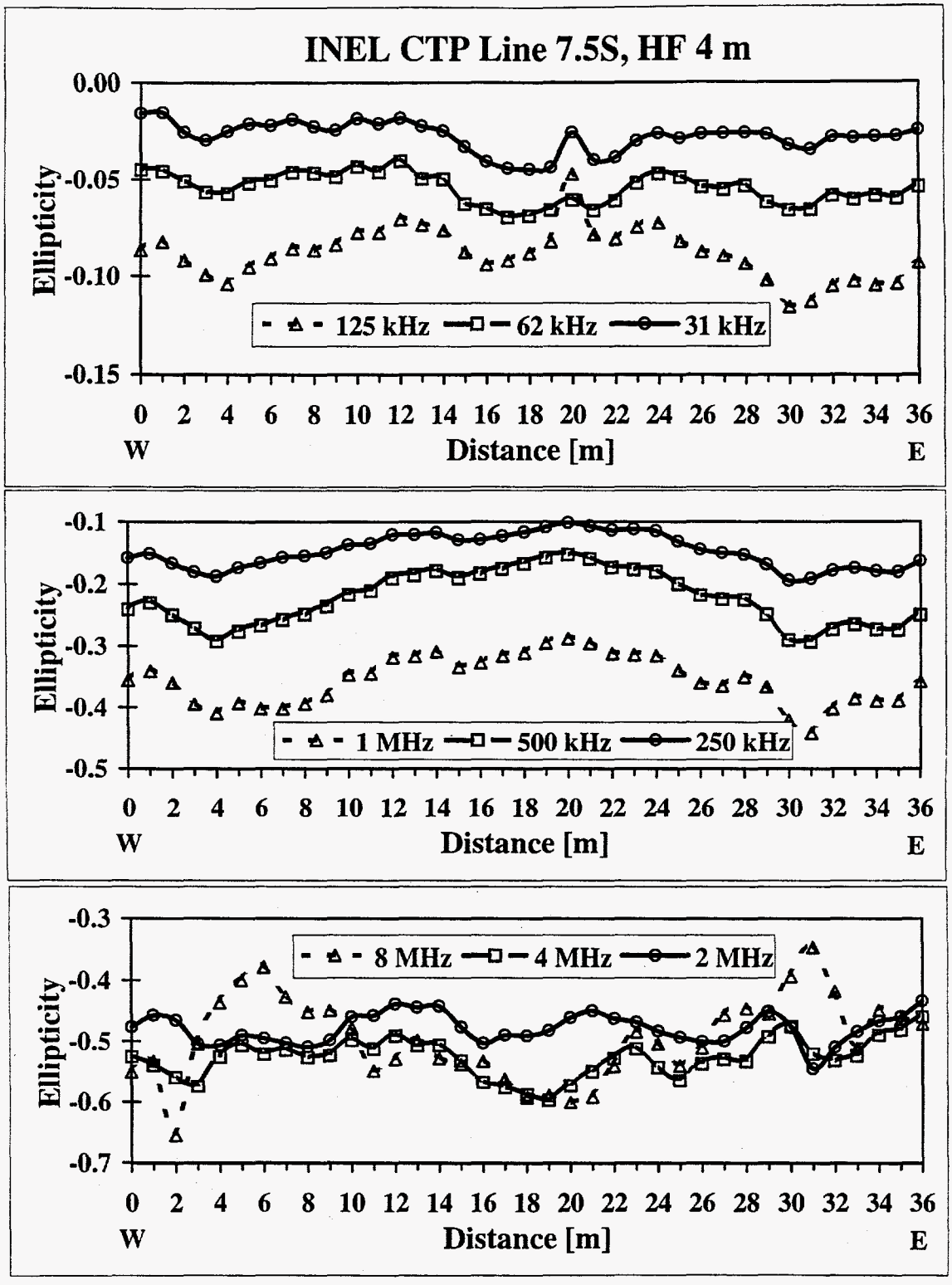

Figure 65. Ellipticity raw data profiles for 9 frequencies from 31 kHz to 8 MHz along INEL CTP line 7.5S for a 4 m HF survey.

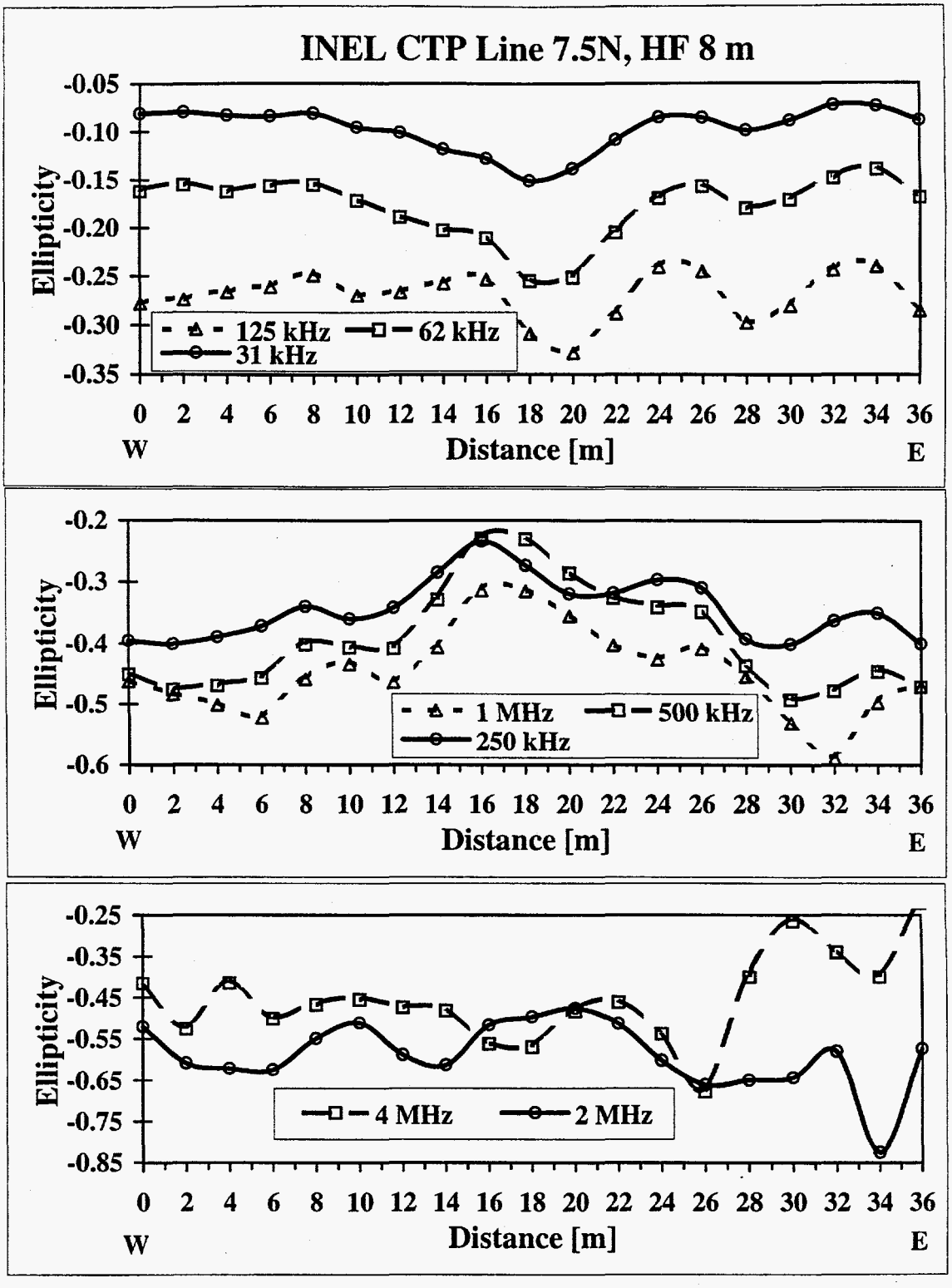

Figure 66. Ellipticity raw data profiles for 8 frequencies from 31 kHz to 4 MHz along INEL CTP line 7.5N for a 8 m HF survey.

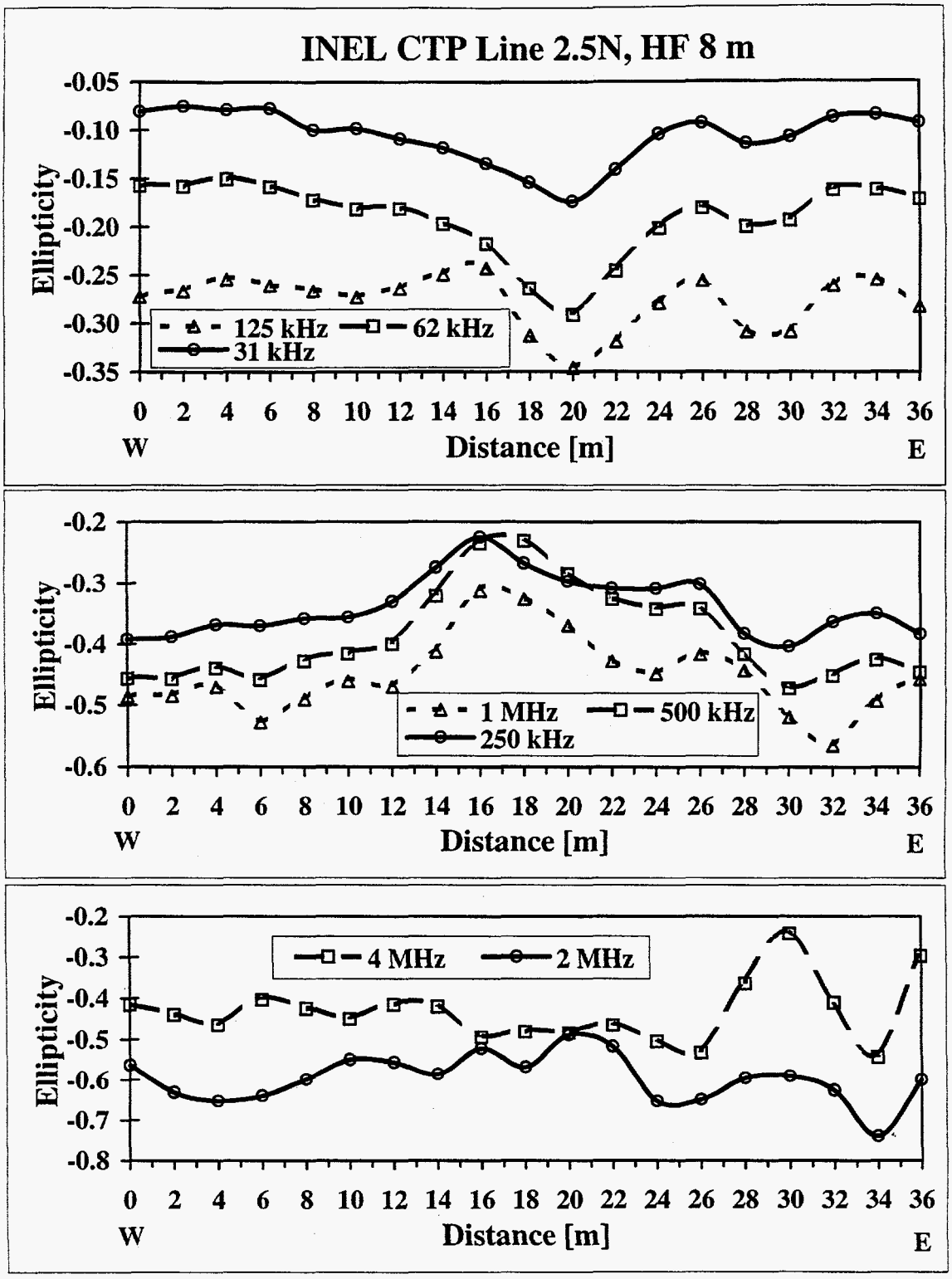

Figure 67. Ellipticity raw data profiles for 8 frequencies from 31 kHz to 4 MHz along INEL CTP line 2.5N for a 8 m HF survey.

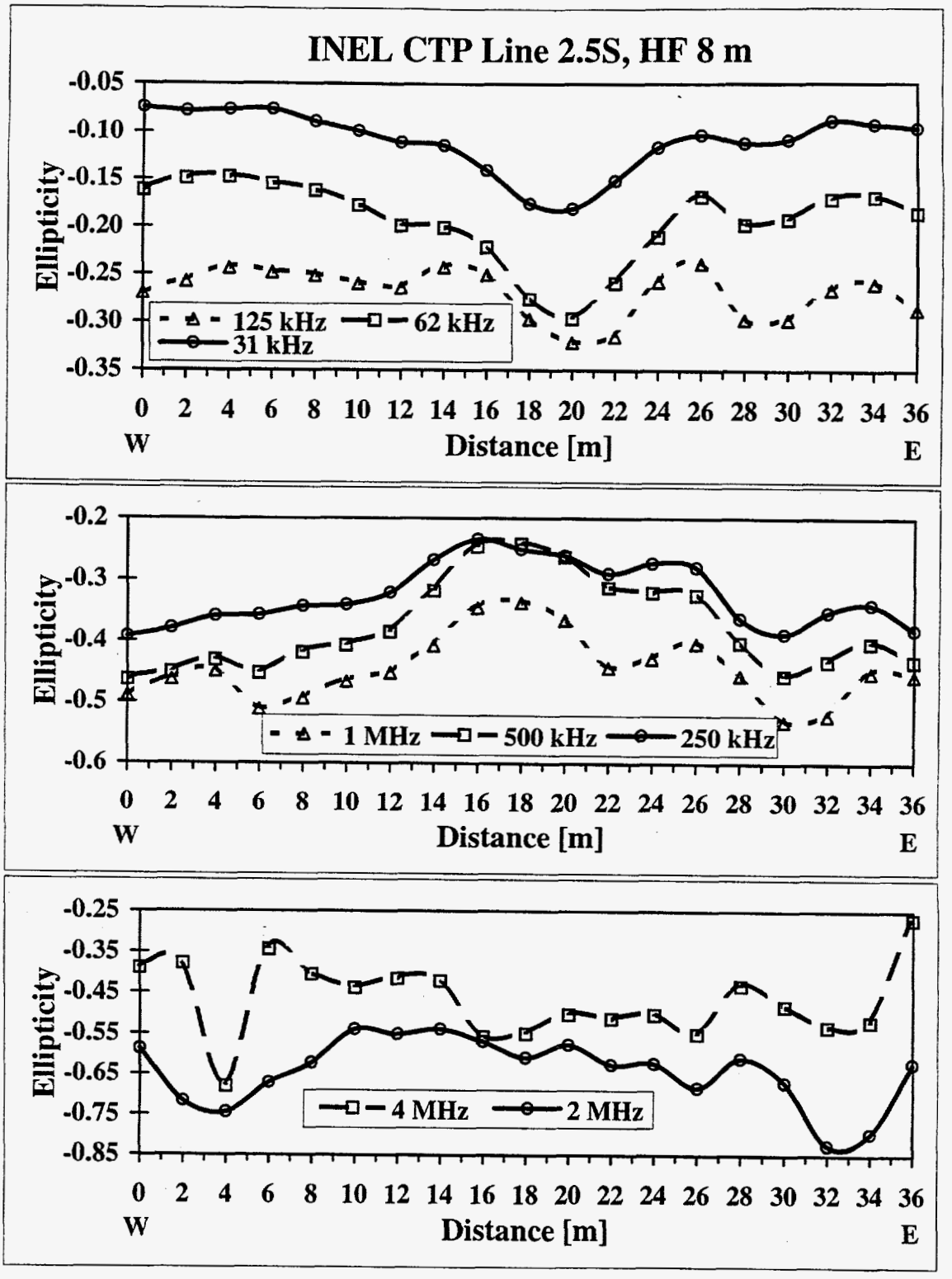

Figure 68. Ellipticity raw data profiles for 8 frequencies from 31 kHz to 4 MHz along INEL CTP line 2.5S for a 8 m HF survey.

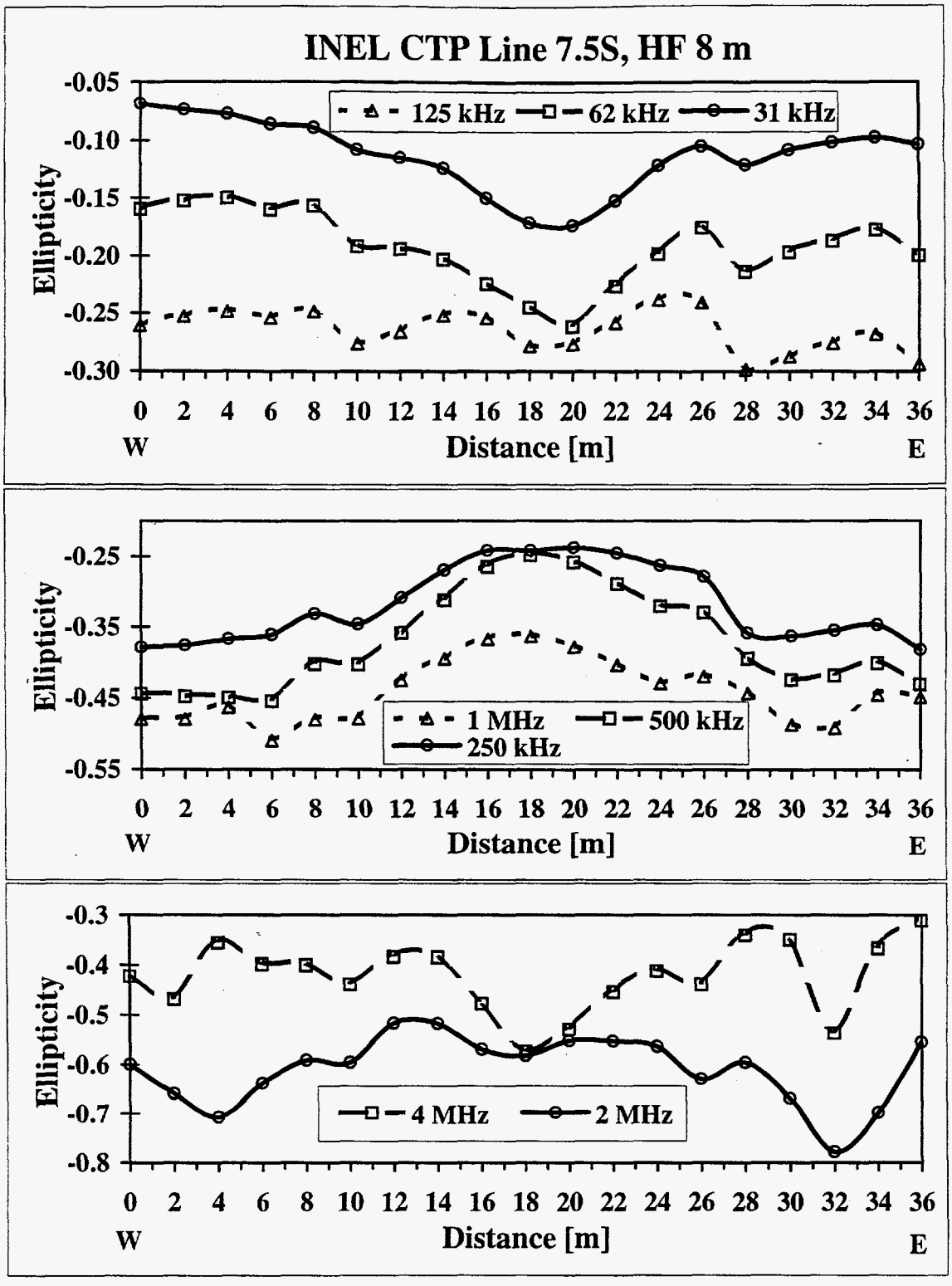

Figure 69. Ellipticity raw data profiles for 8 frequencies from 31 kHz to 4 MHz along INEL CTP line 7.5S for a 8 m HF survey.

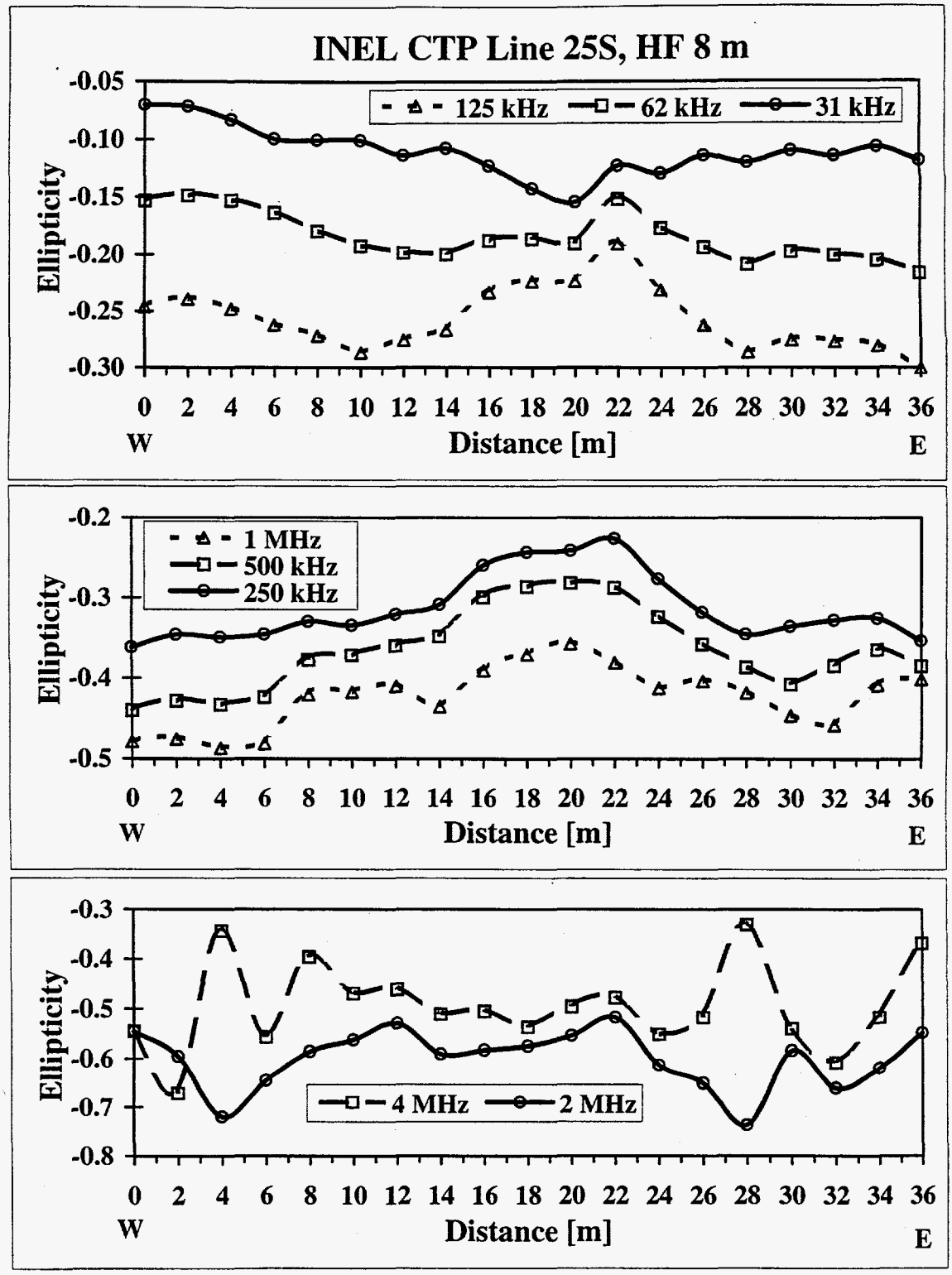

Figure 70. Ellipticity raw data profiles for 8 frequencies from 31 kHz to 4 MHz along INEL CTP line 25S for a 8 m HF survey.

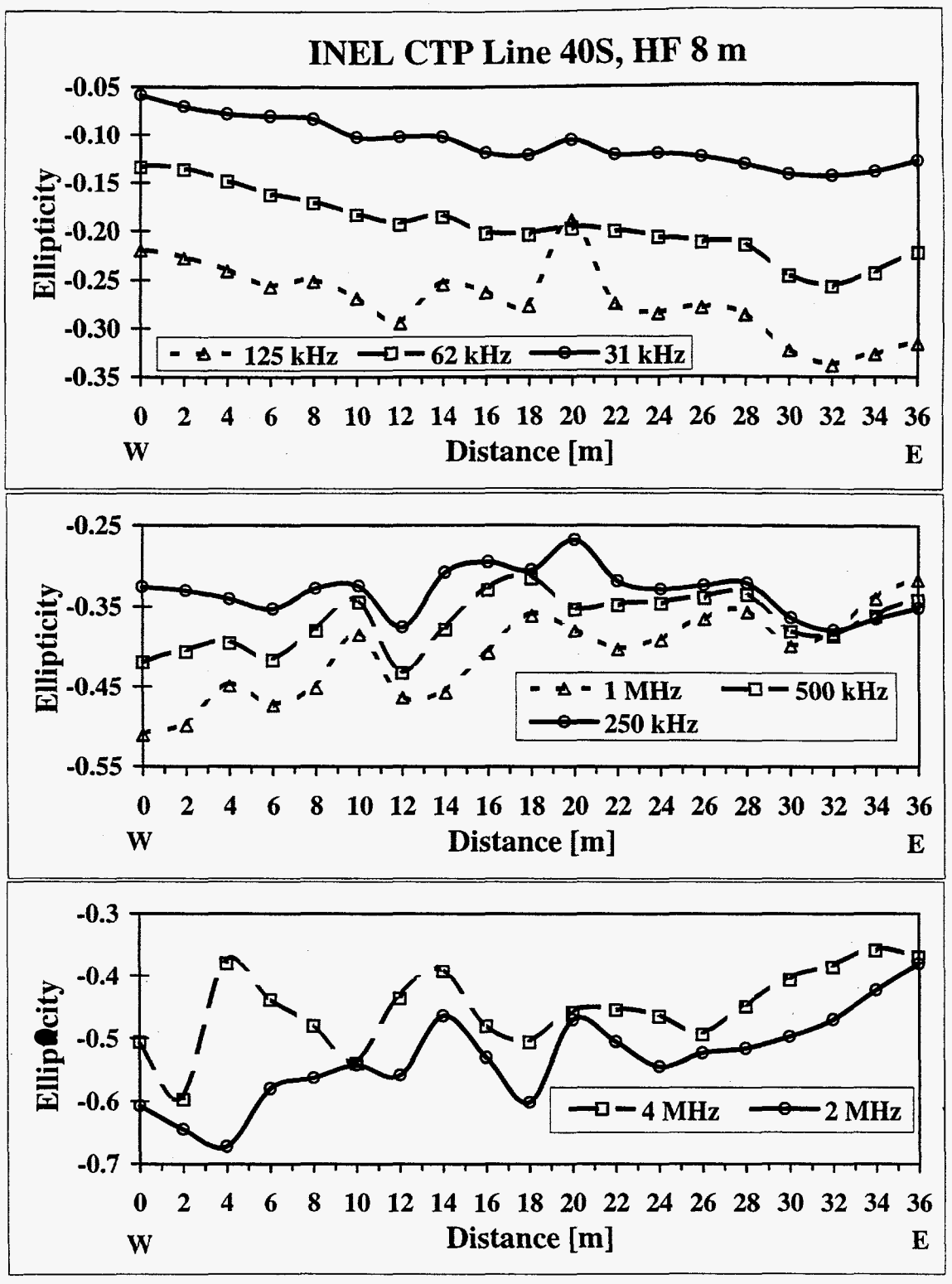

Figure 71. Ellipticity raw data profiles for 8 frequencies from 31 kHz to 4 MHz along INEL CTP line 40S for a 8 m HF survey.

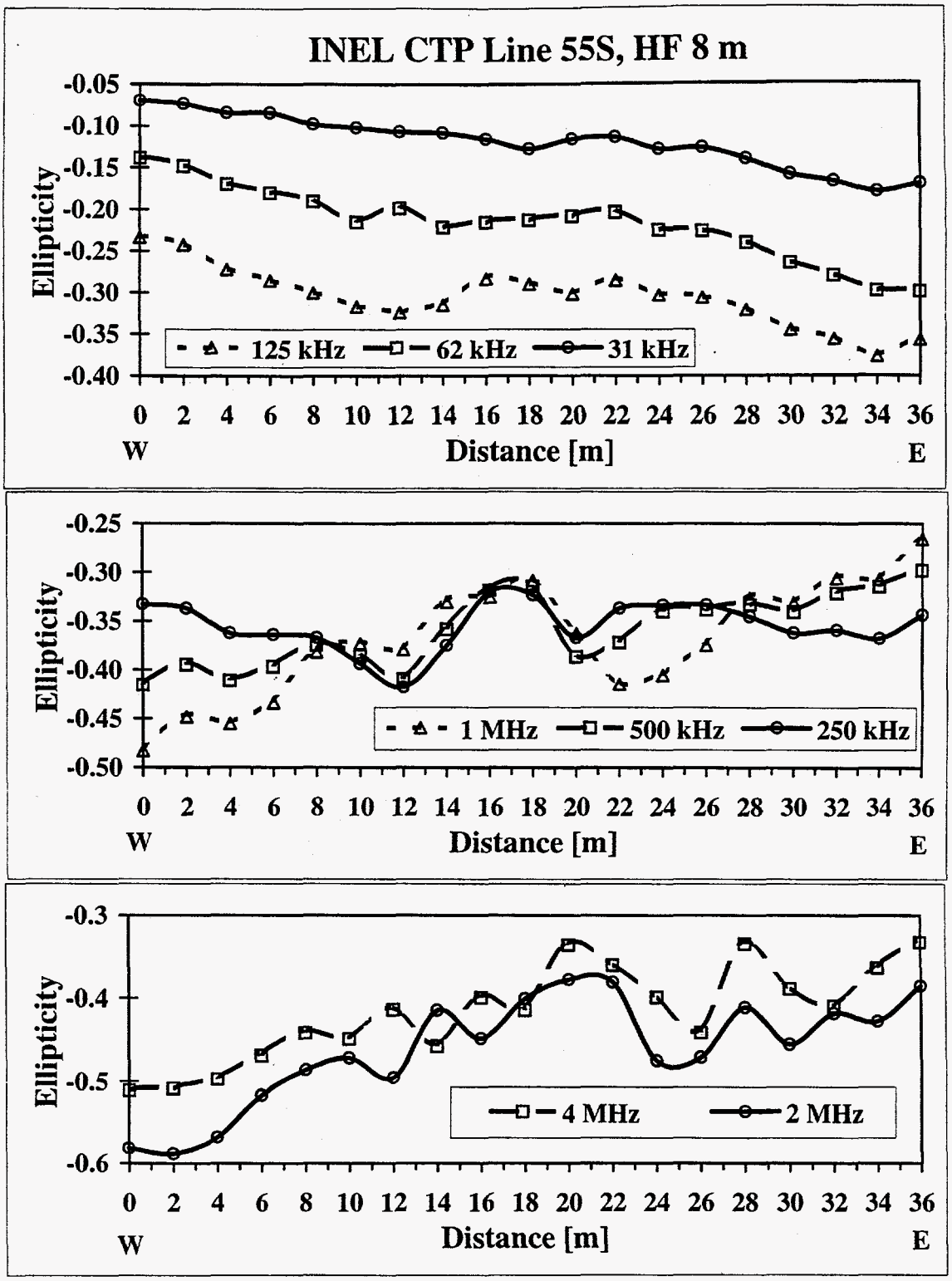

Figure 72. Ellipticity raw data profiles for 8 frequencies from 31 kHz to 4 MHz along INEL CTP line 55S for a 8 m HF survey.

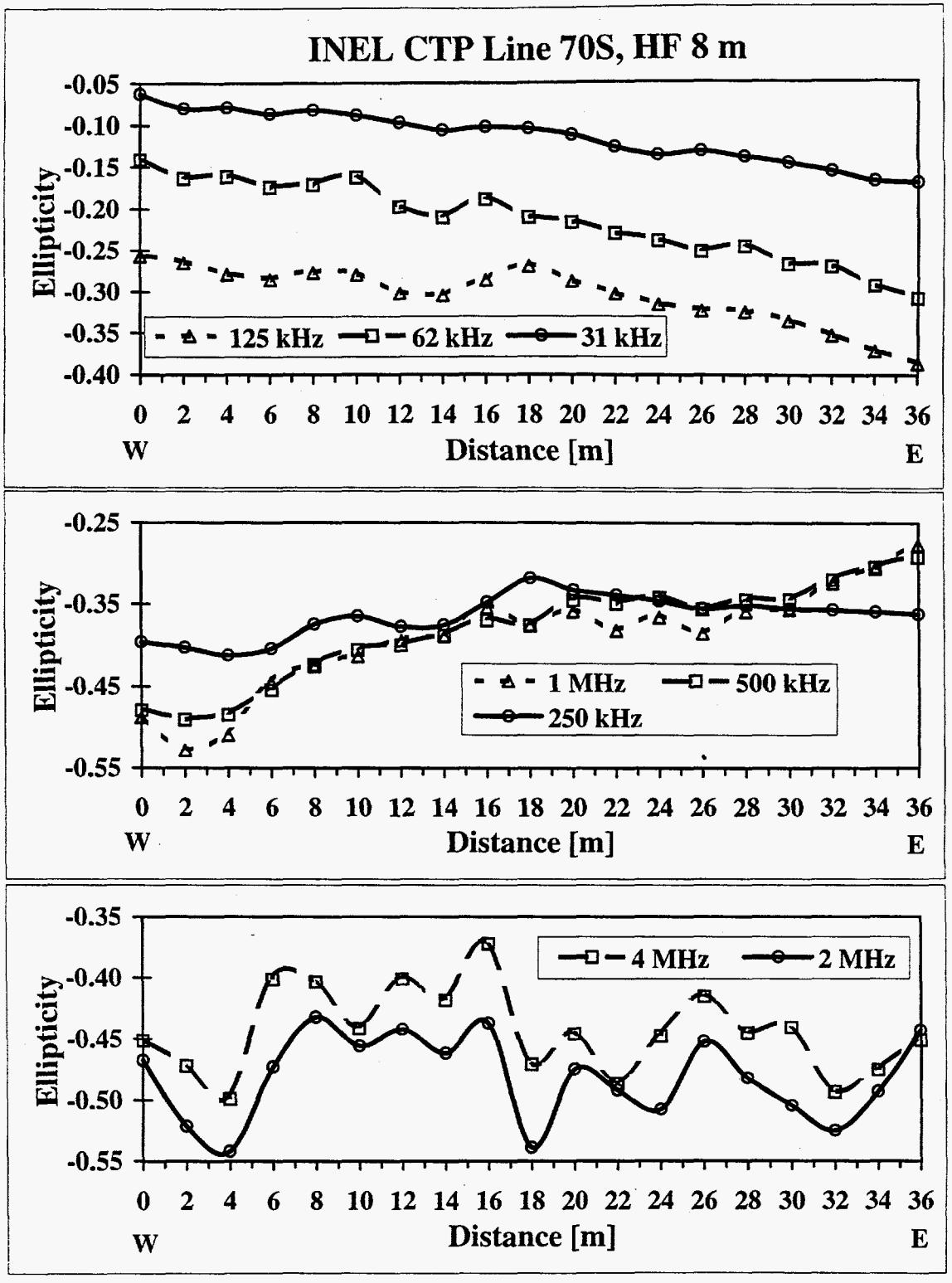

Figure 73. Ellipticity raw data profiles for 8 frequencies from 31 kHz to 4 MHz along INEL CTP line 70S for a 8 m HF survey.

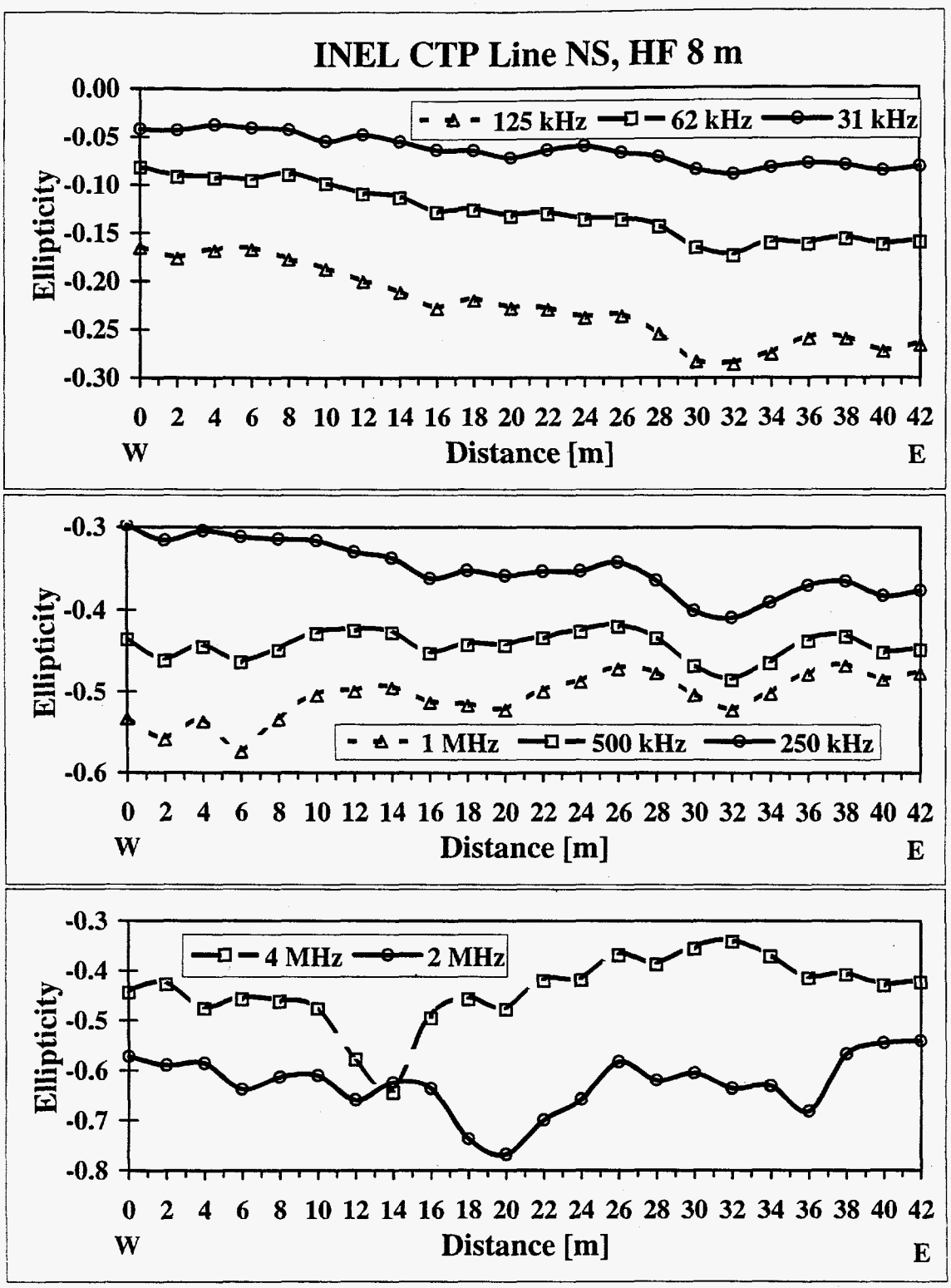

Figure 74. Ellipticity raw data profiles for 8 frequencies from 31 kHz to 4 MHz along INEL CTP line NS for a 8 m HF survey.

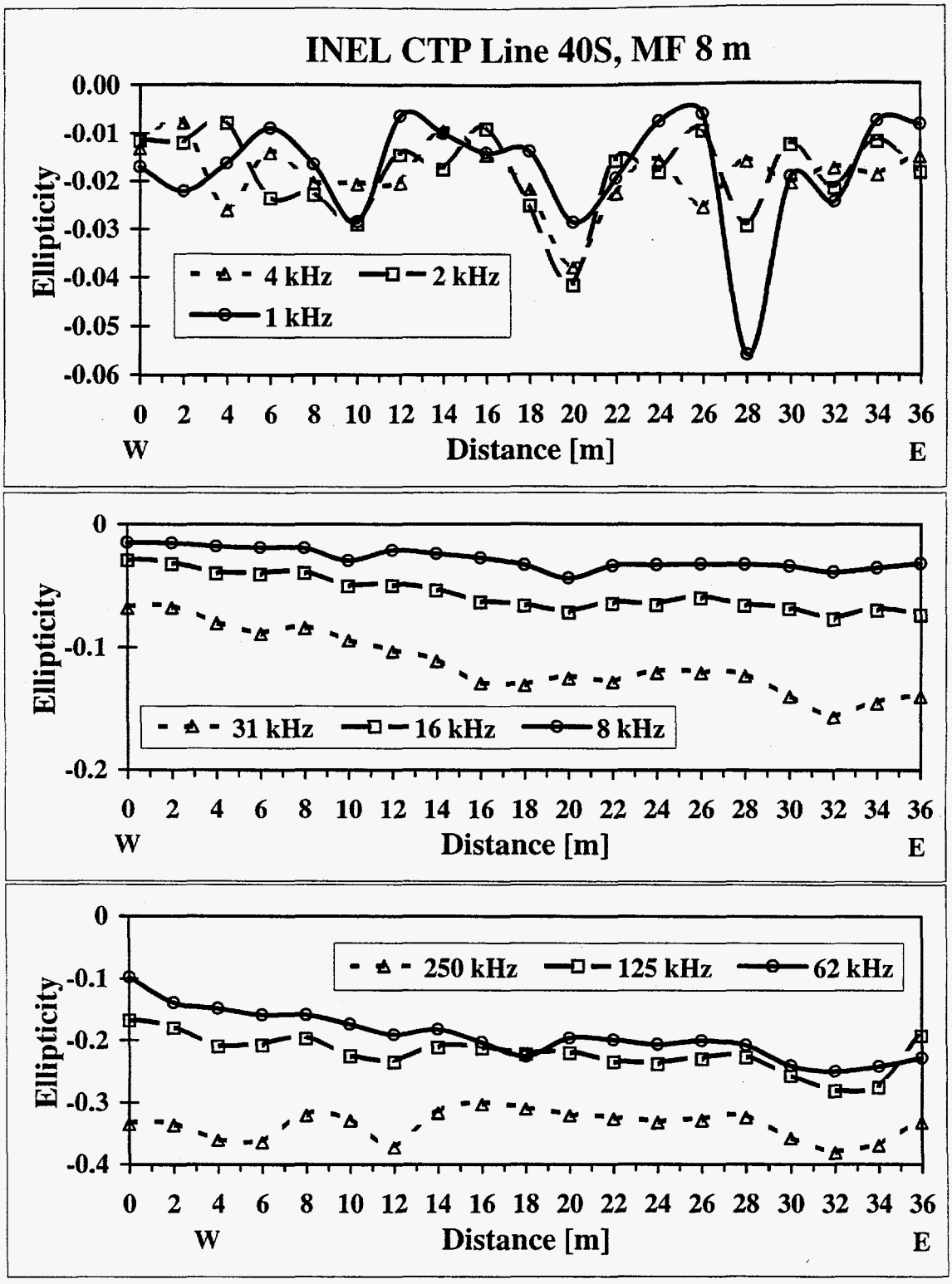

Figure 75. Ellipticity raw data profiles for 9 frequencies from 1 kHz to 250 kHz along INEL CTP line 40S for a 8 m MF survey.

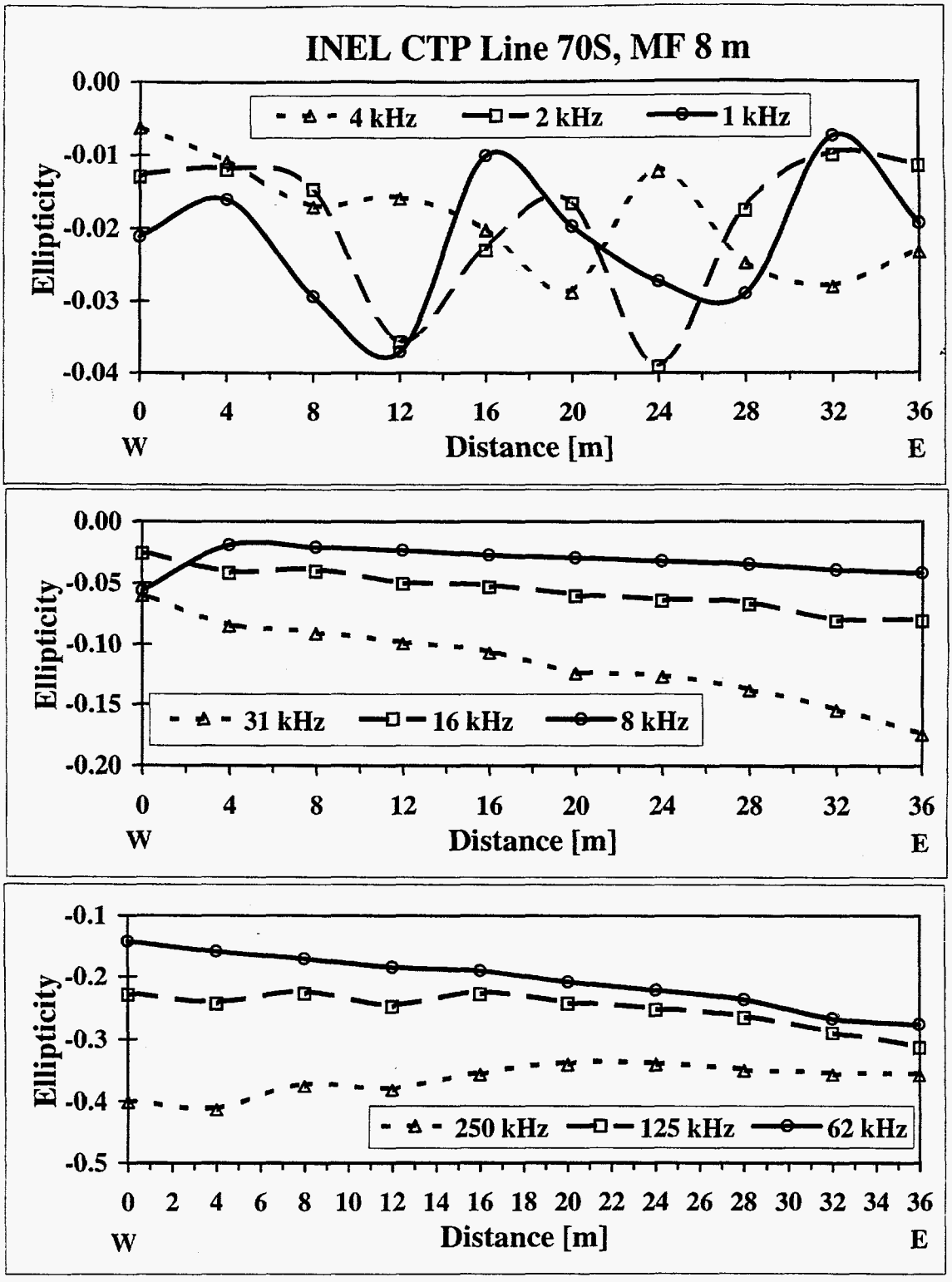

Figure 76. Ellipticity raw data profiles for 9 frequencies from 1 kHz to 250 kHz along INEL CTP line 70S for a 8 m MF survey.

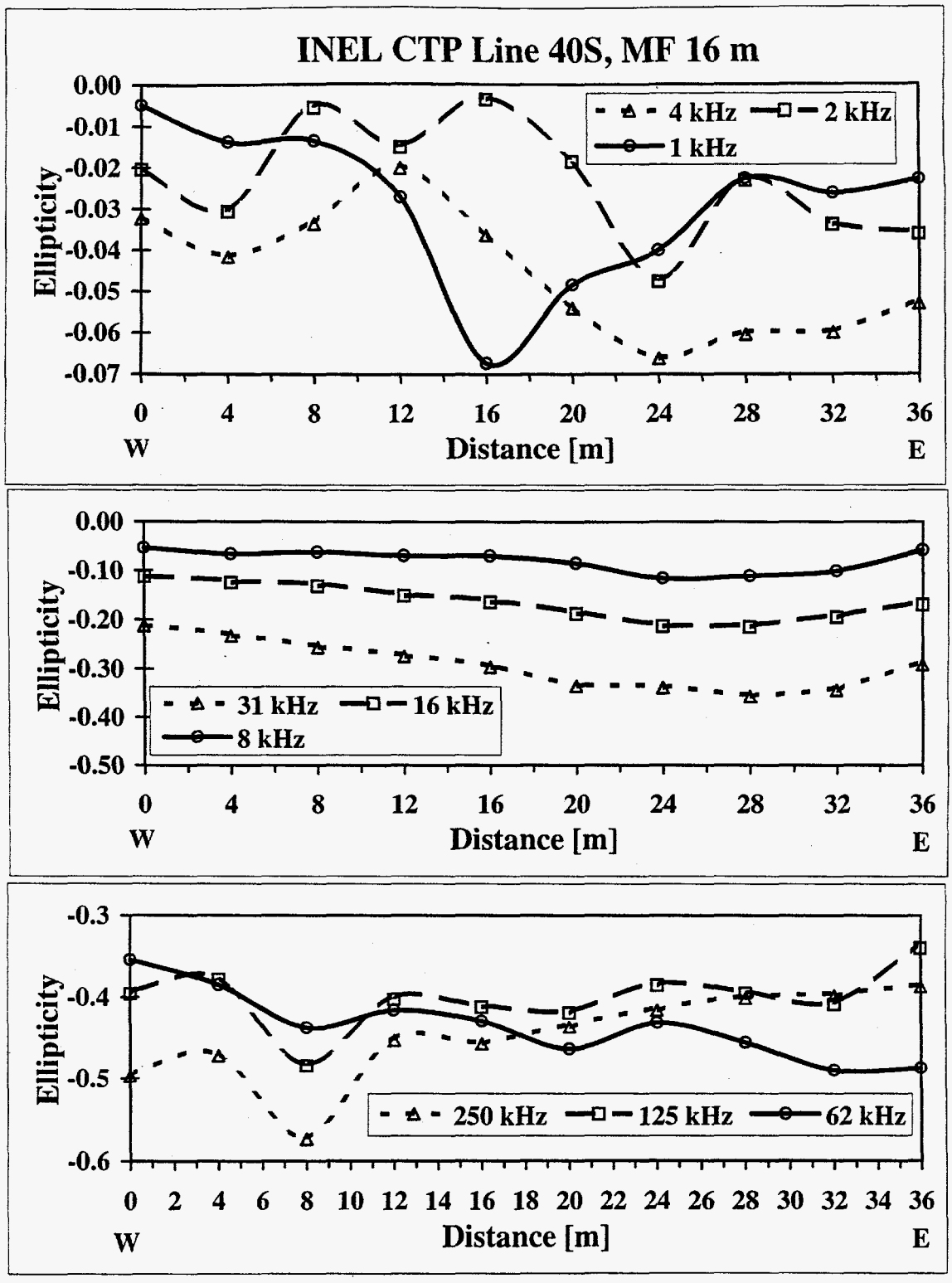

Figure 77. Ellipticity raw data profiles for 9 frequencies from 1 kHz to 250 kHz along INEL CTP line 40S for a 16 m MF survey.

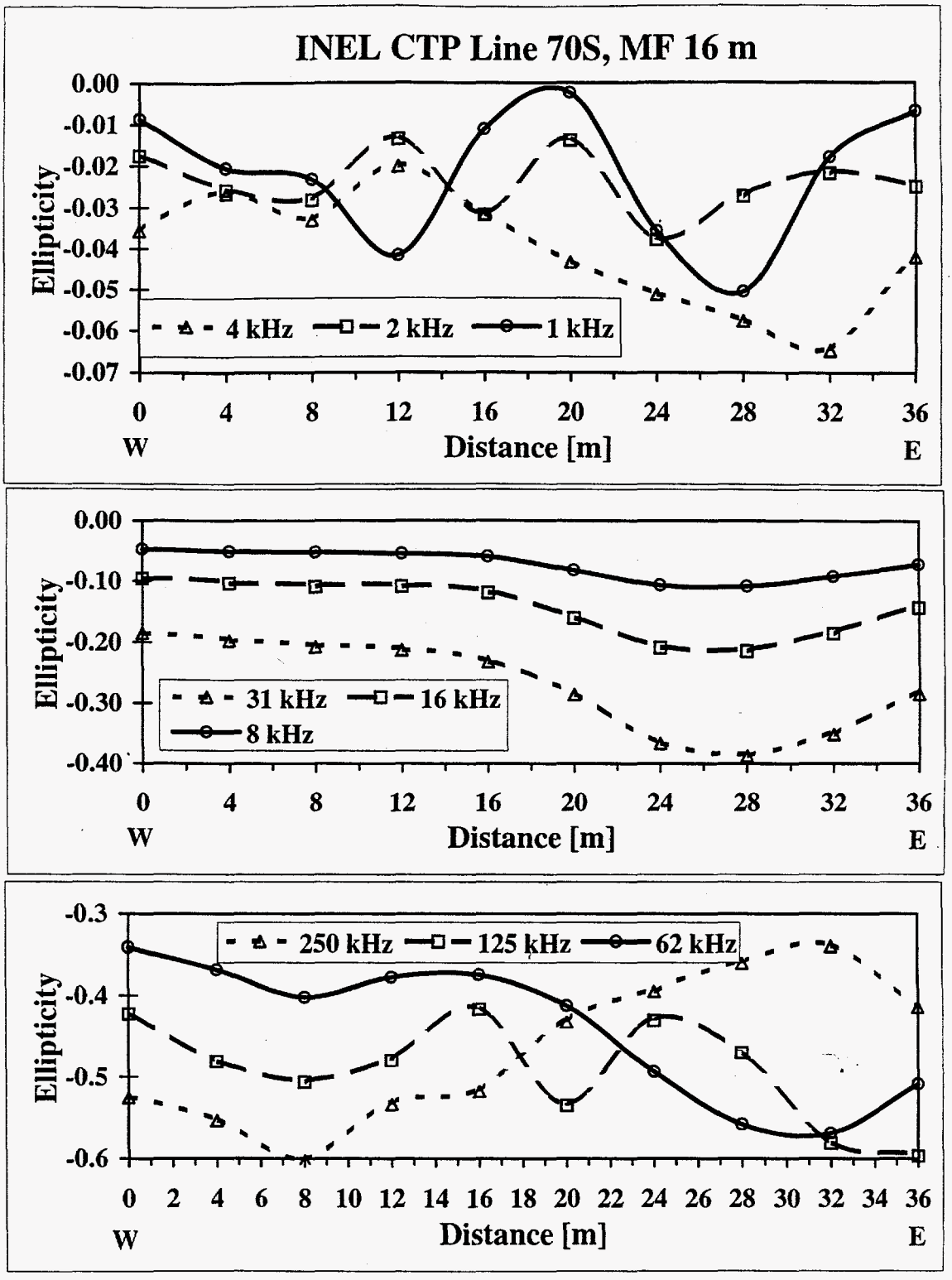

Figure 78. Ellipticity raw data profiles for 9 frequencies from 1 kHz to 250 kHz along INEL CTP line 70S for a 16 m MF survey.

A pit on the north end of the survey area was being excavated while we conducted our measurements. To test whether the excavation was detectable we added a survey line on the west edge of the test area, running north-south past the excavation. The profile line was approximately 6 m away from the west edge of the excavation, which is about the distance the south edge of the excavation is away from line 7.5N. The excavation would extend from stations 6 m to 26 m in our NS line (Figure 63). The resulting ellipticity profiles are shown in Figure 74. No anomaly of the size we observe in the profiles over the CTP was found.

Piecewise Apparent Resistivity Neural Network Interpretation

Two types of 1D neural network interpretation were performed: layered-earth and piecewise apparent resistivity. In areas away from the waste, more representative of a 1D earth, the layered- earth networks produced interpretations that fit the field data. In areas around the waste, the piecewise apparent resistivity networks were better able to fit the data. In areas of strong 3D effects none of the networks could fit the data, which in itself was diagnostic.

The piecewise apparent resistivity networks do not estimate a depth for each estimated resistivity. To get a depth range for our resistivity sections we use an algorithm developed by Thomas (1996). This optimum depth of investigation algorithm estimates the depth for a particular resistivity value which is associated with each frequency and the geometry of the system. Thomas (1996) defines the optimum depth of investigation as the depth where 50% of the earth's influence is from the material below the optimum depth and 50% of the influence is from the material above the optimum depth. Optimum depth of investigation can be considered as the average depth at which the earth responds to the transmitted signal. The optimum depth of investigation algorithm is derived by 1D computer modeling and may therefore not hold for earth structures containing 2D and 3D features (Thomas, 1996). Therefore, we found our depth scale using data collected away from the waste and applied those depths to the whole section. Figures 79 through 86 show the resistivity sections with depth scales, as interpreted by the piecewise apparent resistivity neural networks with an estimated depth from the depth of investigation algorithm. Note that the same depth scale is used for all HF 8 m surveys for easier comparison. This was possible because the resulting depths from the depth of investigation algorithm were within a few centimeters for each of the sections.

The resistivity sections are not gridded or smoothed. Since each interpretation at a station is done independently of surrounding stations, large changes in resistivity can occur. These changes are often meaningful and can be blurred or lost in the gridding process, especially when we are interested in abrupt changes in properties. Translating the survey grid provided to us in feet to our grid in meters, indicates most of the waste lies between stations 12.2 m and 24.4 m. Using the mid-point of the antenna separation as the plot point, we will actually sense targets from 8 m to 28 m for an 8 m antenna separation. In areas of strong 3D effects such as the waste, the resistivity

values are not accurate but the spatial locations of anomalous values should accurately map the waste. The program Spyglass Transform for WINDOWS was used to print the 2D sections.

All HF resistivity depth sections (Figures 79 to 83) show a resistive top layer up to 1.04 m (+/- 0.135 m depth). Figures 79, 80, and 81 also show an increased thickness (down to 1.31 m +/- 0.135 m) in the center of the sections over the pit area. As mentioned earlier, the depth of penetration for the 4 m surveys was not sufficient to see much deeper than just beneath the cap (Figure 84). We believe that the HF 8m surveys were not able to determine the depth to the bottom of the CTP, which means that the bottom of the CTP is deeper than 2.39 m. We expected increased penetration with the MF 8 m surveys. The data quality was quite good and the piecewise apparent resistivity fits to the data were nearly perfect. We could not, however, detect any layering in the interpreted sections (Figure 85) that indicated the bottom of the waste on the bedrock. Layered-earth inversions also failed to detect any boundaries. The MF 16 m surveys should have had sufficient depth of penetration to detect the bedrock on line 70S. The sounding curves we recorded could not be accurately fit by any of our neural networks, indicating 2D or 3D effects. The coarse resolution of the 16 m separation relative to the size of the CTP is reflected in Figure 86 as a lack of detectable features.

In Table 4 the estimated west and east boundaries of the CTP are listed for the HF 8 m coil separation lines.

Line	Coil-Spacing [m]	System	CTP W-Boundary [m]	CTP E-Boundary [m]	Error [m]
7.5N	8	HF	13	27	1
7.5S	8	HF	11	27	1
2.5S	8	HF	12	27	1
2.5N	8	HF	13	27	1
55S	8	HF	9	27	1
40S	8	HF	9	29	1
25S	8	HF	9	27	1

Table 4. Estimated west and east boundaries of the CTP, based on the piecewise apparent neural network resistivity interpretations for the 8 m HF lines, shown in Figures 79 to 82.

Next, we will discuss the individual resistivity sections. The sections start at the greatest depth with the resistivities estimated by the piecewise apparent neural network using the 31 kHz and 62 kHz ellipticities and end in the shallowest row of resistivities

estimated by the piecewise apparent neural network using the ellipticities of 2 MHz and 4 MHz.

Lines 7.5N and 2.5N, HF 8 m

Figure 79 shows the two resistivity sections of the lines 7.5N and 2.5N crossing the CTP over metal drums, stacked 1, 3, 4, and 5 tiers high (Figure 63). The data fits are very good except for stations over the waste, hence it is difficult to draw any conclusions about the resistivities between 14 and 24 m. We note a resemblance of the anomaly in figures 79 and 80 to that produced by the desks in figure 60b. The sharp edges of the anomalies may be due in part to the pit excavation.

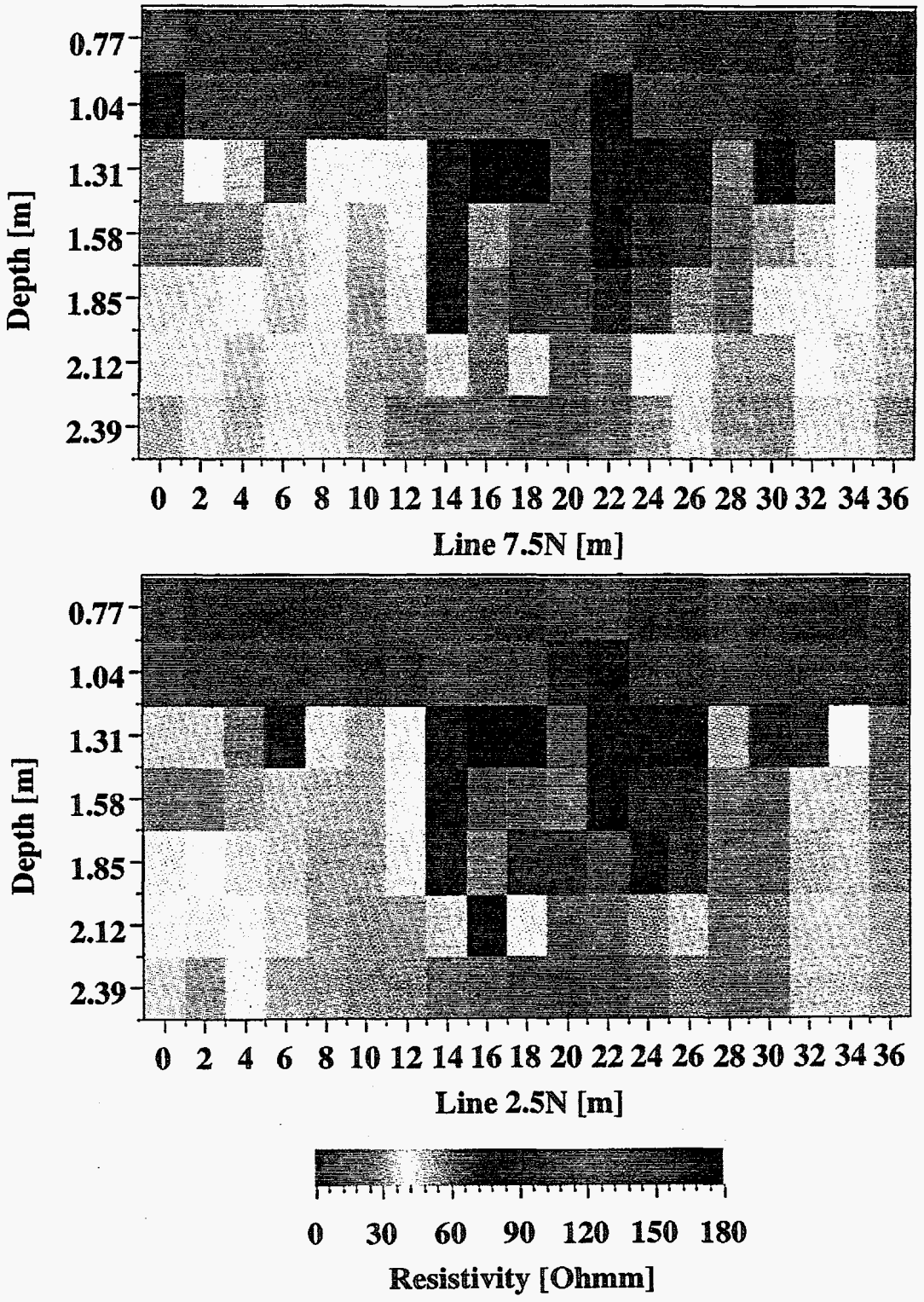

Figure 79. Resistivity depth sections created from piecewise apparent neural network interpretations for the lines 7.5N and 2.5N at the INEL CTP (HF 8 m).

Lines 2.5S and 7.5S, HF 8 m

Figure 80 shows the two resistivity sections of the lines 2.5S and 7.5S crossing the CTP over wooden boxes 2 tiers high filled with metal, asphalt and concrete (Figure 63). Again underneath the resistive cap a conductive anomaly appears in both sections at a depth around 1.85 m and between 15 m and 23 m. This anomaly is due to a bad fit to the data at the lower frequencies.

Line 25S, HF 8 m

The top resistivity section of Figure 81 shows line 25S over wooden boxes similar to the lines shown in Figure 80. The data fits were excellent again until the edges of the actual waste were encountered. The fits for this line, however, are better than those from the previous lines.

Line 40S, HF 8 m

The bottom resistivity section of Figure 81 shows line 40S over two large objects, first a drum stack and then concrete filled steel pipe (Figure 63). A small conductive anomaly shows up between 11 m and 13 m. The data fits are very good for this line.

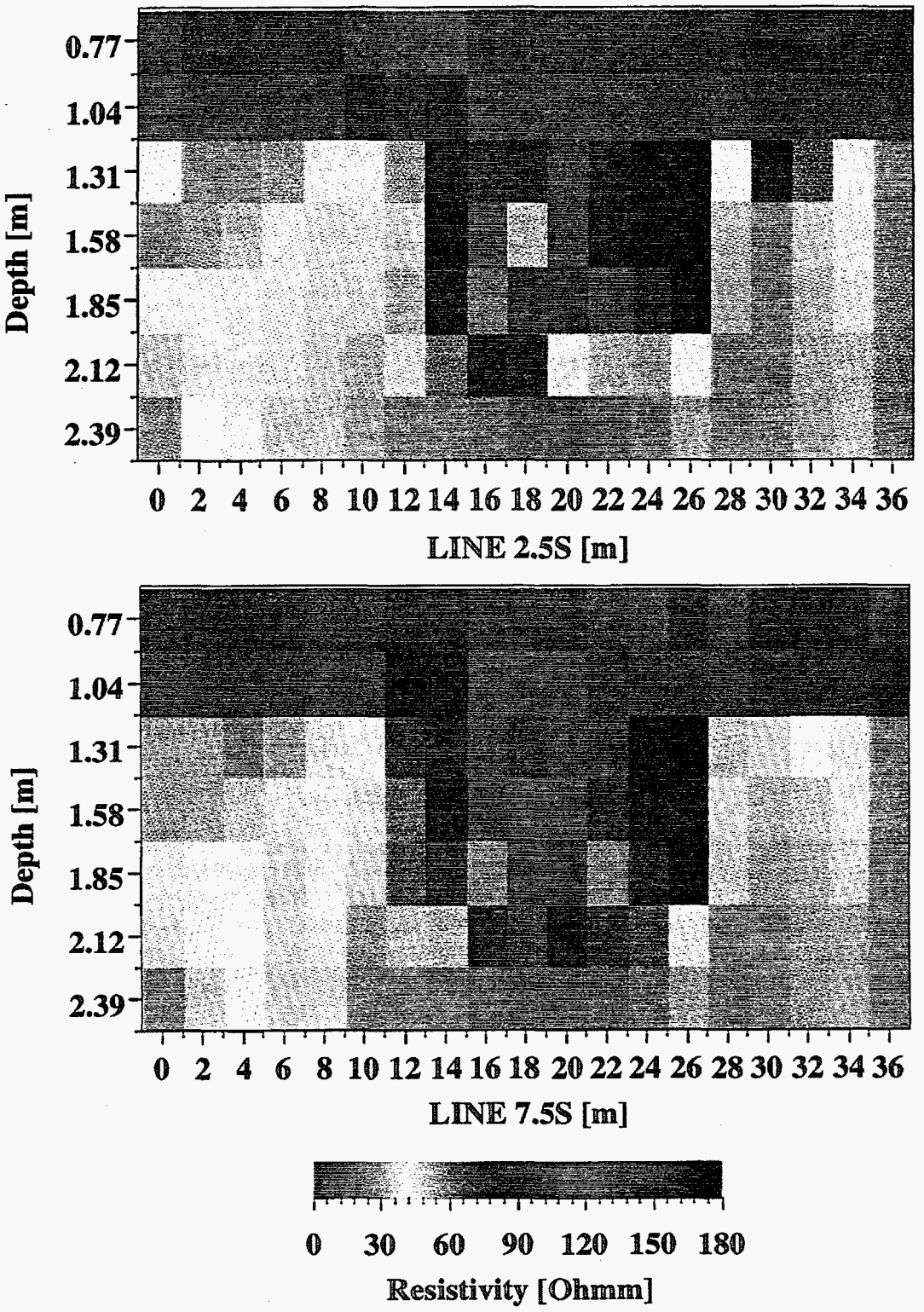

Figure 80. Resistivity depth sections created from piecewise apparent neural network interpretations for the lines 2.5S and 7.5S at the INEL CTP (HF 8 m).

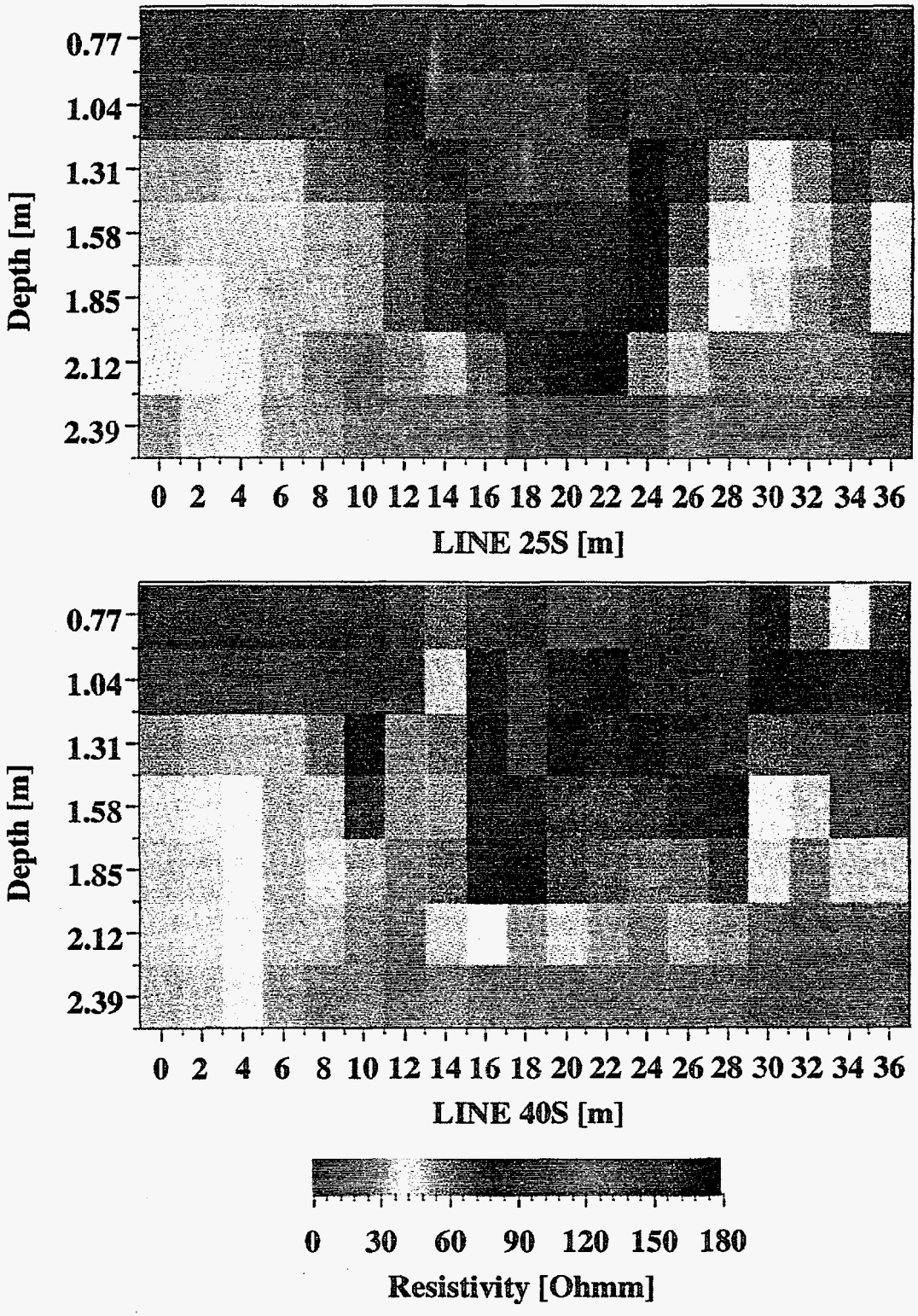

Figure 81. Resistivity depth sections created from piecewise apparent neural network interpretations for the lines 25S and 40S at the INEL CTP (HF 8 m).

Line 55S, HF 8 m

The top resistivity section of Figure 82 shows line 55S over several large objects, crushed drums, a steel tank, drums, and steel casing over concrete vaults (Figure 63). Underneath the resistive cap a large conductive anomaly appears at a depth of 1.31 m between 9 m and 15 m followed by a resistive anomaly. This pattern is very similar to that produced by strongly conductive objects such as the 3 x 5 m aluminum sheet in figure 59. The similarity between the anomalies can also be seen in the ellipticity profile plots in figure 57.

Line 70S, HF 8 m

The bottom resistivity section of Figure 82 shows line 70S, which does not cross any objects (Figure 63). The typical west and east boundaries of the CTP, observed in the other sections do not appear in this section. The piecewise apparent neural networks fit the data well until station 9 m and then failed to fit the rest of the line. If we compare this section to that in figure 83 which is also a background line but away from the pit, we might infer that much of the structure in figure 82 is due perhaps to excavation disturbance.

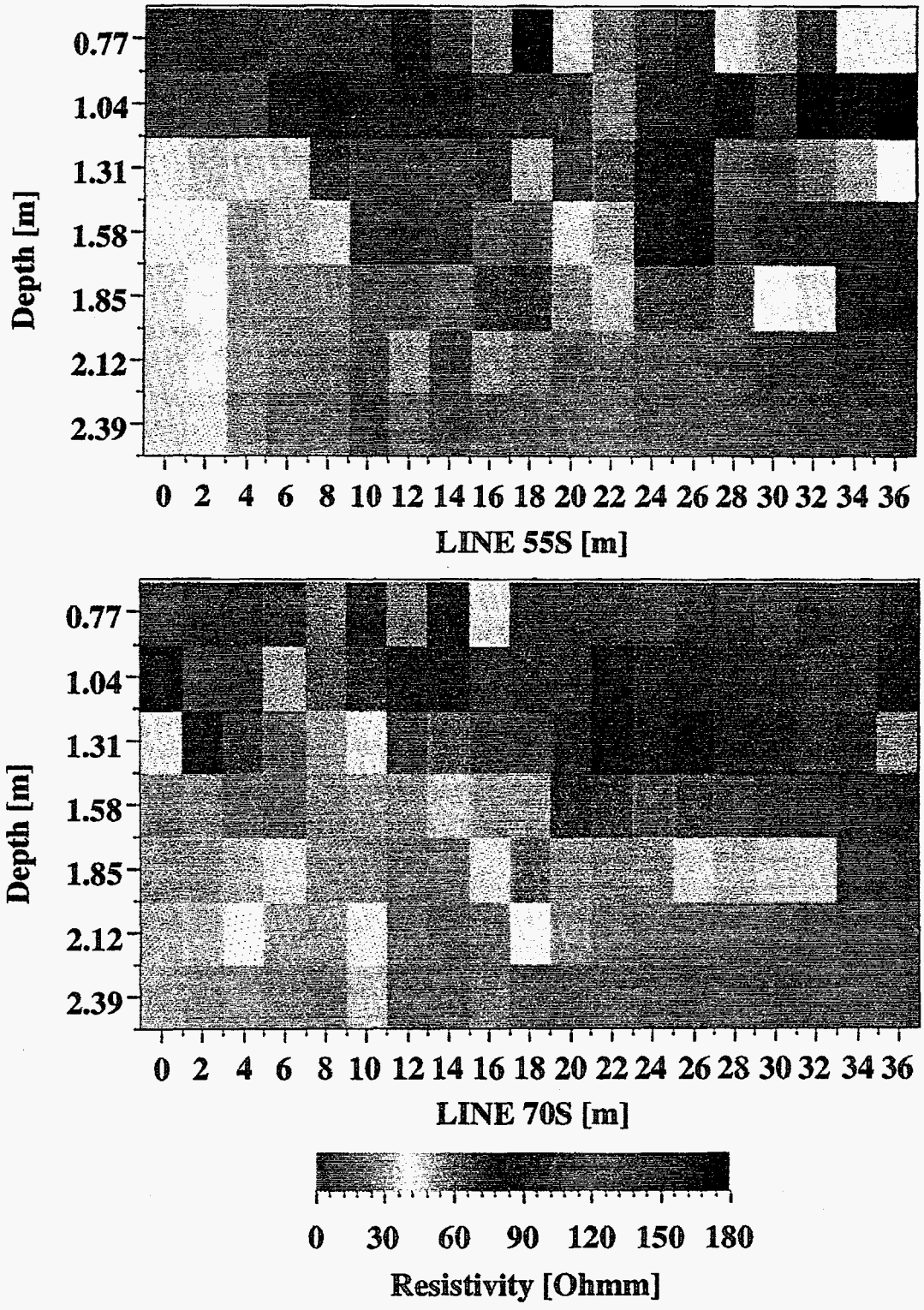

Figure 82. Resistivity depth sections created from piecewise apparent neural network interpretations for the lines 55S and 70S at the INEL CTP (HF 8 m).

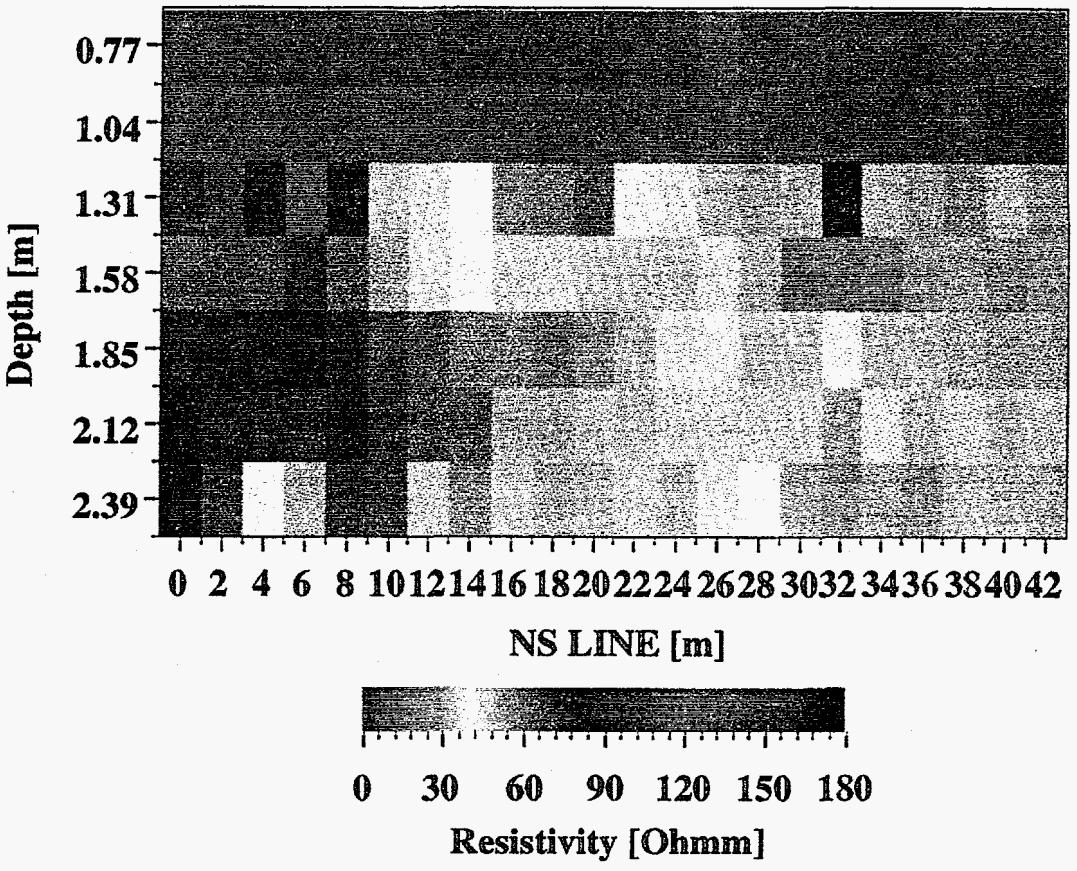

Figure 83. Resistivity depth section created from piecewise apparent neural network interpretations for the NS-line at the INEL CTP (HF 8 m).

Line NS, HF 8 m

Figure 83 shows the resistivity section of the NS line (Figure 63). The excavation extends from station 6 m to 26 m. This section shows a resistive top layer and a slight decrease in resistivity from the north to the south. We cannot determine from one line whether the decrease in resistivity at depth from north to south is due to the natural soil conditions or the excavation. We do not observe a similar resistive anomaly on any other HF 8 m section.

Lines 7.5N and 7.5S, HF 4 m

Figure 84 shows the resistivity sections of the HF 4 m surveys. The resistivity values should be looked at qualitatively and should not be rigorously compared to the HF 8 m or MF sections. A top resistive layer can be identified, outside the CTP going down to 59 cm, while right over the waste between 13.5 m and 24.5 m the resistive cap appears down to 1.01 m. In both sections a conductive anomaly shows up between 15 m and 23 m at a depth of 1.08 m. The conductive anomalies are actually caused by a bad fit to the field data for frequencies 124 kHz and 250 kHz. So, we see resistive cap material to a depth of 1.29 m which is approximately the same depth we observed in the 8 m sections.

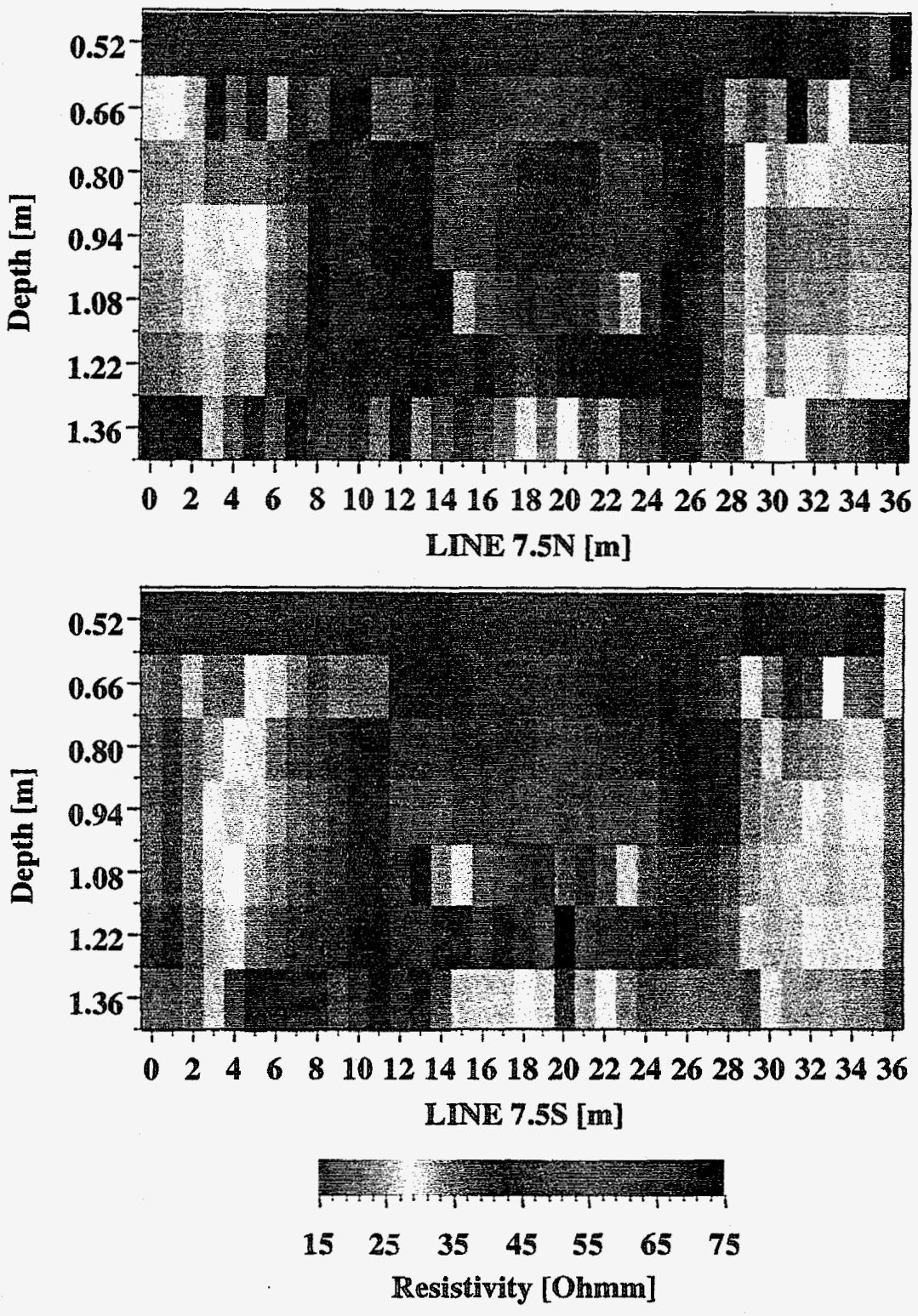

Figure 84. Resistivity depth sections created from piecewise apparent neural network interpretations for the lines 7.5N and 7.5S at the INEL CTP (HF 4 m).

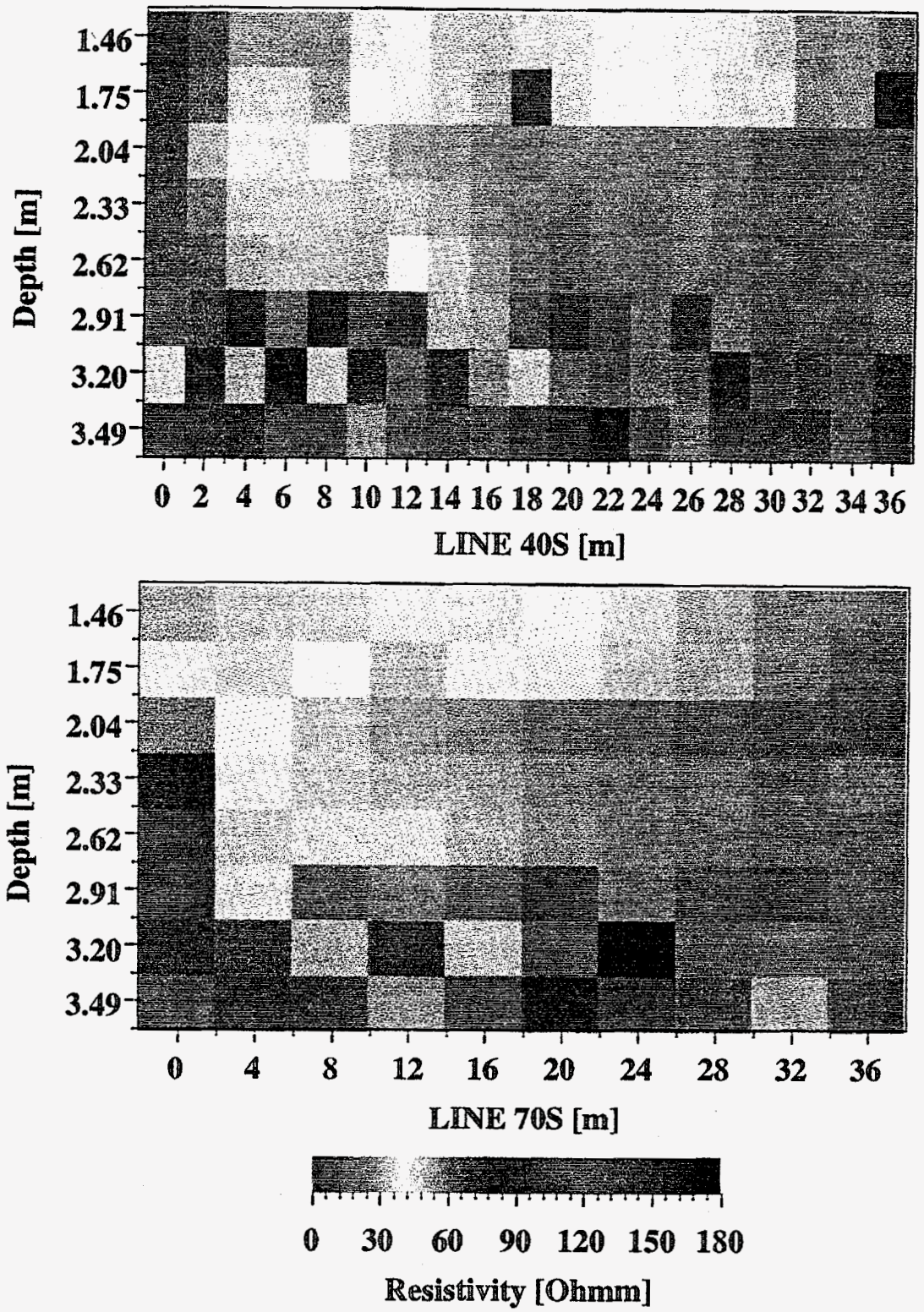

Figure 85. Resistivity depth sections created from piecewise apparent neural network interpretations for the lines 40S and 70S at the INEL CTP (MF 8 m).

Lines 40S and 70S, MF 8 m

The basalt bedrock forms a hill on the south end of the CTP and dips steeply under the test area. We used the MF system at 8 m and 16 m separations to try to determine the depth to bedrock. The MF 8 m data were fit very well by the piecewise apparent resistivity neural networks, suggesting that we could detect only gradational changes with depth (Figure 85). This could mean the bedrock does not have sufficient contrast with the soil to be detected by our system or the depth was greater than 3.3 m.

Lines 40S and 70S, MF 16 m

The MF 16 m data could not be fit by any of the networks, suggesting strong 3D effects. The accuracy of the depth scale in Figure 86 is unknown since the resistivity values on which the depth are based are of dubious accuracy. The ellipticity profiles in Figure 78 clearly show an anomaly at the east end of the survey line. A 3D inversion program may be able to produce a model of bedrock using these data.

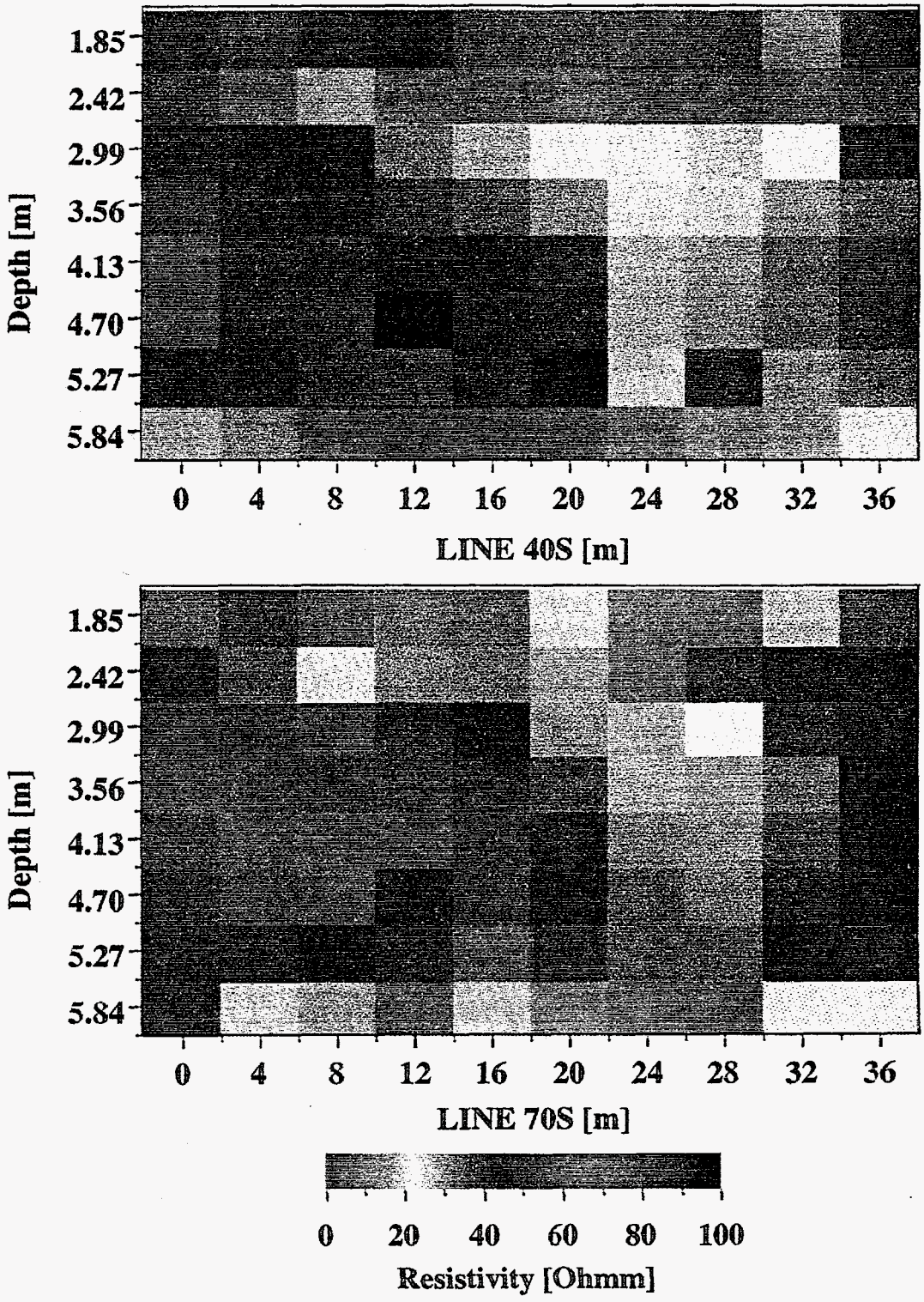

Figure 86. Resistivity depth sections created from piecewise apparent neural network interpretations for the lines 40S and 70S at the INEL CTP (MF 16 m).

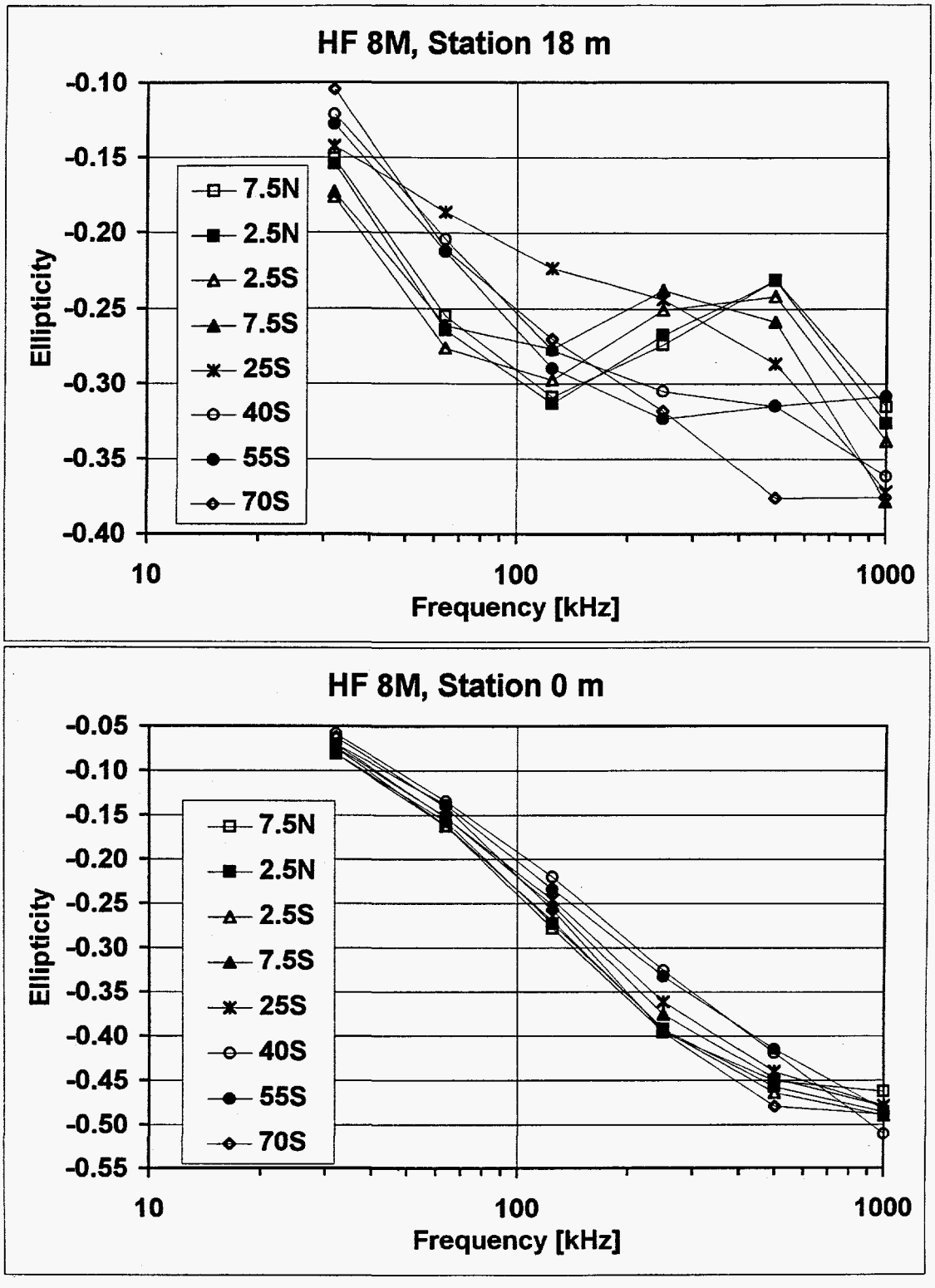

Figure 87. Ellipticity sounding curves plotted for the frequencies 32 kHz to 1 MHz for the stations 18 m (top) and 0 m (bottom) as comparison of all eight surveyed HF 8 m lines.

For HF 8 m ellipticity sounding curves at station 18 m, over the center of the waste, lines 7.5N and 2.5N show similar characteristics to each other (Figure 87); they differ slightly from lines 2.5S and 7.5S which are also similar to each other. Lines 25S, 40S, 55S, and 70S look different from the previous lines. The HF 8 m data is also plotted at station 0 m (40W on local CTP grid) in Figure 87. The ellipticity sounding curves are very different in character for this background station compared to the sounding curves at station 18 m. Note also the different scale for the ellipticity axis in both plots in Figure 87. These differences in sounding curves indicate potential for discriminating waste versus background and type of waste using neural networks.

1D Neural Network Interpretation

The neural network layered-earth interpretations only show good fits to field data in true layered situations; gradational changes in geo-electric properties are better fit by apparent resistivity networks. For the 4 m separation, we did not expect to penetrate substantially beneath the capping material. We tested our two-layer, fixed thickness neural networks on line 7.5S to check our detection of the cap material. We found very good fits to the data with a two layer model away from the waste. An average model for this line was a top layer of 25 ohm-m, 0.6 m thick, and an underlying halfspace of 55 ohm-m material. The dielectric constant of the top layer was nearly always less than 10. Based on training errors in Table 1, we would expect the resistivities to be in error by about 5% and the dielectric constant to be only within 50%. Over the actual waste the fits were poorer but on average were represented by a cap of 40 ohm-m material, 1.6 m deep, overlying a conductive halfspace of 10 to 25 ohm-m.

We also tested the two-layer, fixed thickness nets on 8 m separation data from line 70S. The model fits were quite reasonable but not as good as the first stations on line 7.5S. An average model for the first 10 m of the line was a 35 ohm-m top layer of 3.3 m thickness over a halfspace of 200 ohm-m. The field data could not be fit by any 1D model further along line. The networks were also tested on the north-south line in an attempt to corroborate the models from line 70S. The data fits were rather inconsistent along the north-south line but had in common a 40 ohm-m top layer of approximately 2.5 to 3.5 m thickness over a resistive halfspace in excess of 100 ohm-m.

1D Inversions

We verified the neural network estimates of resistivity by using a 1D inversion program to invert the ellipticities to piecewise apparent resistivities and layered-earth resistivity models.

The piecewise apparent resistivity 1D inversions lead to resistivity sections showing the same structures observed with the piecewise apparent neural networks and described above, with two main differences which are illustrated by Figure 88. The top resistivity section shows the piecewise apparent resistivity 1D inversion results for the line 2.5S (HF, 8 m) and the bottom section the results for line 40S (HF, 8 m). Compared to the

bottom section of Figure 79 the two main differences for line 2.5N are a lower cap resistivity and no shallow conductive anomaly inside the waste area right beneath the cap. The inversion results show no resistivity difference between the surficial layer and the cap material right over the waste, except a small resistive anomaly over the waste (Figure 88). The conductive features are very similar, except that the inversion shows the waste starting at a depth of 2.12 m +/- 0.135 m instead of shallower. The bottom section of Figure 81 shows the neural network equivalent result to the bottom resistivity section in Figure 88. The conductive structure correspond very well, except an anomalous area at the east end of the line which both show a resistive feature at a depth of 1.04 m between stations 32 m and 36 m and differences beneath. Again the comparison shows that the piecewise apparent inversion results see a more uniform surficial-cap top layer, while the piecewise apparent neural network results show a little less resistive cap beneath a resistive surficial layer.

Two-layer and three-layer 1D inversions were performed for each sounding with at least two different starting models, a generic one (e.g. 100 ohm-m 1 m thick over 100 ohm-m) and one derived from the 1D piecewise apparent resistivity interpretations as shown in Figures 79 to 86. The number of frequencies used to invert the data sets was also varied. The goal of the inversions was to verify the multilayer cases appearing in the resistivity sections and to determine a more precise thickness of the resistive top layer. However, the thicknesses and resistivities are varying so much that it was impossible to generate resistivity sections from the inversion results.

The two-layer inversions did not converge to a resistive over conductive earth outside the CTP area, the most common result was a 1 to 10 ohm-m top layer over a 50 to 70 ohm-m second layer. The thickness of the top layer varied from very thin (0.01 m) to 100 m, in either case the boundaries given for the inversions were reached and not meaningful. It appears that the data outside the waste pit were not able to be fit by any two-layer 1D earth models when the dielectric constant was not included as a parameter. However, the soundings over the waste showed a significant difference. The inversions for those stations converged to a resistive 30 to 60 ohm-m top layer over a conductive 2 to 20 ohm-m layer. The thickness of the top layer varied strongly within each line, but overall a thickness of 2 to 4 m was observed. By following the inversion results along a line, it is easy to determine where the boundaries of the waste occur.

The three-layer inversions show a more realistic picture of the survey area, at least with regard to the resistivities. For all stations outside and over the waste the inversion results showed a conductive (2 to 15 ohm-m) thin top layer (1 to 30 cm) over a second layer with highly varying resistivity (hundreds to thousands of ohm-m) with a thickness from 2 to 4 m. The third layer, however, shows significant differences between the areas outside the waste and over the waste. Stations over the waste invert to a conductive (3 to 15 ohm-m) third layer while stations outside the waste show varying resistivities from 15 to 80 ohm-m. The areas where one coil is over the waste and the other outside the waste area show an average resistivity of around 15 ohm-m. The very conductive third layer over the waste indicates that the bottom of the waste can not

be resolved, as already discussed for the piecewise apparent resistivity neural network interpretation above. Overall, the three-layer inversion gives much more realistic resistivity models, however the thicknesses, especially for the resistive second layer, which might be identified with the cap, seem to be to high by at least a factor of 2. So, the resistivity interpretation with inversions are influenced by the 3D effects as well as the layered-earth neural network interpretations.

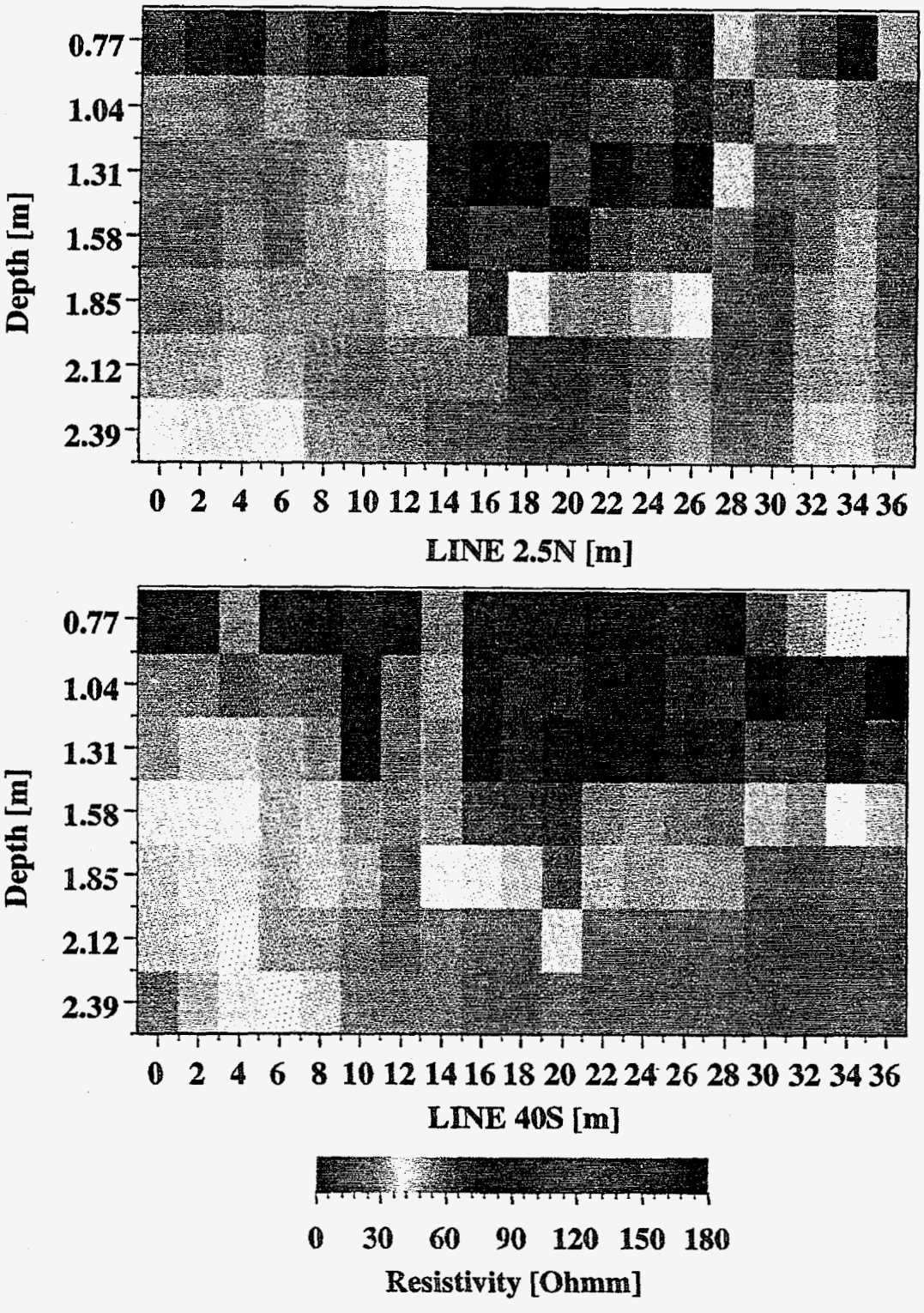

Figure 88. Resistivity depth sections created from piecewise apparent inversion interpretations for the lines 2.5S and 40S at the INEL CTP (HF 8 m).

It seems that the thickness calculated by the depth of investigation algorithm coupled with two-layer fixed thickness nets with dielectric constant give the most realistic depth structure in combination with the piecewise apparent resistivity neural network results.

Neural Network Classifications

The differences in sounding curves for stations moving over the conductive targets and away from them (background) and differences in figure 87 led us to believe that a neural network could learn the characteristics of sounding curves collected over a specific target and classify each station as representing target or background. We further believed that a network could distinguish categories of signatures that might correlate with general waste types.

For the Avra Valley data, a neural network was trained to classify target versus background using ellipticities from 11 frequencies as input and a value of +/- 1 for output (+1 = target, -1 = background). The training set was created based on examining sounding curves along a profile and ellipticity profile plots for each frequency. As an example we would classify the stations from x = -3 m to x = 3 m in figure 57 as being in the target class, while the remaining stations would be classified as background. There are two exceptions, the stations at x = 4 m and x = -4 m are left out of the training set, because of their intermediate nature. One important parameter is the coil separation of the actual survey, because sounding curves are assigned to a location corresponding to the centerpoint between transmitter and receiver. Therefore the soundings are affected by the target at least half a separation away from the target, meaning that for a survey with a 4 m antenna separation, a small target could be classified as up to 2 m wider one either side. The classification results have to be corrected accordingly.

For the CTP data, we used 168 soundings from the HF 8 m surveys and established training classes based on the base map provided us at the time of the survey (Figure 63). Stations 12 through 24 were classified as being waste and stations outside this range were categorized as background. The NS line and line 70S were entirely background. All of the NS line was used for testing along with eight other randomly selected stations. A radial basis function network was trained using ellipticities from 11 frequencies as input and a value of + / - 1 for output (+1 = waste, -1=background). Fifty radial basis functions were used in the classification layer and a hidden layer with four nodes was placed between the classification and output layers. The classification layer was trained for 4,860 iterations and the hidden and output layers were trained for 25,140 iterations once the classification layer was trained. The RMS error for the 134 training samples was 0.2181 at the conclusion of training. Classification rates of 0.9986 and 1.0 were achieved for the background and waste classes. Only one station was misclassified; the station was on the edge of the waste on line 7.5S and was classified as waste when we identified it as background. Only one station in the test set was misclassified, station 5 on line 40S was very weakly classified as waste when it was labeled background. Figure 89 shows a map of the network results. Since the networks

produce continuous values from -1 to +1 we can judge the confidence of the classification based on how close each pixel is to the desired class value. In other words, we have a lot of confidence in pixels that are black or white and less confidence in the pixels that are lighter or darker than the rest of those in their class. The map in Figure 89 is scaled in meters with the upper left corner representing station 40W, Line 7.5N in the local CTP coordinate system.

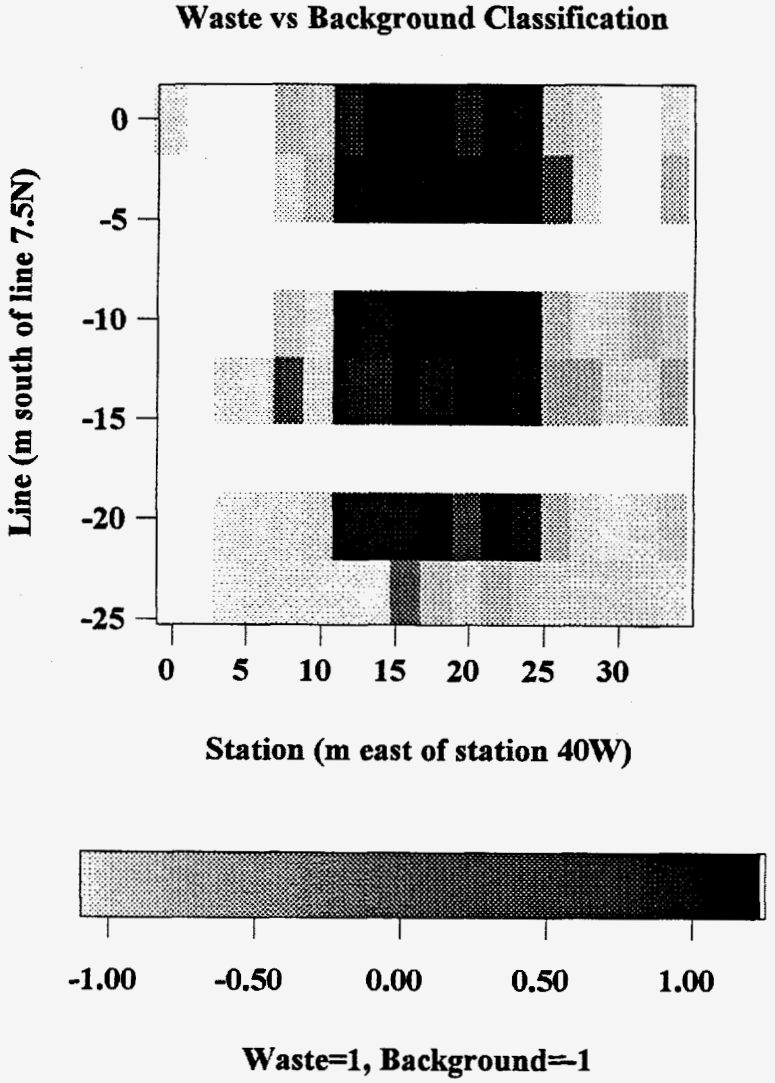

Figure 89. Classification map of waste versus background from a neural network. Values near -1 represent background, values near +1 represent waste.

We used data from both sites to test our ability to extrapolate from one site to the other, we trained separate networks with data from each site and then tested each network with the data from the other site. Each network could classify data from its training site with near perfect accuracy but could only classify data from the other site with 60% accuracy. There was not enough commonality in ellipticity signatures to account for all the variations at each site. The next step involved combining some training data from each site and then testing on data from both sites. The neural network was now able to accurately classify nearly 100% of the data from both sites. As data are collected at more sites and added to the training set, the robustness of the classification should continue to improve.

With the data easily classified as target or waste the next step was to try to distinguish between types of waste. This could only be accomplished with the a priori knowledge provided by the map in Figure 63. We have no information regarding the accuracy of the map. Station locations were compared to the map and labeled as one of five categories: background, drums, boxes, crushed drums, and pipes. A radial basis function similar in design to the one described above was trained on 137 samples for 30,000 iterations. Seven stations were randomly withdrawn for testing. In the training set, five stations that were labeled as being over drums were misclassified instead as background. In the test set, two stations over boxes were misclassified as background (Figure 90). This labeled classification procedure indicates areas of similar signatures rather than waste type itself. If the ellipticity sounding curves were not similar in each of the categories, then the classification could not be accomplished. Features other than waste type, however, could account for the similarities (such as depth, fill material, cap characteristics, etc.).

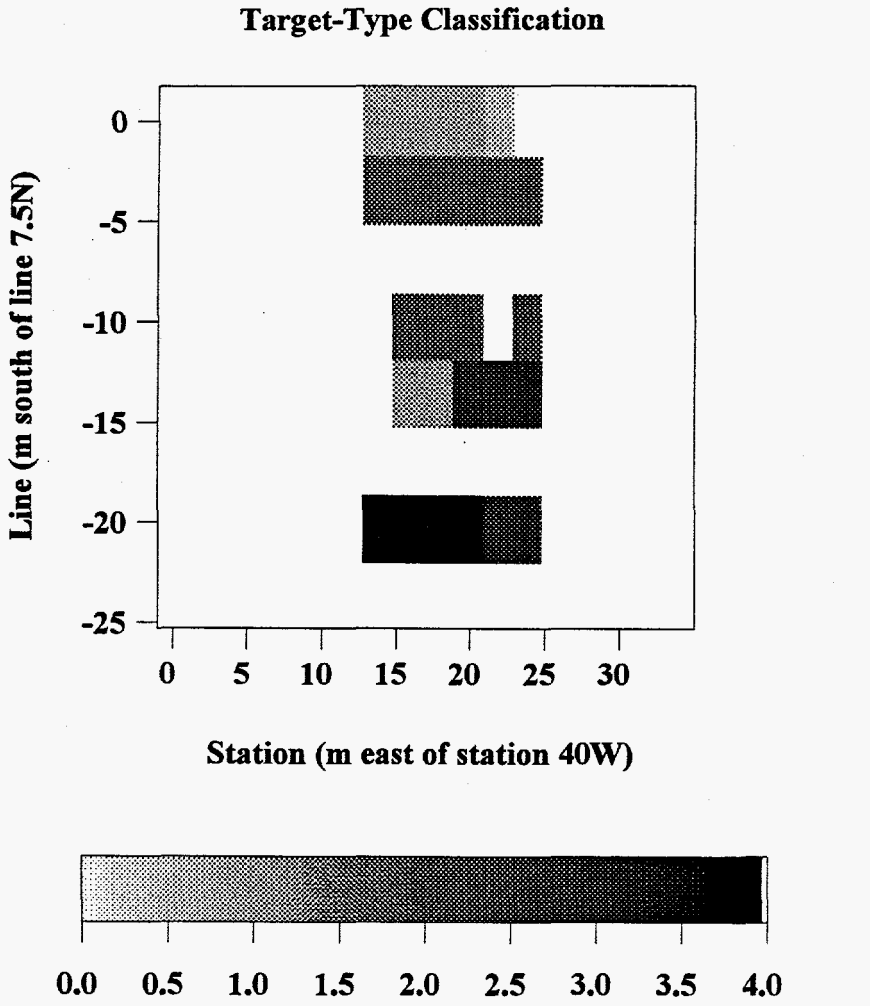

Figure 90. Classification map of waste type from a neural network.

IDAHO NATIONAL ENGINEERING LABORATORY ACID-PIT SURVEY

Background

We conducted a second survey at the Idaho National Engineering Laboratory (INEL) near Idaho Falls, Idaho from December 3, 1996 to December 10, 1996. The weather during much of this survey was severe and temperatures were below 0° F at times. We found that the conduit cables on the receiver and transmitter coils fractured in the extreme cold. We had been able to operate with no problems due to cold during the previous INEL survey, when temperatures were around freezing. As a result of these problems, many of the frequencies were not operational during this survey. For those frequencies that were operational, we obtained excellent data.

Location

The survey was conducted at the Radioactive Waste Management Complex (RWMC) at INEL. The location of INEL is shown in Figure 91 and the location of the RWMC and the acid pit are shown in Figure 92 (Jorgensen et al., 1994). This site is a high-security area. Up to one-half of each field day was spent getting through security, being scanned for radiation, and making arrangements for escorts.

Figure 93 shows the location of our survey lines. The rectangular area outlined by the survey flag symbols is the approximate location of the acid pit. The station spacing for all lines was 2 meters and the line spacing was 4 meters. For all the measurements, the transmitter was on the west, the receiver was on the east, and the survey was run from west to east. The plotting point for the measured data was always at the midpoint of the array. This map also shows the locations of wells, roads, and other surface features. The acid pit boundaries extended from approximately 16 N to 16 S and from 26 E to 86 E. Within these boundaries, acid containing radioactive materials and other contaminants had been dumped into the soil. The precise location of the contaminants is not well known. Our survey at this site was intended to be an operational survey which would help in the remediation of the site as well as demonstrate the capabilities of the system.

Figure 94 shows a photograph of the site with our receiver ATV on one of the survey lines. The site contains some areas with surface radioactivity as shown by the sign in the foreground. The site is flat except for some berms near the ends of the survey lines.

We ran one line through the middle of the survey area (the line labeled 0 or L4 on Figure 93) with the MF system and a coil spacing of 16 m. We then ran 7 lines using the HF system, all at a coil spacing of 8 m.

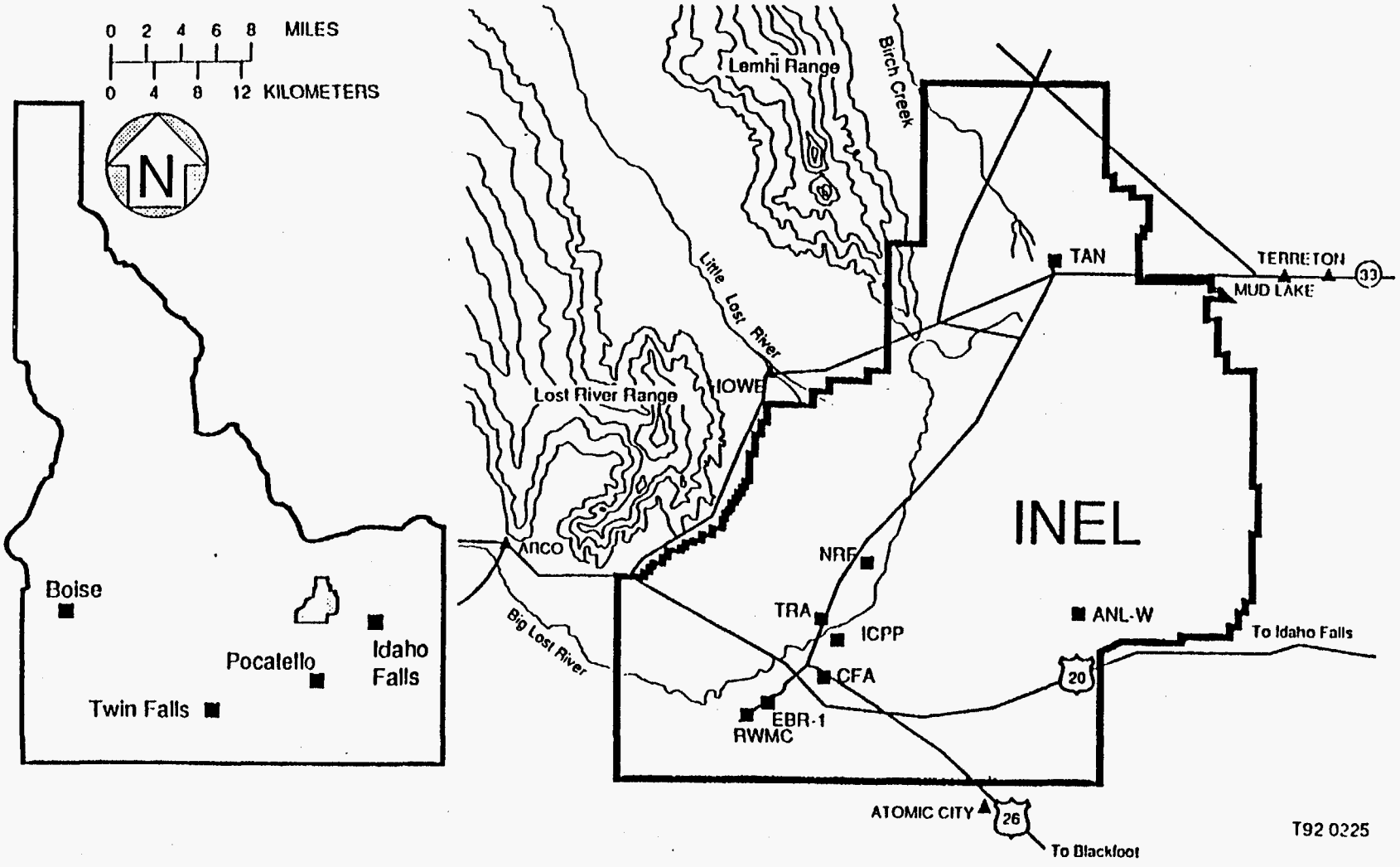

Figure 91. Location map of INEL (Jorgensen et al., 1994).

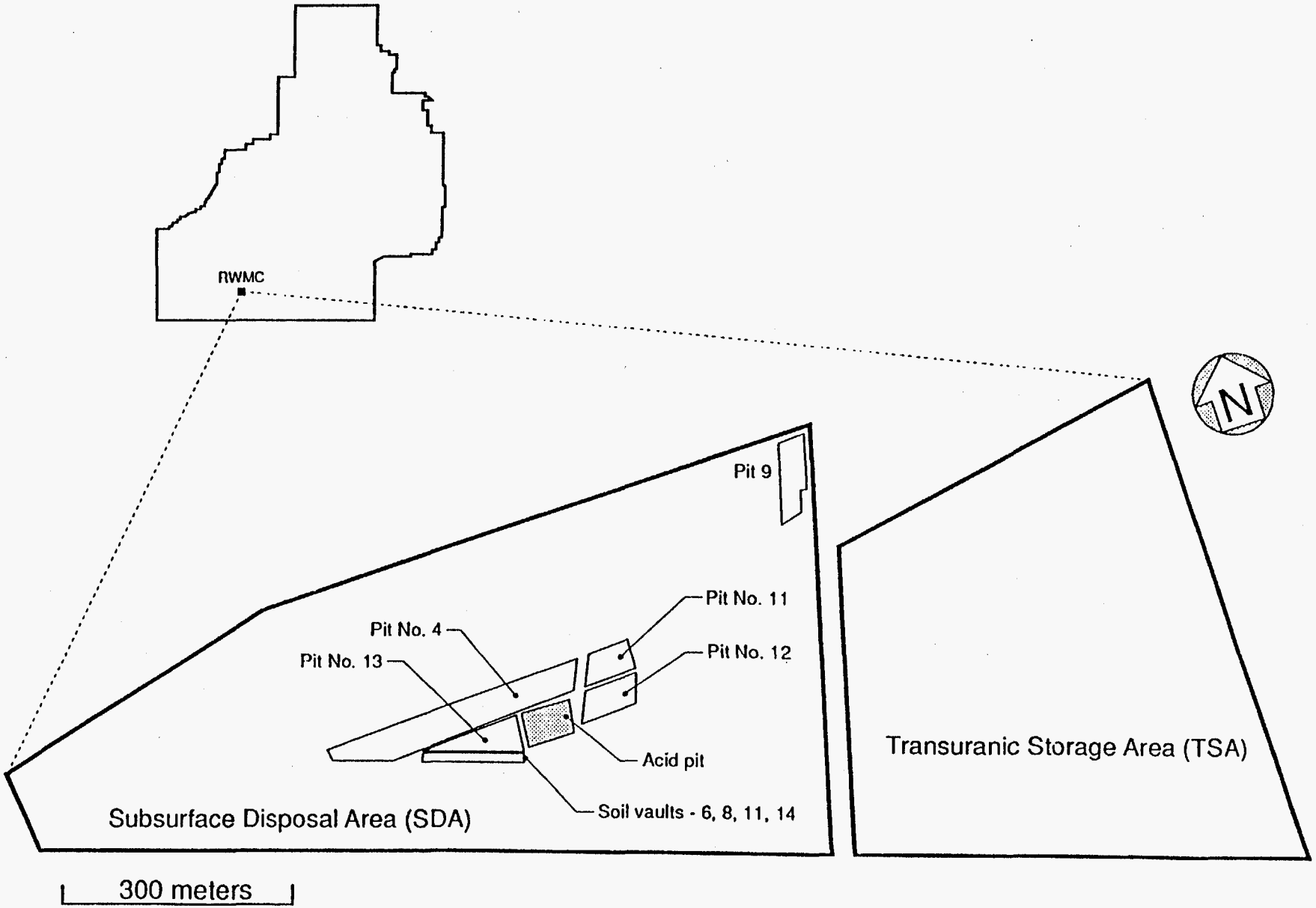

Figure 92. Location map of the RWMC and the Acid Pit (Jorgensen et al., 1994).

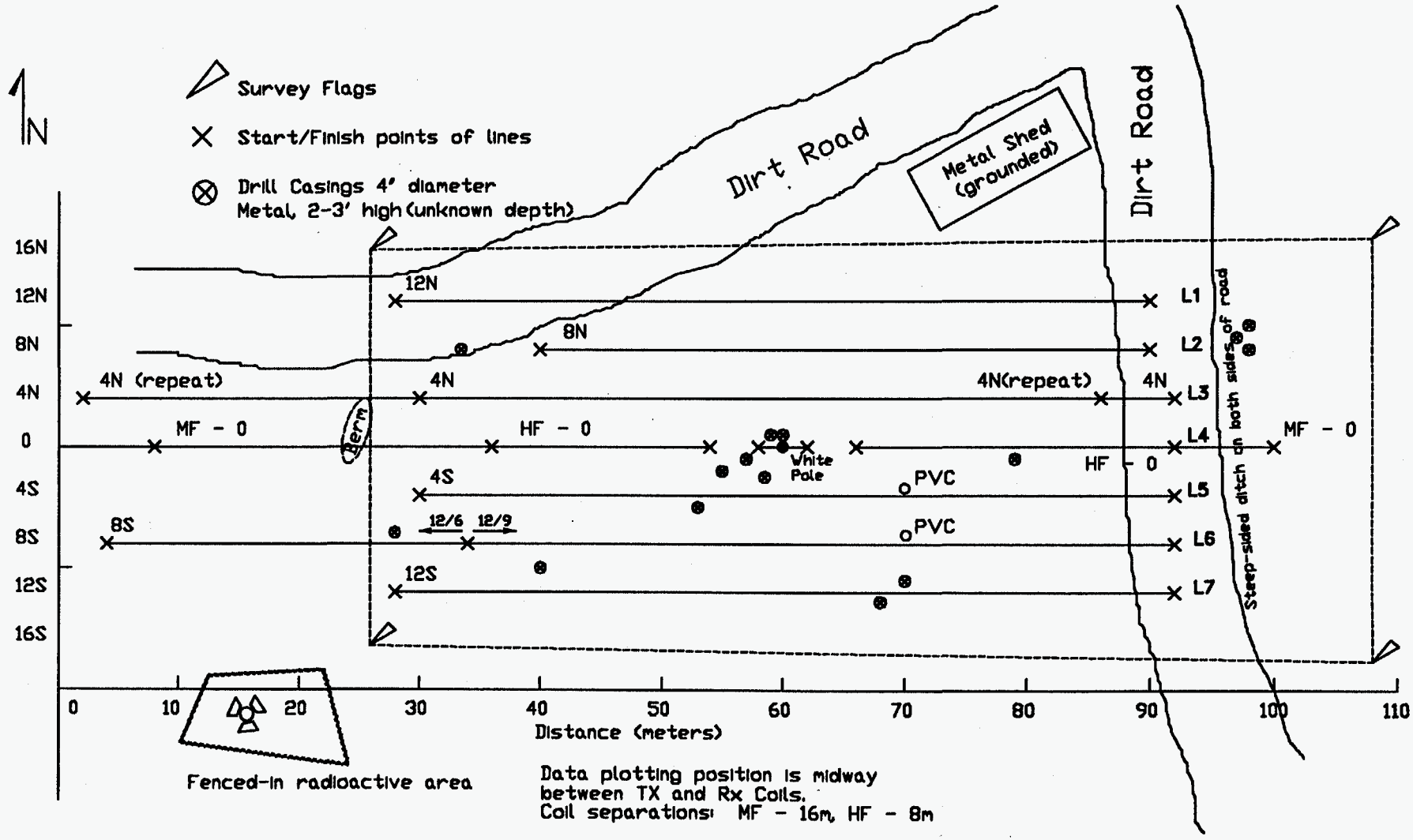

Figure 93. Survey-line locations and surface-features map.

Figure 94. Photograph of the Acid Pit survey area and the receiver ATV on a survey line.

MF, 16 m Results

Our initial line used the MF (1 kHz to 1 MHz) system at a 16 m coil separation and 2 m station spacing. Because of the instrumentation problems related to the sub-zero temperatures, we were only able to obtain one high-quality frequency - - 250 kHz. Figure 95 shows the ellipticity data for this line. The distance scale on this plot corresponds to the distance scale on the location map in Figure 93.

Figure 96 shows halfspace inversion results corresponding to the ellipticity data in Figure 95. A homogeneous half space resistivity (or apparent resistivity) was determined which matched the ellipticity value at each profile location. The apparent resistivities vary from 5 to 10 ohm-m over the center of the pit area and 25 to 30 ohm-m over the eastern part of the profile line. The depth of investigation for these measurements was determined using the method described in Thomas (1996). For a frequency of 250 kHz, for a coil separation of 16 m, and for the range of resistivities shown on Figure 96, the depth of investigation varies from 1.5 to 3 m.

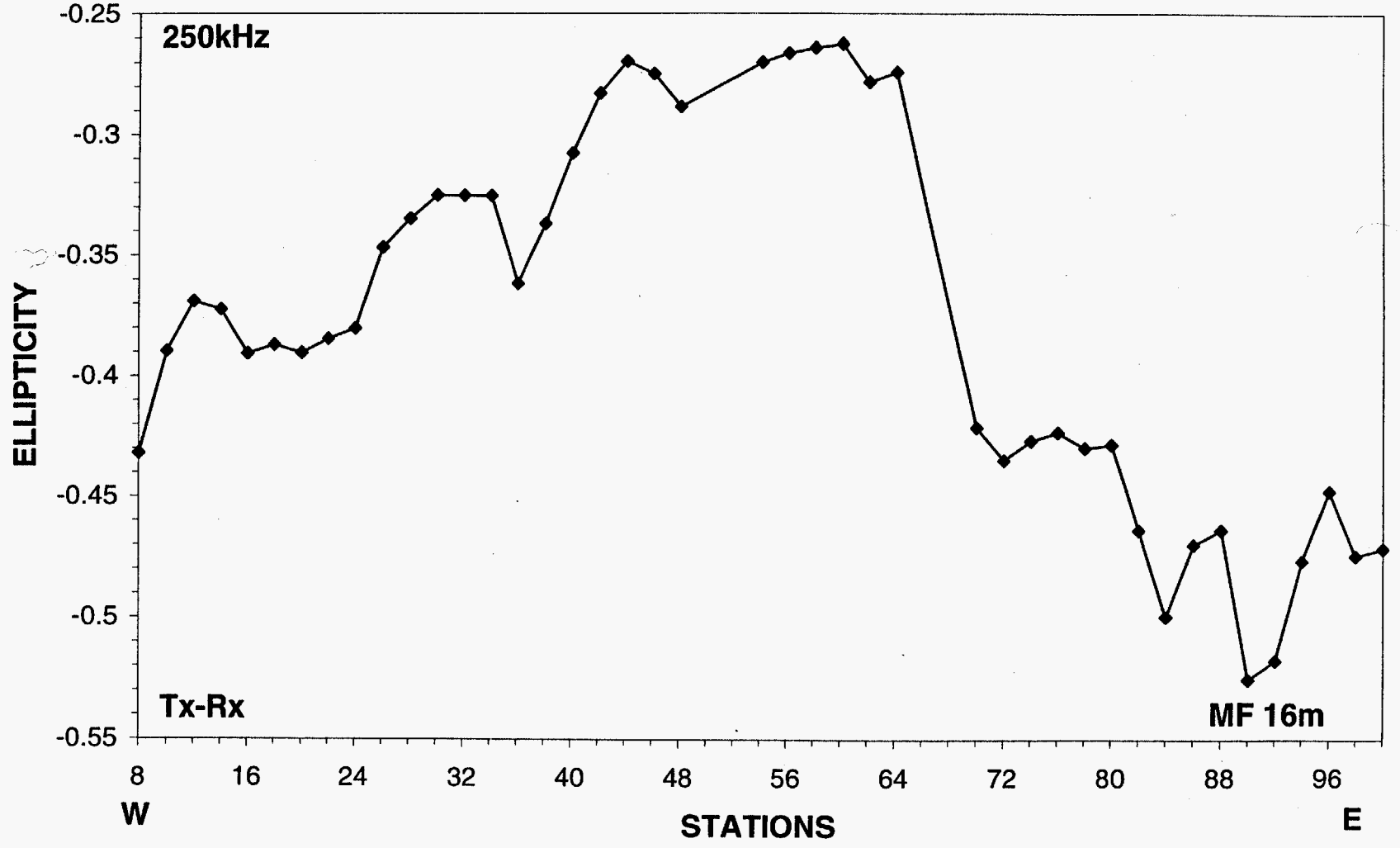

Figure 95. Ellipticity data for the MF system, 16 m coil spacing, 250 kHz center-line.

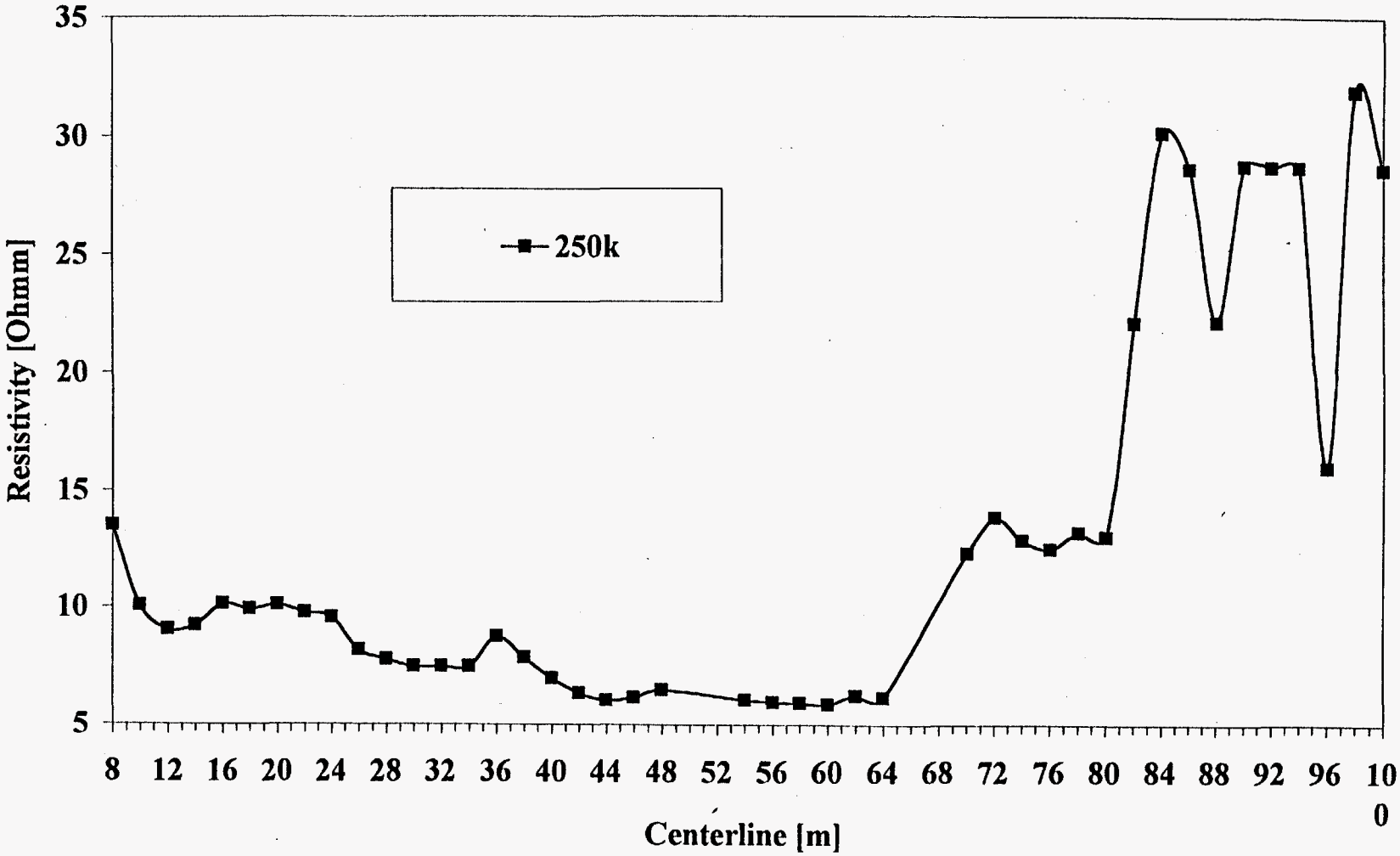

Figure 96. Apparent-resistivity data corresponding to the MF, 16 m, 250 kHz ellipticity data in Figure 95. Depth of investigation for this frequency, spacing, and range of resistivities is approximately 1.5 - 3 m.

HF, 8 m Results

We surveyed a total of 7 lines using the HF system (31 kHz to 32 MHz) with a coil separation of 8 m and a 2 m station spacing. Because of the instrumentation problems related to the sub-zero temperatures, we were only able to obtain two high-quality frequencies - - 62 kHz and 500 kHz. Figures 97 and 98 show the contoured ellipticity values for 62 kHz and 500 kHz respectively. Both frequencies outline an anomalous area near the center of the pit boundaries. The 62 kHz map shows more-negative ellipticities over this anomaly and the 500 kHz map shows less-negative ellipticities over this anomaly.

Figure 99 shows the repeatability of the 62 kHz data. The second data set was collected one day after the first. The major features on this profile repeat very well.

Figure 100 shows the apparent resistivity map corresponding to the ellipticity data in Figure 97. A low-resistivity zone (20-30 ohm-m) occurs near the center of the acid-pit region, but offset somewhat to the south. The surrounding (background) resistivities are in the 40 to 50 ohm-m range. The low apparent resistivities in this central region are interpreted as being caused by the presence of contaminants, including heavy metals and the acid plume. The low apparent resistivities on the western end of the survey area are probably due to solid waste in an adjacent cell. The low apparent resistivities on the eastern end of the survey area are probably due to buried utilities adjacent to the road. The depth of investigation for 62 kHz and 8 m spacing and the range of resistivities shown on this map varies from 2 to 2.5 m.

Converting the 500 kHz ellipticity data to apparent resistivities presented some unanticipated complications. Figure 101 shows our initial attempt at inverting these data. A starting point of 100 ohm-m was used for the inversion. The resistivity anomaly shown in the center of this map is a high-resistivity anomaly. This high-resistivity anomaly occurs where the 62 kHz map showed a low-resistivity anomaly. Furthermore, the resistivities on this map are completely unrealistic. We would not expect resistivities well above 100 ohm-m in these soils based on other measurements of electrical properties at this site.

Figure 102 shows plots of ellipticity versus resistivity for a homogeneous half space. For 62 kHz there is no ambiguity in the selection of the appropriate resistivity. Over a reasonable range of resistivities, there is only one resistivity corresponding to a measured ellipticity. For 500 kHz, there are two reasonable resistivities that could correspond to a measured ellipticity. The map in Figure 101 used resistivities from the high-resistivity branch (right-hand side) of Figure 102.

Figure 103 shows an apparent resistivity map that used resistivity values from the low-resistivity branch (left-hand side) of Figure 102. This map is in general agreement with the 62 kHz map in Figure 100. Furthermore, the resistivities are reasonable, when

compared with the MF line results (Figure 96), which had an unambiguous resistivity determined by the measured ellipticity. We therefore use this map as our best estimate of the 500 kHz resistivity. The high resistivities at the north and east sides of this map may actually cross into the high-resistivity branch region. We would need more frequencies and or more coil spacings to resolve this ambiguity. Normally, when we record all 11 frequencies and use multiple spacings with our system, the point at which we cross from one branch to another is evident.

The depth of investigation corresponding to 500 kHz, 8 m spacing, and the interpreted range of resistivities is 0.5 to 1.5 m. A low-resistivity zone (2.5-3.5 ohm-m) occurs near the center of the acid-pit region, in the same region as the 62 kHz low-resistivity anomaly. The surrounding (background) resistivities are in the 5 to 10 ohm-m range but could be a bit higher as described in the previous paragraph. The low apparent resistivities in this central region are interpreted as being caused by the presence of contaminants, including heavy metals and the acid plume. The resistivities at 500 kHz are even lower than the resistivities at 62 kHz. This indicates that the contamination may be greater at shallow depths. The low apparent resistivities on the western end of the survey area are again interpreted as being due to solid waste in an adjacent cell. We also see low apparent resistivities on the eastern end of the survey area which are presumably due to buried utilities adjacent to the road.

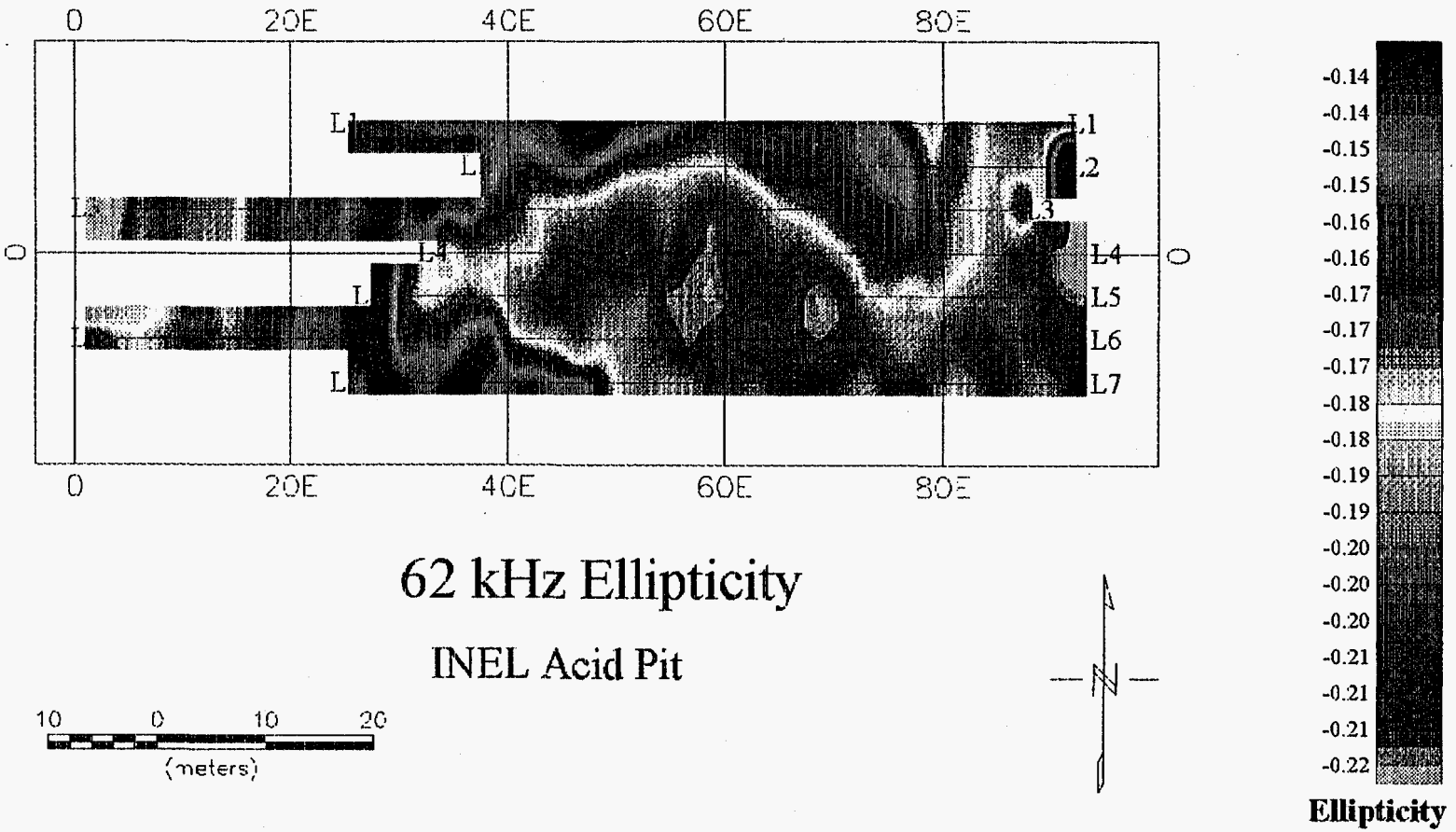

Figure 97. Contoured ellipticity values for the 7 lines of 62 kHz data.

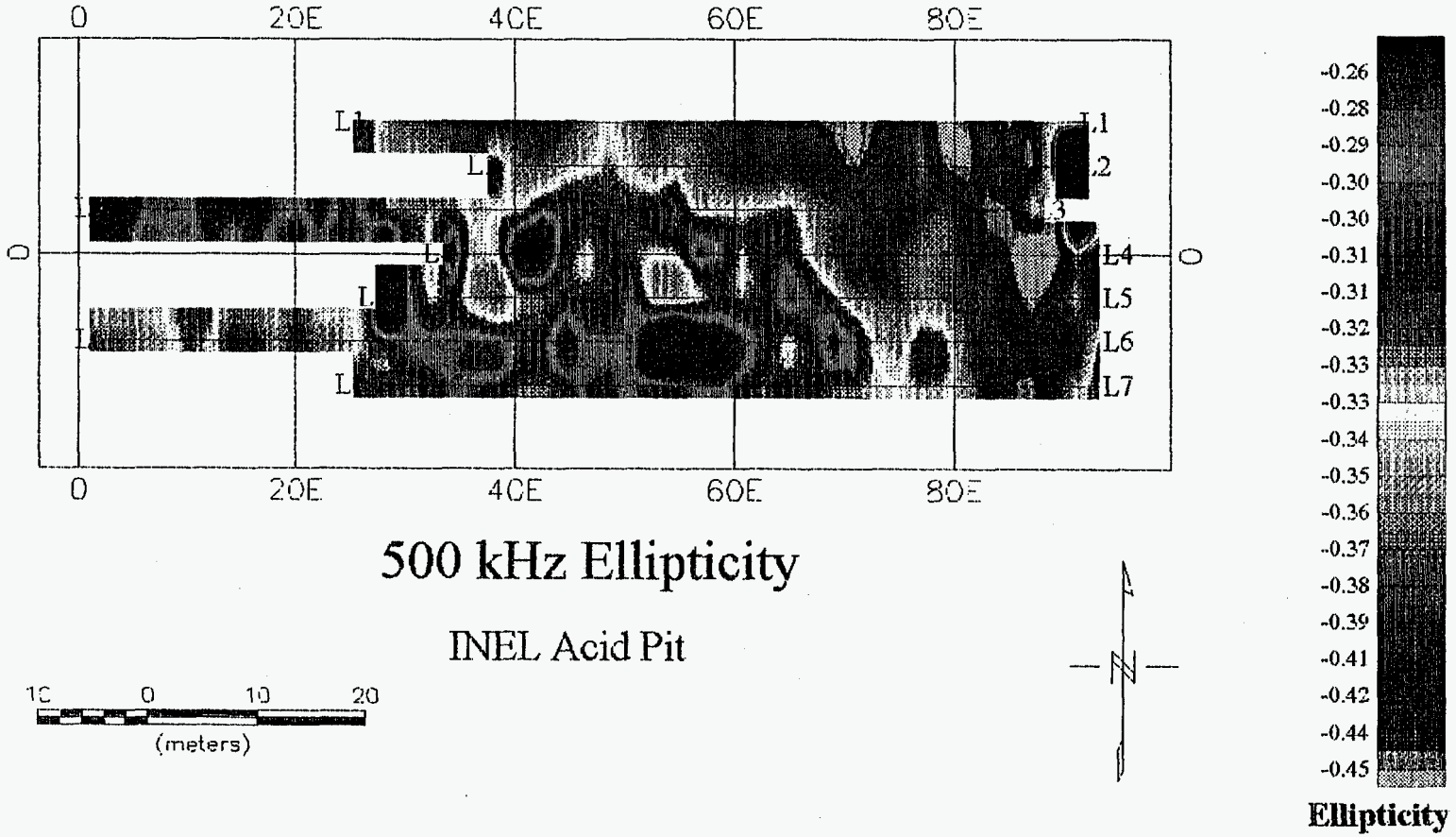

Figure 98. Contoured ellipticity values for the 7 lines of 500 kHz data.

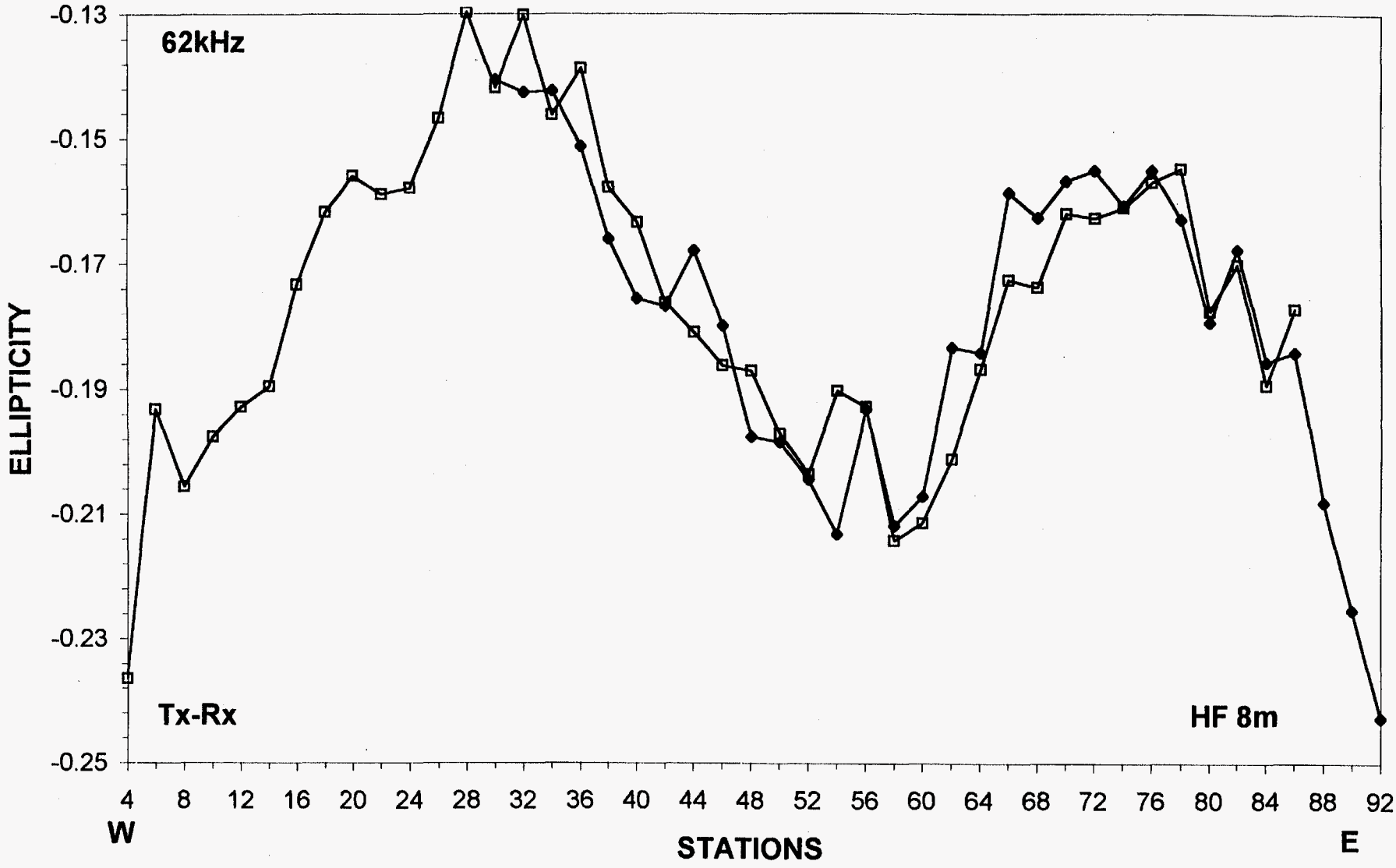

Figure 99. Repeat 62 kHz data. The data shown by square symbols were taken one day later than the data shown by closed diamonds.

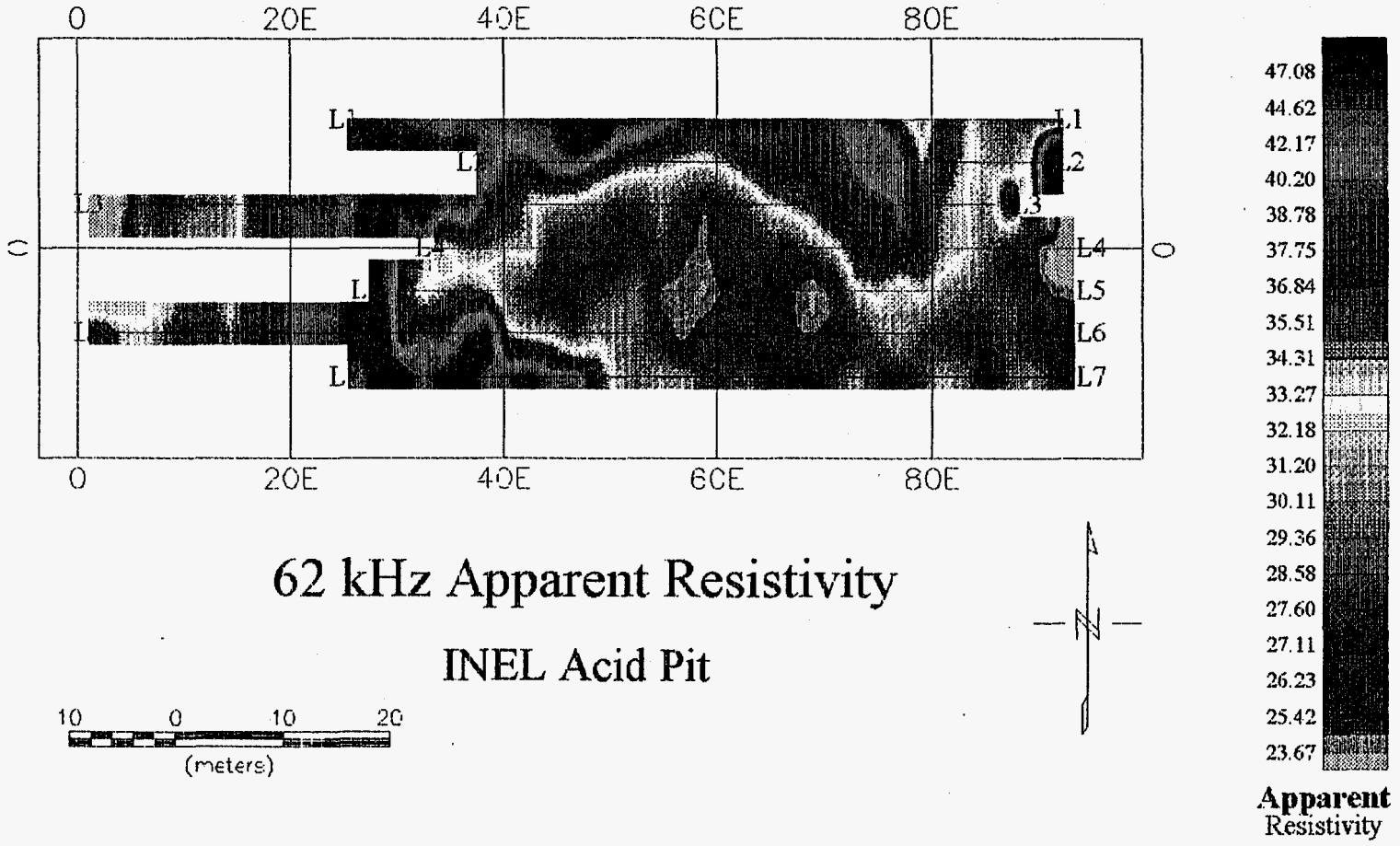

Figure 100. Contoured 62 kHz apparent-resistivity data corresponding to the ellipticity data in Figure 97. Depth of investigation for this frequency, spacing, and range of resistivities is approximately 2 - 2.5 m.

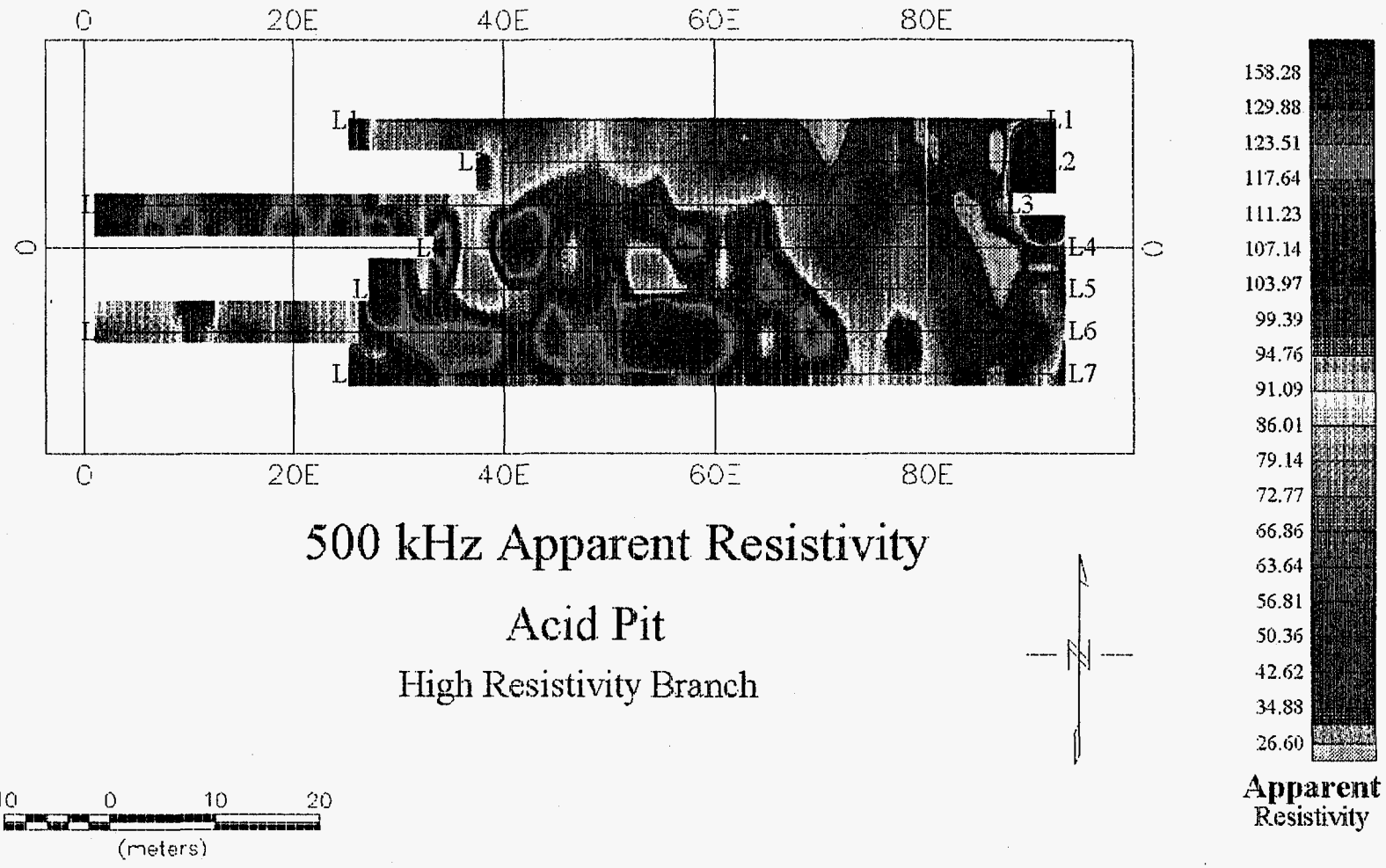

Figure 101. Contoured 500 kHz apparent-resistivity data corresponding to the ellipticity data in Figure 98. See text for explanation of "high-resistivity branch."

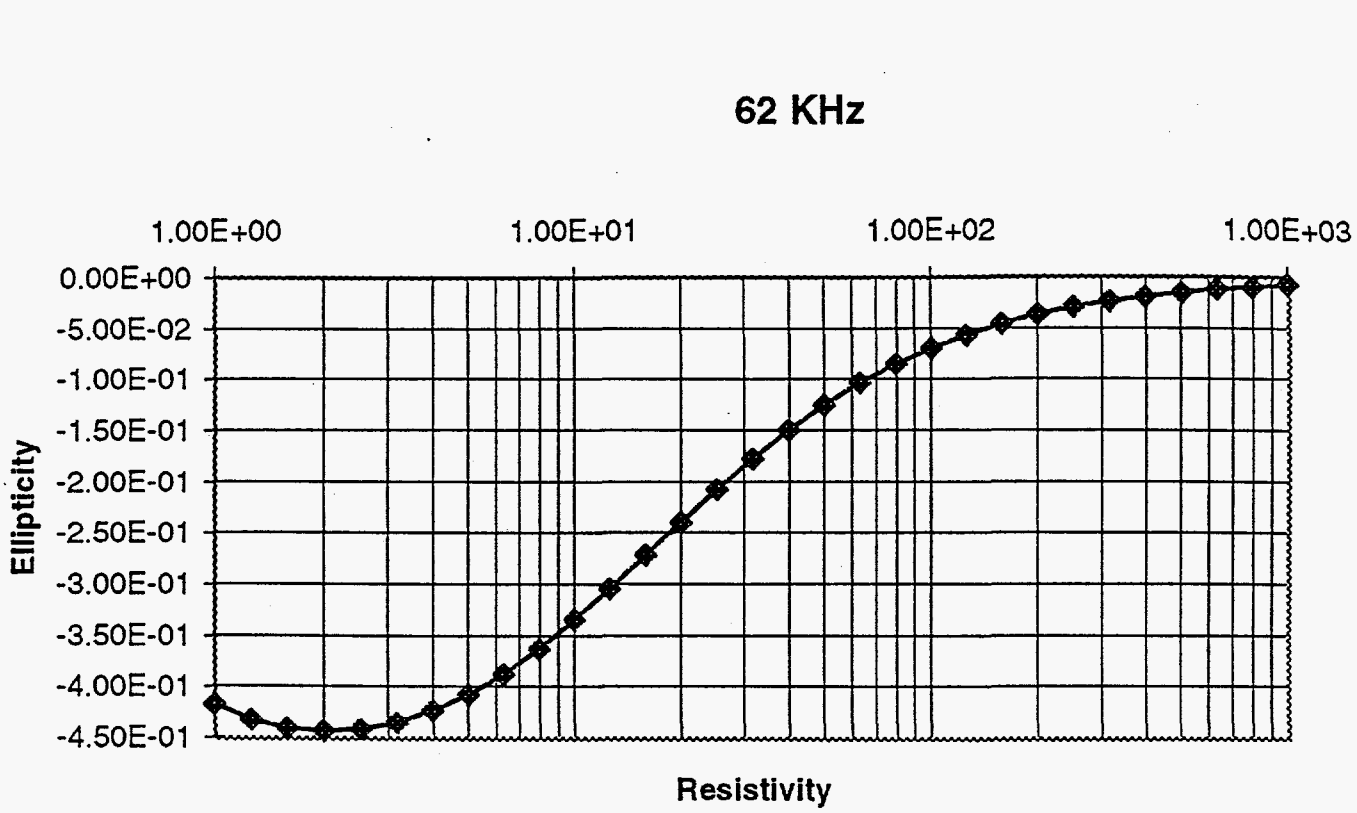

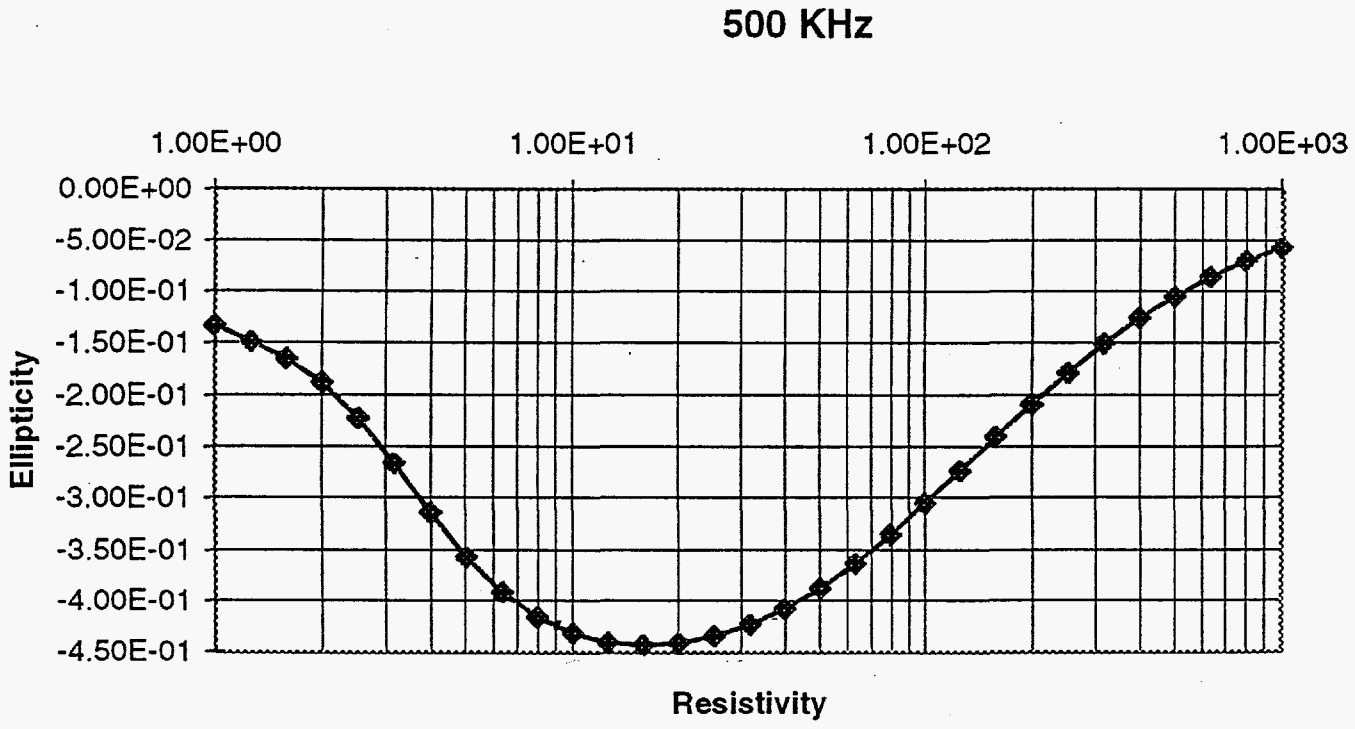

Figure 102. Ellipticity versus half-space resistivity plots for 62 and 500 kHz.

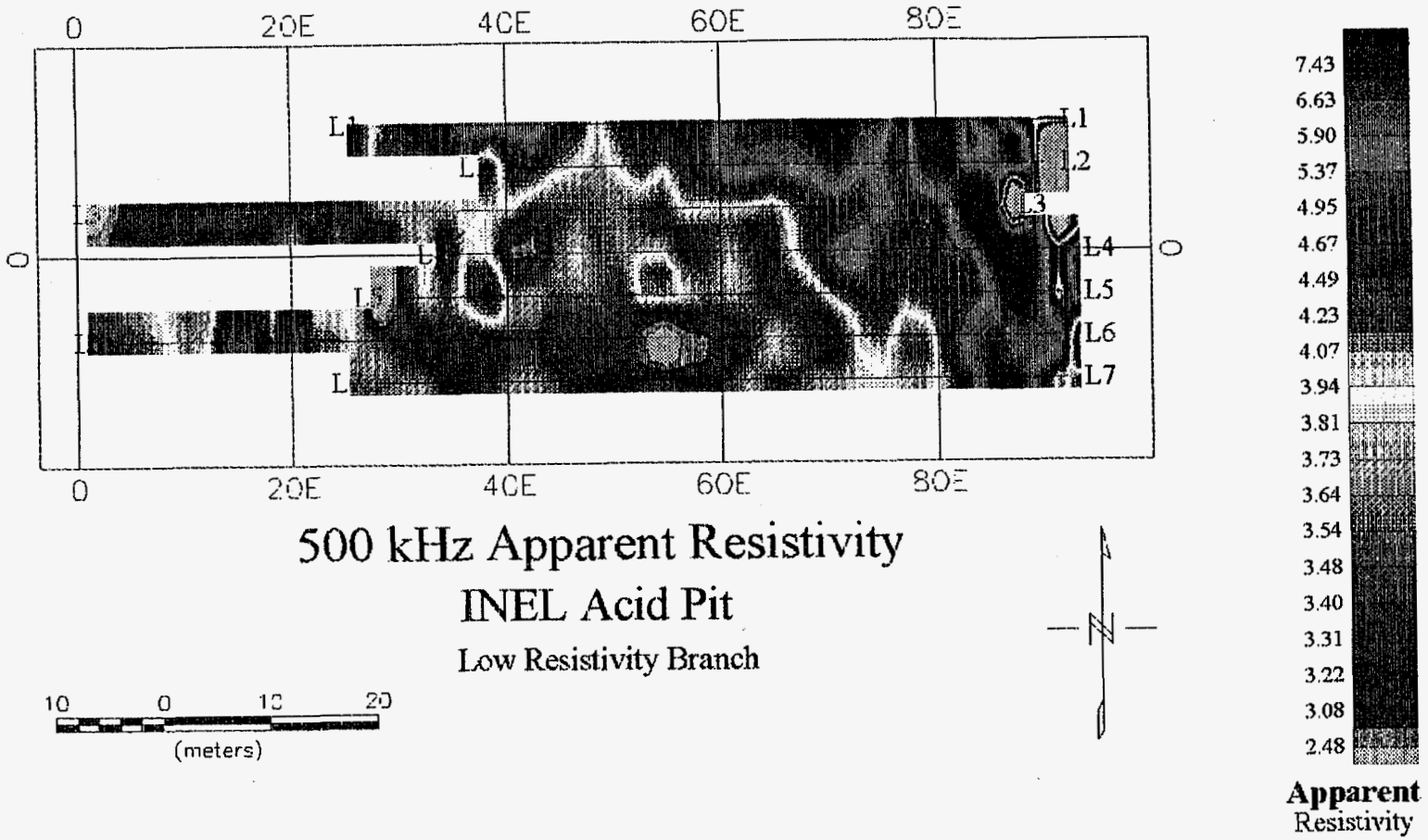

Figure 103. Contoured 500 kHz apparent-resistivity data corresponding to the ellipticity data in Figure 98. Depth of investigation for this frequency, spacing, and range of resistivities is approximately 0.5 - 1.5 m. See text for explanation of "low-resistivity branch."

Previous surveys at the INEL Acid Pit

MacLean (1993) ran a time domain electromagnetic (TDEM) survey over the Acid Pit. He found that the TDEM survey "did not show any response that can be correlated to the historical boundaries of the pit." Hasbrouck (1989) ran a ground conductivity survey using a Geonics EM31. This survey used a 4 m station spacing and 4 m line spacing (Hasbrouck, personal communication, 1997). This station and line spacing was similar to our data density (4 m line spacing and 2 m station spacing). Figure 104 shows a map of conductivities determined with the EM31. The EM31 survey showed a conductivity high (resistivity low) in the center of the acid pit site at generally the same location where we mapped a resistivity low. The EM31 survey does not appear to show the detail in the spatial extent that is apparent in the ellipticity survey results in Figures 100 and 103. The EM31 instrument uses a single frequency and therefore does not provide information from multiple depths. The wide frequency band that can be recorded with the ellipticity system can provide a map of the resistivities from shallow to large depths.

Conclusions

The combination of dense profiling, high-accuracy measurements, and multiple frequency information in the ellipticity survey provides an opportunity for much more detailed information on the contaminant location (both spatially and with depth) than can be obtained from conventional EM surveys. High-frequency, Ground Penetrating Radar (GPR), which can provide high-resolution images of the subsurface in some areas, has far too limited a depth of penetration (order of tens of cm) in these INEL soils to be of any use for mapping contaminants in the Acid Pit.

Now that we have some information on the type of anomaly to expect at the site, and after repair of our coil cables, we could collect much more information on the spatial extent and depth extent of the contaminants. By collecting data at many more frequencies and spacings, a complete three-dimensional picture of the contaminants could be constructed.

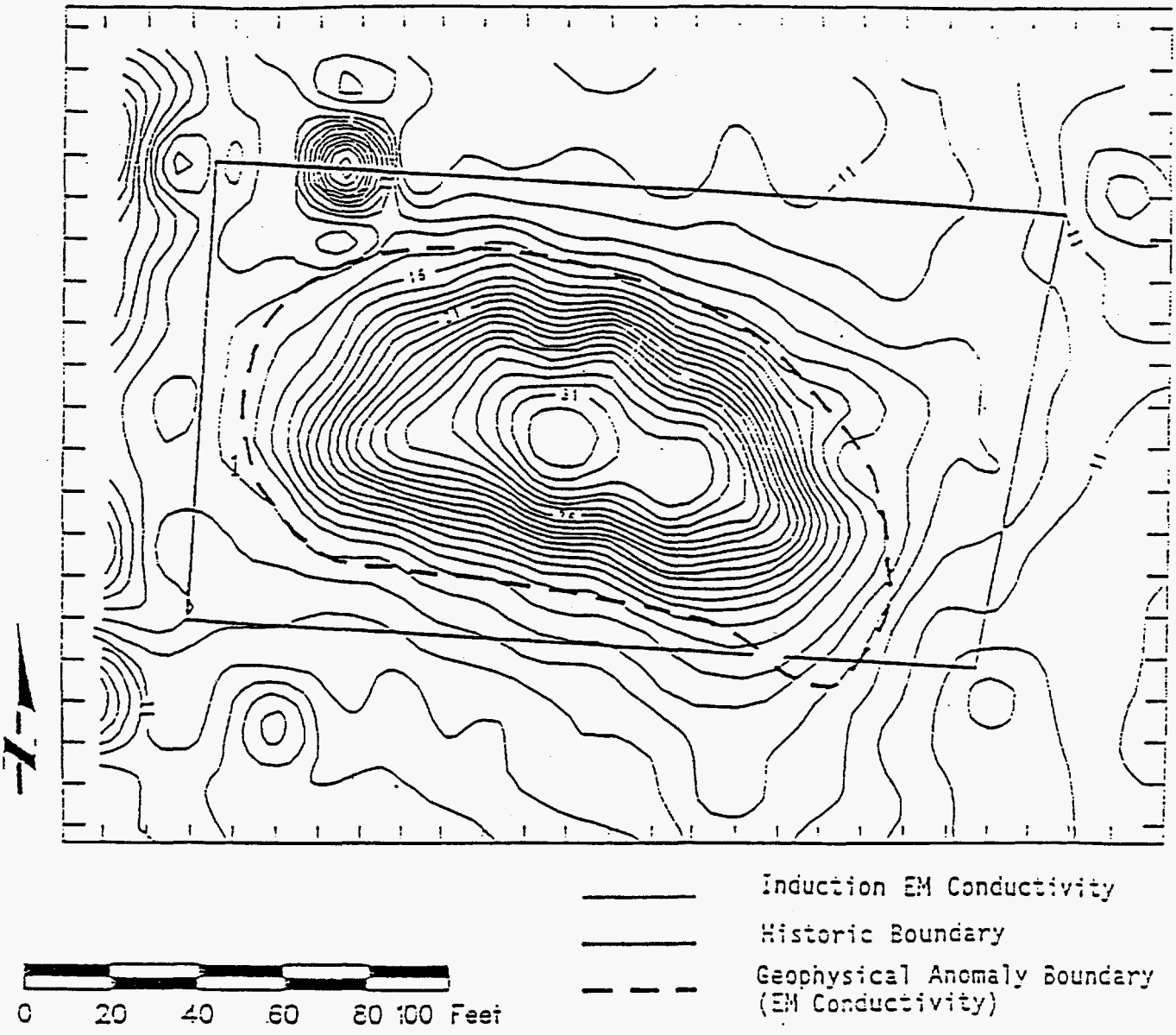

Figure 104. Contoured induction electromagnetic conductivity data (Hasbrouck, 1989).

CONCLUSIONS

The ellipticity system and neural network interpretation have been successfully tested in the field during four separate experiments: (1) using the physical modeling facility; (2) using buried targets at Avra Valley; (3) at the INEL Cold Test Pit; and (4) at the INEL acid pit.

The system was tested on a variety of targets to test depth of penetration, spatial resolution, tolerance to geologic and cultural noise. The depth of penetration is a function of antenna separation and resistivity of the ground. Results described in the previous sections indicate that we achieved a depth penetration of up to approximately one-half the antenna separation. A target as small as 7 cm diameter was resolvable in the physical modeling tank. High frequencies appear more sensitive to geologic noise, possibly due to variations in moisture content and shallow heterogeneities. Targets were tested in different soil types, moisture conditions, and cover material at INEL and Avra Valley. Targets ranged from resistive to conductive at the INEL site. The system successfully operated in the presence of most noise sources. A procedure has been developed to cancel electric field interference of high frequencies.

Neural networks were trained and tested on both synthetic and field data. The data visualization system we developed allows the user to efficiently interpret the data and provide quality control and assurance by showing interpreted fits to the field data in near-real time. Classification maps have been made for the INEL site that show target location and type. Responses from buried targets are complicated and are low amplitude, making interpretation by eye or graphical methods very difficult. The neural networks, however, are able to exploit the subtle variations in ellipticity to provide fast, accurate interpretations.

Like other major advances in sensor technology, our system has raised many opportunities for new experiments and interpretation approaches. Now that we have an excellent data acquisition capability, it is clear that the future lies in using these data. Advancements in interpretation and visualization, especially at frequencies above 2 MHz, need to be continued. We look forward to an opportunity to work closely with the EM interpretation project at INEL and LBL.

As experience is gained, survey design should be optimized to exploit the characteristics of each new site. We believe more exposure to operational problems in the DOE complex is needed to further refine all the capabilities of our high-resolution EM system. We will be proposing surveys at selected DOE sites in order to optimize the capabilities of this technology for DOE and other users in the Federal government and industry.

RELATED REPORTS

Ten reports have been written which describe the details of the EM system design and the neural network interpretation programs.

1) A High Frequency (32KHz-32MHz) Tri-axial Loop Antenna for an Electromagnetic Ellipticity Survey System, by Patrick S. Debroux and Ben K. Sternberg.

2) Design of a 32 KHz-32 MHz Transmitting Antenna for the LASI Ellipticity System, by Tao Liang and Ben K. Sternberg.

3) Testing the LASI HF Ellipticity System for FCC and ANSI Field-Intensity Regulation Compliance, by Melissa A. Stubben, Patrick S. Debroux, and Ben K. Sternberg.

4) Block Diagrams, Circuit Diagrams, Mechanical Drawings, and Photographs for a High-Frequency (31 KHz-32 MHz) Electromagnetic Ellipticity Survey System, by James M. Laird and Ben K. Sternberg.

5) Functional Description of EMSIS Software, by Terence Leach.

6) User's Manual for EMSIS, by Terence Leach.

7) User's Manual for XFER, by Terence Leach.

8) Neural Network Interpretation of High-frequency Ellipticity Data: 31 kHz-32 MHz, by Mary M. Poulton and Ralf A. Birken.

9) Data Visualization and Interpretation, by Ralf A. Birken and Mary M. Poulton.

10) A Laboratory Study of Electrical Properties of Soils from Avra Valley in a Frequency Range from 100 Hz to 100 MHz, by Tsylya M. Levitskaya and Ben K. Sternberg.

REFERENCES

Bak, N., Sternberg, B., Dvorak, S., and Thomas, S., 1993, Rapid high-accuracy electromagnetic soundings using a novel four-axis coil to measure magnetic field ellipticity: J. Applied Geophysics, 2, 235-245.

Birken, R. and Poulton, M., 1995, Neural Network interpretation scheme for frequency-domain electromagnetic ellipticity surveys: Proceedings of the SAGEEP '95, April 23-26, Orlando, FL, 349-357.

Birken, R., Poulton, M., and Sternberg, B., 1996, Physical modeling of small shallow conductive 3D-targets with high-frequency electromagnetics: Proceedings of the Second Environmental and Engineering Geophysical Society European Section Meeting, September 2-5, Nantes, France.

Birken, R., and Poulton, M., 1997a, Estimating resistivity and dielectric constant from high-frequency electromagnetic ellipticity data using neural networks: accepted in Proceedings of the High-Resolution Geophysics Workshop, January 6-8, Tucson, AZ.

Birken, R., and Poulton, M., 1997b, Neural network interpretation of high-frequency electromagnetic data: accepted in Proceedings of the SAGEEP '97, March 23-26, Reno, NV.

Fullagher, P., 1984, A uniqueness theorem for horizontal loop electromagnetic frequency soundings: Geophys. J. R. Astr. Soc., 559-566.

Haykin, S., 1994, Neural networks, A comprehensive foundation: MacMillan.

Hoversten, G., 1981, A comparison of time and frequency domain EM sounding techniques: Ph.D. Thesis, Univ. of California, Berkeley, 169 pp.

Hoversten, G., and Becker, A., 1995, EM1DSH with EMMODEL a Motif GUI: Numerical modeling of multiple thin 3D sheets in a layered earth: Univ. of California, Berkeley Report, June 12.

Jorgensen, D.K., Kuhns, D.J., King, J.J., and Loehr, C.A., 1994, WAG-7 operable unit (OU) 7-02 acid pit track 2 summary report, Idaho National Engineering Lab., EG&G Idaho, Inc., Idaho Falls, for U.S. D.O.E., Report No. EGG-ERD-10242.

Mac Lean, H.D., 1993, Time domain electromagnetic survey of three waste burial pits at INEL radioactive waste management complex, Chem-Nuclear Geotech, Inc., for U.S. D.O.E., Report No. DOE/ID/12584-130, Vol. 1.

Moody, J., and Darken, C., 1989, Fast learning in networks of locally-tuned processing units: Neural Computation, 1, 281-294.

Poulton, M., and Birken, R., 1997, Estimating one-dimensional models from frequency-domain electromagnetic data using modular neural networks: accepted in IEEE Geoscience and Remote Sensing journal.

Spies, B., and Frischknecht, F., 1991, Electromagnetic sounding: in M. Nabighian ed., Electromagnetic Methods in Applied Geophysics, Vol. 2, 285-425.

Sternberg, B., and Nopper, R., 1990, High-accuracy simultaneous calibration of signal measuring systems: Meas. Sci. Technol., 1, 225-230.

Sternberg, B., and Poulton, M., 1994, High-resolution subsurface imaging and neural network recognition: Proceedings of the symposium on the application of geophysics to engineering and environmental problems: SAGEEP '94, March 27-31, Boston, MA, 2, 847-855.

Sternberg, B., Thomas, S., Bak, N., and Poulton, M., 1991, High-resolution electromagnetic imaging of subsurface contaminant plumes: EPRI report RP-2485-11, Palo Alto, CA.

Thomas, S., 1996, Modeling and testing the LASI electromagnetic subsurface imaging system: Ph.D. Thesis, University of Arizona, Tucson, 193 pp.

Whiteside, H., and King, R., 1964, The loop antenna as a probe: IEEE Trans. On Ant. And Prop., 291-297.